MIGRATION AND VELOCITY ANALYSIS BY WAVEFIELD EXTRAPOLATION

A DISSERTATION
SUBMITTED TO THE DEPARTMENT OF GEOPHYSICS
AND THE COMMITTEE ON GRADUATE STUDIES
OF STANFORD UNIVERSITY
IN PARTIAL FULFILLMENT OF THE REQUIREMENTS
FOR THE DEGREE OF
DOCTOR OF PHILOSOPHY

Paul Constantin Sava
October 2004

© Copyright by Paul Constantin Sava
All Rights Reserved

I certify that I have read this dissertation and that in my opinion it is fully adequate, in scope and quality, as a dissertation for the degree of Doctor of Philosophy.

Biondo L. Biondi
(Principal Adviser)

I certify that I have read this dissertation and that in my opinion it is fully adequate, in scope and quality, as a dissertation for the degree of Doctor of Philosophy.

Jon F. Claerbout

I certify that I have read this dissertation and that in my opinion it is fully adequate, in scope and quality, as a dissertation for the degree of Doctor of Philosophy.

Jerry M. Harris

Approved for the University Committee on Graduate Studies:

To my Teachers...

Abstract

The *goal* of this thesis is to design new methods for imaging complex geologic structures of the Earth's Lithosphere. Seeing complex structures is important for both exploration and non-exploration studies of the Earth and it involves, among other things, dealing with complex wave propagation in media with large velocity contrasts.

The *approach* I use to achieve this goal is depth imaging using acoustic waves. This approach consists of two *components*: migration and migration velocity analysis. No accurate imaging is possible without accurate, robust and efficient solutions to both components.

The main technical *requirements* I impose on both imaging components call for the use of as much information as possible from the recorded wavefields, design of methods consistent with one-another, and accurate modeling of wave phenomena within the constraints of the available computational resources.

I address both migration and migration velocity analysis in the general *framework* of one-way wavefield extrapolation. In this context, both imaging components are consistent and use the entire acoustic wavefields with accurate, robust and computationally feasible techniques.

The migration state-of-the-art involves downward continuation of wavefields recorded at the Earth's surface. I introduce *Riemannian wavefield extrapolation* as a general framework for wavefield extrapolation. Downward continuation or extrapolation in tilted coordinates are special cases. With this technique, I overcome the steep-dip limitation of downward continuation, while retaining the main characteristics of wave-equation techniques.

Riemannian wavefield extrapolation propagates waves in semi-orthogonal coordinate systems that conform with the general direction of wave propagation. Therefore, extrapolation is done forward relative to the direction in which waves propagate, so I achieve high-angle accuracy with small-angle operators. Riemannian wavefield extrapolators can also be used for diving waves that cannot be easily handled using conventional downward continuation.

The velocity estimation state-of-the-art involves traveltime tomography from sparse reflectors picked on migrated images. I introduce *wave-equation migration velocity analysis* as a more accurate and robust alternative. With this technique, I overcome the instability of traveltime tomography caused by ray tracing in areas with high velocity contrasts.

I formulate wave-equation MVA with an operator based on linearization of wavefield extrapolation using the first-order Born approximation. I define the optimization objective function in the space of migrated images, in contrast with wave-equation tomography with objective function defined in the space of recorded data. Since the entire images are sensitive to migration velocities, I use image perturbations for optimization, in contrast with traveltime tomography which employs traveltime perturbations picked at selected locations. I construct image perturbations with residual migration operators by measuring flatness of angle-domain common image gathers, or by measuring spatial focusing of diffracted energy.

Preface

All of the figures in this thesis are marked with one of the three labels: [ER], [CR], and [NR]. These labels define to what degree the figure is reproducible from the data directory, source code and parameter files provided on the web version of this thesis [1].

ER denotes Easily Reproducible. My claim is that you can reproduce such figures from the programs, parameters, and data included in the electronic document. I assume that you have a UNIX workstation with Fortran, C, X-Window system, and the software on the webpage at your disposal. Before the publication of the electronic document, someone else in the SEP group tested my claims by destroying and rebuilding all ER figures.

CR denotes Conditional Reproducibility. My claim is that the commands are in place to reproduce the figure if certain resources are available. For example, you might need a large or proprietary data set. You may also need a super computer, or you might simply need a large amount of time (more than two hours) on a workstation. Before the publication of the electronic document, someone else in the SEP group tested my claims by following all rules used to generate a figure.

CR figures in Chapter 3 and Chapter 4 require more than several hours of processing on a Linux computer cluster. The real datasets used in the examples are part of the SEP data library. CR figures in Chapter 6 use proprietary Gulf of Mexico data which cannot be distributed with the thesis. They also require processing on Linux computer clusters for one day or more.

[1] http://sepwww.stanford.edu/public/docs/sep118

NR denotes Non-Reproducible. This class of figure is considered non-reproducible. Figures in this class are scans and artists' drawings.

Acknowledgments

I am dedicating this thesis to my *Teachers*, by which I mean family, friends, professors and others who knowingly or unknowingly have taught me something throughout my life. I am grateful to all, since who I am and what I know is due to them to the largest degree.

My learning journey began with my immediate family, parents and grandparents, from whom I learned the values of hard work, high standards and focus on what is important. My parents, in particular, dedicated much of their energy and resources to their children's education. My current achievements are their achievements, to a large degree, and I am grateful for the education they gave me, which is their most valuable and most enduring gift.

I am grateful to the Stanford Exploration Project students, faculty and sponsors, without whose support I could not have completed this thesis. My advisers, Biondo Biondi and Jon Claerbout, helped me get started on my research and bombarded me with ideas and advice, but then allowed me to venture at will in uncharted research territory. This is what I think great advising is all about, and both deserve recognition for fulfilling their duty. I am also grateful to the SEP alumni, whose outstanding achievements turned SEP into one of the leaders in seismic imaging and who remain a model for current and future generations of students.

Of all my SEP colleagues, Sergey Fomel deserves a special mention. He was my student mentor upon my arrival at SEP many years back, officemate for some years, a frequent collaborator in many research projects ever since, and remains a close friend today. James Rickett, Antoine Guitton and Jeff Shragge have also been influential collaborators at various times of my SEP years and I am grateful for their insight and challenges to my thinking.

I have also benefited from interaction with my other SEP colleagues of older or younger

generations: Morgan Brown, Marie Clapp, Daniel Rosales, Louis Vaillant, Gabriel Alvarez, Alejandro Valenciano, Nick Vlad, Bill Curry, Jesse Lomask, Guojian Shan, Brad Artman and Thomas Tisserant. We have shared way too many seminar hours, although I think that in some strange way this brought us closer, helped us understand each-other better and stimulated collaboration and research.

I would also like to thank Diane Lau who helped me in countless occasions do what was necessary to bypass seemingly impossible administrative hurdles. She made my life at Stanford much easier than it could have been. I am a grateful beneficiary of her kindness and generous support.

I am also grateful to close friends of older SEP generations, mainly Mihai Popovici, who many years ago brought me straight from San Francisco International Airport to Mitchell Building (where Jon promptly added me to the seminar list). I had no idea then that it would take me so long to make the trip back, but it was a fine ride and I enjoyed it a lot.

Finally, I would like to thank my ultimate teachers, Diana and Iulia, who with love, patience and generosity teach me every day what real life is all about. There are no words to express how happy and grateful I am to have them by my side.

Contents

Abstract **vii**

Preface **ix**

Acknowledgments **xi**

1 Introduction **1**

1.1 Motivation 1

1.2 Seismic depth imaging 2

1.2.1 Migration 2

1.2.2 Velocity estimation 3

1.3 Thesis overview and contributions 3

2 Riemannian wavefield extrapolation **7**

2.1 Overview 7

2.2 Introduction 7

2.3 Acoustic wave-equation 12

2.4 One-way wave-equation 14

2.5 Mixed-domain solutions to the one-way wave-equation 17
2.6 Finite-difference solutions to the one-way wave equation 18
2.7 Examples 20
2.8 Discussion 32
2.9 Conclusions 36
2.10 Acknowledgment 36

3 Angle-domain common image gathers **37**
3.1 Overview 37
3.2 Introduction 37
3.3 Angle gathers in the image-space 40
3.4 Regularization of the angle-domain 43
3.5 Examples 44
3.6 Discussion 50
3.7 Conclusions 53
3.8 Acknowledgment 55

4 Prestack residual migration **57**
4.1 Overview 57
4.2 Introduction 58
4.3 Stolt migration 59
4.4 Prestack Stolt residual migration 60
4.5 Common-azimuth Stolt residual migration 61

4.6 Examples 62
4.7 Discussion 71
4.8 Conclusions 72
4.9 Acknowledgment 72

5 Wave-equation migration velocity analysis **73**

5.1 Overview 73
5.2 Introduction 74
5.3 Recursive wavefield extrapolation 76
5.4 WEMVA objective function 79
5.5 WEMVA operator 81
5.6 Cycle skipping in image perturbations 85
5.7 Linearized image perturbations 89
5.8 WEMVA sensitivity kernels 91
5.8.1 Fréchet derivative integral kernels 95
5.8.2 Sensitivity kernels examples 104
5.9 WEMVA cost 105
5.10 Conclusions 107
5.11 Acknowledgment 108

6 Examples **109**

6.1 Simple WEMVA example 109
6.2 Subsalt WEMVA examples 112

6.2.1 Sigsbee 2A synthetic model 114
6.2.2 2D field data example 125
6.2.3 3D field data example 135
6.3 Diffraction-focusing WEMVA example 151
6.3.1 Delineation of rough salt bodies 152
6.3.2 Imaging of GPR data 162
6.3.3 Discussion 163
6.4 Conclusions 166
6.5 Acknowledgment 167

7 Conclusions **169**

A Riemannian wavefield extrapolation **171**
A.1 2D point-source ray coordinates 171
A.2 2D finite-difference solution to the 15° equation 172

B Angle-domain common image gathers **175**
B.1 Reflection angle formula 175

C Wave-equation migration velocity analysis **177**
C.1 First-order Born scattering operators 177
C.2 Linearized image perturbations 181

Bibliography **185**

List of Figures

2.1 Ray coordinate systems are superior to tilted coordinate systems for imaging overturning waves using one-way wavefield extrapolators. Overturning reflected energy may become evanescent in tilted coordinate systems (a), but stays non-evanescent in ray coordinate systems (b). 10

2.2 Extrapolated energy is attenuated at beam boundaries (a), but is propagated in a Riemmanian coordinate system (b). 11

2.3 Simple linear gradient model: Panels (a) and (c) correspond to Cartesian coordinates, and panels (b) and (d) correspond to ray coordinates. Velocity model with an overlay of the ray coordinate system initiated by a point source at the surface (a); image obtained by downward continuation in Cartesian coordinates with the 15° equation (c); velocity model with an overlay of the ray coordinate system (b); image obtained by wavefield extrapolation in ray coordinates with the 15° equation (d). 22

2.4 Simple linear gradient model: the image obtained by downward continuation in Cartesian coordinates with the 15° equation (a); the image in panel (a) interpolated to ray coordinates (b); image obtained by extrapolation in ray coordinates with the 15° equation (d); the image in panel (d) interpolated to Cartesian coordinates (c). 23

2.5 Gaussian anomaly model: Panels (a) and (c) correspond to Cartesian coordinates, and panels (b) and (d) correspond to ray coordinates. Velocity model with an overlay of the ray coordinate system initiated by a point source at the surface (a); image obtained by downward continuation in Cartesian coordinates with the 15° equation (c); velocity model with an overlay of the ray coordinate system (b); image obtained by wavefield extrapolation in ray coordinates with the 15° equation (d). 25

2.6 Gaussian anomaly model: the image obtained by downward continuation in Cartesian coordinates with the 15° equation (a); the image in panel (a) interpolated to ray coordinates (b); image obtained by extrapolation in ray coordinates with the 15° equation (d); the image in panel (d) interpolated to Cartesian coordinates (c). 26

2.7 Marmousi model: Panels (a) and (c) correspond to Cartesian coordinates, and panels (b) and (d) correspond to ray coordinates. Velocity model with an overlay of the ray coordinate system initiated by a point source at the surface (a); image obtained by downward continuation in Cartesian coordinates with the 15° equation (c); velocity model with an overlay of the ray coordinate system (b); image obtained by wavefield extrapolation in ray coordinates with the 15° equation (d). 27

2.8 Marmousi model: the image obtained by downward continuation in Cartesian coordinates with the 15° equation (a); the image in panel (a) interpolated to ray coordinates (b); image obtained by extrapolation in ray coordinates with the 15° equation (d); the image in panel (d) interpolated to Cartesian coordinates (c). 28

2.9 Marmousi model: Velocity model (a); image obtained by wavefield extrapolation in ray coordinates using the 15° equation (b) and the split-step equation (c); image obtained using downward continuation in Cartesian coordinates with the 45° equation (d), the 15° equation (e) and the split-step equation (f). 29

2.10 Marmousi model: Velocity model (a); image obtained by wavefield extrapolation in ray coordinates using the 15° equation (b) and the split-step equation (c); image obtained using downward continuation in Cartesian coordinates with the 45° equation (d), the 15° equation (e) and the split-step equation (f). 30

2.11 The effect of neglecting the first order terms in Riemannian wavefield extrapolation. From left to right the velocity model with an overlay of the ray coordinate system (a), extrapolation with equation (2.13) including the first order terms (b), and extrapolation with the simplified equation (2.16) (c). Panels (b) and (c) are gained equally, illustrating that the changes caused by neglecting the first-order terms affect the amplitudes and not the kinematics. 31

2.12 A comparison of wavefields computed by time-domain acoustic finite-difference modeling (a), and wavefields computed by Riemannian wavefield extrapolation (b). 33

2.13 Shot-profile migration sketch. Sources (a) and receivers (b) are both extrapolated in a ray coordinate system appropriate for overturning waves. 35

3.1 Offset-domain and angle-domain common image gathers. A schematic comparison between Kirchhoff and wave-equation methods. 39

3.2 Reflection rays in an arbitrary-velocity medium. 41

3.3 Ideal offset-domain and angle-domain common image gathers. 45

3.4 2D synthetic model: from top to bottom, reflectivity model, correct and incorrect slownesses. 47

3.5 Synthetic model imaged using the *correct* velocity model: section obtained by imaging at zero time and zero offset (top), angle gather created in the image space (bottom left), and angle gather created in the data space (bottom right). 48

3.6 Synthetic model imaged using the *incorrect* velocity model: section obtained by imaging at zero time and zero offset (top), angle gather created in the image space (bottom left), and angle gather created in the data space (bottom right). 49

3.7 2D real data example: seismic section obtained by imaging at zero time and zero offset. 50

3.8 2D real data example: from left to right, offset-gather (right panel) and angle gathers, computed in the image-space (middle panel) and the data-space (right panel) 51

3.9 2D real data example: a comparison of an angle gather obtained without regularization (left) and an angle gather obtained with regularization (right). . . . 52

3.10 3D common-azimuth example: seismic section obtained by imaging at zero time and zero offset. The vertical line corresponds to the CIGs in Figure 3.11. 53

3.11 3D common-azimuth example: offset-gather (left panel) and angle gather (right panel) corresponding to the vertical line in Figure 3.10. 54

4.1 Synthetic model. From top to bottom, slowness model, reflectivity model and the zero offset section of the modeled 2D prestack data. 64

4.2 Migrated image (zero offset section) and angle-domain CIG for the synthetic data in Figure 4.1 obtained using the correct velocity model. 65

4.3 Migrated image (zero offset section) and angle-domain CIG for the synthetic data in Figure 4.1 obtained using the incorrect velocity model scaled by $\rho = 0.8$. 65

4.4 Residually migrated image (zero offset section) and angle-domain CIG for the synthetic data in Figure 4.1 obtained from the image in Figure 4.3 after residual migration with the correct velocity ratio $\rho = 0.8$. 66

4.5 Migrated image of the North Sea data. The area of interest is surrounded by the thick box. 66

4.6 Prestack Stolt residual migration for a range of velocity ratio parameters (ρ) from 1.0 to 0.92. All panels correspond to the box in Figure 4.5. 68

4.7 A comparison of the original image (top panel) with the improved images obtained by residual moveout (middle panel) and the image after residual migration with a constant velocity ratio parameter $\rho = 0.94$ (bottom panel). All panels correspond to the box in Figure 4.5. 69

4.8 A comparison of the original image (top panel) with the image obtained by residual migration (middle panel) with a spatially varying ρ. The velocity ratio parameter ρ is ranging from 0.91 to 1.00 (bottom panel). All panels correspond to the box in Figure 4.5. 70

5.1 WEMVA flowchart. Box A: background wavefield. Box B: forward WEMVA operator. Box C: adjoint WEMVA operator. 82

5.2 Monochromatic WEMVA example: background wavefield (a), slowness perturbation (b), wavefield perturbation (c), slowness backprojection (d). 84

5.3 Wide-band WEMVA example: background image (a), slowness perturbation (b), image perturbation (c), slowness backprojection (d). 85

5.4 Comparison of image perturbations obtained as a difference between two migrated images (b) and as the result of the forward WEMVA operator applied to the known slowness perturbation (c). Panel (a) depicts the background image corresponding to the background slowness. Since the slowness perturbation is small (0.1%), the image perturbations in panels (b) and (c) are practically identical. 86

5.5 Comparison of slowness backprojections using the WEMVA operator applied to image perturbations computed as a difference between two migrated images (b,d) and as the result of the forward WEMVA operator applied to a known slowness perturbation (c,e). Panel (a) depicts the background image corresponding to the background slowness. Since the slowness perturbation is small (0.1%), the image perturbations in panels (b) and (c), and the fat rays in panels (d) and (e) are practically identical. 88

5.6 Comparison of image perturbations obtained as a difference between two migrated images (b) and as the result of the forward WEMVA operator applied to the known slowness perturbation (c). Panel (a) depicts the background image corresponding to the background slowness. Since the slowness perturbation is large (20%), the image perturbations in panels (b) and (c) are different from each-other. 90

5.7 Comparison of slowness backprojections using the WEMVA operator applied to image perturbations computed as a difference between two migrated images (b,d) and as the result of the forward WEMVA operator applied to a known slowness perturbation (c,e). Panel (a) depicts the background image corresponding to the background slowness. Since the slowness perturbation is large (20%), the image perturbations in panels (b) and (c) and the fat rays in panels (d) and (e) are different from each-other. Panel (d) shows the typical behavior associated with the breakdown of the Born approximation. 92

5.8 A schematic description of the method used for computing linearized image perturbations. The dashed line corresponds to image changes described by residual migration with various values of the velocity ratio parameter (ρ). The straight solid line corresponds to the linearized image perturbation computed with an image gradient operator applied to the reference image scaled at every point by the difference of the velocity ratio parameter $\Delta\rho$. 93

5.9 Comparison of slowness backprojections using the WEMVA operator applied to image perturbations computed with the differential image perturbation operator (b,d) and as the result of the forward WEMVA operator applied to a known slowness perturbation (c,e). Panel (a) depicts the background image corresponding to the background slowness. Despite the fact that the slowness perturbation is large (20%), the image perturbations in panels (b) and (c) and the fat rays in panels (d) and (e) are practically identical, both in shape and in magnitude. 94

5.10 The dependence of sensitivity kernels to frequency and image perturbation. From top to bottom, the frequency range is $1-4$ Hz, $1-8$ Hz, $1-16$ Hz and $1-32$ Hz. The left column corresponds to kinematic image perturbations, and the right column corresponds to dynamic image perturbations. The wavefield is produced from a point source. 96

5.11 The dependence of sensitivity kernels to frequency and image perturbation. From top to bottom, the frequency range is $1-4$ Hz, $1-8$ Hz, $1-16$ Hz and $1-32$ Hz. The left column corresponds to kinematic image perturbations, and the right column corresponds to dynamic image perturbations. The wavefield is produced by a horizontal incident plane-wave. 97

5.12 3D slowness model. 98

5.13 3D sensitivity kernels for wave-equation MVA. The frequency range is $1-16$ Hz. The kernels are complicated by the multipathing occurring as waves propagate through the rough salt body. The image perturbation corresponds to a kinematic shift. 99

5.14 3D sensitivity kernels for wave-equation MVA. The frequency range is $1-16$ Hz. The kernels are complicated by the multipathing occurring as waves propagate through the rough salt body. The image perturbation corresponds to an amplitude scaling. 100

5.15 Cross-section of 3D sensitivity kernels for wave-equation MVA. The left panel corresponds to an image perturbation produced a kinematic shift, while the right panel corresponds to an image perturbation produced by amplitude scaling. The lowest sensitivity occurs in the center of the kinematic kernel (left). In contrast, the maximum sensitivity occurs in the center of the kernel (right). 101

6.1 Comparison of common image gathers for image perturbations obtained as a difference between two migrated images (c), as the result of the forward WEMVA operator applied to the known slowness perturbation (d), and as the result of the differential image perturbation operator applied to the background image (e). Panel (a) depicts the background image corresponding to the background slowness, and panel (b) depicts an improved image obtained from the background image using residual migration. 110

6.2 WEMVA applied to a simple model with flat reflectors. The background image (a), the image updated after one non-linear iteration (b), and the image computed with the correct slowness (c). 111

6.3 WEMVA applied to a simple model with flat reflectors. The zero-offset of the image perturbation (a), the slowness update after the first non-linear iteration (b), and the convergence curve of the first linear iterations (c). 111

6.4 Wavepaths for frequencies between 1 and 26 Hz for various locations in the image and a point on the surface. Each panel is an overlay of three elements: the slowness model, the wavefield corresponding to a point source on the surface at $x = 16$ km, and wavepaths from a point in the subsurface to the source. 115

6.5 Frequency dependence of wavepaths between a location in the image and a point on the surface. The different wavepaths correspond to frequency bands of $1-5$ Hz (top), $1-16$ Hz (middle) and $1-64$ Hz (bottom). The larger the frequency band, the narrower the wavepath. 116

6.6 Sigsbee 2A synthetic model. The background slowness model (top) and the correct slowness perturbation (bottom). 117

6.7 Migration with the correct slowness. Sigsbee 2A synthetic model. The zero offset of the prestack migrated image (top) and angle-domain common image gathers at equally spaced locations in the image (bottom). Each ADCIG corresponds roughly to the location right above it. 118

6.8 Migration with the background slowness. Sigsbee 2A synthetic model. The zero offset of the prestack migrated image (top) and angle-domain common image gathers at equally spaced locations in the image (bottom). Each ADCIG corresponds roughly to the location right above it. 119

6.9 Residual migration for a CIG at $x = 10$ km. Sigsbee 2A synthetic model. The top panel depicts angle-domain common image gathers for all values of the velocity ratio, and the bottom panel depicts semblance panels used for picking. All gathers are stretched to eliminate the vertical movement corresponding to different migration velocities. The overlain line indicates the picked values at all depths. 121

6.10 Sigsbee 2A synthetic model. The top panel depicts the velocity ratio difference $\Delta\rho = 1 - \rho$ at all locations, and the bottom panel depicts a weight indicating the reliability of the picked values at every location. The picks in the shadow zone around $x = 12$ km are less reliable than the picks in the sedimentary region around $x = 8$ km. All picks inside the salt are disregarded. 122

6.11 Sigsbee 2A synthetic model. The correct slowness perturbation (top) and the inverted slowness perturbation (bottom). 123

6.12 Migration with the updated slowness. Sigsbee 2A synthetic model. The zero offset of the prestack migrated image (top) and angle-domain common image gathers at equally spaced locations in the image (bottom). Each ADCIG corresponds roughly to the location right above it. 124

6.13 Angle-domain common image gathers at $x = 8$ km. Sigsbee 2A synthetic model. Each panel corresponds to a different migration velocity: migration with the correct velocity (left), migration with the background velocity (center) and migration with the updated velocity (right). 126

6.14 Angle-domain common image gathers at $x = 10$ km. Sigsbee 2A synthetic model. Each panel corresponds to a different migration velocity: migration with the correct velocity (left), migration with the background velocity (center) and migration with the updated velocity (right). 127

6.15 Angle-domain common image gathers at $x = 12$ km. Sigsbee 2A synthetic model. Each panel corresponds to a different migration velocity: migration with the correct velocity (left), migration with the background velocity (center) and migration with the updated velocity (right). 128

6.16 Gulf of Mexico data. Migrated image superimposed on slowness (top), residual migration picks (middle), and picking weight (bottom). The migration corresponds to the background slowness. 130

6.17 Gulf of Mexico data. Residual migration for a common image gather about one third from the left edge of the image in figure 6.16. Angle-domain CIGs (left) and semblance (right) with the picked velocity ratio. 131

6.18 Gulf of Mexico data. Migrated image superimposed on slowness (top), residual migration picks (middle), and picking weight (bottom). The migration corresponds to the updated slowness after iteration 1. Compare with figure 6.16. 132

6.19 Gulf of Mexico data. Migrated image superimposed on slowness (top), residual migration picks (middle), and picking weight (bottom). The migration corresponds to the updated slowness after iteration 2. Compare with figure 6.16. 133

6.20 A comparison of normal incidence WEMVA (top panel) with prestack WEMVA (bottom panel). Prestack inversion produces anomalies with higher vertical resolution, due to the increased angular coverage. 134

6.21 Image and velocity comparison for various types of velocity updates in WEMVA. From top to bottom, the image created with the background velocity (top), the image created with the velocity updated with normal incidence WEMVA (middle), and the image created with the velocity updated with prestack WEMVA (bottom). 136

6.22 3D Gulf of Mexico example. Initial slowness model. Compare with Figure 6.32. 137

6.23 3D Gulf of Mexico example. Initial image. Compare with Figure 6.33. . . . 138

6.24 3D Gulf of Mexico example. Box selected for WEMVA. 139

6.25 3D Gulf of Mexico example. Velocity ratio perturbation picked after residual migration. 140

6.26 3D Gulf of Mexico example. Data residual weight. 141

6.27 3D Gulf of Mexico example. Image perturbation. 141

6.28 3D Gulf of Mexico example. Slowness perturbation. 142

6.29 3D Gulf of Mexico example. Data residual function of iterations. 143

6.30 3D Gulf of Mexico example. Initial slowness model in the inversion box. Compare with Figure 6.31. 144

6.31 3D Gulf of Mexico example. Updated slowness model in the inversion box. Compare with Figure 6.30. 144

6.32 3D Gulf of Mexico example. Updated slowness model. Compare with Figure 6.22. 145

6.33 3D Gulf of Mexico example. Updated image. Compare with Figure 6.23. . . 146

6.34 3D Gulf of Mexico example. Inline comparison of initial (left) and final (right) models. Image stack (top), angle gathers (middle) and image semblance (bottom). 147

6.35 3D Gulf of Mexico example. Inline comparison of initial (left) and final (right) models. Image stack (top), angle gathers (middle) and image semblance (bottom). 148

6.36 3D Gulf of Mexico example. Crossline comparison of initial (left) and final (right) models. Image stack (top), angle gathers (middle) and image semblance (bottom). 149

6.37 3D Gulf of Mexico example. Crossline comparison of initial (left) and final (right) models. Image stack (top), angle gathers (middle) and image semblance (bottom). 150

6.38 Zero-offset synthetic data used for focusing migration velocity analysis. . . . 153

6.39 Zero-offset migrated image for the synthetic data in figure 6.38: velocity model (a), and migrated image (b). Migration using the initial $v(z)$ velocity model. 154

6.40 Residual migration applied to the image migrated with the initial velocity model, figure 6.39. From top to bottom, the images correspond to the ratios $\rho = 1.04, 1.00, 0.96, 0.92, 0.88$. 156

6.41 Residual migration picks (a) and the associated confidence weights (b). . . . 157

6.42 Slowness perturbation (a), derived from an image perturbation (b) derived from the background image in figure 6.39 and the velocity ratio picks in figure 6.41. 158

6.43 Zero-offset migrated image for the synthetic data in figure 6.38: velocity model (a), and migrated image (b). Migration using the updated velocity. . . 159

6.44 Prestack migrated images using the initial velocity model (a) and the updated velocity model (b). The top panels depict image stacks and the bottom panels depict angle-domain common image gathers. 160

6.45 Angle-domain common image gather obtained after migration with the initial velocity model (a) and the updated velocity model (b). 161

6.46 Zero-offset GPR data used for focusing migration velocity analysis. 162

6.47 Zero-offset migrated images for the data in figure 6.46 using the initial velocity (a) and the updated velocity (b). 164

6.48 Detail of the images depicted in figure 6.47. Migration with the initial velocity (a), updated slowness model (b) and migration with the updated slowness (c). The window corresponds to $x = 20 - 24$ ft and $z = 2$ ft. 165

6.49 Detail of the images depicted in figure 6.47. Migration with the initial velocity (a), updated slowness model (b) and migration with the updated slowness (c). The window corresponds to $x = 34$ ft and $z = 1.8$ ft 165

Chapter 1

Introduction

1.1 Motivation

A good geological understanding of the Earth requires integration of different types of data from various sources. However, some of the most successful geophysical investigation methods for the Earth's Lithosphere are based on seismic data. In particular, seismic data can be used to create images of the Earth from waves reflected on discontinuities of rock properties in the subsurface (Karcher, 1973). These methods, commonly referred to as *seismic imaging* aim at creating maps of the Earth's reflectivity function of spatial location, from which we can derive information about the physical properties of the rocks at those locations. Estimating rock properties is the real goal of seismic processing in general, and it should be the goal of seismic imaging in particular.

The elastic wavefields of reflected seismic waves recorded at the surface of the Earth carry enormous information about the physical properties of the subsurface. However, those wavefields have traditionally been underutilized, both due to limits of computing power and due to limits of knowledge regarding imaging methodology. One of the recurrent themes in seismic imaging over the past decades was that of approximation, e.g. *data approximation* – acoustic vs. elastic, *model approximation* – $v(z)$ vs. $v(x,y,z)$ or isotropic vs. anisotropic, *operator approximation* – rayfield-based vs. wavefield-based, etc.

Those approximations were driven by practical considerations, since the initial targets of seismic imaging were simple enough to justify using crude approximations. However, as the targets of seismic imaging become more complex, the methodology required needs to increase in complexity and use more of the information carried by the recorded elastic wavefields. The past decades have shown tremendous progress in this respect, as illustrated by many accurate images of complicated targets. The pace of innovation is gaining speed, and we are likely to witness more progress in imaging methodology in the coming years. This thesis is a stepping stone along this path.

1.2 Seismic depth imaging

Depth imaging requires two main elements: velocity estimation and depth migration. Depth migration requires a velocity model, and velocity estimation requires a migrated image. This circular dependency is usually solved in an iterative loop, part of a large optimization problem. Clearly, accurate imaging is not ultimately possible unless both the migration and velocity analysis problems are solved accurately.

The current state-of-the-art in seismic imaging has wave-equation migration standing for the depth migration algorithm and traveltime tomography standing for the velocity estimation algorithm. Although this pair of methods proved successful in cases of many complicated structures, neither one is ideal for the task, as illustrated by their failures (Gray et al., 2001). The goal of this thesis is to push the limits for both, and design more accurate and powerful methodologies for the future.

1.2.1 Migration

The state-of-the-art in migration methodology is represented by migration using downward continuation (Claerbout, 1985). Such methods are accurate, robust, and capable of handling models with large and sharp velocity variations. These methods naturally handle multipathing occurring in complex geology. However, migration by downward continuation limits angular accuracy since it is designed for energy propagating mainly in the vertical direction.

A first goal of this thesis is to eliminate the dip limitation of wave-equation migration. The solution proposed involves wavefield extrapolation in general Riemannian coordinates which follow the general direction of wave propagation in the physical space. In this case, extrapolation is done forward relative to the direction of wave propagation, and not in the arbitrary downward direction as in conventional migration.

1.2.2 Velocity estimation

The state-of-the-art in velocity estimation is represented by traveltime tomography (Bishop et al., 1985; Al-Yahya, 1989; Stork, 1992; Etgen, 1993; Kosloff et al., 1996). Such methods are fast and accurate for relatively simple models with small velocity contrasts. However, traveltime tomography often fails due to the instability of ray tracing for complex velocity models with sharp boundaries.

A second goal of this thesis is to overcome those limitations by designing a velocity analysis method based on wavefield extrapolation. A method of this type naturally inherits the characteristics of wavefield extrapolation, mainly robustness in presence of large and sharp velocity contrasts, band-limited model sensitivity and multipathing.

Conventional migration velocity analysis employs *traveltime perturbations* derived from moveout measurements on migrated common image gathers. In this dissertation, I modify this methodology to employ *image perturbations*, which can be defined either from moveout differences and/or from spatial focusing. Such analysis requires development of image perturbation methods (residual migration) and techniques for analysis of image quality (angle transformation).

1.3 Thesis overview and contributions

Riemannian wavefield extrapolation: In Chapter 2, I extend one-way wavefield extrapolation to a general coordinate framework which can be described using Riemannian

geometry. Such natural coordinates allow for accurate wave propagation in arbitrary directions (Sava and Fomel, 2004), in contrast with conventional downward continuation which favors waves propagating vertically. A special case of Riemannian coordinates is represented by ray coordinates obtained by ray tracing in a smooth background medium. This method can be used for imaging of steeply dipping reflectors or overturning reflections.

Angle-domain common image gathers: In Chapter 3, I present a method for constructing angle-domain common image gathers (reflectivity function of scattering angle) from images obtained by wavefield extrapolation. The method described in this thesis operates in the image space, which enables transformations between the angle and offset domains without data remigration. Since the transformation to the angle-domain is separated from the migration itself, this method can be used to construct angle gathers for shot-geophone migration (Sava and Fomel, 2003), for shot-profile migration (Rickett and Sava, 2002), for converted waves (Rosales and Rickett, 2001), and for reverse-time imaging (Biondi and Shan, 2002). The method can also be used for AVA studies (Sava et al., 2001a), for multiple suppression after migration (Sava and Guitton, 2004), or for migration velocity analysis (Chapter 5).

Prestack Stolt residual migration: In Chapter 4, I extend to the prestack domain the residual migration method introduced by Stolt (1996). Residual migration produces images corresponding to velocities described by a scalar ratio relative to the velocity of the original migration (Sava, 2003). The method is formulated in the Fourier domain, therefore it is fast and robust. I use this residual migration method for constructing image perturbations for wave-equation migration velocity analysis (Chapter 5).

Wave-equation migration velocity analysis: In Chapter 5, I present the theory of migration velocity analysis using wavefield extrapolation (Sava and Biondi, 2004a). This velocity analysis method inherits the characteristics of wavefield extrapolation, mainly robustness in presence of large and sharp velocity contrasts, bandlimited model sensitivity and multipathing. The velocity updates are derived from image perturbations using a linearized operator based on the first-order Born approximation. The image perturbations are constructed based on focusing or moveout information measured on angle-domain

common image gathers (Chapter 3), using a linearized version of prestack residual migration (Chapter 4).

Examples: In Chapter 6, I present examples of wave-equation migration velocity analysis. An important application is for subsalt imaging (Sava and Biondi, 2004b), where ray-based methods often fail. I demonstrate that wave-equation migration velocity analysis is capable of updating velocity subsalt, since it inherits the robustness and accuracy of the underlying wavefield extrapolation technique. I define prestack image perturbations based on angle-domain common image gathers (Chapter 3) and residual migration (Chapter 4). Another important application is for velocity analysis using diffracted data (Sava et al., 2004). In this application, I define image perturbations based only on spatial focusing information obtained using residual migration (Chapter 4).

Chapter 2

Riemannian wavefield extrapolation

2.1 Overview

Riemannian spaces are prescribed by non-orthogonal curvilinear coordinates. In this chapter, I generalize one-way wavefield extrapolation to semi-orthogonal Riemannian coordinate systems, that include, but are not limited to, ray coordinate systems. I obtain a one-way wavefield extrapolation method which can be used for waves propagating in arbitrary directions, in contrast with downward continuation which is used for waves propagating mainly in the vertical direction. Ray coordinate systems can be initiated either from point sources, or from plane waves incident at various angles. Since wavefield propagation happens mostly along the extrapolation direction, this method enables us to use inexpensive finite-difference or mixed-domain extrapolators to achieve high angle accuracy. The main applications of this method include imaging of steeply dipping or overturning reflections.

2.2 Introduction

Imaging complex geology is one of the main challenges of today's seismic processing. Of the many seismic imaging methods available, downward continuation (Claerbout, 1985) is accurate, robust, and capable of handling models with large and sharp velocity variations.

This method naturally handles the multipathing that occurs in complex geology and provide a band-limited solution to the seismic imaging problem. Furthermore, as computational power increases, such methods are gradually moving into the mainstream of seismic processing. This explains why one-way wave extrapolation has been a subject of extensive theoretical research in the recent years (Ristow and Ruhl, 1994; de Hoop, 1996; Huang and Wu, 1996; Thomson, 1999; Biondi, 2002).

However, migration by downward continuation imposes strong limitations on the dip of reflectors that can be imaged since, by design, it favors downward propagating energy. Upward propagating energy, for example overturning waves, can be imaged in principle using downward continuation methods (Hale et al., 1992), although the procedure is difficult, particularly for prestack data. In contrast, Kirchhoff-type methods based on ray-traced traveltimes can image steep dips and handle overturning waves, although those methods are far less reliable in complex velocity models given their asymptotic assumption (Gray et al., 2001).

The steep-dip limitation of downward continuation techniques has been addressed in several ways:

- A first option is to increase the angular accuracy of the extrapolation operator, for example by employing methods from the Fourier finite-difference (FFD) family (Ristow and Ruhl, 1994; Biondi, 2002), or the Generalized Screen Propagator (GSP) family (de Hoop, 1996; Huang and Wu, 1996). The enhancements brought about by these methods have two costs: (1) they increase the cost of extrapolation, and (2) they do not guarantee unconditional stability.

- A second option is to perform the wavefield extrapolation in tilted coordinate systems (Etgen, 2002), or by designing sources that favor illumination of particular regions of the image (Rietveld and Berkhout, 1994; Chen et al., 2002). We can thus increase angular accuracy, although these methods are best suited for only a subset of the model (a salt flank, for example), and potentially decrease the accuracy in other regions of the model. In complex geology, defining an optimal tilt angle for the extrapolation grid is not obvious.

- A third possibility is hybridization of wavefield and ray-based techniques, either in the

form of Gaussian beams (Cervený, 2001; Hill, 1990, 2001; Gray et al., 2002), coherent states (Albertin et al., 2001, 2002), or beam-waves (Brandsberg-Dahl and Etgen, 2003). Such techniques are quite powerful, since they couple wavefield methods with multipathing and band-limited properties, with ray methods, which deliver arbitrary directions of propagation, even overturning. Beams can be understood as localized wave packets propagating in the preferential direction (Wu et al., 2000). Numerically, they are usually implemented using localized extrapolation paths. Extrapolation beams may leave shadow zones in various parts of the model, which hamper their imaging abilities. Furthermore, extrapolation beams have limited width, and do not allow diffractions from sharp features in the velocity model to develop completely without being attenuated at the boundaries. In addition, the narrow extrapolation domain generates beam superposition artifacts, such as beam boundary effects.

We can recognize that Cartesian coordinates for downward and tilted continuation or along beams of limited spatial extent, are just mathematical conveniences that do not reflect a physical reality. A better idea is to reformulate wavefield extrapolation in general Riemannian coordinates that conform with the general direction of wave propagation, thus the name *Riemannian wavefield extrapolation* (RWE). We can formulate the wavefield extrapolation theory in arbitrary 3D semi-orthogonal Riemannian spaces (Riemann, 1953), where the extrapolation direction is orthogonal to all other directions. Examples of such coordinate systems include, but are not limited to, fans of rays emerging from a source point, or bundles of rays initiated by plane waves of arbitrary initial dips at the source. For constant background velocity, this method reduces to extrapolation in polar/spherical coordinates (Nichols, 1994, 1996), or extrapolation in tilted coordinates (Etgen, 2002). This method is also closely related to Huygens wavefront tracing (Sava and Fomel, 2001), which represents a finite-difference solution to the eikonal equation in ray coordinates.

The main strength of this method is that the coordinate system can follow the waves, which may overturn, such that we can use one-way extrapolators to image diving waves (Figure 2.1). We can also use inexpensive extrapolators with limited angle accuracy (e.g. 15°), since, in principle, we are never too far from the wave propagation direction, and those methods deliver unconditional stability. We are also not confined to the extent of any individual extrapolation

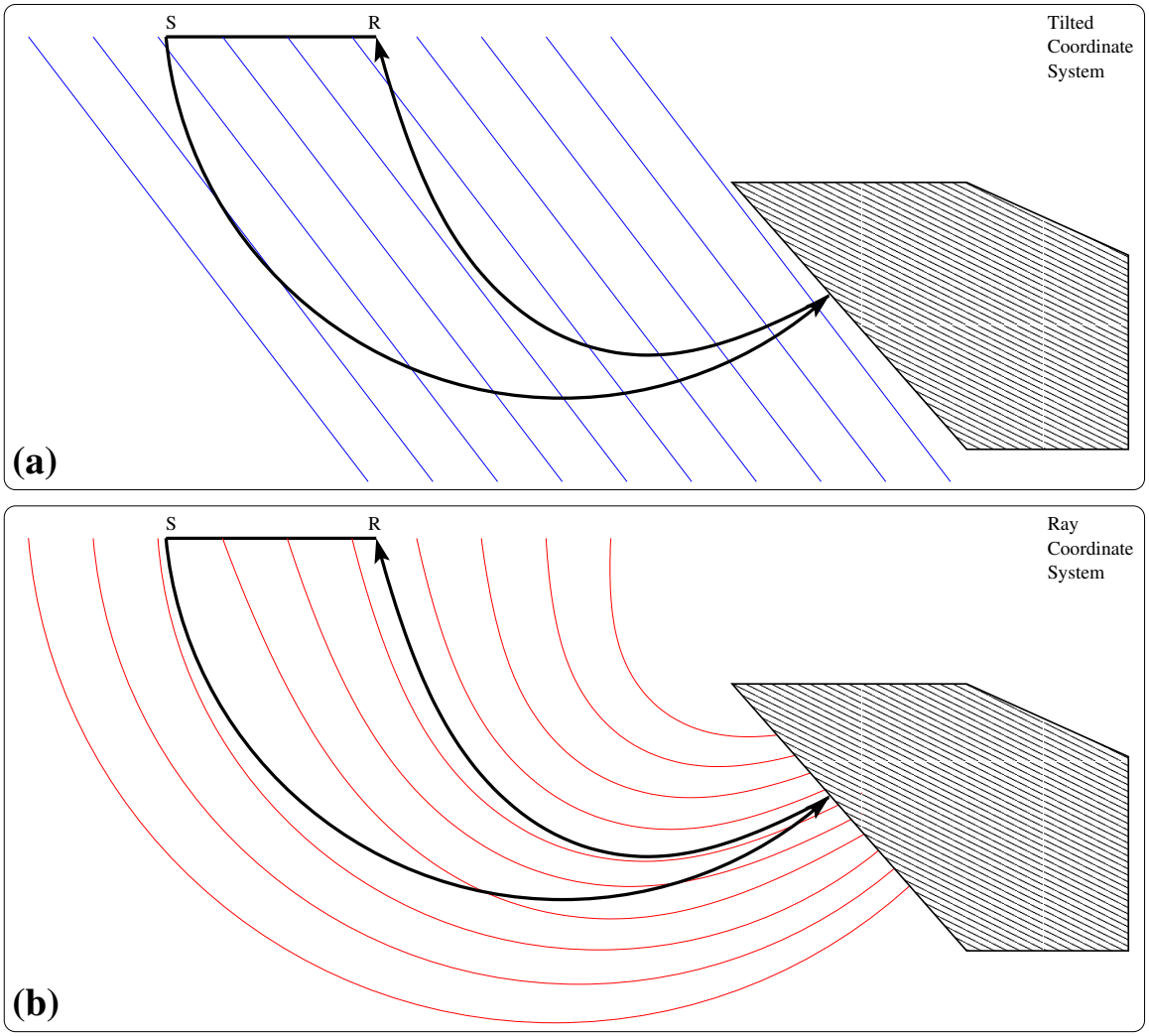


Figure 2.1: Ray coordinate systems are superior to tilted coordinate systems for imaging overturning waves using one-way wavefield extrapolators. Overturning reflected energy may become evanescent in tilted coordinate systems (a), but stays non-evanescent in ray coordinate systems (b). rwe-overturned [NR]

beam, therefore we can track diffractions for their entire spatial extent (Figure 2.2).

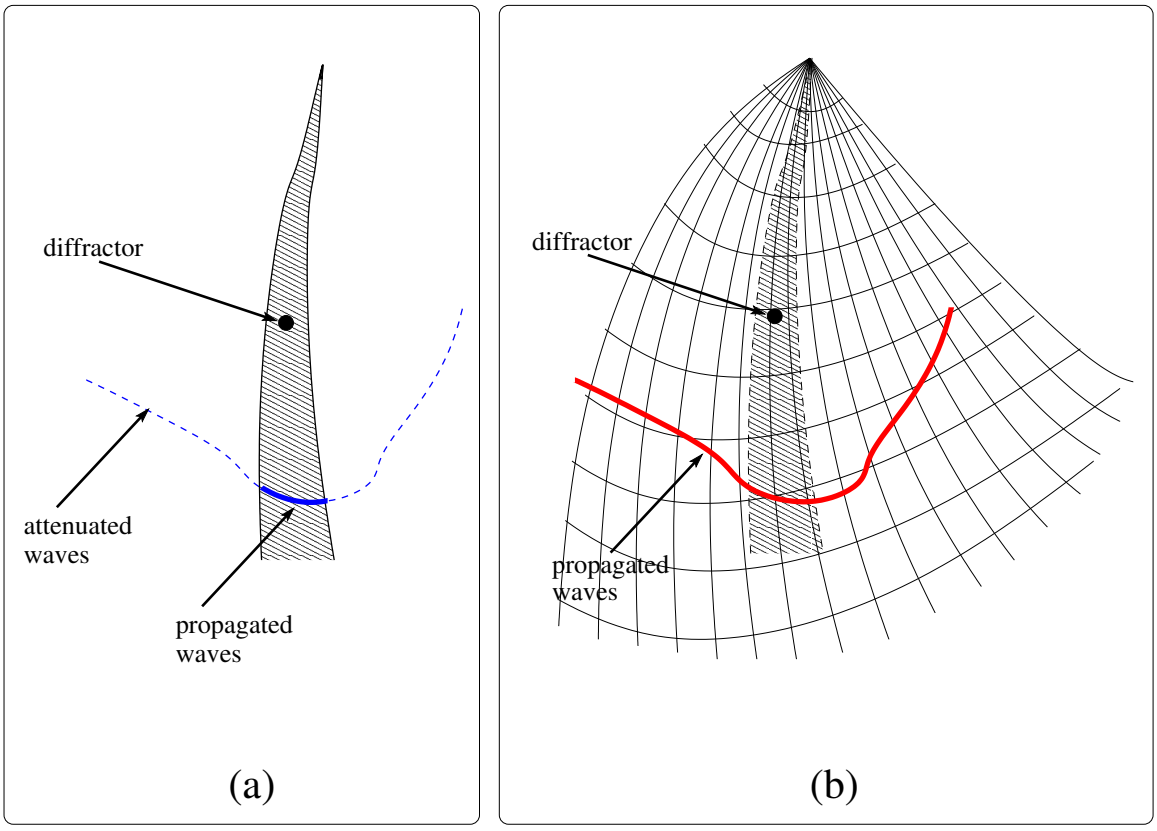


Figure 2.2: Extrapolated energy is attenuated at beam boundaries (a), but is propagated in a Riemmanian coordinate system (b). rwe-beams [NR]

2.3 Acoustic wave-equation

The acoustic propagation of a monochromatic wave is governed by the Helmholtz equation:

$$\Delta \mathcal{U} = -\frac{\omega^2}{v^2}\mathcal{U}\,, \tag{2.1}$$

where ω is temporal frequency, v is the spatially variable wave propagation velocity, and $\mathcal{U}$ represents a wavefield.

The Laplacian operator acting on a scalar function $\mathcal{U}$ in an arbitrary Riemannian space with coordinates $\boldsymbol{\xi} = \{\xi_1, \xi_2, \xi_3\}$ takes the form

$$\Delta \mathcal{U} = \sum_{i=1}^{3} \frac{1}{\sqrt{|\boldsymbol{g}|}} \frac{\partial}{\partial \xi_i} \left(\sum_{j=1}^{3} g^{ij} \sqrt{|\boldsymbol{g}|} \frac{\partial \mathcal{U}}{\partial \xi_j} \right), \tag{2.2}$$

where g^{ij} is a component of the associated metric tensor, and $|\boldsymbol{g}|$ is its determinant (Synge and Schild, 1978). The differential geometry of any coordinate system is fully represented by the metric tensor g^{ij}.

The expression simplifies if one of the coordinates, e.g. the coordinate of one-way wave extrapolation ξ_1, is orthogonal to the other coordinates (ξ_2, ξ_3). The metric tensor reduces to

$$\left[g_{ij}\right] = \begin{bmatrix} E & F & 0 \\ F & G & 0 \\ 0 & 0 & \alpha^2 \end{bmatrix}, \tag{2.3}$$

where E, F, G, and α are differential forms that can be found from mapping Cartesian coordinates $\boldsymbol{x} = \{x_1, x_2, x_3\}$ to general Riemannian coordinates $\boldsymbol{\xi} = \{\xi_1, \xi_2, \xi_3\}$, as follows:

$$\begin{aligned} E &= \sum_k \frac{\partial x_k}{\partial \xi_1} \frac{\partial x_k}{\partial \xi_1}, \\ F &= \sum_k \frac{\partial x_k}{\partial \xi_1} \frac{\partial x_k}{\partial \xi_2}, \\ G &= \sum_k \frac{\partial x_k}{\partial \xi_2} \frac{\partial x_k}{\partial \xi_2}, \\ \alpha^2 &= \sum_k \frac{\partial x_k}{\partial \xi_3} \frac{\partial x_k}{\partial \xi_3}. \end{aligned} \tag{2.4}$$

The associated metric tensor $\left[g^{ij}\right] = \left[g_{ij}\right]^{-1}$ has the matrix

$$\left[g^{ij}\right] = \begin{bmatrix} +G/J^2 & -F/J^2 & 0 \\ -F/J^2 & +E/J^2 & 0 \\ 0 & 0 & 1/\alpha^2 \end{bmatrix}, \tag{2.5}$$

where $J^2 = E\,G - F^2$. The metric determinant takes the form

$$|\boldsymbol{g}| = \alpha^2\, J^2\,. \tag{2.6}$$

Substituting equations (2.5) and (2.6) into (2.2), and making the notations $\xi_1 = \xi$, $\xi_2 = \eta$, and $\xi_3 = \zeta$, with ζ orthogonal to both ξ and η, we obtain the Helmholtz wave equation (2.1) for propagating waves in a 3D semi-orthogonal Riemannian space:

$$\frac{1}{\alpha\, J}\left[\frac{\partial}{\partial\zeta}\left(\frac{J}{\alpha}\frac{\partial\mathcal{U}}{\partial\zeta}\right)+\frac{\partial}{\partial\xi}\left(G\frac{\alpha}{J}\frac{\partial\mathcal{U}}{\partial\xi}-F\frac{\alpha}{J}\frac{\partial\mathcal{U}}{\partial\eta}\right)+\frac{\partial}{\partial\eta}\left(E\frac{\alpha}{J}\frac{\partial\mathcal{U}}{\partial\eta}-F\frac{\alpha}{J}\frac{\partial\mathcal{U}}{\partial\xi}\right)\right]=-\frac{\omega^2}{v^2}\mathcal{U}. \tag{2.7}$$

In equation (2.7), $v(\xi,\eta,\zeta)$ is the wave propagation velocity mapped to Riemannian coordinates.

For the special case of two dimensional spaces ($F = 0$ and $G = 1$), the Helmholtz wave equation reduces to the simpler form:

$$\frac{1}{\alpha J}\left[\frac{\partial}{\partial\zeta}\left(\frac{J}{\alpha}\frac{\partial\mathcal{U}}{\partial\zeta}\right)+\frac{\partial}{\partial\xi}\left(\frac{\alpha}{J}\frac{\partial\mathcal{U}}{\partial\xi}\right)\right]=-\frac{\omega^2}{v^2}\mathcal{U}\,, \tag{2.8}$$

which corresponds to a curvilinear orthogonal coordinate system.

Particular examples of coordinate systems for one-way wave propagation are:

Cartesian (propagation in depth): $x_1 = \xi$, $x_2 = \eta$, $x_3 = \zeta$,

$$\begin{aligned} E &= G = \alpha = J = 1\,, \\ F &= 0\,. \end{aligned}$$

Cylindrical (propagation in radius): $x_1 = \zeta\,\cos\xi$, $x_2 = \zeta\,\sin\xi$, $x_3 = \eta$,

$$\begin{aligned} E &= J = \zeta^2\,, \\ G &= \alpha = 1\,, \\ F &= 0\,. \end{aligned}$$

Spherical (propagation in radius): $x_1 = \zeta \sin\xi \cos\eta$, $x_2 = \zeta \sin\xi \sin\eta$, $x_3 = \zeta \cos\xi$,

$$\begin{aligned} E &= \zeta^2 \,, \\ G &= \zeta^2 \sin^2\xi \,, \\ \alpha &= 1 \,, \\ J &= \zeta^2 \sin\xi \,, \\ F &= 0 \,. \end{aligned}$$

Ray family (propagation along rays): ξ and η represent parameters defining a particular ray in the family (i.e. the ray take-off angles), J is the geometrical spreading factor, related to the cross-sectional area of the ray tube (Cervený, 2001). The coefficients E, F, G, and J are easily computed by finite-difference approximations with the Huygens wavefront tracing technique (Sava and Fomel, 2001). If the propagation parameter ζ is taken to be time along the ray, then α equals the propagation velocity v.

2.4 One-way wave-equation

Equation (2.7) can be used to describe two-way propagation of acoustic waves in a semi-orthogonal Riemannian space. For one-way wavefield extrapolation, we need to modify the acoustic wave equation (2.7) by selecting a single direction of propagation.

In order to simplify the computations, I introduce the following notation:

$$\begin{aligned} c_{\zeta\zeta} &= \frac{1}{\alpha^2} \,, \\ c_{\xi\xi} &= \frac{G}{J^2} \,, \\ c_{\eta\eta} &= \frac{E}{J^2} \,, \\ c_{\xi\eta} &= \frac{F}{J^2} \,, \\ c_{\zeta} &= \frac{1}{\alpha\, J} \frac{\partial}{\partial \zeta} \left(\frac{J}{\alpha} \right) \,, \end{aligned}$$

$$
\begin{aligned}
c_\xi &= \frac{1}{\alpha J}\left[\frac{\partial}{\partial \xi}\left(G\frac{\alpha}{J}\right)-\frac{\partial}{\partial \eta}\left(F\frac{\alpha}{J}\right)\right], \\
c_\eta &= \frac{1}{\alpha J}\left[\frac{\partial}{\partial \eta}\left(E\frac{\alpha}{J}\right)-\frac{\partial}{\partial \xi}\left(F\frac{\alpha}{J}\right)\right].
\end{aligned} \tag{2.9}
$$

All quantities in equations (2.9) are only function of the chosen coordinate system, and do not depend on the extrapolated wavefield. They can be computed by finite-differences for any choice of Riemannian coordinates which fulfill the orthogonality condition indicated earlier. In particular, we can use ray coordinates to compute those coefficients. With these notations, the acoustic wave-equation can be written as:

$$
c_{\zeta\zeta}\frac{\partial^2 \mathcal{U}}{\partial \zeta^2}+c_{\xi\xi}\frac{\partial^2 \mathcal{U}}{\partial \xi^2}+c_{\eta\eta}\frac{\partial^2 \mathcal{U}}{\partial \eta^2}+c_\zeta\frac{\partial \mathcal{U}}{\partial \zeta}+c_\xi\frac{\partial \mathcal{U}}{\partial \xi}+c_\eta\frac{\partial \mathcal{U}}{\partial \eta}+c_{\xi\eta}\frac{\partial^2 \mathcal{U}}{\partial \xi\,\partial \eta}=-\frac{\omega^2}{v^2}\mathcal{U}\,. \tag{2.10}
$$

For the particular case of Cartesian coordinates ($c_\xi = c_\eta = c_\zeta = 0, c_{\xi\xi} = c_{\eta\eta} = c_{\zeta\zeta} = 1, c_{\xi\eta} = 0$), the Helmholtz equation (2.10) reduces to its familiar form

$$
\frac{\partial^2 \mathcal{U}}{\partial \zeta^2}+\frac{\partial^2 \mathcal{U}}{\partial \xi^2}+\frac{\partial^2 \mathcal{U}}{\partial \eta^2}=-\frac{\omega^2}{v^2}\mathcal{U}\,. \tag{2.11}
$$

From equation (2.10), we can directly deduce the modified form of the dispersion relation for the wave-equation in a semi-orthogonal 3D Riemannian space:

$$
-c_{\zeta\zeta}k_\zeta^2-c_{\xi\xi}k_\xi^2-c_{\eta\eta}k_\eta^2+ic_\zeta k_\zeta+ic_\xi k_\xi+ic_\eta k_\eta-c_{\xi\eta}k_\xi k_\eta=-\omega^2 s^2\,. \tag{2.12}
$$

For one-way wavefield extrapolation, we need to solve the quadratic equation (2.12) for the wavenumber of the extrapolation direction k_ζ, and select the solution with the appropriate sign to extrapolate waves in the desired direction:

$$
k_\zeta = i\frac{c_\zeta}{2c_{\zeta\zeta}}\pm\sqrt{\frac{(\omega s)^2}{c_{\zeta\zeta}}-\left(\frac{c_\zeta}{2c_{\zeta\zeta}}\right)^2-\left[\frac{c_{\xi\xi}}{c_{\zeta\zeta}}k_\xi^2-i\frac{c_\xi}{c_{\zeta\zeta}}k_\xi\right]-\left[\frac{c_{\eta\eta}}{c_{\zeta\zeta}}k_\eta^2-i\frac{c_\eta}{c_{\zeta\zeta}}k_\eta\right]-\frac{c_{\xi\eta}}{c_{\zeta\zeta}}k_\xi k_\eta}\,. \tag{2.13}
$$

The solution with the positive sign in equation (2.13) corresponds to propagation in the positive direction of the extrapolation axis ζ.

For the particular case of Cartesian coordinates ($c_\xi = c_\eta = c_\zeta = 0, c_{\xi\xi} = c_{\eta\eta} = c_{\zeta\zeta} =$

$1, c_{\xi\eta} = 0$), the one-way wavefield extrapolation equation takes the familiar form

$$k_\zeta = \pm\sqrt{(\omega s)^2 - k_\xi^2 - k_\eta^2}\,. \tag{2.14}$$

Equation (2.13) specialized for the case of 2D coordinate systems obtained by ray tracing is further discussed in Appendix A.

We can use the wavenumber k_ζ for recursive wavefield extrapolation of the data recorded on the acquisition surface using the relation

$$\mathcal{U}_{\zeta+\Delta\zeta} = \mathcal{U}_\zeta e^{ik_\zeta \Delta\zeta}\,, \tag{2.15}$$

where $\Delta\zeta$ is the discrete extrapolation step.

We can simplify the Riemannian wavefield extrapolation method by dropping the first-order terms in equation (2.13). According to the theory of characteristics for second-order hyperbolic equations (Courant and Hilbert, 1989), these terms affect only the amplitude of the propagating waves. To preserve the kinematics, it is sufficient to keep only the second order terms of equation (2.13):

$$k_\zeta = \pm\sqrt{\frac{(\omega s)^2}{c_{\zeta\zeta}} - \frac{c_{\xi\xi}}{c_{\zeta\zeta}}k_\xi^2 - \frac{c_{\eta\eta}}{c_{\zeta\zeta}}k_\eta^2 - \frac{c_{\xi\eta}}{c_{\zeta\zeta}}k_\xi k_\eta}\,. \tag{2.16}$$

The coordinate system coefficients for Riemannian wavefield extrapolation given by equations (2.9) have singularities at caustics, e.g., when the geometrical spreading term J, defining a cross-sectional area of a ray tube, goes to zero. In the following examples, I use simple numerical regularization to avoid this problem, by adding a small non-zero quantity to the denominators to avoid division by zero.

2.5 Mixed-domain solutions to the one-way wave-equation

We can use equation (2.13) to construct a numerical solution to the one-way wave equation in the mixed (ω, k), (ω, x) domain. The extrapolation wavenumber described in equation (2.13)

is, in general, a function dependent on several quantities

$$k_\zeta = k_\zeta\left(s, c_j\right) \,, \tag{2.17}$$

where $s\left(\zeta,\xi,\eta\right)$ is slowness, and $c_j\left(\zeta,\xi,\eta\right) = \left\{c_\xi, c_\eta, c_\zeta, c_{\xi\xi}, c_{\eta\eta}, c_{\zeta\zeta}, c_{\xi\eta}\right\}$ are coefficients computed numerically from the definition of the coordinate system, as indicated by equations (2.9). Specifying a coordinate system, implicitly defines all coefficients c_j.

We can write the extrapolation wavenumber k_ζ as a first-order Taylor expansion relative to a reference medium:

$$k_\zeta = k_{\zeta 0} + \left.\frac{\partial k_\zeta}{\partial s}\right|_{s_0, c_{j\,0}} (s - s_0) + \sum_{c_j} \left.\frac{\partial k_\zeta}{\partial c_j}\right|_{s_0, c_{j\,0}} \left(c_j - c_{j\,0}\right) \,, \tag{2.18}$$

where $s\left(\zeta,\xi,\eta\right)$ and $c_j\left(\zeta,\xi,\eta\right)$ represent the spatially variable slowness and coordinate system parameters, and s_0 and $c_{j\,0}$ are the constant reference values at every extrapolation step.

The first part of equation (2.18), corresponding to the extrapolation wavenumber in the reference medium $k_{\zeta\,0}$, is implemented in the Fourier $(\omega - k)$ domain, while the second part, corresponding to the spatially variable medium coefficients, is implemented in the space $(\omega - x)$ domain.

If we make the further simplifying assumptions that $k_\xi \approx 0$ and $k_\eta \approx 0$, we can write

$$k_\zeta = k_{\zeta 0} + \left.\frac{\partial k_\zeta}{\partial s}\right|_0 (s - s_0) + \left.\frac{\partial k_\zeta}{\partial c_{\zeta\zeta}}\right|_0 \left(c_{\zeta\zeta} - c_{\zeta\zeta 0}\right) + \left.\frac{\partial k_\zeta}{\partial c_\zeta}\right|_0 \left(c_\zeta - c_{\zeta 0}\right) \,, \tag{2.19}$$

where

$$\begin{aligned}
\left.\frac{\partial k_\zeta}{\partial s}\right|_0 &= \frac{2\omega\left(\omega s_0\right)}{\sqrt{4 c_{\zeta\zeta 0}\left(\omega s_0\right)^2 - c_{\zeta 0}^2}} \,, \\
\left.\frac{\partial k_\zeta}{\partial c_{\zeta\zeta}}\right|_0 &= -\frac{i c_{\zeta 0}}{2 c_{\zeta\zeta 0}^2} + \frac{c_{\zeta 0}^2 - 2 c_{\zeta\zeta 0}\left(\omega s_0\right)^2}{2 c_{\zeta\zeta 0}^2 \sqrt{4 c_{\zeta\zeta 0}\left(\omega s_0\right)^2 - c_{\zeta 0}^2}} \,, \\
\left.\frac{\partial k_\zeta}{\partial c_\zeta}\right|_0 &= \frac{i}{2 c_{\zeta\zeta 0}} - \frac{c_{\zeta 0}}{2 c_{\zeta\zeta 0} \sqrt{4 c_{\zeta\zeta 0}\left(\omega s_0\right)^2 - c_{\zeta 0}^2}} \,.
\end{aligned} \tag{2.20}$$

By "0", I denote the reference medium (s_0, c_{j_0}). In principle, we could also use many reference media, followed by interpolation, similarly to the phase-shift plus interpolation (PSPI) technique of Gazdag and Sguazzero (1984).

For the particular case of Cartesian coordinates ($c_\zeta = 0, c_{\zeta\zeta} = 1$), equation (2.19) reduces to

$$k_\zeta = k_{\zeta 0} + \omega(s - s_0) \ , \tag{2.21}$$

which corresponds to the popular split-step Fourier (SSF) extrapolation method (Stoffa et al., 1990).

2.6 Finite-difference solutions to the one-way wave equation

Alternative solutions to the one-way wave-equation are obtained with pure finite-differencing methods in the $\omega - x$ domain, which can be implemented either as implicit (Claerbout, 1985), or as explicit methods (Hale, 1991). For the same stencil size, implicit methods are more accurate and robust than explicit methods, but harder to implement in 3D. However, explicit methods of comparable accuracy can be designed using larger stencils.

For implicit methods, various approximations to the square root in equation (2.13) lead to approximate equations of different orders of accuracy. For downward continuation in Cartesian coordinates, those methods are known by their respective angular accuracy as the 15° equation, 45° equation and so on. Although the meanings of 15°, 45° are undefined in ray coordinates where the extrapolation axis is time, we can still write approximations for the numerical finite-difference solutions using analogous approximations.

With the notation

$$k_o^2 = \frac{(\omega s)^2}{c_{\zeta\zeta}} - \left(\frac{c_\zeta}{2 c_{\zeta\zeta}} \right)^2 \ , \tag{2.22}$$

we can simplify the one-way wave equation (2.13) as

$$k_\zeta = i \frac{c_\zeta}{2 c_{\zeta\zeta}} + \sqrt{k_o^2 - \left[\frac{c_{\xi\xi}}{c_{\zeta\zeta}} k_\xi^2 - i \frac{c_\xi}{c_{\zeta\zeta}} k_\xi \right] - \left[\frac{c_{\eta\eta}}{c_{\zeta\zeta}} k_\eta^2 - i \frac{c_\eta}{c_{\zeta\zeta}} k_\eta \right] - \frac{c_{\xi\eta}}{c_{\zeta\zeta}} k_\xi k_\eta} \ . \tag{2.23}$$

A simple way of deriving the 15° equation is by a second-order Taylor series expansion of the extrapolation wavenumber k_ζ function of the variables k_ξ and k_η:

$$k_\zeta\left(k_\xi,k_\eta\right) \approx k_\zeta\left(k_\xi=0,k_\eta=0\right) + \left.\frac{\partial k_\zeta}{\partial k_\xi}\right|_0 k_\xi + \left.\frac{\partial k_\zeta}{\partial k_\eta}\right|_0 k_\eta + \\ + \frac{1}{2}\left.\frac{\partial^2 k_\zeta}{\partial k_\xi^2}\right|_0 k_\xi^2 + \left.\frac{\partial^2 k_\zeta}{\partial k_\xi \partial k_\eta}\right|_0 k_\xi k_\eta + \frac{1}{2}\left.\frac{\partial^2 k_\zeta}{\partial k_\eta^2}\right|_0 k_\eta^2 \,. \tag{2.24}$$

Introducing equation (2.23) into equation (2.24), we obtain an equivalent form for the 15° equation in a semi-orthogonal 3D Riemannian space:

$$k_\zeta \approx i\frac{c_\zeta}{2c_{\zeta\zeta}} + k_o + \frac{i\,c_\xi}{2c_{\zeta\zeta}\,k_o}k_\xi + \frac{1}{2\,k_o}\left[\left(\frac{c_\xi}{2c_{\zeta\zeta}\,k_o}\right)^2 - \frac{c_{\xi\xi}}{c_{\zeta\zeta}}\right]k_\xi^2 \\ + \frac{i\,c_\eta}{2c_{\zeta\zeta}\,k_o}k_\eta + \frac{1}{2\,k_o}\left[\left(\frac{c_\eta}{2c_{\zeta\zeta}\,k_o}\right)^2 - \frac{c_{\eta\eta}}{c_{\zeta\zeta}}\right]k_\eta^2 \\ + \frac{1}{2\,k_o}\left[\frac{c_\xi c_\eta}{2c_{\zeta\zeta}^2\,k_o^2} - \frac{c_{\xi\eta}}{c_{\zeta\zeta}}\right]k_\xi k_\eta \,. \tag{2.25}$$

Equation (2.25) specialized for the case of 2D coordinate systems obtained by ray tracing is further discussed in Appendix A.

For the particular case of Cartesian coordinates ($c_\xi = c_\eta = c_\zeta = 0, c_{\xi\xi} = c_{\eta\eta} = c_{\zeta\zeta} = 1, c_{\xi\eta} = 0$, $k_o = \omega s$),

$$k_\zeta \approx \omega s - \frac{1}{2\omega s}\left(k_\xi^2 + k_\eta^2\right) \,, \tag{2.26}$$

which is the usual form of the 15° equation.

2.7 Examples

I illustrate the RWE method with several synthetic examples of various degrees of complexity. In all examples, I use extrapolation in 2D orthogonal Riemannian spaces (ray coordinates), and compare the results with extrapolation in Cartesian coordinates. I present images obtained by migration of synthetic datasets represented by events equally spaced in time. In these

examples, I use synthetic data from point sources located on the surface. After I migrate these data in depth, I obtain images which are representations of Green's functions from the chosen source point. In all examples, (x,z) are Cartesian coordinates and (τ,γ) are ray coordinates for point sources. In all examples, γ stands for shooting angle and τ for one-way traveltime from the source.

The first example is designed to illustrate the method in a fairly simple, albeit not completely realistic, model. I use a 2D model with horizontal and vertical gradients $v(x,z) = 250 + 0.2\ x + 0.15\ z$ m/s which gives waves propagating from a point source a pronounced tendency to overturn (Figure 2.3). The model also contains a diffractor located around $x = 3800$ m and $z = 3000$ m.

I use ray tracing to create an orthogonal ray coordinate system corresponding to a point source on the surface at $x = 6000$ m. Figure 2.3(a) shows the velocity model and the rays in the original Cartesian coordinate system (x,z). Figure 2.3(b) shows the one-to-one mapping of the velocity model from Cartesian coordinates (x,z) into ray coordinate (τ,γ) using the functions $x(\tau,\gamma)$ and $z(\tau,\gamma)$ obtained by ray tracing. The diffractor is mapped to $\tau = 2.4$ s and $\gamma = -18^\circ$ measured from the vertical. The synthetic data I use is represented by impulses at the source location at every 0.25 s. In ray coordinates, this source is represented by a plane-wave evenly distributed over all shooting angles γ. Ideally, an image obtained by migrating such a dataset is a representation of the acoustic wavefield produced by a source that pulsates periodically.

Figure 2.3(c) shows the image obtained by downward continuation in Cartesian coordinates using the standard 15° equation. Figure 2.3(d) shows the image obtained by wavefield extrapolation using the ray-coordinate 15° equation. The overlays in panels (c) and (d) are wavefronts at every 0.25 s and rays shot at every 20° to facilitate comparisons between the images in ray and Cartesian coordinates.

Figure 2.4 is a direct comparison of the results obtained by extrapolation in the two coordinate systems. The image created by extrapolation in Cartesian coordinates (a) is mapped to ray coordinates (b). The image created by extrapolation in ray coordinates (d) is mapped to

Cartesian coordinates (c). Since I use the same velocity for ray tracing and for wavefield extrapolation, I expect the wavefields and the overlain wavefronts to be in agreement. The most obvious mismatch occurs in regions where the 15° equation fails to extrapolate correctly at steep dips $\gamma = -20^\circ \ldots -50^\circ$. This is not surprising since, as its name indicates, this equation is only accurate up to 15°. However, this limitation is eliminated in ray coordinates, because the coordinate system brings the extrapolator in a reasonable position and at a good angle, although the extrapolator uses an equation of a similar order of accuracy.

Another interesting observation in Figures 2.4 (a) and (c) concerns the diffractor present in the velocity model. When I extrapolate in Cartesian coordinates, the diffraction is only accurate to a small angle relative to the extrapolation direction (vertical). In contrast, the diffraction develops relative to the propagation direction when computed in ray coordinates, thus being more accurate after mapping to Cartesian coordinates. We can also observe that the diffractions created by the anomaly in the velocity model are not at all limited in the ray coordinate domain. In a beam-type approach, such diffraction would not develop beyond the extent of the beam in which it arises. Neighboring extrapolation beams are completely insensitive to the velocity anomaly.

The second example is a smooth velocity with a negative Gaussian anomaly that creates a triplication of the ray coordinate system (Figure 2.5). Everything other than the velocity model is identical to its counterpart in the preceding example. Similarly to Figure 2.3, panels (a) and (c) correspond to Cartesian coordinates, and panels (b) and (d) correspond to ray coordinates. Using regularization of the ray coordinates parameters, I extrapolate through the triplication. The discrepancy between the wavefields and the corresponding wavefronts highlight the decreasing accuracy in the caustic region caused by the parameter regularization. The "butterfly" in Figure 2.6 (b) is another indication that the ray coordinate system is triplicating and that the Cartesian coordinates are multi-valued function of ray coordinates. None of this happens when I extrapolate in ray coordinates (d) and interpolate to Cartesian coordinates (c) since the mappings $x(\tau, \gamma)$ and $z(\tau, \gamma)$ are single-valued.

Comparing panels (a) and (c) of Figure 2.6, we can notice that the triplication tails at, for example, $x \approx 7000$ m and $z \approx 4000$ m extend farther with the Cartesian extrapolator (a) than with the Riemannian extrapolator (c). The triplications create internal boundaries in the

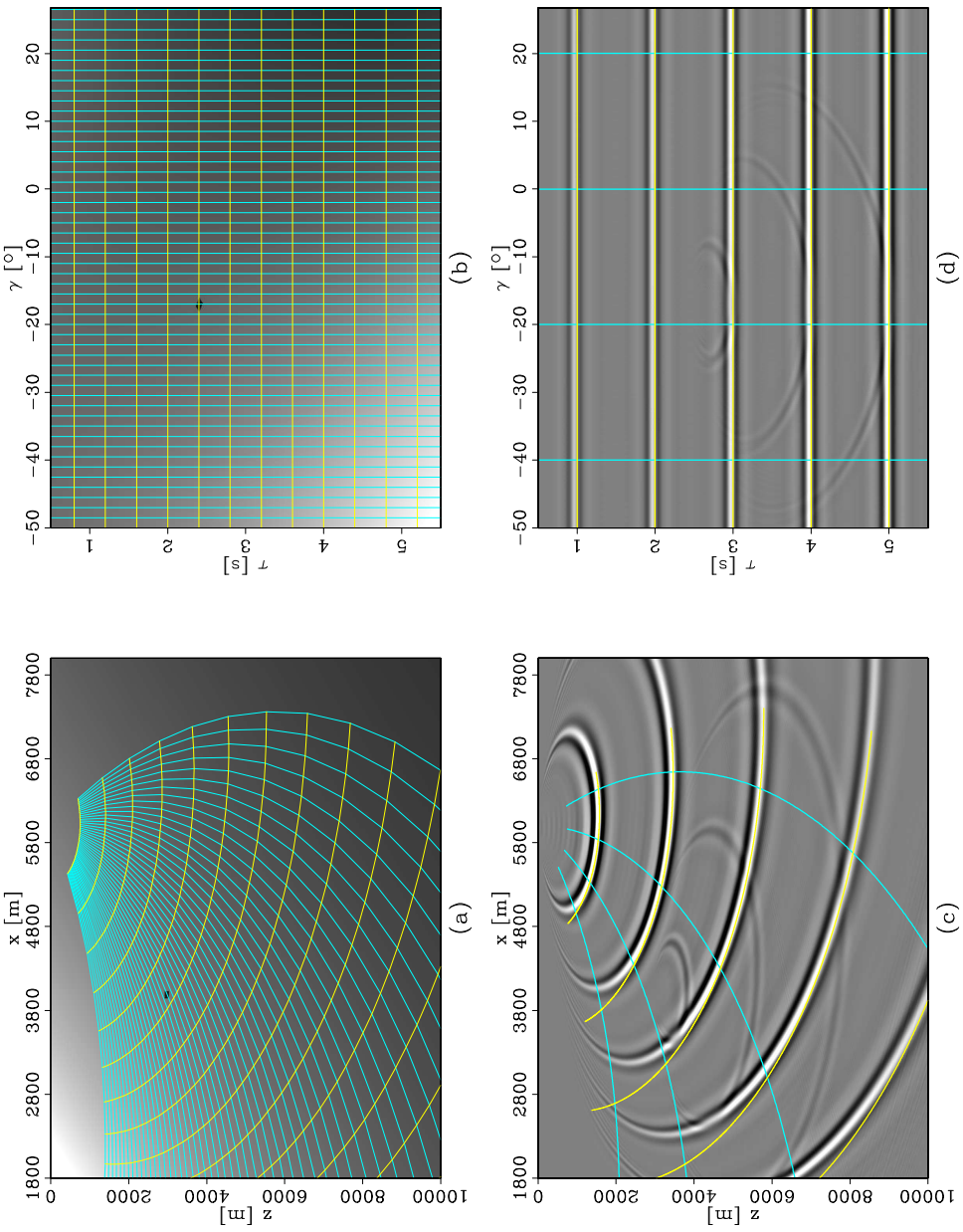


Figure 2.3: Simple linear gradient model: Panels (a) and (c) correspond to Cartesian coordinates, and panels (b) and (d) correspond to ray coordinates. Velocity model with an overlay of the ray coordinate system initiated by a point source at the surface (a); image obtained by downward continuation in Cartesian coordinates with the 15° equation (c); velocity model with an overlay of the ray coordinate system (b); image obtained by wavefield extrapolation in ray coordinates with the 15° equation (d). rwe-RCsi1.com.ps [ER]

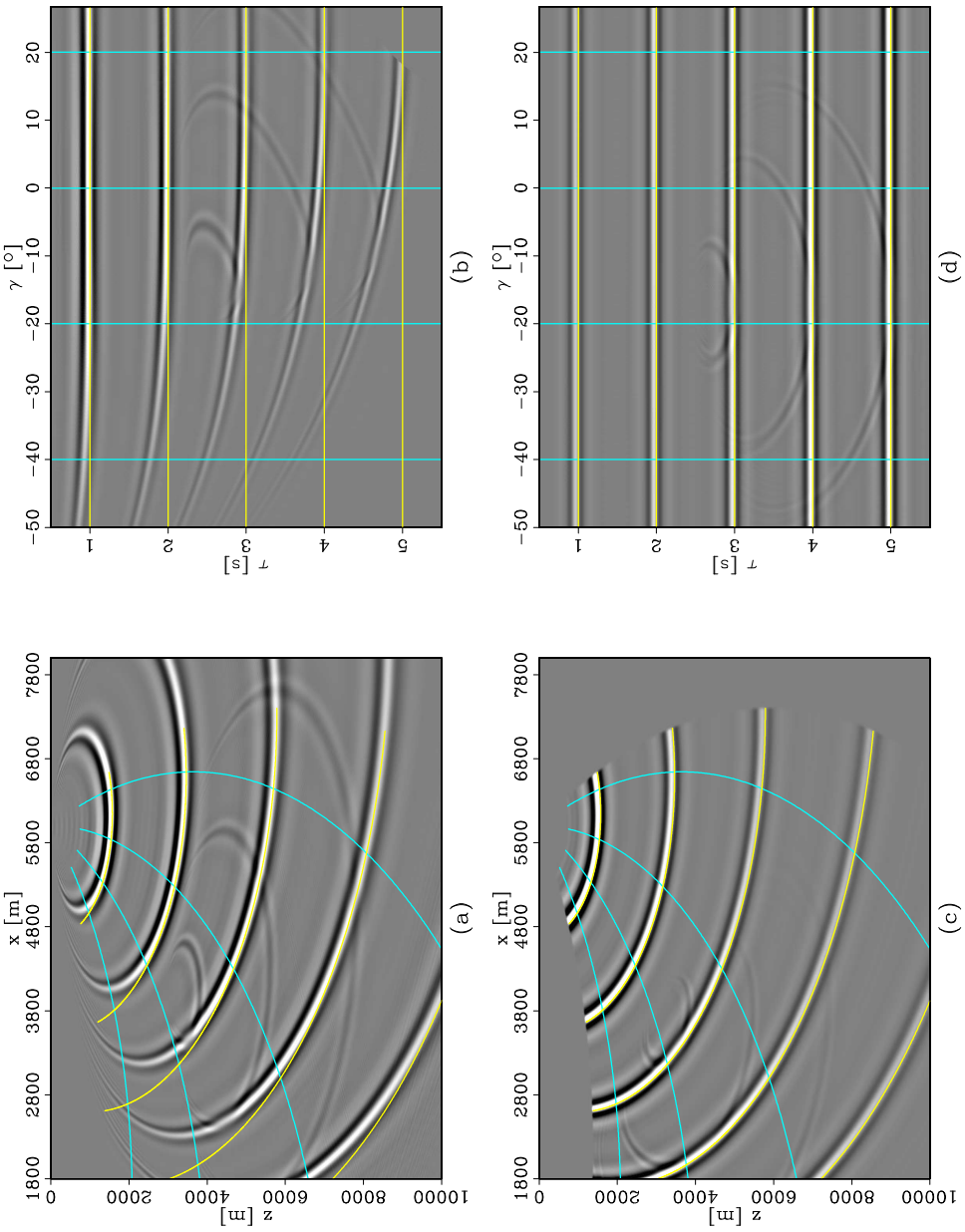


Figure 2.4: Simple linear gradient model: the image obtained by downward continuation in Cartesian coordinates with the 15° equation (a); the image in panel (a) interpolated to ray coordinates (b); image obtained by extrapolation in ray coordinates with the 15° equation (d); the image in panel (d) interpolated to Cartesian coordinates (c). rwe-RCsi1.f15.ps [ER]

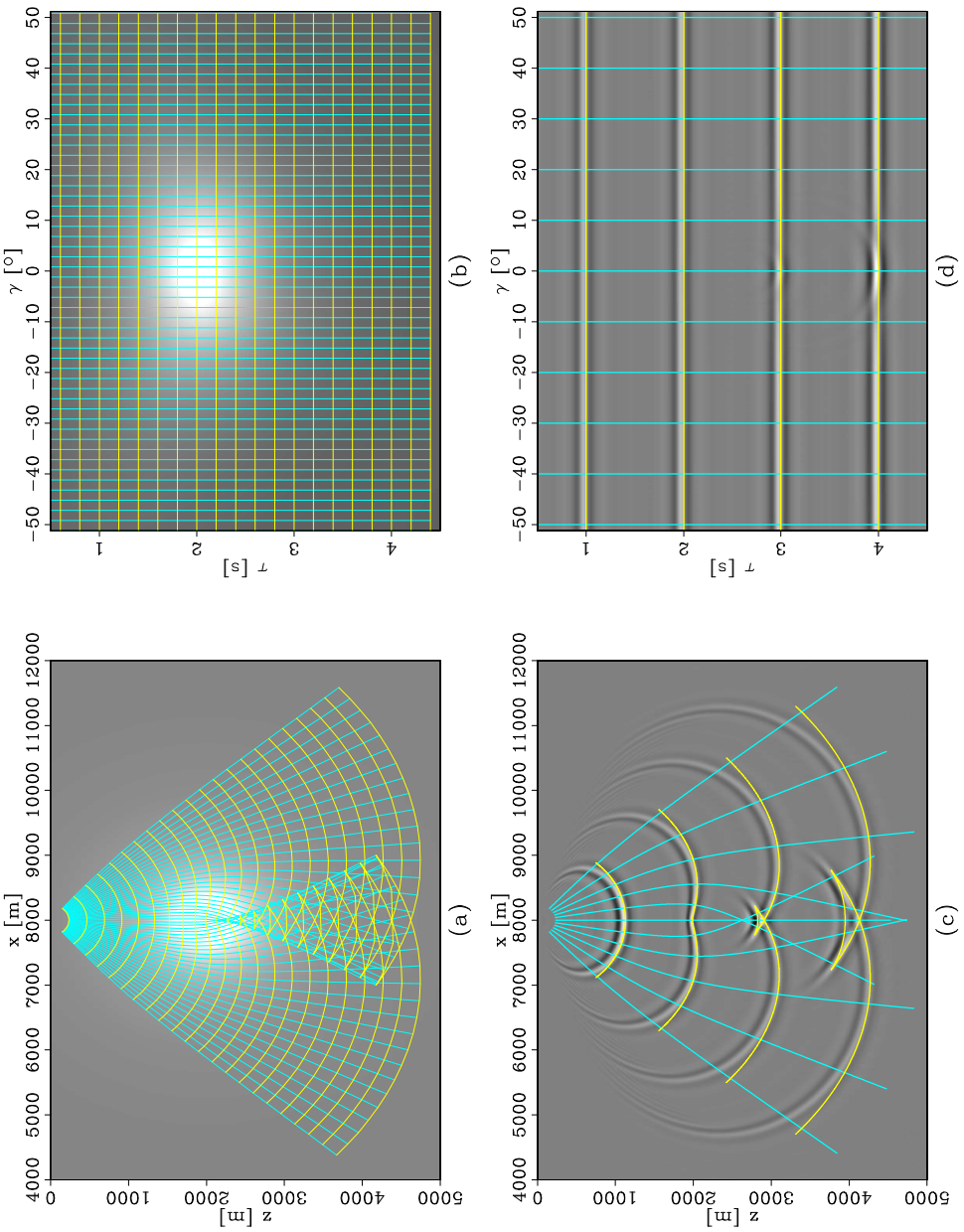


Figure 2.5: Gaussian anomaly model: Panels (a) and (c) correspond to Cartesian coordinates, and panels (b) and (d) correspond to ray coordinates. Velocity model with an overlay of the ray coordinate system initiated by a point source at the surface (a); image obtained by downward continuation in Cartesian coordinates with the 15° equation (c); velocity model with an overlay of the ray coordinate system (b); image obtained by wavefield extrapolation in ray coordinates with the 15° equation (d). rwe-RCga1.com.ps [ER]

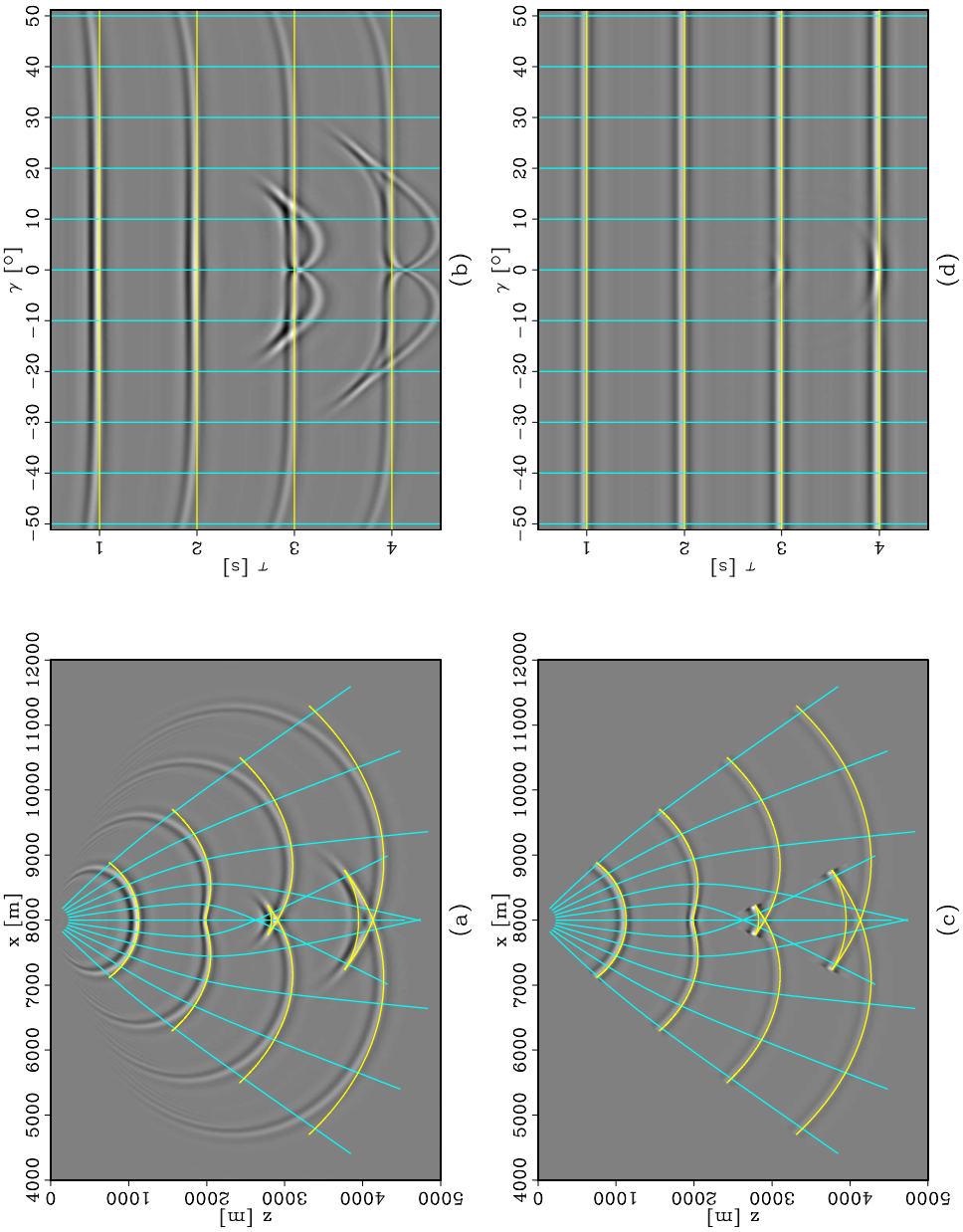


Figure 2.6: Gaussian anomaly model: the image obtained by downward continuation in Cartesian coordinates with the 15° equation (a); the image in panel (a) interpolated to ray coordinates (b); image obtained by extrapolation in ray coordinates with the 15° equation (d); the image in panel (d) interpolated to Cartesian coordinates (c). rwe-RCga1.f15.ps [ER]

coordinate system which are better avoided.

The next example uses the more complicated Marmousi model. Figure 2.7 shows the velocity models mapped into the two different domains, and the wavefields obtained by extrapolation in each one of them. I create the ray coordinate system by ray tracing in a smooth version of the model, and extrapolate in the rough version. The source is located on the surface at $x = 5000$ m.

In this example, the wavefields triplicate in both domains (Figure 2.8). Since I am using a 15° equation, extrapolation in Cartesian coordinates is only accurate for the small incidence angles, as observed in panels (a) and (b). In contrast, extrapolating in ray coordinates (d) does not have the same angular limitation, which can be seen after mapping back to Cartesian coordinates (c).

Figure 2.9 is a close-up comparison of the wavefields obtained by extrapolation with different methods in different domains. Panel (a) is a window of the velocity model for reference. Panels (b) and (c) are obtained by extrapolation in ray coordinates using the 15° and split-step equations, respectively. Panels (d), (e) and (f) are obtained by downward continuation in Cartesian coordinates using the 45°, 15° and split-step equations, respectively. The ray-coordinate extrapolation results are similar to the Cartesian coordinates results in the regions where the wavefields propagate mostly vertically, but are different in the regions where the wavefields propagate almost horizontally.

Figure 2.10 is another close-up comparison of the wavefields obtained by extrapolation with different methods in different domains. The panel structure is similar to the one in Figure 2.9. This window is chosen to capture the portion of the wavefield which is well described kinematically by extrapolation in Cartesian coordinates with the 15°. We can observe that the amplitude behavior of Riemannian extrapolation coincides with that of Cartesian extrapolation.

Figure 2.11 illustrates the difference between wavefield extrapolation using equation (2.13), panel (b) and wavefield extrapolation using equation (2.16), panel (c). Kinematically, the two images are equivalent and the main changes are related to amplitudes. Panels (b) and (c) have the same clip to highlight the point that only the amplitudes change but not

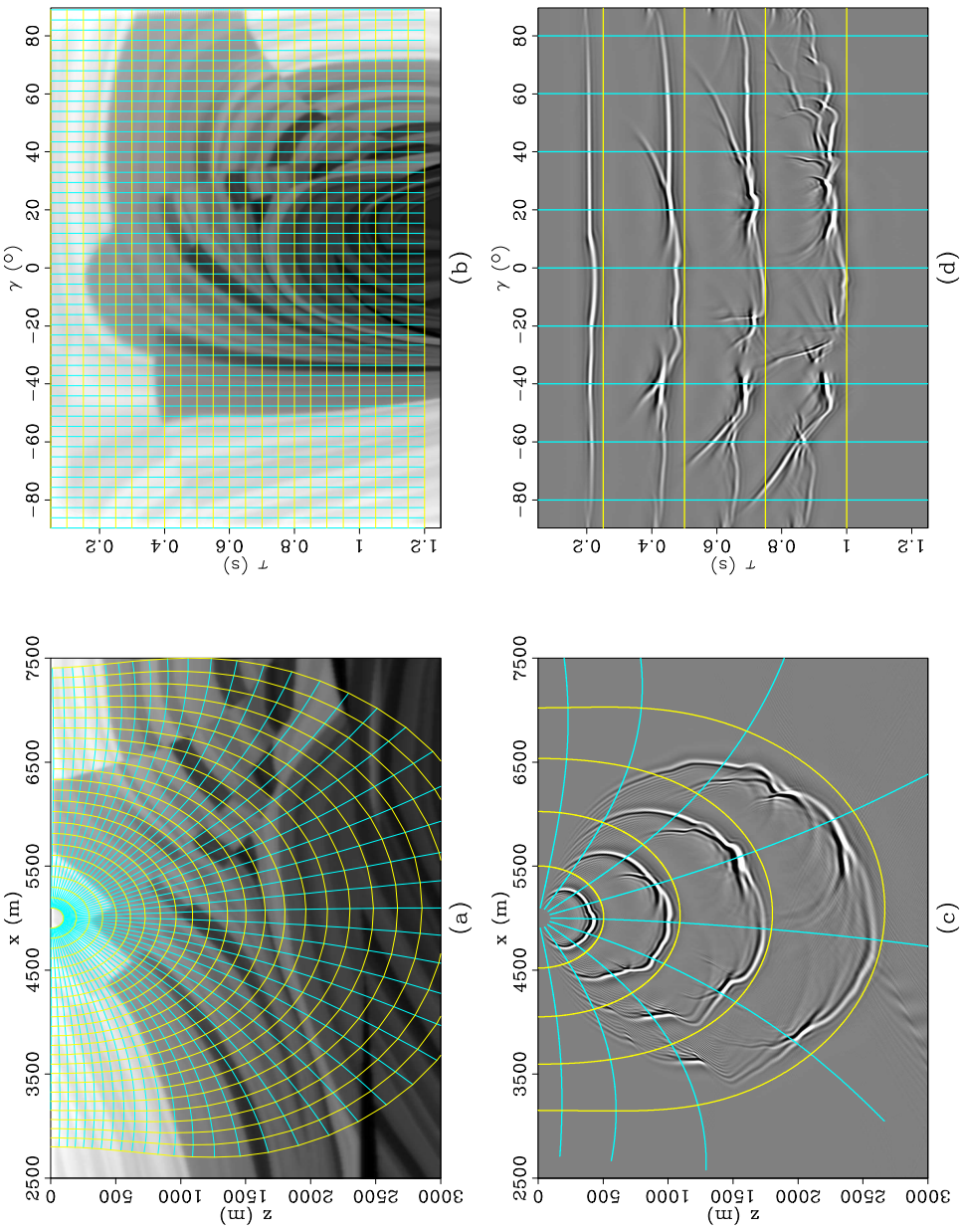


Figure 2.7: Marmousi model: Panels (a) and (c) correspond to Cartesian coordinates, and panels (b) and (d) correspond to ray coordinates. Velocity model with an overlay of the ray coordinate system initiated by a point source at the surface (a); image obtained by downward continuation in Cartesian coordinates with the 15° equation (c); velocity model with an overlay of the ray coordinate system (b); image obtained by wavefield extrapolation in ray coordinates with the 15° equation (d). rwe-RCma4.com.ps [ER]

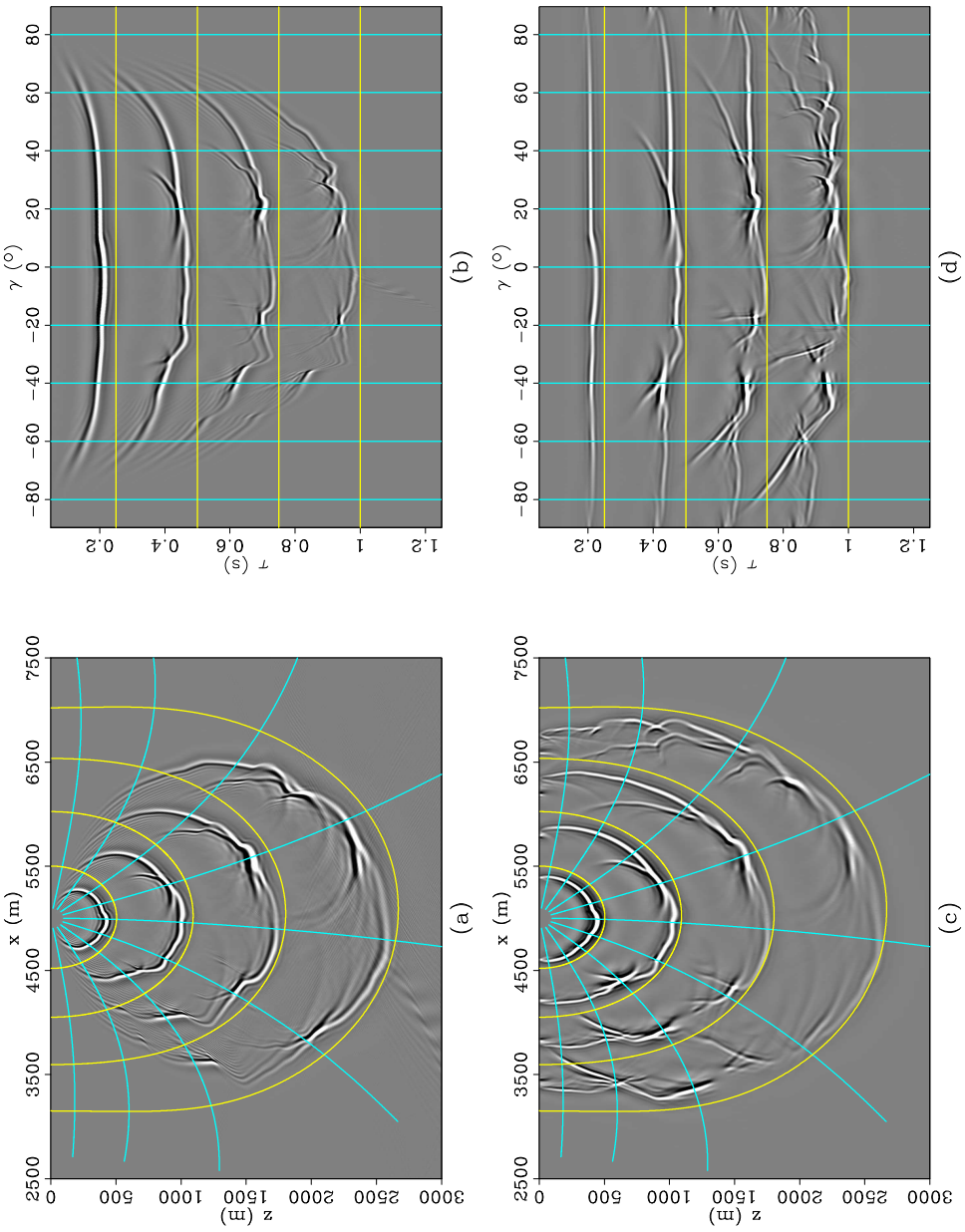


Figure 2.8: Marmousi model: the image obtained by downward continuation in Cartesian coordinates with the 15° equation (a); the image in panel (a) interpolated to ray coordinates (b); image obtained by extrapolation in ray coordinates with the 15° equation (d); the image in panel (d) interpolated to Cartesian coordinates (c). rwe-RCma4.f15.ps [ER]

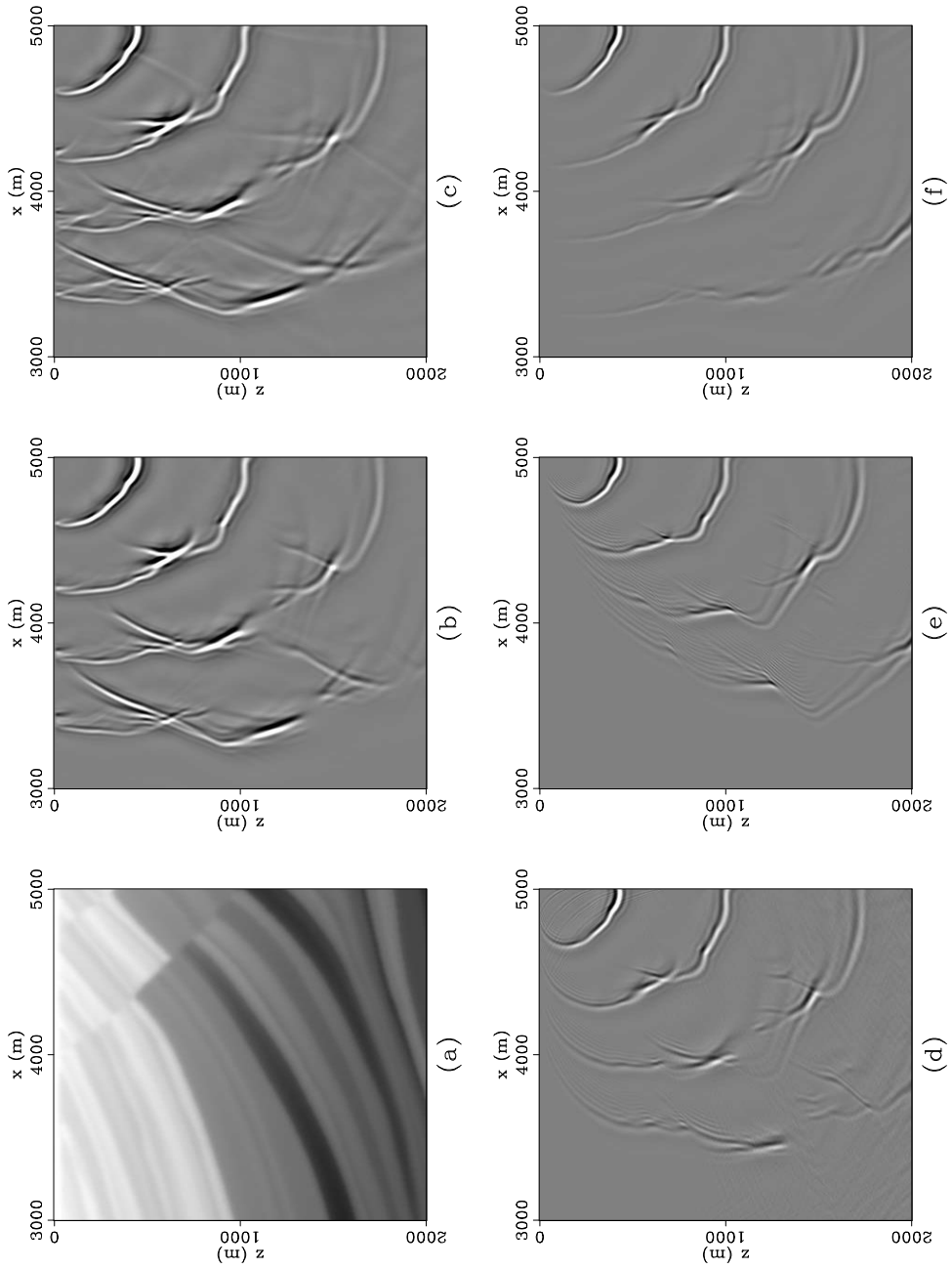


Figure 2.9: Marmousi model: Velocity model (a); image obtained by wavefield extrapolation in ray coordinates using the 15° equation (b) and the split-step equation (c); image obtained using downward continuation in Cartesian coordinates with the 45° equation (d), the 15° equation (e) and the split-step equation (f). rwe-RCma4.zom.ps [ER]

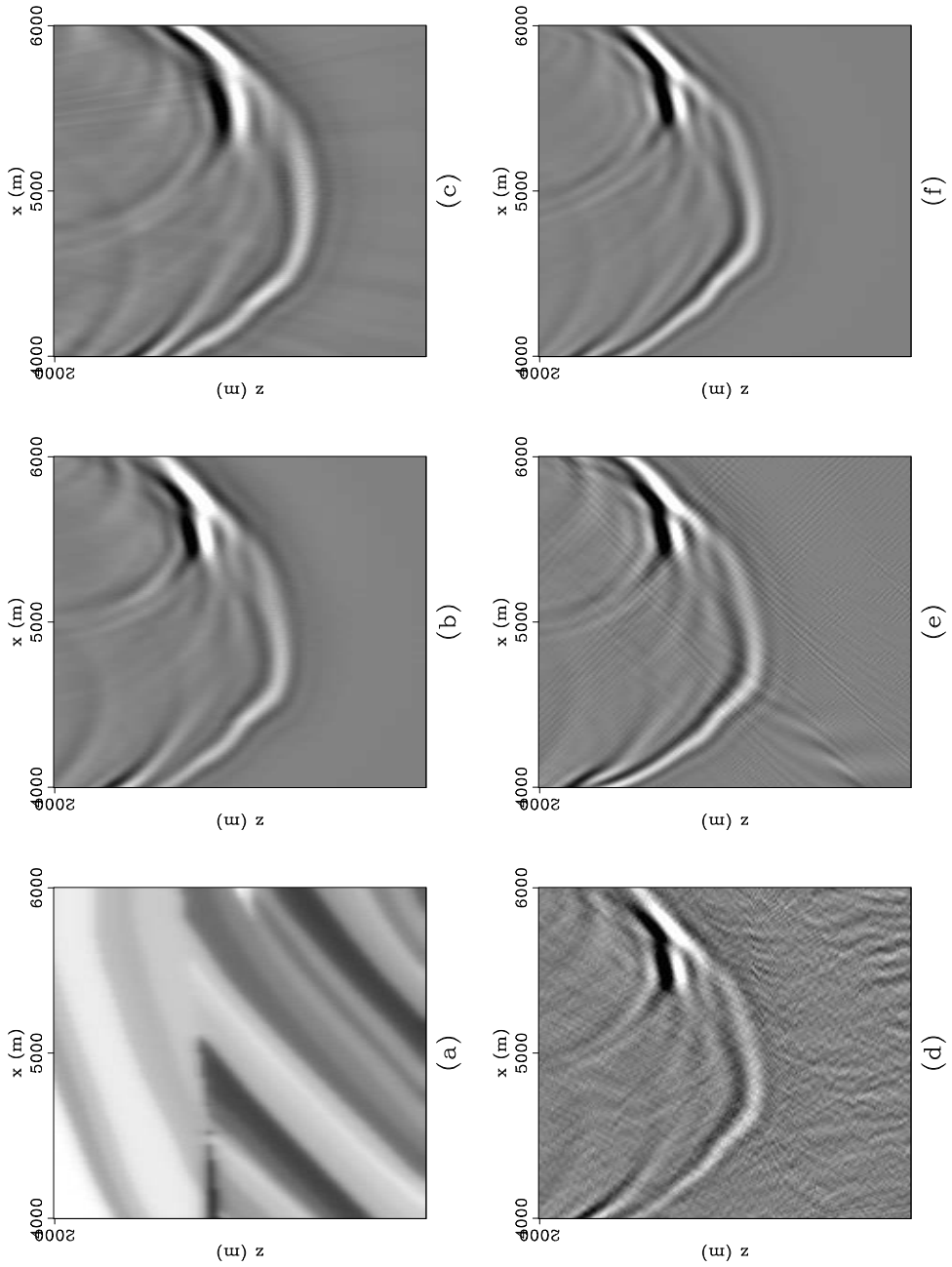


Figure 2.10: Marmousi model: Velocity model (a); image obtained by wavefield extrapolation in ray coordinates using the 15° equation (b) and the split-step equation (c); image obtained using downward continuation in Cartesian coordinates with the 45° equation (d), the 15° equation (e) and the split-step equation (f). rwe-RCma4.yom.ps [ER]

the kinematics.

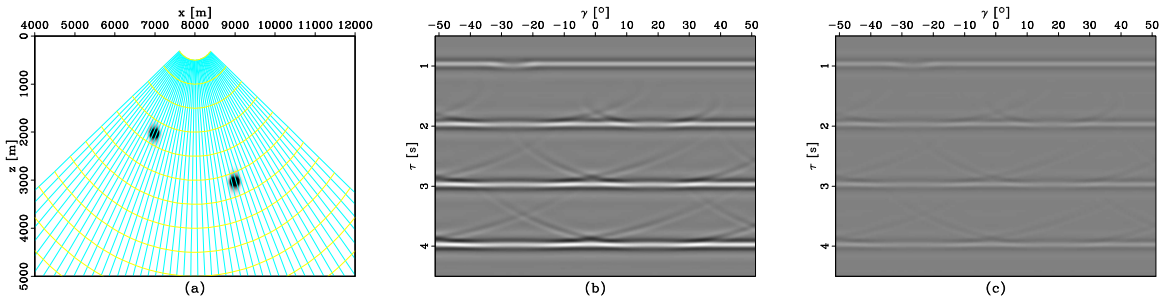


Figure 2.11: The effect of neglecting the first order terms in Riemannian wavefield extrapolation. From left to right the velocity model with an overlay of the ray coordinate system (a), extrapolation with equation (2.13) including the first order terms (b), and extrapolation with the simplified equation (2.16) (c). Panels (b) and (c) are gained equally, illustrating that the changes caused by neglecting the first-order terms affect the amplitudes and not the kinematics. rwe-RCga2.kin.ps [ER]

Figure 2.12 shows a comparison between time domain acoustic finite-difference modeling (a), and Riemannian wavefield extrapolation (b) for a point source. The Marmousi velocity model is smoothed to avoid backscattered energy in panel (a) in order to facilitate a comparison with the one-way wavefield extrapolator in panel (b).

Despite being computed with a one-way extrapolator, the wavefield in panel (b) captures accurately all the important features of the reference wavefield depicted in panel (a), including triplications and amplitude variations. Some of the diffractions in panel (b) are not as well developed as their counterparts in panel (a) due to the limited angular accuracy of the 15° approximation. Regardless of accuracy, the computed Riemannian wavefield could not be achieved with Cartesian-based downward continuation.

2.8 Discussion

Coordinate system construction: The ray coordinate systems do not need to be created using the same velocity model as the one used for extrapolation. We can use a smooth velocity model to create the coordinate system by ray tracing, and then interpolate the

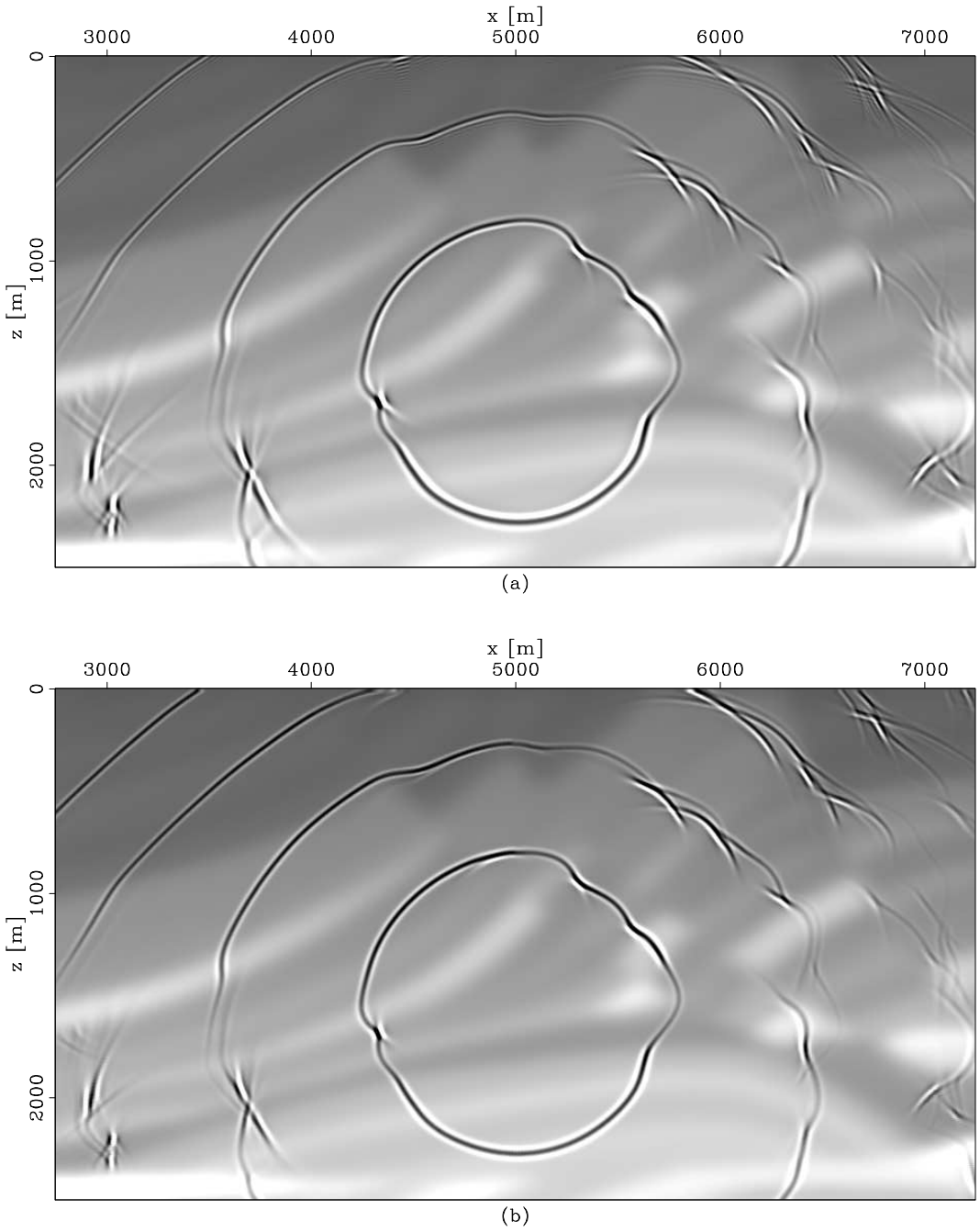


Figure 2.12: A comparison of wavefields computed by time-domain acoustic finite-difference modeling (a), and wavefields computed by Riemannian wavefield extrapolation (b). rwe-RCma2.fdm.ps [ER,M]

rough velocity, similarly to the method used by Brandsberg-Dahl and Etgen (2003). An alternative method of creating ray coordinate systems is discussed by Shragge and Sava (2004). The coordinate system can be initiated from a point source or an arbitrary surface in 3D (or a line in 2D) which positions it optimally relative to the imaging target. Furthermore, with Riemannian wavefield extrapolation, we can address a particular target in the image and thus we do not need to construct a coordinate system which is appropriate for the entire image.

Coordinate system regularization: The coordinate system coefficients for Riemannian wavefield extrapolation given by equations (2.9) have singularities at caustics, i.e. when the geometrical spreading term J, defining a cross-sectional area of a ray tube, is zero. We can address this problem through a simple numerical regularization, by adding a small non-zero quantity to the denominators to avoid division by zero. This strategy worked reasonably well for the current examples, although better strategies are needed.

In principle, it is best if coordinate system triplications are avoided. However, for velocity models with large contrasts (e.g. salt), avoiding such triplications may require large smoothing prior to ray tracing. In these situations, there is a strong possibility that the waves do not propagate close to the extrapolation axis, thus requiring higher-order terms in the extrapolator at increased cost.

Prestack data: My current examples of Riemannian wavefield extrapolation are based on equation (2.13) which corresponds to the single-square root (SSR) equation of standard Cartesian wavefield extrapolation. Riemannian wavefield extrapolation can be extended to prestack data either for shot-profile, plane-wave or S-G migration by appropriate definitions of the underlying ray coordinate system. Figure 2.13 is a schematic representation of shot-profile migration in ray coordinates, where both source and receivers are extrapolated in the same ray coordinate system appropriate for a particular set of overturning waves. This is also an illustration of how Riemannian wavefield extrapolation can be used for target-oriented wave-equation migration. In general, source and receiver wavefields can be migrated in different coordinate systems, with the imaging condition applied after interpolation to common (Cartesian) coordinates.

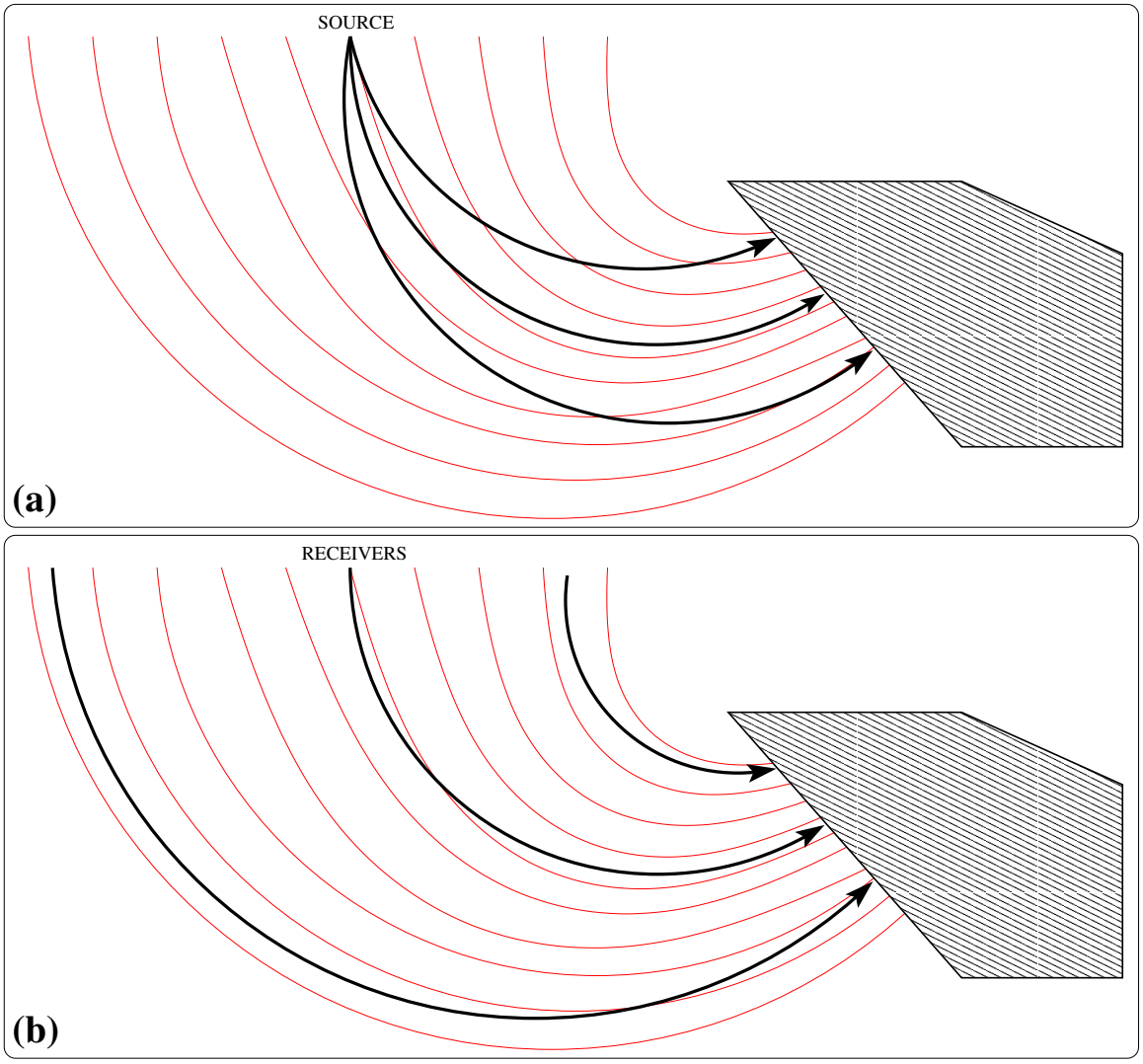


Figure 2.13: Shot-profile migration sketch. Sources (a) and receivers (b) are both extrapolated in a ray coordinate system appropriate for overturning waves. rwe-spmig [NR]

Interpolation: The images created with wavefield extrapolation in Riemannian coordinates require interpolation to a Cartesian coordinate system. This is a shared difficulty of all methods operating on non-Cartesian grids. In the current implementation, I use simple sinc-type interpolation based on the explicit mapping of the Cartesian coordinates (x, z) function of the ray coordinates (τ, γ) given by ray tracing.

Cost: The main cost of an implicit finite-difference solution to the one-way equation in Riemannian coordinates is related to solving a tridiagonal system in 2D (Claerbout, 1985) or a pentadiagonal system in 3D (Rickett et al., 1998). In this respect, the cost of Riemannian wavefield extrapolation is identical to the cost of Cartesian downward continuation for the same number of samples. However, computing the coefficients of the tridiagonal system adds modestly to the cost, since they can be precomputed ahead of time.

A second consideration is that we are comparing extrapolation in different domains (space for downward continuation and shooting angle for Riemannian extrapolation). Since in Riemannian coordinates we extrapolate at small angles, we can sample the wavefronts less and achieve same or better angular accuracy than in Cartesian coordinates at lower cost.

2.9 Conclusions

This chapter extends one-way wavefield extrapolation to Riemannian spaces which are described by non-orthogonal curvilinear coordinate systems. I use semi-orthogonal Riemannian coordinates that include, but are not limited to, ray coordinate systems.

I define an acoustic wave-equation for semi-orthogonal Riemannian coordinates, from which I derive a one-way wavefield extrapolation equation. I use ray coordinates that can be initiated either from a point source, or from an incident plane wave at the surface. Many other types of coordinates are acceptable, as long as they fulfill the semi-orthogonal condition of the acoustic wave equation in Riemannian coordinates.

Since wavefield propagation is mostly coincident with the extrapolation direction, we can

use inexpensive 15° finite-difference or mixed-domain extrapolators to achieve high-angle accuracy. If the ray coordinate system overturns, this method can be used to image overturning waves with one-way wavefield extrapolation.

Riemannian coordinates are better suited for wavefield extrapolation, because they do not restrict wave propagation to the preferential vertical direction but allow numerical wave extrapolation to follow the direction of the natural wave propagation. Coordinate system triplications pose challenges that can be solved numerically, but which are better avoided.

2.10 Acknowledgment

I would like to acknowledge Sergey Fomel with whom I collaborated on developing the Riemannian wavefield extrapolation method (Sava and Fomel, 2004).

Chapter 3

Angle-domain common image gathers

3.1 Overview

Migration in the angle-domain creates seismic images for different reflection angles. This chapter presents a method for computing angle-domain common image gathers from seismic images obtained by depth migration using wavefield extrapolation. This method operates on prestack migrated images and produces the output as a function of the reflection angle and not as a function of offset ray-parameter as in other alternative approaches. The method amounts to a radial-trace transform in the Fourier domain and is equivalent to a slant stack in the space domain. Thus, we obtain angle gathers using a stretch technique that enables us to impose smoothness through regularization. This method is accurate, fast, robust, and easy to implement. The main applications of this method are in the migration velocity analysis and amplitude versus angle analysis. This chapter develops the angle gather transformation in 2D.

3.2 Introduction

Traditionally, migration velocity analysis and amplitude versus offset (AVO) studies employ offset-domain common image gathers (ODCIG), since most of the relevant information is not described by the zero-offset images. There are two kinds of ODCIGs: those produced by

Kirchhoff migration, and those produced by migration by wavefield continuation, commonly referred to as *wave-equation* migration. These two kinds of ODCIGs have different meanings: for a perfectly known velocity model, the ODCIGs generated by Kirchhoff migration produce flat events, while the ODCIGs generated by wave-equation migration produce events perfectly focused at zero offset. There is no simple relationship between these two types of ODCIGs, as one involves the concept of flat gathers, while the other involves the concept of focused events. Furthermore, the offset used in the Kirchhoff ODCIGs is a data parameter, while the offset used in the wave-equation ODCIGs is a model parameter, since it characterizes the migrated image after focusing at the reflection point and not the recorded data.

Wave-equation migration is a powerful and accurate imaging tool in complex areas. However, offset-domain common image gathers fail to properly characterize complex propagation paths because, among other things, of the ambiguity of reflector positions caused by multipathing, which make interpretation and migration velocity analysis difficult (Nolan and Symes, 1996).

The problems observed for ODCIGs can be alleviated using angle-domain common image gathers (ADCIG) which are representations of the seismic images sorted by the incidence angle at the reflection point. ADCIGs can be produced either by Kirchhoff methods (Xu et al., 1998; Brandsberg-Dahl et al., 1999) or by wave-equation methods (de Bruin et al., 1990; Prucha et al., 1999; Mosher and Foster, 2000). Unlike ODCIGs, ADCIGs produced with either kind of method have similar characteristics since they simply describe the reflectivity as a function of incidence angle at the reflector (Figure 3.1). However, Stolk and Symes (2002) argue that even in perfectly known but strongly refracting media, Kirchhoff ADCIGs are hampered by significant artifacts caused by the asymptotic assumptions of ray-based imaging.

This section focuses on ADCIGs computed in relation with wave-equation migration. Angle gathers can be obtained using wave-equation techniques either for shot-profile migration, as described by de Bruin et al. (1990), or for shot-geophone migration, as described by Prucha et al. (1999) or Mosher and Foster (2000). In both cases, angle gathers are evaluated using slant-stacks of the downward-continued wavefield, prior to imaging. I refer to these techniques as *data-space* methods since they involve the downward-continued wavefield before imaging. These data-space methods produce angle gathers as a function of offset ray-parameter (p_h),

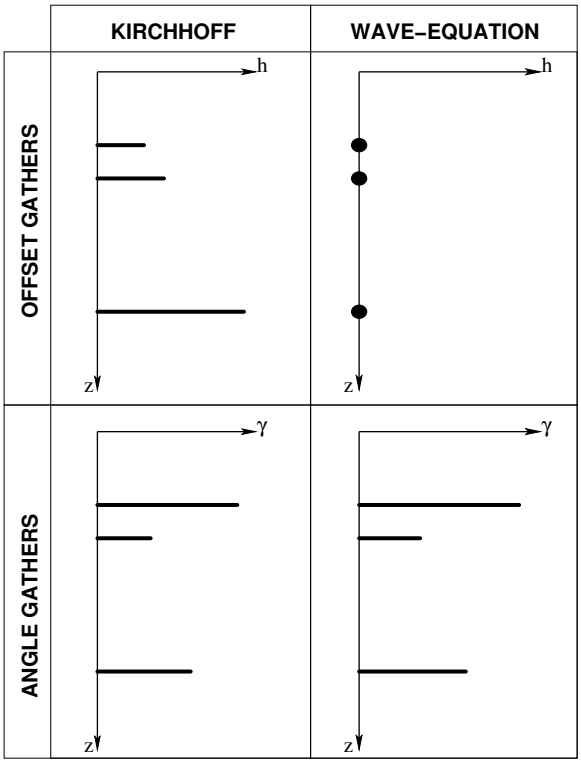


Figure 3.1: Offset-domain and angle-domain common image gathers. A schematic comparison between Kirchhoff and wave-equation methods. adcig-odcig [NR]

instead of the true reflection angle.

Here, I present an alternative method that enables us to compute angle gathers after imaging. I refer to this technique as an *image-space* method since it does not involve the wavefields anymore, but the prestack images obtained by imaging at zero time but not at zero offset. I show that this method directly produces angle gathers as a function of the reflection angle, as opposed to the data-space methods which produce angle gathers as a function of offset ray-parameter. The image-space method allows for a convenient, robust and slightly more efficient implementation than the data-space method. I also show that for both the data-space and image-space methods, the slant-stack transformation can be easily implemented as a radial-trace transform in the frequency-wavenumber domain, as described by Ottolini (1982).

3.3 Angle gathers in the image-space

Angle gathers can be conveniently formed in the frequency-wavenumber domain using wavefield-continuation imaging methods. If we consider that in constant velocity media, t is the travel-time from the source to the reflector and back to the receiver at the surface, h is half the offset between the source and the receiver, z is the depth of the reflection point, α is the geologic dip, and γ is the reflection angle (Figure 3.2), we can write

$$\frac{\partial t}{\partial h} = \frac{2\cos\alpha \sin\gamma}{v} \tag{3.1}$$

and

$$\frac{\partial t}{\partial z} = \frac{2\cos\alpha \cos\gamma}{v}. \tag{3.2}$$

From equations (3.1) and (3.2), using the implicit functions theorem, we can write

$$\tan\gamma = -\left.\frac{\partial z}{\partial h}\right|_{t,x}, \tag{3.3}$$

relation which is the basis for the angle gather method. The full derivation of equation (3.3) is included in Appendix B.

Equation (3.3) is derived in constant velocity media, but it remains perfectly valid in a differential sense in any arbitrary velocity media, if we consider h to be half the offset at the reflector depth. The offset at depth characterizes the downward-continued wavefield and, as Figure 3.2 shows, this is the offset associated with the wavefield as it approaches the reflection surface and not the surface offset. In this context, the half-offset h can be seen as an image parameter, different from the offset at the surface which is a data parameter.

In the frequency-wavenumber domain, formula (3.3) takes the simple form

$$\tan\gamma = -\frac{k_h}{k_z}, \tag{3.4}$$

where k_z and k_h are the depth and frequency wavenumbers.

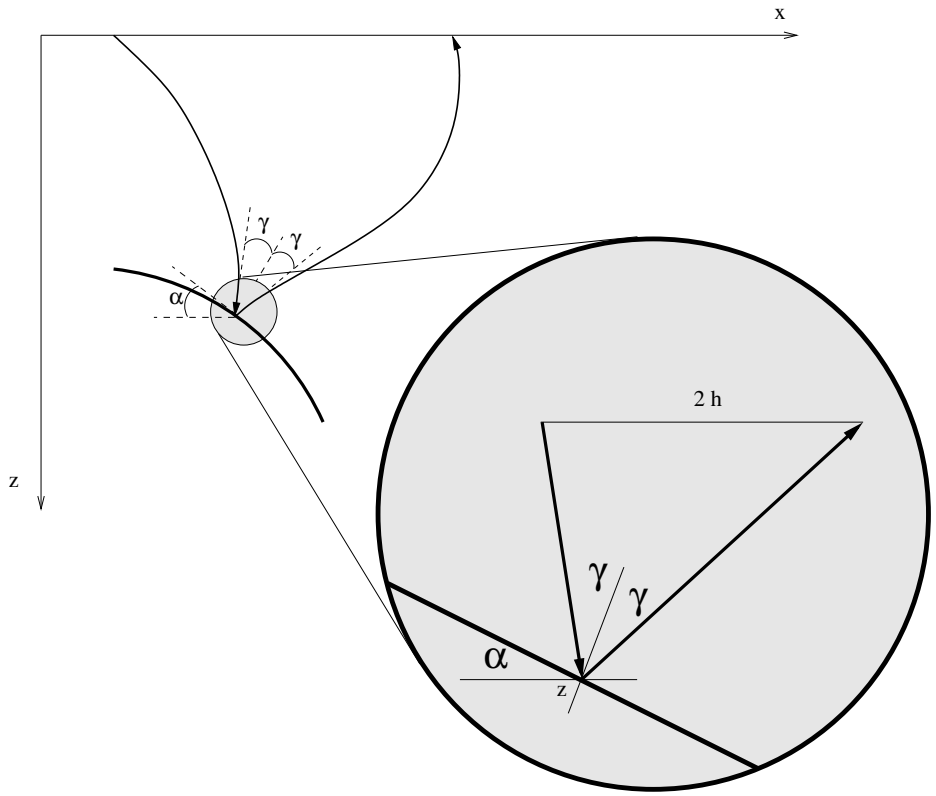


Figure 3.2: Reflection rays in an arbitrary-velocity medium. adcig-local [NR]

Equation (3.4) indicates that angle gathers can be formed using frequency-domain algorithms. Wave-equation migration is ideally suited to compute angle gathers using such a method, since the migration output is precisely described by the offset at the reflector depth and not by the surface offset.

We can also recognize that equation (3.1) simply describes the offset ray-parameter (p_h) of the propagating wave at the incidence with the reflector. Using the definition

$$p_h = \left.\frac{\partial t}{\partial h}\right|_{z,x} \tag{3.5}$$

it follows that we can write a relation similar to equation (3.4) to evaluate the offset ray-parameter in the Fourier-domain:

$$p_h = \frac{k_h}{\omega}. \tag{3.6}$$

Both Equations (3.4) and (3.6) can be used to compute image gathers through radial trace transforms in the Fourier domain (Appendix B). The major difference is that equation (3.4) operates in the image space, while equation (3.6) operates in the data space.

Other major differences between the two methods are the following:

1. The image-space method is completely decoupled from migration, therefore conversion to reflection angle can be thought of as a post-processing after migration. Such post processing is useful because it allows conversion from the angle-domain back to the offset-domain without re-migration, a conclusion which does not hold true for the data-space method, where the transformation is a function of the data frequency. The transformation also allows for post-processing of the migrated images, e.g. angle gather anti-aliasing (Biondi, 2004).

2. The angles we obtain using equation (3.4) are geometrical measures of the reflection angle. For AVA purposes, it is convenient to have the reflection amplitudes described as a function of reflection angle and not as a function of offset ray-parameter, in which case conversion to reflection angle requires dip and velocity information, as seen in equation (3.1). The meaning of the amplitude variation with angle in the ADCIGs

created using this method depends on the properties of the migration algorithm from which the common image gathers are created (Sava et al., 2001b). One of the following examples demonstrates that a correct implementation of this method can preserve the amplitude pattern resulting from migration.

3. Computing angle gathers in the image space requires acurate knowledge of velocity, since this gets encoded in the migrated image, and implicitly, in angle gathers. In contrast, the p_h gathers computed in the data space are insensitive to velocity inaccuracy, since the transformation only requires data space quantities. However, conversion of p_h to reflection angle γ is influenced by errors in the velocity maps (Biondi, 2004).

3.4 Regularization of the angle-domain

The angle gather transformation introduced in this chapter amounts to a stretch of the offset to reflection angle according to equation (3.4). The stretch takes every point on the offset wavenumber axis and repositions it on the angle axis, most likely not on a regular grid. Therefore, we need to interpolate the unevenly sampled axis to the regular one, i.e. we need to solve a simple linear interpolation problem

$$\mathbf{Lm} \approx \mathbf{d}\,, \tag{3.7}$$

where the model ($\mathbf{m}$) is represented by the evenly-spaced values on the angle axis, the data ($\mathbf{d}$) is represented by the unevenly-spaced values on the angle axis, and $\mathbf{L}$ represents a 1D linear interpolation operator. Both $\mathbf{m}$ and $\mathbf{d}$ in equation (3.7) are Fourier-domain quantities. Since parts of the model space are not covered because of the uneven distribution of the data, we need to regularize the interpolation process and solve a system such as

$$\begin{aligned} \mathbf{Lm} &\approx \mathbf{d} \\ \epsilon\mathbf{Hm} &\approx 0 \end{aligned} \tag{3.8}$$

where ($\mathbf{H}$) represents a 1D regularization operator (1D gradient, for example). The least-squares solution to the system (3.8) takes the usual form

$$\mathbf{m} = \left(\mathbf{L}^T\mathbf{L} + \epsilon^2\mathbf{H}^T\mathbf{H}\right)^{-1}\mathbf{L}^T\mathbf{d}. \tag{3.9}$$

In the special case of the angle-domain stretch, the inverted factor on the right side of equation (3.9) is a tridiagonal matrix and can be easily inverted using a tridiagonal solver. However, given the sparseness of the stretched data, the least-squares tridiagonal matrix corresponding to the operator $\mathbf{L}$ has zeros present along the diagonals, which results in instability during inversion and artifacts in the angle gathers. Regularization fills those gaps and the inversion of the matrix in equation (3.9) is well-behaved.

Finally, I emphasize that regularization is not applied in the space domain, but in the Fourier domain and so this method does not smooth reflection events spatially. Consequently, the amplitude response in ADCIGs is not altered, although, as noted earlier, there are other reasons why direct AVA interpretation is not straightforward.

3.5 Examples

The first example represents a simple image-gather with one seismic event perfectly focused at zero offset (Figure 3.3). As expected, conversion to the angle-domain produces a flat event, which fattens out at high angles due to the finite sampling of the offset axis. This phenomenon is a consequence of the acquisition geometry, and not a property of the conversion to the angle-domain. The top panels of Figure 3.3 show the amplitude of this simple event as a function of offset (left) and as a function of reflection angle (right). The conversion to angle produces a flat amplitude curve, as expected for this perfectly focused event. If this event is produced using true amplitude migration, then the reflectivity function of angle (AVA) produced by this algorithm is also true amplitude.

The second example is a 2D synthetic model with dipping reflectors at various angles. I generate the synthetic data using wavefield-continuation modeling and then image it using

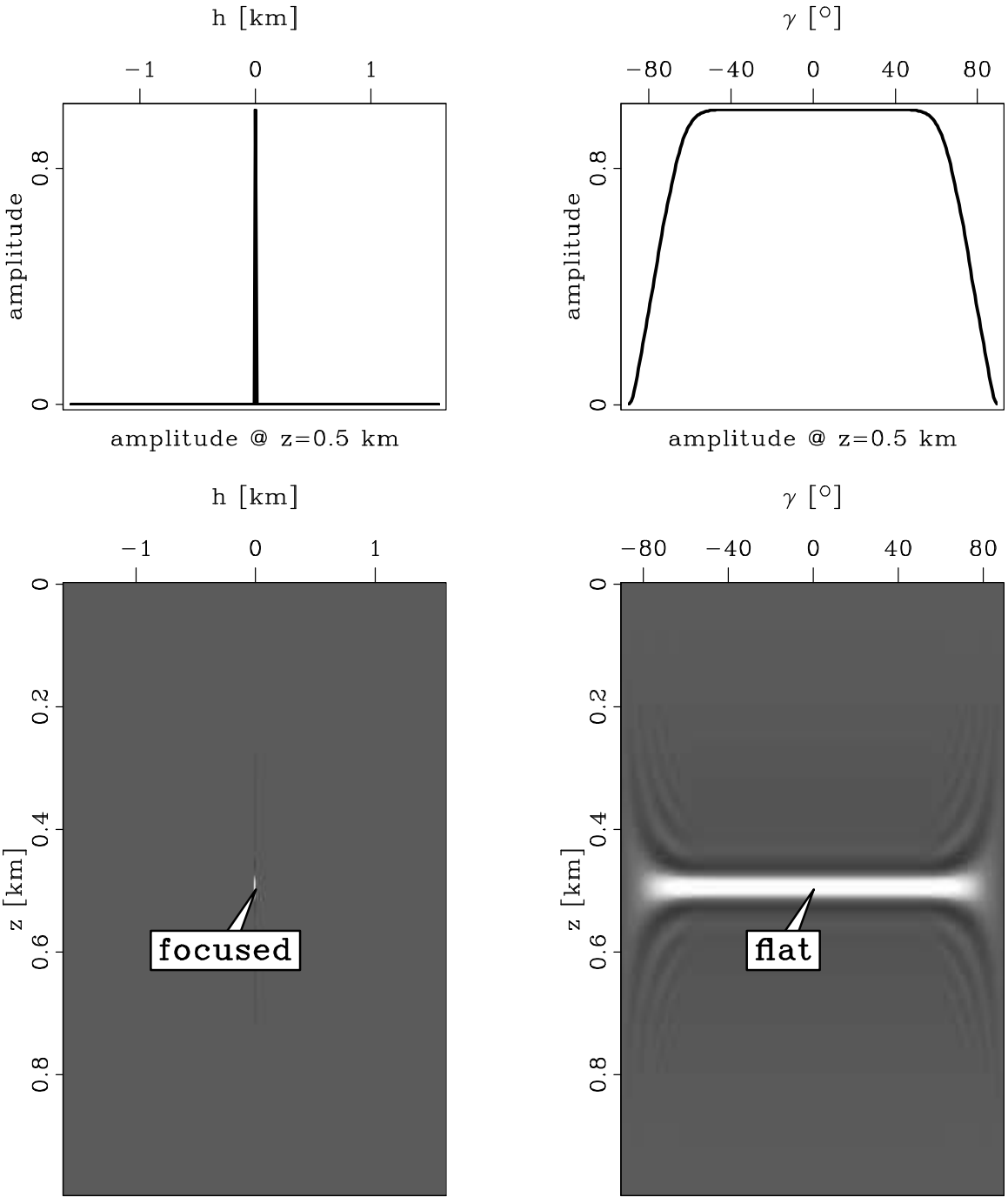


Figure 3.3: Ideal offset-domain and angle-domain common image gathers. adcig-simplesyn [ER]

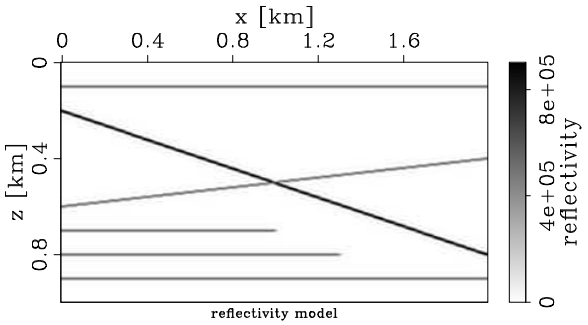
correct and incorrect velocities. The ADCIGs are flat for the case of correct velocity (Figure 3.5), but they are not flat for the case of incorrect velocity (Figure 3.6). The bottom panels show ADCIGs computed in the image and data spaces at the location indicated by the vertical line at 1.2 km. The velocity changes in the upper part of the model from 1.75 km/s in the correct model to 1.5 km/s in the incorrect one. Since I have simulated wide offset data, the deeper flat events do not suffer much from reduced angular coverage. However, the limited acquisition causes a reduction in angular coverage for the steeply dipping fault.

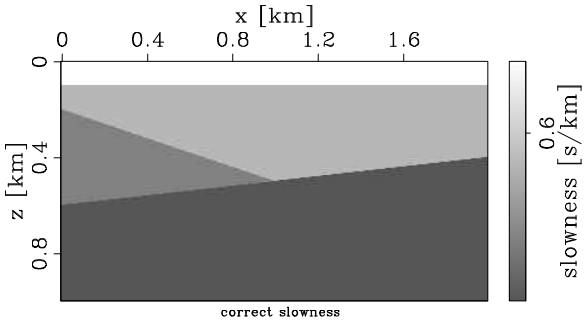
Figures 3.5 and 3.6 also show the different amplitude behavior between the image space and data space methods: for the image space method, the amplitudes decrease as a function of angle, while for the data space method, the amplitudes increase as a function of offset ray-parameter. This observation shows that AVA analysis on any of the two kinds of angle gathers is problematic (Sava et al., 2001b).

The third example concerns a real dataset acquired over a region with fairly simple geology (Figure 3.7). This dataset was first analyzed by Kjartansson (1979) and it is part of the SEP data library. Figure 3.8 shows image gathers at $x = 7.5$ km. As theoretically predicted, at the imaging step most of the energy is concentrated around zero offset. After the conversion to the angle-domain, almost all the events are flat, although some show slight moveout, indicating migration and/or velocity inaccuracies. For this example, too, we can observe the same difference in amplitude behavior of the data space versus the image space method as for the synthetic example in Figures 3.5 and 3.6.

Figure 3.9 demonstrates the effect of regularization in the angle-domain. In the left panel, I present an angle gather created without regularization ($\epsilon = 0.0$), and on the right I present the same angle gather obtained with regularization ($\epsilon = 1.0$), according to equation (3.9). The left panel is populated with artifacts caused by the non-uniform sampling of the ADCIG due to the radial trace transform in the Fourier domain. In contrast, the panel on the right shows fewer artifacts, which makes the reflections much easier to interpret.

The fourth example concerns a 3D common-azimuth (Biondi and Palacharla, 1996) data set from the North Sea (Vaillant et al., 2000). This dataset was donated to SEP by Elf and it is part of the SEP data library. Figure 3.10 is an inline extracted from the 3D seismic cube and





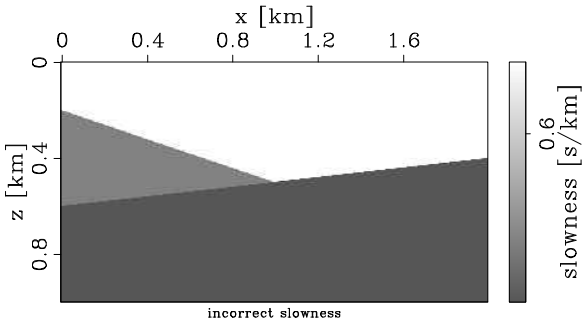


Figure 3.4: 2D synthetic model: from top to bottom, reflectivity model, correct and incorrect slownesses. adcig-frcmodel [ER]

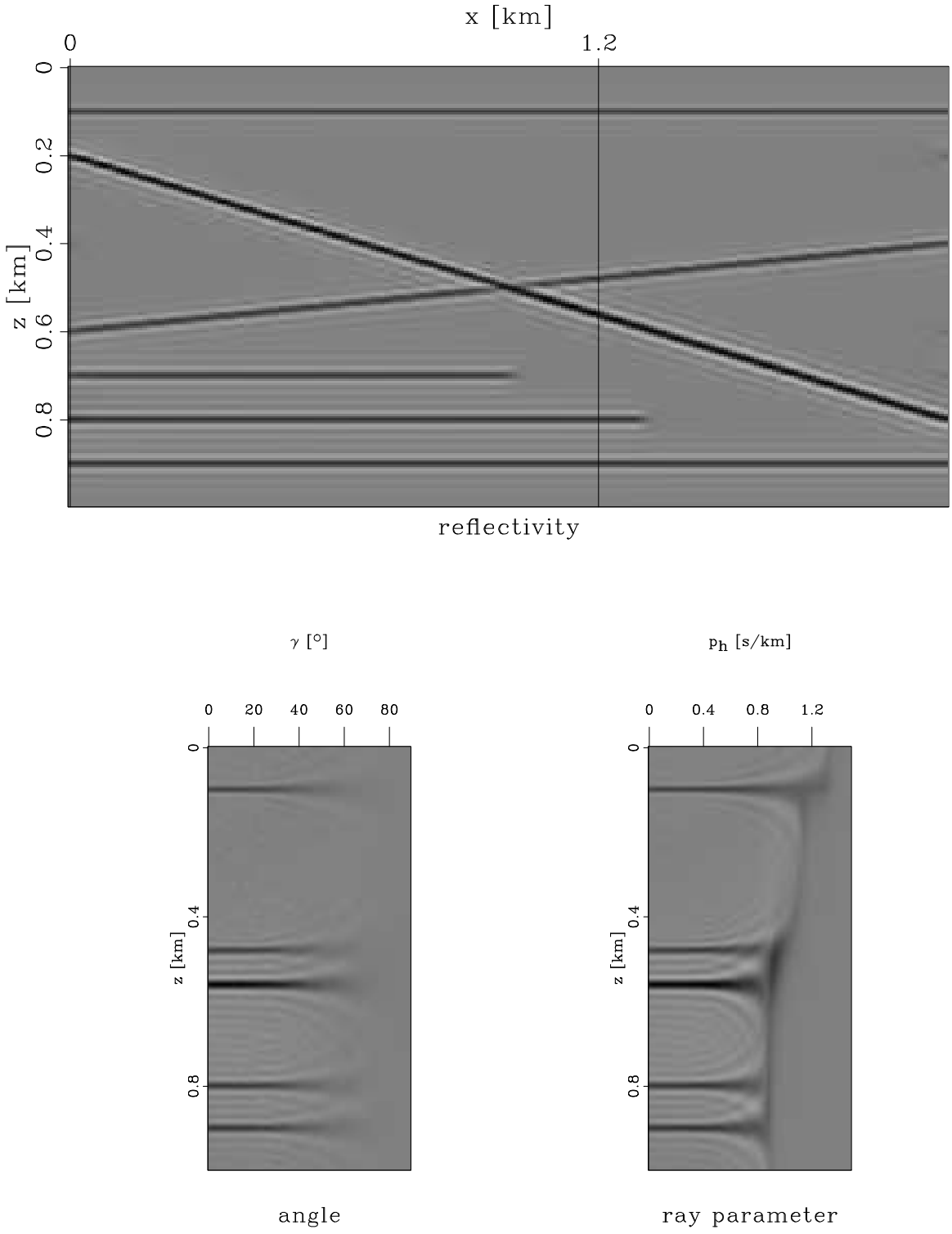


Figure 3.5: Synthetic model imaged using the *correct* velocity model: section obtained by imaging at zero time and zero offset (top), angle gather created in the image space (bottom left), and angle gather created in the data space (bottom right). adcig-frcimgC [CR]

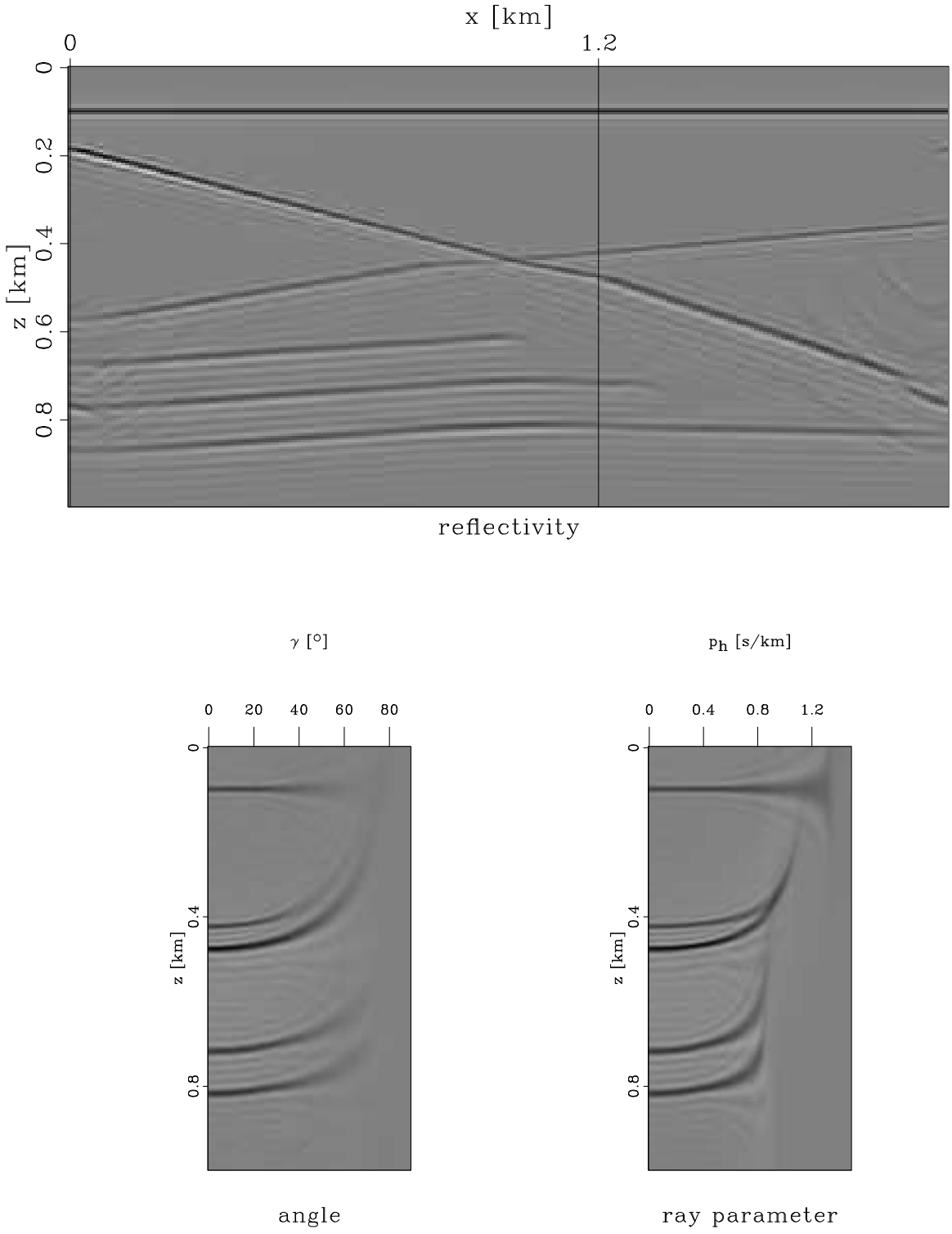


Figure 3.6: Synthetic model imaged using the *incorrect* velocity model: section obtained by imaging at zero time and zero offset (top), angle gather created in the image space (bottom left), and angle gather created in the data space (bottom right). adcig-frcimg0 [CR]

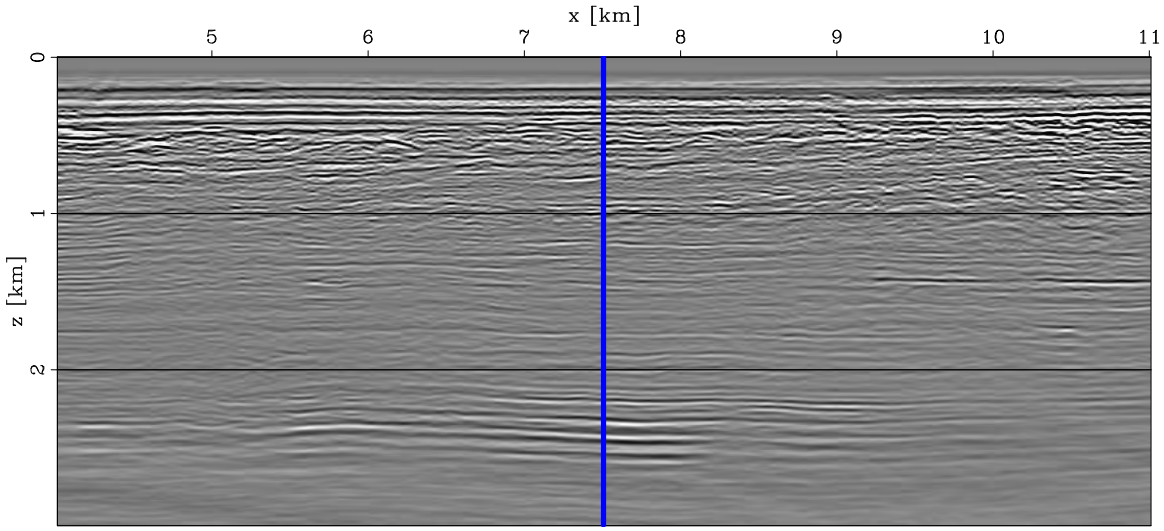


Figure 3.7: 2D real data example: seismic section obtained by imaging at zero time and zero offset. adcig-kjamig [CR]

shows a salt body in the middle of the section, surrounded by fairly flat reflectors. Figure 3.11 shows an image gather at $x = 4.0$ km, presented in the offset-domain (left panel) and in the angle-domain (right panel). As before, most of the energy is imaged around zero offset, which translates in fairly flat events in the angle gather indicating that both the migration and the velocity model are correct. The geometry of the reflectors in this example are fairly simple, although the waves propagate through a complicated salt area.

3.6 Discussion

Several points emphasize the main qualities of this angle-transform method:

- This method produces the output as a function of the incidence angle at the reflector, and not as a function of offset ray-parameter. This makes the results more open to interpretation, and potentially allows for consistent quantitative AVA analysis if the amplitudes are handled correctly during migration (Sava et al., 2001b).
- This method generates angle gathers after and not during migration, thus enabling us to

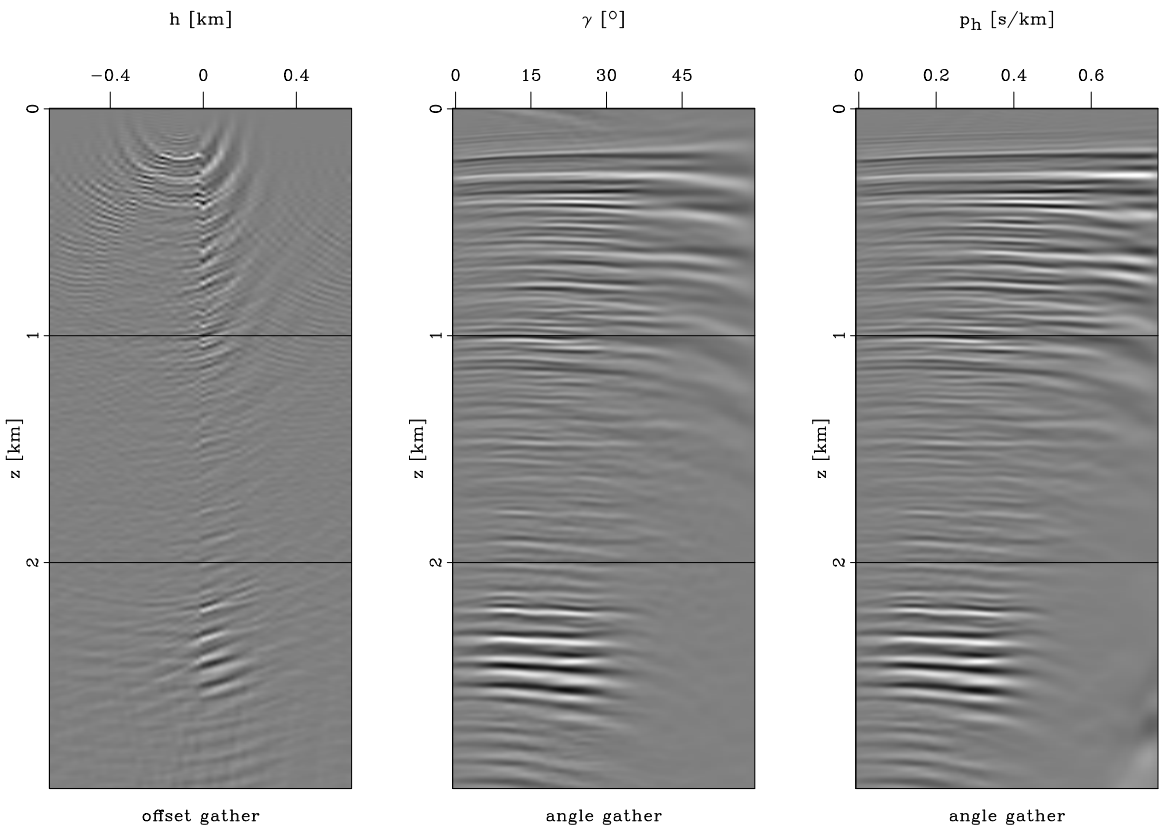


Figure 3.8: 2D real data example: from left to right, offset-gather (right panel) and angle gathers, computed in the image-space (middle panel) and the data-space (right panel) adcig-kjacig [CR]

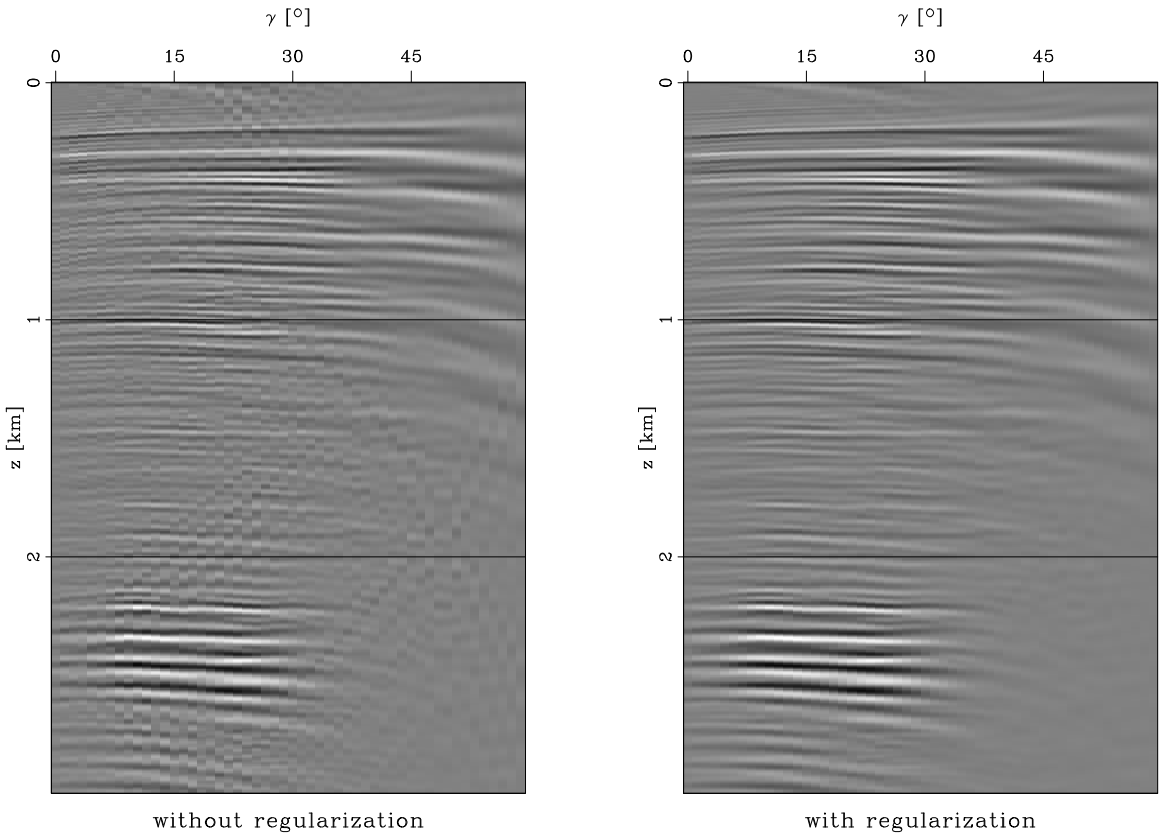


Figure 3.9: 2D real data example: a comparison of an angle gather obtained without regularization (left) and an angle gather obtained with regularization (right). adcig-kjaeps [CR]

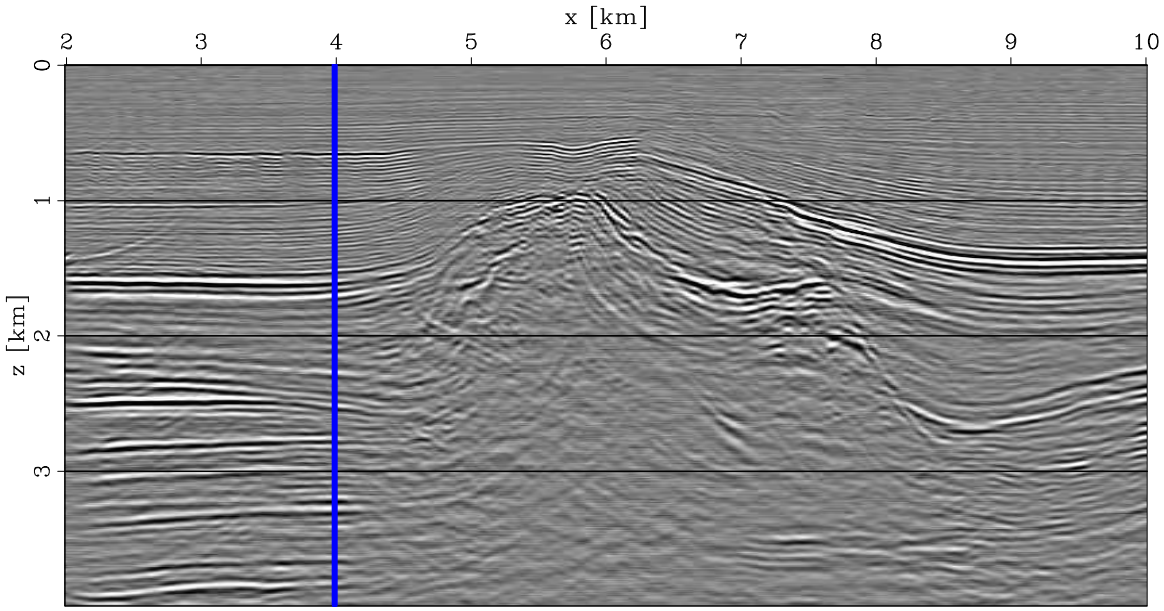


Figure 3.10: 3D common-azimuth example: seismic section obtained by imaging at zero time and zero offset. The vertical line corresponds to the CIGs in Figure 3.11. adcig-l7dmig [CR]

shuttle between the angle and offset domains without re-migrating the data. Since the transformation to the angle-domain is separated from the migration itself, this method can be used both for shot-geophone downward-continuation migration, as exemplified here, or for shot-profile downward-continuation migration (Rickett and Sava, 2002). The method can also be generalized to the cases of converted waves (Rosales and Rickett, 2001), or two-way wave propagation (Biondi and Shan, 2002).

- This method enables inexpensive regularization of the angle-domain leading to gathers with events that vary smoothly along the angle axis. The increased S/N ratio helps reveal weak events that would otherwise be harder to interpret.

3.7 Conclusions

This chapter presents a method for computing angle-domain common image gathers from wave-equation depth-migrated images. I produce angle gathers from migrated images with a

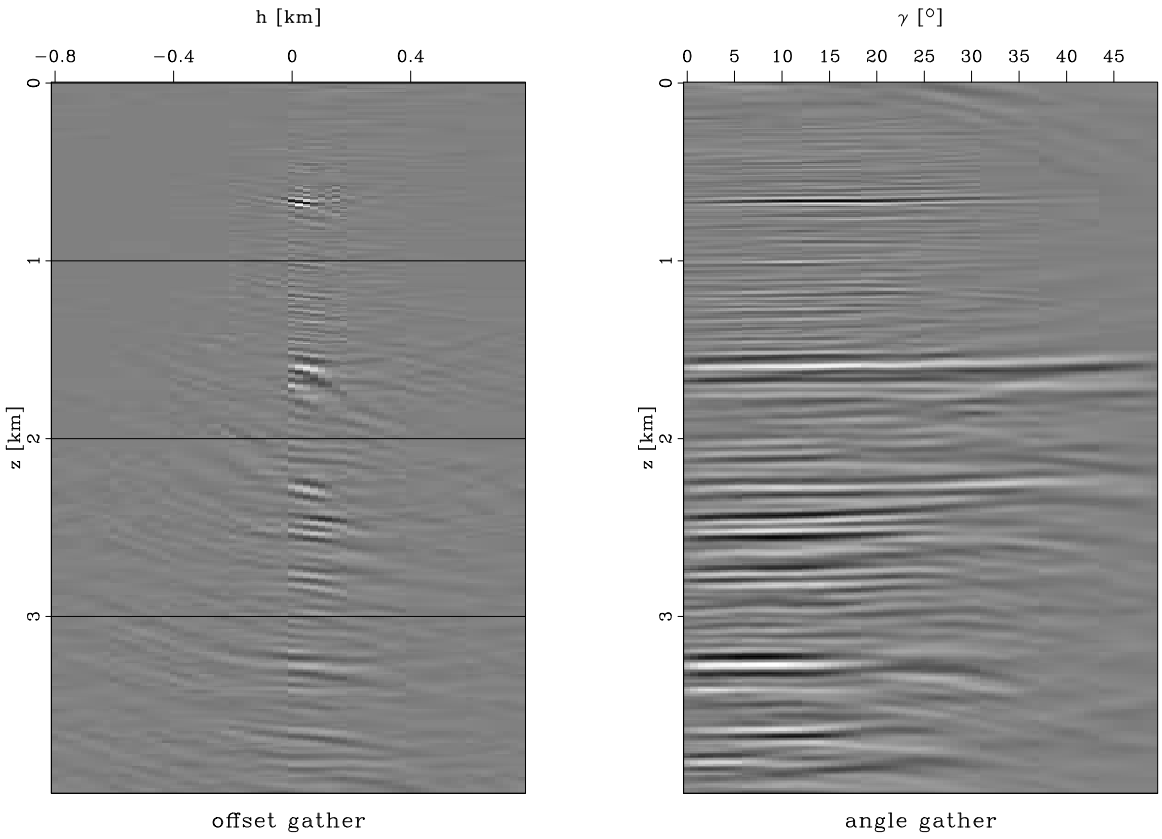


Figure 3.11: 3D common-azimuth example: offset-gather (left panel) and angle gather (right panel) corresponding to the vertical line in Figure 3.10. adcig-l7dcig [CR]

process which is completely detached from migration. The output of this image-space method is a function of reflection angle, and not function of offset ray-parameter.

I show that this method is, in essence, a radial trace transform in the Fourier domain, and therefore equivalent to a slant stack in the space domain. The method is fully applicable to arbitrary models, with high image complexity and lateral velocity variations.

I implement the method using a stretch technique with model regularization, thus reducing the artifacts caused by non-uniform sampling due to the Fourier-domain radial-trace transforms. The method is accurate, fast, robust, easy to implement, and can be used for real prestack data for simple imaging or in applications related to migration velocity analysis (MVA) and amplitude versus angle (AVA) analysis.

Extensions to 3D are presented by Biondi and Symes (2004), Biondi and Tisserant (2004) and Fomel (2004).

3.8 Acknowledgment

I would like to acknowledge Sergey Fomel with whom I collaborated on developing this angle transformation for images migrated by downward continuation (Sava and Fomel, 2003).

Chapter 4

Prestack residual migration

4.1 Overview

Prestack Stolt residual migration can be applied to seismic images that are depth migrated using wavefield extrapolation techniques. Residual migration allows us to estimate velocity inaccuracy not only by measuring flatness of angle-domain common image gathers, but also by measuring focusing along the spatial axes. Therefore, residual migration is useful in conjunction with a migration velocity analysis tool capable of using such information for velocity updates.

Residual migration can be implemented efficiently in the frequency-wavenumber domain as a function of a scalar parameter relating the background velocity to a trial velocity. Although the theory is developed assuming constant velocity, the method can be used for depth-migrated images produced with smoothly varying velocity models, since the residually migrated images depend only on the ratio of the reference and updated velocities. This method closely resembles Stolt-stretch techniques, and so it inherits Stolt's method speed and convenience. The main applications of this method are in migration velocity analysis (MVA) where it can be used to investigate the effects of gross velocity changes on the migrated image, and as a tool for residual image enhancement employed by more sophisticated MVA methods, for example by wave-equation migration velocity analysis Chapter 5.

4.2 Introduction

Residual migration has proved useful both in imaging and in migration velocity analysis. Rothman et al. (1985) show that post-stack residual migration can improve the focusing of migrated sections. They also show that migration with a given velocity (v) is equivalent to migration with a reference velocity (v_0) followed by residual migration with a velocity (v_r) that can be expressed as a function of v_0 and v.

Residual migration has also been used in velocity analysis. Al-Yahya (1989, 1987) discusses a residual migration operator in the prestack domain, and show that it can be posed as a function of a non-dimensional parameter (ρ), the ratio of the reference velocity to the updated velocity. Etgen (1988, 1990) defines a kinematic residual migration operator as a cascade of NMO and DMO, and shows that it is only a function of the non-dimensional parameter (ρ) defined by Al-Yahya. Finally, Stolt (1996) defines a prestack residual migration operator in the (ω,k) domain, and shows that, as in the post-stack case, it depends on the reference (v_0) and the correct (v) migration velocities, but not on a residual velocity (v_r).

In this section, I review prestack Stolt residual migration, and show that it, too, can be formulated as a function of a non-dimensional parameter that is the ratio of the reference (v_0) and updated (v) velocities. Consequently, we can use Stolt residual migration in the prestack domain to obtain a better-focused image without making explicit assumptions about the velocity magnitude. Although, strictly speaking, the method is developed for constant velocity, numerical examples show that it can be used in an approximate way for images migrated with smoothly varying velocity $v(x,y,z)$ which departs from the constant velocity assumption.

An alternative to the residual migration technique presented in this section is a suite of full depth migrations with velocities at a percentage change from a reference velocity. Although more accurate, such a technique is also more expensive and not much more useful than residual migration, except for a complicated geological model which violates the residual migration assumptions.

This method has direct application in wave-equation migration velocity analysis (Chapter 5). In WEMVA, we invert for perturbations of the velocity model starting from perturbations of the seismic image. A quick residual migration technique is ideally suited for this task, since we are less interested in the accuracy of the perturbed images than in the direction of the change that needs to be applied to the velocity model in order to improve the image.

4.3 Stolt migration

Prestack Stolt migration can be summarized (Claerbout, 1985) as a succession of transformations from seismic data to seismic images as follows:

$$d(t,\mathbf{m},\mathbf{h}) \rightarrow \mathcal{D}(\omega,\mathbf{k}_m,\mathbf{k}_h) \rightarrow \mathcal{R}(k_z,\mathbf{k}_m,\mathbf{k}_h) \rightarrow r(z,\mathbf{m},\mathbf{h}). \tag{4.1}$$

where d and r are representations of the data and image in the space domain, while $\mathcal{D}$ and $\mathcal{R}$ are the equivalent representations in the Fourier domain. In equation (4.1), t stands for time, $\mathbf{m}$ for midpoint location, $\mathbf{h}$ for half-offset, and z for depth.

The central component of prestack Stolt migration is the re-mapping from the $(\omega,\mathbf{k}_m,\mathbf{k}_h)$ domain to the $(k_z,\mathbf{k}_m,\mathbf{k}_h)$ domain, where ω and k_z represent, the temporal frequency and the depth wavenumber respectively, and $\mathbf{k}_m = (k_{mx},k_{my})$ and $\mathbf{k}_h = (k_{hx},k_{hy})$ represent the midpoint and offset wavenumbers.

If we consider the representation of the input data in shot-receiver coordinates, the mapping takes the form

$$k_z = \frac{1}{2}\sqrt{\frac{\omega^2}{v^2} - |\mathbf{k}_r|^2} + \frac{1}{2}\sqrt{\frac{\omega^2}{v^2} - |\mathbf{k}_s|^2}, \tag{4.2}$$

where $\mathbf{k}_r$ and $\mathbf{k}_s$ stand for, respectively, the receiver and the source wavenumbers. From equation (4.2) we can express ω as a function of k_z:

$$\omega^2 = v^2 \frac{\left[4k_z^2 + (|\mathbf{k}_r| - |\mathbf{k}_s|)^2\right]\left[4k_z^2 + (|\mathbf{k}_r| + |\mathbf{k}_s|)^2\right]}{16k_z^2}. \tag{4.3}$$

We can obtain an equation equivalent to (4.3) in midpoint-offset coordinates, if we make

the usual change of variables:

$$\begin{aligned} \mathbf{k}_r &= \mathbf{k}_m + \mathbf{k}_h \\ \mathbf{k}_s &= \mathbf{k}_m - \mathbf{k}_h. \end{aligned} \tag{4.4}$$

4.4 Prestack Stolt residual migration

In general, residual migration improves the quality of an image without re-migration of the original data; instead, a transformation is applied to the current migrated image.

In prestack Stolt residual migration, we attempt to correct the effects of migrating with an inaccurate reference velocity by applying a transformation to images transformed to the Fourier domain. Supposing that the initial migration was done with the velocity v_0, and that the correct velocity is v, we can use equation (4.2) to derive k_{z0}, the vertical wavenumber for the reference velocity, and k_z, the vertical wavenumber for the correct velocity.

Mathematically, the goal of prestack Stolt residual migration is to obtain k_z from k_{z0}. If we elliminate ω from k_{z0} and k_z, and make the notation $\rho = \frac{v_0}{v}$, we obtain the residual migration equation for full 3D prestack seismic images:

$$\begin{aligned} k_z = &\frac{1}{2}\sqrt{\rho^2 \frac{\left[4k_{z0}^2+(|\mathbf{k}_r|-|\mathbf{k}_s|)^2\right]\left[4k_{z0}^2+(|\mathbf{k}_r|+|\mathbf{k}_s|)^2\right]}{16k_{z0}^2} - |\mathbf{k}_r|^2} \\ &+\frac{1}{2}\sqrt{\rho^2 \frac{\left[4k_{z0}^2+(|\mathbf{k}_r|-|\mathbf{k}_s|)^2\right]\left[4k_{z0}^2+(|\mathbf{k}_r|+|\mathbf{k}_s|)^2\right]}{16k_{z0}^2} - |\mathbf{k}_s|^2}, \end{aligned} \tag{4.5}$$

which can also be represented in midpoint-offset coordinates using the change of variables in equation (4.4). If we make the change of variables

$$\mu^2 = \frac{\left[4{k_{z0}}^2 + (\mathbf{k}_r - \mathbf{k}_s)^2\right]\left[4{k_{z0}}^2 + (\mathbf{k}_r + \mathbf{k}_s)^2\right]}{16{k_{z0}}^2}. \tag{4.6}$$

we obtain a simplified version of equation (4.5):

$$k_z = \frac{1}{2}\sqrt{\rho^2\mu^2 - |\mathbf{k}_s|^2} + \frac{1}{2}\sqrt{\rho^2\mu^2 - |\mathbf{k}_r|^2}\,. \tag{4.7}$$

In the 3D post-stack case, when $\mathbf{k}_h = \mathbf{0}$, equation (4.5) becomes:

$$k_z = \sqrt{\rho^2 \left[k_{z0}^2 + |\mathbf{k}_m|^2\right] - |\mathbf{k}_m|^2}. \tag{4.8}$$

In the 2D prestack case ($k_{my} = 0$ and $k_{mx} = 0$), we can write equation (4.5) as:

$$\begin{aligned} k_z = &\tfrac{1}{2}\sqrt{\rho^2 \frac{\left[k_{z0}^2 + k_{hx}^2\right]\left[k_{z0}^2 + k_{mx}^2\right]}{k_{z0}^2} - (k_{mx} + k_{hx})^2} \\ &+ \tfrac{1}{2}\sqrt{\rho^2 \frac{\left[k_{z0}^2 + k_{hx}^2\right]\left[k_{z0}^2 + k_{mx}^2\right]}{k_{z0}^2} - (k_{mx} - k_{hx})^2}. \end{aligned} \tag{4.9}$$

For 2D post-stack data, equations (4.8) and (4.9) become

$$k_z = \sqrt{\rho^2 \left[k_{z0}^2 + k_{mx}^2\right] - k_{mx}^2}, \tag{4.10}$$

which can also be written in the familiar form (Stolt, 1996):

$$\omega = \sqrt{\omega_0^2 + k_{mx}^2 \left(v_0^2 - v^2\right)}, \tag{4.11}$$

where, by definition, $\omega_0 = k_{z0} v_0$, and $\omega = k_z v$.

4.5 Common-azimuth Stolt residual migration

Common-azimuth data represent subsets of 3D prestack data that have been recorded or transformed to a common azimuth, which corresponds to zero cross-line offsets ($\mathbf{h}_y = 0$). Stolt migration for common-azimuth data involves the use of the following dispersion relation (Biondi and Palacharla, 1996):

$$k_{zx} = \frac{1}{2}\sqrt{\frac{\omega^2}{v^2} - (k_{mx} - k_{hx})^2} + \frac{1}{2}\sqrt{\frac{\omega^2}{v^2} - (k_{mx} + k_{hx})^2}, \tag{4.12}$$

where the depth wavenumber for the common-azimuth dataset (k_z) is written as

$$k_z = \sqrt{{k_z}_x^2 - {k_m}_y^2}. \tag{4.13}$$

We can rewrite equations (4.12) and (4.13) for a given reference velocity (v_0) and obtain the corresponding depth wavenumbers k_{zx0} and k_{z0}. Mathematically, the goal of common-azimuth Stolt residual migrations is also to obtain k_z from k_{z0}. Again, we can achieve this by eliminating the frequency ω from the expressions for k_{z0} and k_z, which leads to the 3D common-azimuth residual migration equations:

$$\left\{ \begin{array}{l} k_{zx} = \frac{1}{2}\sqrt{\rho^2 \frac{\left[k_{z0}^2 + {k_m}_y^2 + {k_h}_x^2\right]\left[k_{z0}^2 + {k_m}_y^2 + {k_m}_x^2\right]}{k_{z0}^2 + {k_m}_y^2} - (k_{mx} - k_{hx})^2} \\ \qquad + \frac{1}{2}\sqrt{\rho^2 \frac{\left[k_{z0}^2 + {k_m}_y^2 + {k_h}_x^2\right]\left[k_{z0}^2 + {k_m}_y^2 + {k_m}_x^2\right]}{k_{z0}^2 + {k_m}_y^2} - (k_{mx} + k_{hx})^2} \\ k_z = \sqrt{{k_z}_x^2 - {k_m}_y^2}\,, \end{array} \right. \tag{4.14}$$

where, by definition, $\rho = \frac{v_0}{v}$. If we make the change of variables

$$\mu_c^2 = \frac{\left[{k_{z0}}^2 + {k_m}_y^2 + {k_h}_x^2\right]\left[{k_{z0}}^2 + {k_m}_y^2 + {k_m}_x^2\right]}{{k_{z0}}^2 + {k_m}_y^2}. \tag{4.15}$$

we obtain a simplified version of equations (4.14):

$$\left\{ \begin{array}{l} k_{zx} = \frac{1}{2}\sqrt{\rho^2\mu_c^2 - (k_{mx} - k_{hx})^2} + \frac{1}{2}\sqrt{\rho^2\mu_c^2 - (k_{mx} + k_{hx})^2} \\ k_z = \sqrt{{k_z}_x^2 - {k_m}_y^2}\,, \end{array} \right. \tag{4.16}$$

For 2D data, where $k_{my} = 0$, $k_z \equiv k_{zx}$ and $k_{z0} \equiv k_{zx0}$, equations (4.14) reduce to the 2D prestack equation (4.9) and post-stack equation (4.10) forms.

4.6 Examples

I illustrate the residual migration technique with one synthetic and one real data example.

The first example is a simple 2D model with a 4 dipping reflectors embedded in a velocity model which varies smoothly both as a function of horizontal position and as a function of depth. Figure 4.1 shows, from top to bottom, the slowness model, the reflectivity model and the zero offset of the 2D modeled data. The data were generated with a wavefield-continuation operator (Claerbout, 1985; Ristow and Ruhl, 1997; Rousseau and de Hoop, 1998). The maximum offset of the simulated data is 2.56 km, and the velocity ranges between 2.0 km/s in the upper left corner to 2.4 km/s in the lower right corner.

To test the prestack Stolt residual migration, I migrate the synthetic data using wavefield-continuation with the mixed-domain split-step Fourier method. The tests are carried out using two velocity models: the correct velocity, and an incorrect velocity model which is obtained from the correct one by scaling with a factor of 0.8.

Figure 4.2 shows the image obtained using the correct velocity model. The left panel represents the zero offset section of the image obtained by 2D prestack downward-continuation migration. The right panel represents a common image gather in the angle domain (Chapter 3), extracted at the horizontal location $x = 1$ km.

Figure 4.3 shows the image obtained using the incorrect velocity model. Since this velocity is smaller than the correct one, the image is strongly undermigrated, and the events in the angle-domain common image gathers bend strongly upward.

Figure 4.4 shows the result of applying Stolt residual migration using the correct velocity ratio ($\rho = 0.8$) to the undermigrated image in Figure 4.3. The result is a well focused image, with reasonably flat angle gathers. This result shows that, although only approximate for variable velocity media, the method outlined in this section can successfully operate on depth migrated images despite the assumption of constant velocity made in the derivation. Of course, there is no guarantee that the method will be successful on arbitrary velocity models. However, on fairly smooth models, Stolt residual migration can at least indicate the direction of the changes that improve the migrated image.

The second example concerns a real dataset from a complex salt dome region in the North Sea (Vaillant et al., 2000). This dataset was donated to SEP by Elf and it is part of the SEP

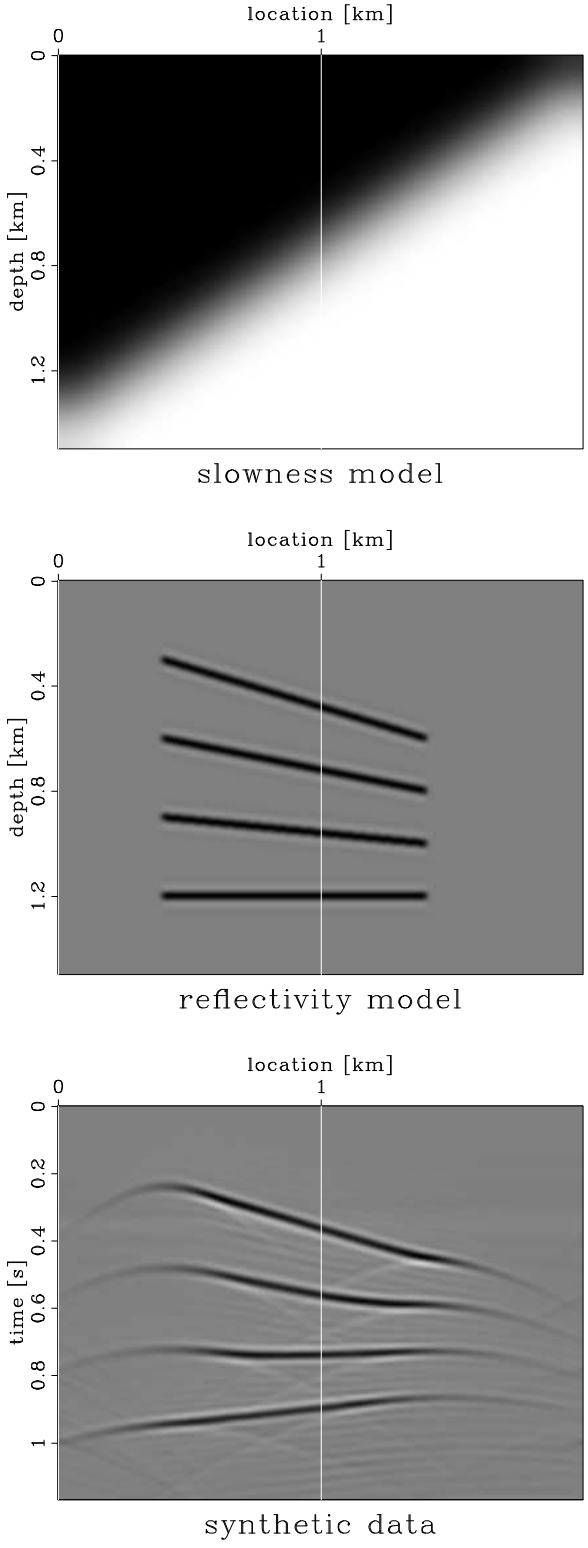


Figure 4.1: Synthetic model. From top to bottom, slowness model, reflectivity model and the zero offset section of the modeled 2D prestack data. storm-synt.model [ER]

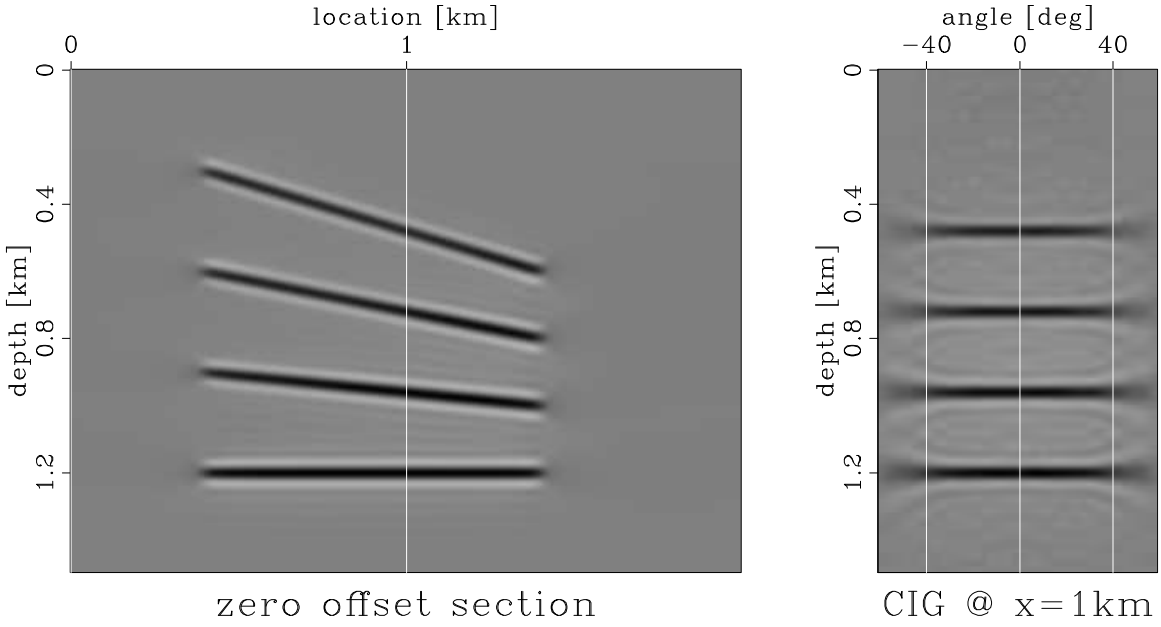


Figure 4.2: Migrated image (zero offset section) and angle-domain CIG for the synthetic data in Figure 4.1 obtained using the correct velocity model. storm-synt.RC.zhm [ER]

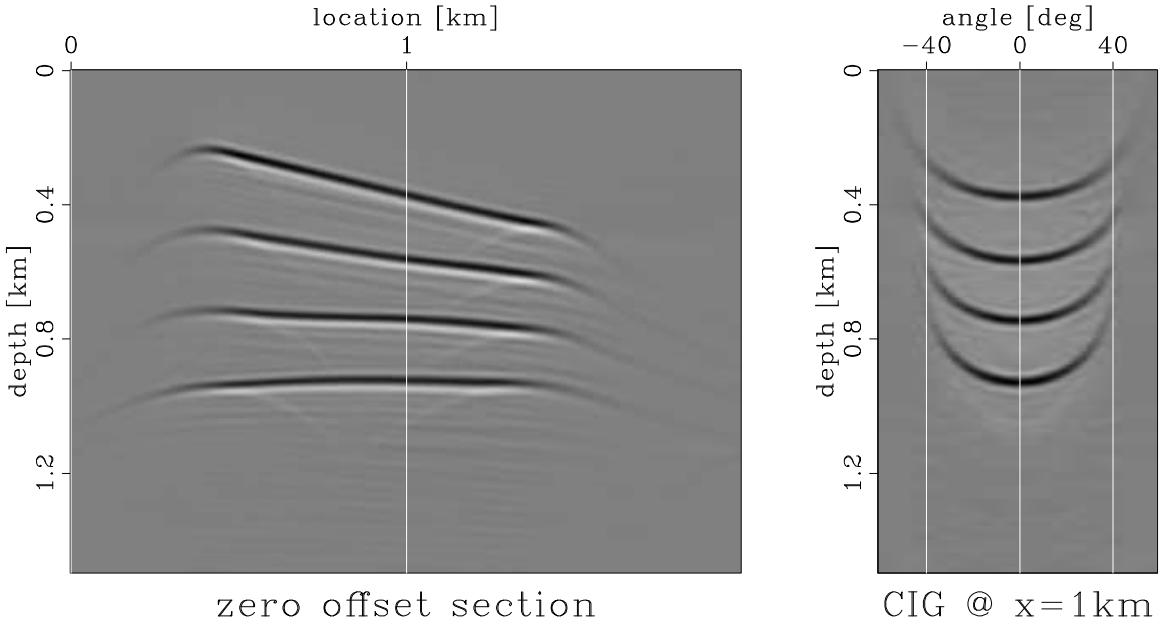


Figure 4.3: Migrated image (zero offset section) and angle-domain CIG for the synthetic data in Figure 4.1 obtained using the incorrect velocity model scaled by $\rho = 0.8$. storm-synt.R0.zhm [ER]

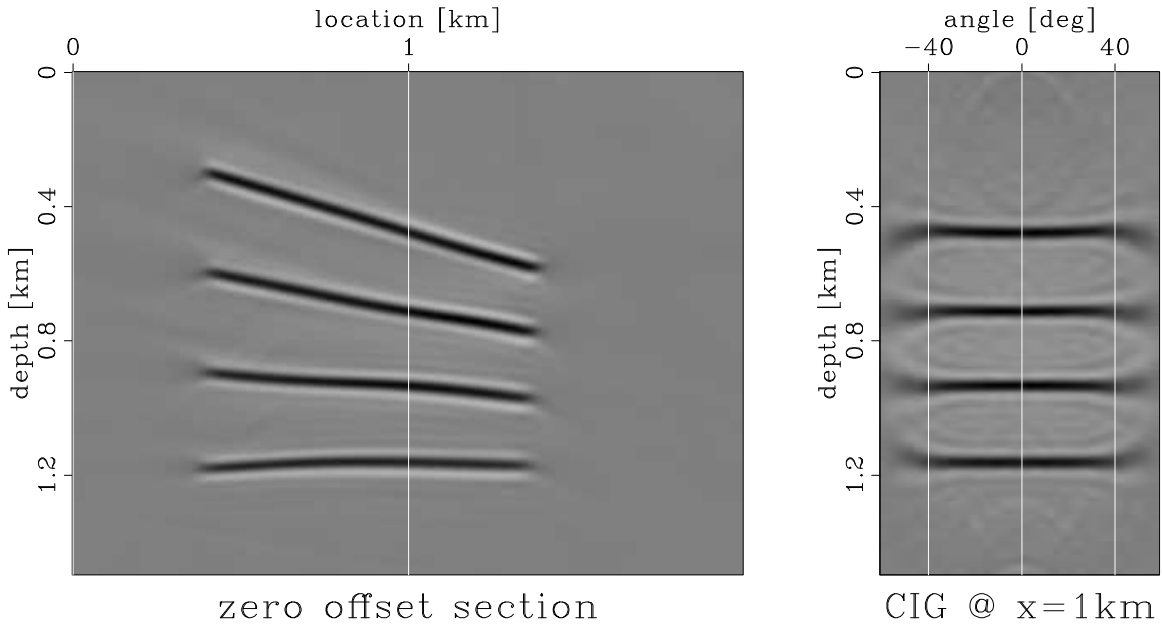


Figure 4.4: Residually migrated image (zero offset section) and angle-domain CIG for the synthetic data in Figure 4.1 obtained from the image in Figure 4.3 after residual migration with the correct velocity ratio $\rho = 0.8$. storm-synt.R0.srm [ER]

data library. Figure 4.5 shows a zero-offset section obtained by 2D prestack downward-continuation migration. We can clearly distinguish the salt body and the sediment layers. However, the area under the salt overhang is not imaged correctly, mostly due the inaccuracies in the velocity model (Vaillant et al., 2000).

The errors in this image are too complex for a simple algorithm like the one outlined in this section to be fully successful. We cannot hope to recover the exact structure under the salt overhang just by residual migration. However, we can use the speed of such an algorithm to investigate whether any other piece of the image can be brought in focus, and to determine roughly in which direction we need to modify the velocity model.

Figure 4.6 shows the result of residual migration. Each one of the 9 panels corresponds to the box depicted in Figure 4.5. The images are obtained for various values of the parameter ρ ranging from $\rho = 1.0$ to $\rho = 0.92$ as labeled in the figure.

We can observe several things: the top of salt, which was not well focused in the original

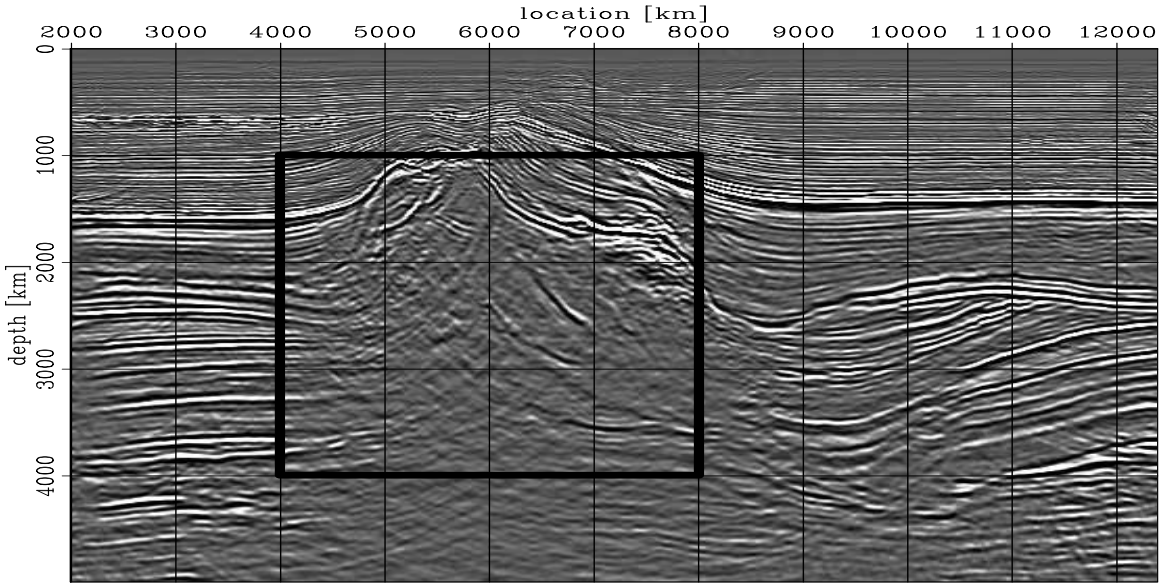


Figure 4.5: Migrated image of the North Sea data. The area of interest is surrounded by the thick box. storm-saltreal.raw [CR]

image ($\rho = 1.0$), is better focused in some of the panels corresponding to lower values of the parameter ρ; the salt overhang is brought into much better focus, particularly in the panel corresponding to $\rho = 0.94$ around $x = 6000$ and $z = 3000$; the sediments that are practically impossible to track in the original image are more coherent and can be traced much deeper under the salt overhang on the image corresponding to $\rho = 0.94$.

Figure 4.7 is a comparison between the original image ($\rho = 1.00$, top panel) and the image obtained by prestack Stolt residual migration that best resolves the salt overhang and sediments underneath ($\rho = 0.94$, bottom panel). For comparison, the middle panel shows an image obtained by residual moveout which also shows an improvement over the original image, but not as good as the one obtained by residual migration. This is understandable, since residual moveout does not allow energy to move between midpoints, while residual migration does.

Finally, if we carefully analyze the images in Figure 4.6, we can observe that various parts of the image are in good focus at different values of the ratio parameter ρ. This leads to the conclusion that none of the panels in Figure 4.6 alone can serve as an improved image at all

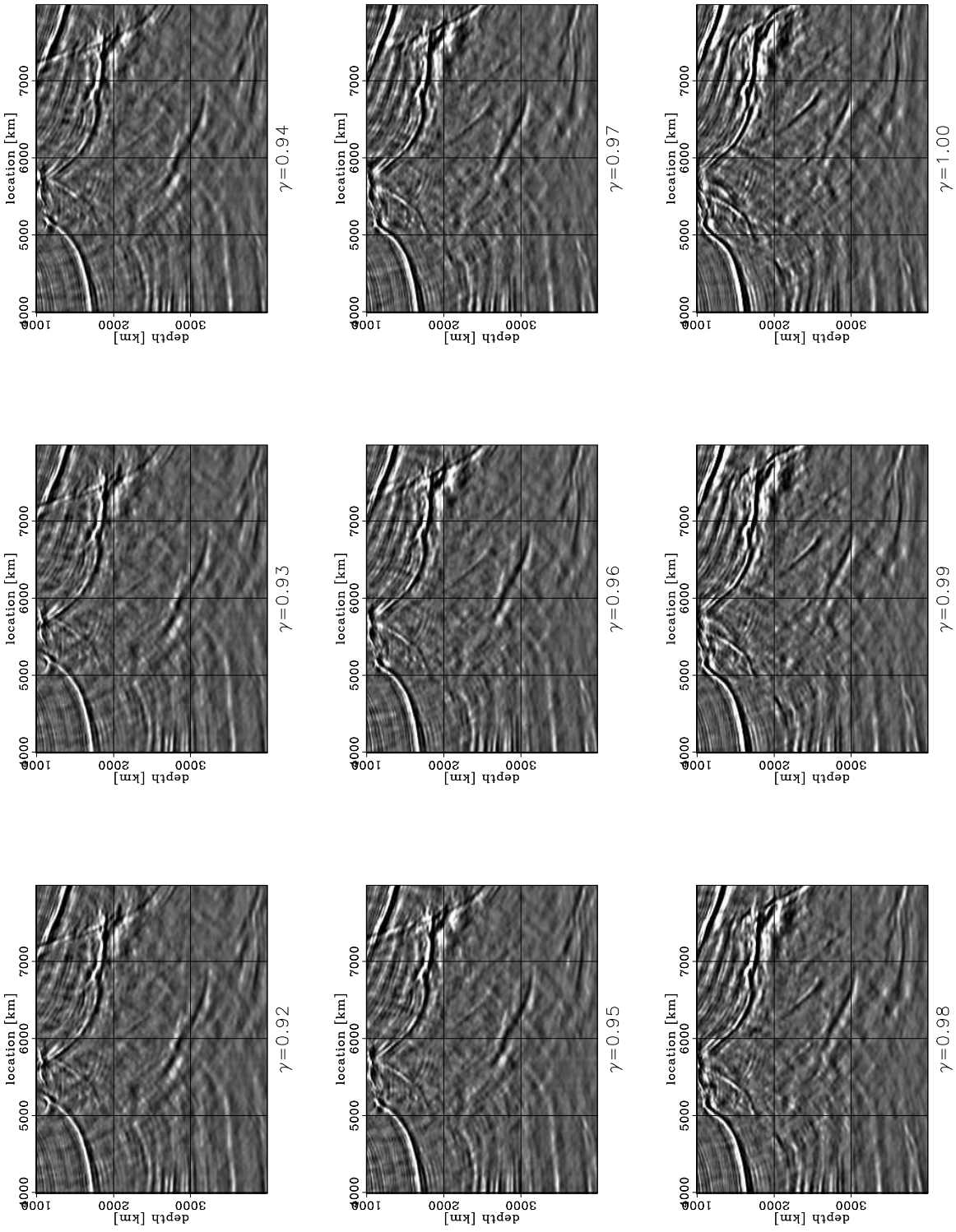
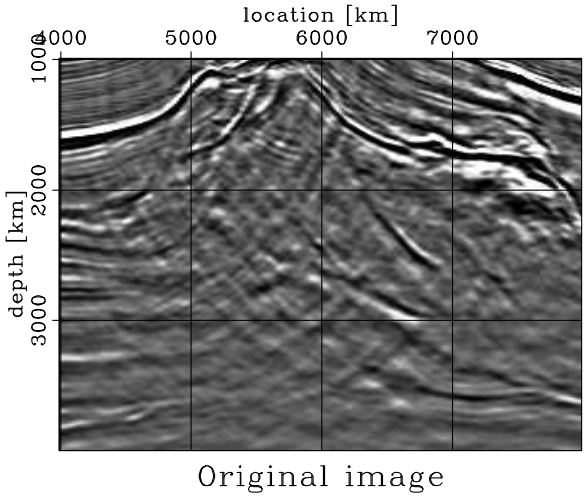
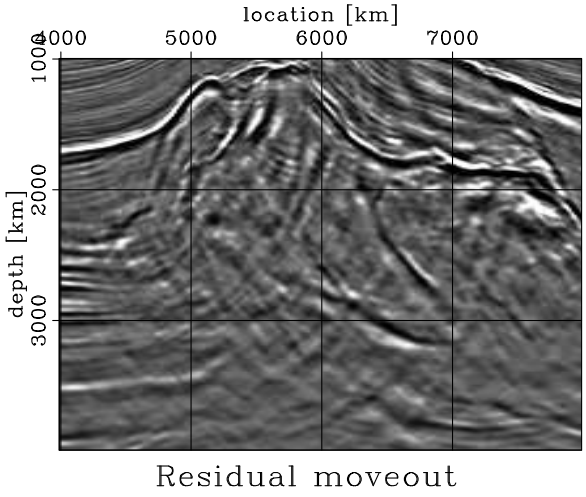


Figure 4.6: Prestack Stolt residual migration for a range of velocity ratio parameters (ρ) from 1.0 to 0.92. All panels correspond to the box in Figure 4.5. storm-saltreal.srm [CR]





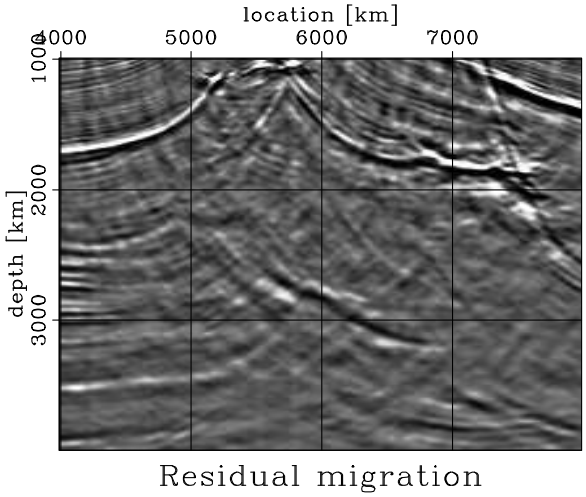


Figure 4.7: A comparison of the original image (top panel) with the improved images obtained by residual moveout (middle panel) and the image after residual migration with a constant velocity ratio parameter $\rho = 0.94$ (bottom panel). All panels correspond to the box in Figure 4.5. storm-saltreal.constant [CR]

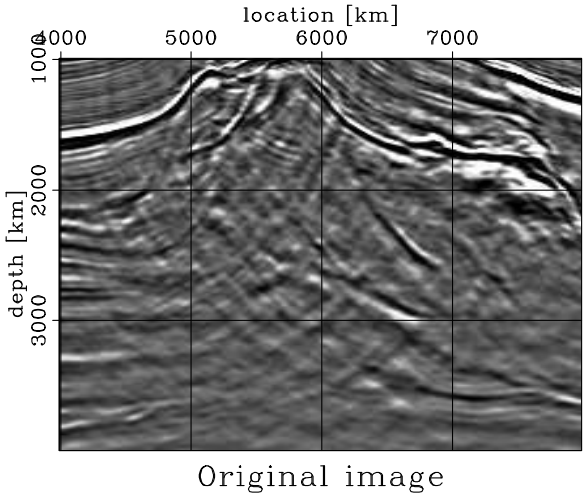
locations in the image. One possible solution to this problem is to create a smooth interpolation map which slices through the various images at different values of ρ for every location in the image. Figure 4.8 shows such a result: the top and middle images are respectively the original and improved images for variable ρ, and the bottom panel is the interpolation map used to extract the middle panel.

4.7 Discussion

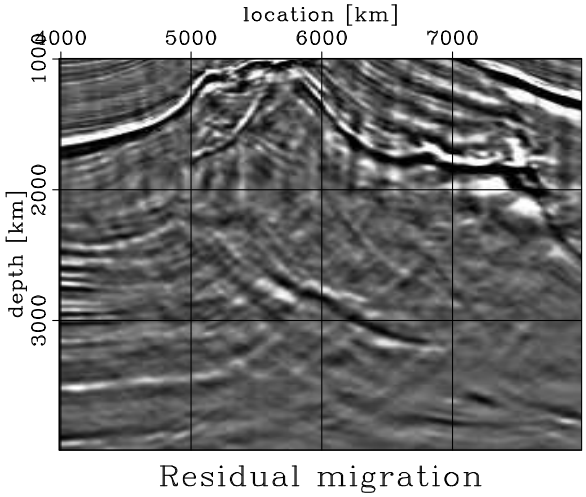
The preceding section shows that we can formulate prestack Stolt residual migration without directly assuming the new velocity to which we residually migrate the data. Instead, we can select a ratio of the current velocity to the updated one ($\rho = v_0/v$). This conclusion is true in the 3D case (equations (4.5) and (4.8)), the 2D case (equations (4.9) and (4.10)), and the case of 3D common-azimuth data (equations (4.14).

Stolt (1996) comments that, in the post-stack case, the frequency after time migration can be related to the frequency of the original data and the difference of the squares of the two velocities, before and after residual migration (equation (4.11)). However, he also shows that such a conclusion is no longer true in the prestack case. If we reformulate Stolt residual migration as a function of the ratio of two velocities, we can apply the process to images which have been depth-migrated with arbitrary velocity models. This is technically possible because the equations do not operate with velocity differences, but with velocity ratios. The residual migration transforms using a scaled version of the original velocity field. In this formulation, prestack Stolt residual migration is a constant velocity ratio method, and not a constant velocity one. It is important to understand that this approach is an approximation and it may not work in regions of extreme complexity and large velocity contrasts. Furthermore, the method is correct only from a kinematic point of view, and does not incorporate amplitude corrections.

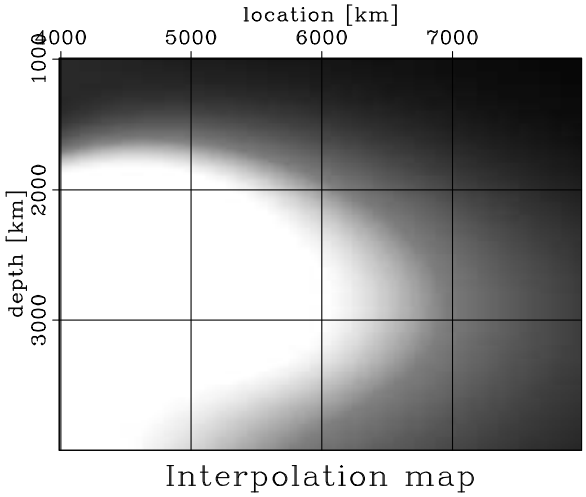
An extension of this method can go beyond constant velocity ratios. Since it is a fast, Stolt-type technique, we can run a large number of different residual migrations at different velocity ratios and then pick the values of the ratio parameter $\rho(x, y, z)$ that give the best image at every location in space. This method is therefore a good companion to wave-equation migration



Original image



Residual migration



Interpolation map

Figure 4.8: A comparison of the original image (top panel) with the image obtained by residual migration (middle panel) with a spatially varying ρ. The velocity ratio parameter ρ is ranging from 0.91 to 1.00 (bottom panel). All panels correspond to the box in Figure 4.5. storm-saltreal.variable [CR]

velocity analysis (Chapter 5), where the goal is to obtain improved images regardless of the procedure we use.

4.8 Conclusions

This section shows that we can reformulate prestack Stolt residual migration such that it becomes applicable to depth-migrated images. In essence, the residual migration introduced here is a Stolt-stretch method; therefore, it retains both the advantages and the disadvantages of Stolt-type techniques.

The main benefit of this method is that we can residually migrate by assuming given ratios between the current and updated velocities, rather than fixing the new velocities directly. In this way, we can apply Stolt residual migration to images that have been migrated with an arbitrary velocity map, not only to those migrated with constant velocity. This conclusion is valid for all types of seismic images, from 2D post-stack, to 3D prestack, including 3D common-azimuth.

The method discussed in this section is cheap to apply; therefore one of its main uses is in the area of repeated residual image enhancement, with applications to wave-equation migration velocity analysis, or as a simple technique to create velocity maps in field exploration.

4.9 Acknowledgment

I would like to acknowledge Biondo Biondi for stimulating discussion on extending Stolt residual migration to the prestack domain (Sava, 2003).

Chapter 5

Wave-equation migration velocity analysis

5.1 Overview

This chapter presents a migration velocity analysis (MVA) method based on wavefield extrapolation. Similar to conventional MVA, this method aims at iteratively improving the quality of the migrated image, as measured by flatness of angle-domain common image gathers over the aperture angle axis. However, instead of inverting the depth errors measured in ADCIGs using ray-based tomography, I invert "image perturbations" using a linearized wave-equation operator. This operator relates perturbations of the migrated image to perturbations of the migration velocity. I use prestack Stolt residual migration to define the image perturbations that maximize focusing and flatness of ADCIGs.

The linearized velocity analysis operator relates slowness perturbations to image perturbations based on a truncation of the Born scattering series to the first order term. To avoid divergence of the inversion procedure when the velocity perturbations are too large for the Born linearization of the wave-equation, I do not invert directly the image perturbations obtained by residual migration, but a linearized version of those image perturbations. The linearized image perturbations are computed by a linearized prestack residual migration operator applied to the background image.

5.2 Introduction

Seismic imaging is a two-step process: velocity estimation and migration. As the velocity function becomes more complex, the two steps become more and more interdependent. In complex depth imaging problems, velocity estimation and migration are applied iteratively in a loop. To ensure that this iterative imaging process converges to a satisfactory model, it is crucial that the migration and the velocity estimation are consistent with each other.

Kirchhoff migration often fails in areas of complex geology, such as sub-salt, because the wavefield is severely distorted by lateral velocity variations leading to complex multipathing. As the shortcomings of Kirchhoff migration have become apparent (O'Brien and Etgen, 1998), there has been renewed interest in wave-equation migration and computationally efficient 3D prestack depth migration methods have been developed (Biondi and Palacharla, 1996; Biondi, 1997; Mosher et al., 1997). However, no corresponding progress has been made in the development of Migration Velocity Analysis (MVA) methods based on the wave-equation. My goal is to fill this gap through a method that, at least in principle, can be used in conjunction with any downward-continuation migration method. In particular, this methodology can be applied to downward continuation based on the Double Square Root (Yilmaz, 1979; Claerbout, 1976; Popovici, 1996) or common-azimuth (Biondi and Palacharla, 1996) equations.

As for migration, wave-equation MVA (WEMVA) is intrinsically more robust than ray-based MVA because it avoids the well-known instability problems that rays encounter when the velocity model is complex and has sharp boundaries. The transmission component of finite-frequency wave propagation is mostly sensitive to the smooth variations in the velocity model. Consequently, WEMVA produces smooth, stable velocity updates. In most cases, no smoothing constraints are needed to assure stability in the inversion. In contrast, ray-based methods require strong smoothing constraints to avoid divergence. These smoothing constraints often reduce the resolution of the inversion that would be otherwise possible given the characteristics of the data (e.g. geometry, frequency content, signal-to-noise ratio, etc.). Eliminating, or substantially reducing, the amount of smoothing increases the resolution of the final velocity model.

Wave-equation MVA belongs to a much larger family of methods using wavefield-based

tomography or inversion techniques for velocity estimation, ultrasonic data or for surface and crosswell seismic data (Cohen and Bleistein, 1979; Mueller, 1980; Devaney, 1981; Clayton and Stolt, 1981; Devaney, 1982; Devaney and Oristaglio, 1984; Tarantola, 1984, 1986; Stolt and Weglein, 1985; Harris, 1987; Wu and Toksoz, 1987; Pratt and Worthington, 1988; Mora, 1987, 1989; Woodward, 1992; Woodward and Rocca, 1988; Harris and Wang, 1996; Pratt, 1999; Pratt and Shipp, 1999). The main reason for the large interest in wavefield-base tomography methods is related to the potential for robustness and high resolution that all such methods proclaim.

A well-known limitation of wave-equation tomography or MVA is represented by the linearization of the wave equation based on the truncation of the Born scattering series to the first order term. This linearization is hereafter referred to as the *Born approximation*. If the phase differences between the modeled and recorded wavefields are larger than a fraction of the wavelet, then the assumptions made under the Born approximation are violated and the velocity inversion methods diverge (Woodward, 1992; Pratt, 1999; Dahlen et al., 2000; Hung et al., 2000). Overcoming these limitations is crucial for a practical MVA tool. This goal is easier to accomplish with methods that optimize an objective function that is defined in the image space than with methods that optimize an objective function that is defined in the data space.

Wave-equation MVA also employs the Born approximation to linearize the relationship between the velocity model and the image. However, I "manipulate" the image perturbations to assure that they are consistent with the Born approximation, and replace the image perturbations with their linearized counterparts. I compute image perturbations by analytically linearizing the image-enhancement operator (e.g prestack residual migration presented in Chapter 4) and applying this linearized operator to the background image. Therefore, the linearized image perturbations are approximations to the non-linear image perturbations that are caused by arbitrary changes of the velocity model. Since I linearize both operators (migration and residual migration) with respect to the amplitude of the images, the resulting linear operators are consistent with each other. Therefore, the inverse problem converges for a wider range of velocity anomalies than the one implied by the Born approximation.

This method is more similar to conventional MVA than other proposed wave-equation

methods for estimating the background velocity model (Noble et al., 1991; Bunks et al., 1995; Forgues et al., 1998) because it maximizes the migrated image quality instead of matching the recorded data directly. I define the quality of the migrated image by flatness of the migrated angle-domain common image gathers (Chapter 3) along the aperture angle axis. In this respect, this method is related to Differential Semblance Optimization (DSO) (Symes and Carazzone, 1991; Shen et al., 2003) and Multiple Migration Fitting (Chavent and Jacewitz, 1995). With respect to DSO, this method has the advantage that at each iteration it optimizes an objective function that rewards flatness in the ADCIGs globally (for all the angles at the same time), and not just locally as DSO does (minimizing the discrepancies between the image at each angle and the image at the adjacent angles). This characteristic should speed-up the convergence, although I have no formal proof for this assertion.

This section describes the theoretical foundations of wave-equation MVA with simple examples illustrating the main concepts and techniques. In Chapter 6 I present applications of wave-equation MVA to the challenging problem of velocity estimation under salt. Here, I begin by discussing wavefield scattering in the context of one-way wavefield extrapolation methods. Then, I introduce the objective function for optimization and finally address the limitations introduced by the Born approximation. Appendix C details the wave-equation scattering operator and the computation of linearized image perturbations.

5.3 Recursive wavefield extrapolation

Imaging by wavefield extrapolation (WE) is based on recursive continuation of the wavefields ($\mathcal{U}$) from a given depth level to the next by means of an extrapolation operator ($\mathbf{E}$):

$$\mathcal{U}_{z+\Delta z} = \mathbf{E}_z\left[\mathcal{U}_z\right] . \tag{5.1}$$

Here and hereafter, I use the following notation conventions: $\mathbf{A}\,[x]$ means operator $\mathbf{A}$ applied to x, and $f\,(x)$ means function f of argument x. The subscripts z or $z+\Delta z$ indicate quantities corresponding to the depth levels z and $z+\Delta z$, respectively.

This recursive equation (5.1) can also be explicitly written in matrix form as

$$\begin{pmatrix} \mathbf{1} & 0 & 0 & \cdots & 0 & 0 \\ -\mathbf{E}_0 & \mathbf{1} & 0 & \cdots & 0 & 0 \\ 0 & -\mathbf{E}_1 & \mathbf{1} & \cdots & 0 & 0 \\ \vdots & \vdots & \vdots & \vdots & \vdots & \vdots \\ 0 & 0 & 0 & \cdots & -\mathbf{E}_{n-1} & \mathbf{1} \end{pmatrix} \begin{pmatrix} \mathcal{U}_0 \\ \mathcal{U}_1 \\ \mathcal{U}_2 \\ \vdots \\ \mathcal{U}_n \end{pmatrix} = \begin{pmatrix} \mathcal{D}_0 \\ 0 \\ 0 \\ \vdots \\ 0 \end{pmatrix},$$

or in a more compact notation as:

$$(\mathbf{1} - \mathbf{E})\,\mathcal{U} = \mathcal{D}, \tag{5.2}$$

where the vector $\mathcal{D}$ stands for data, $\mathcal{U}$ for the extrapolated wavefield at all depth levels, $\mathbf{E}$ for the extrapolation operator and $\mathbf{1}$ for the identity operator. Here and hereafter, I make the distinction between quantities measured at a particular depth level (e.g. $\mathcal{U}_z$), and the corresponding vectors denoting such quantities at all depth levels (e.g. $\mathcal{U}$).

After wavefield extrapolation, we can obtain an image by applying, at every depth level, an imaging operator ($\mathbf{R}_z$) to the extrapolated wavefield $\mathcal{U}_z$:

$$\mathcal{R}_z = \mathbf{R}_z\left[\mathcal{U}_z\right], \tag{5.3}$$

where $\mathcal{R}_z$ stands for the image at some depth level. A commonly used imaging operator ($\mathbf{R}_z$) involves summation over the temporal frequencies. We can write the same relation in compact matrix form as:

$$\mathcal{R} = \mathbf{R}\mathcal{U}\,. \tag{5.4}$$

$\mathcal{R}$ stands for the image, and $\mathbf{R}$ stands for the imaging operator which is applied to the extrapolated wavefield $\mathcal{U}$ at all depth levels.

A perturbation $\Delta\mathcal{U}$ of the wavefield at some depth level can be derived from the background wavefield by a simple application of the chain rule to equation (5.1):

$$\Delta\mathcal{U}_{z+\Delta z} = \mathbf{E}_z\left[\Delta\mathcal{U}_z\right] + \Delta\mathcal{V}_{z+\Delta z}\,, \tag{5.5}$$

where $\Delta\mathcal{V}_{z+\Delta z} = \Delta\mathbf{E}_z\left[\mathcal{U}_z\right]$ represents the scattered wavefield generated at $z+\Delta z$ by the interaction of the wavefield $\mathcal{U}_z$ with a perturbation of the velocity model at depth z. $\Delta\mathcal{U}_{z+\Delta z}$ is the accumulated wavefield perturbation corresponding to slowness perturbations at all levels

above. It is computed by extrapolating the wavefield perturbation $\Delta\mathcal{U}_z$ from the level above, plus the scattered wavefield $\Delta\mathcal{V}_{z+\Delta z}$ at this level.

Equation (5.5) is also a recursive equation which can be written in matrix form as

$$\begin{pmatrix} \mathbf{1} & 0 & 0 & \cdots & 0 & 0 \\ -\mathbf{E}_0 & \mathbf{1} & 0 & \cdots & 0 & 0 \\ 0 & -\mathbf{E}_1 & \mathbf{1} & \cdots & 0 & 0 \\ \vdots & \vdots & \vdots & \vdots & \vdots & \vdots \\ 0 & 0 & 0 & \cdots & -\mathbf{E}_{n-1} & \mathbf{1} \end{pmatrix} \begin{pmatrix} \Delta\mathcal{U}_0 \\ \Delta\mathcal{U}_1 \\ \Delta\mathcal{U}_2 \\ \vdots \\ \Delta\mathcal{U}_n \end{pmatrix} = \begin{pmatrix} \mathbf{0} & 0 & 0 & \cdots & 0 & 0 \\ \Delta\mathbf{E}_0 & \mathbf{0} & 0 & \cdots & 0 & 0 \\ 0 & \Delta\mathbf{E}_1 & \mathbf{0} & \cdots & 0 & 0 \\ \vdots & \vdots & \vdots & \vdots & \vdots & \vdots \\ 0 & 0 & 0 & \cdots & \Delta\mathbf{E}_{n-1} & \mathbf{0} \end{pmatrix} \begin{pmatrix} \mathcal{U}_0 \\ \mathcal{U}_1 \\ \mathcal{U}_2 \\ \vdots \\ \mathcal{U}_n \end{pmatrix},$$

or in a more compact notation as:

$$(\mathbf{1}-\mathbf{E})\,\Delta\mathcal{U} = \Delta\mathbf{E}\mathcal{U}. \tag{5.6}$$

The operator $\Delta\mathbf{E}$ stands for a perturbation of the extrapolation operator $\mathbf{E}$. The quantity $\Delta\mathbf{E}\mathcal{U}$ represents a scattered wavefield, and is a function of the perturbation in the medium by the scattering relations derived in Appendix C. For the case of single scattering, we can write that

$$\Delta\mathcal{V}_{z+\Delta z} \equiv \Delta\mathbf{E}_z\left[\mathcal{U}_z\right] = \mathbf{E}_z\left[\mathbf{S}_z\left(\widetilde{\mathcal{U}}_z\right)\left[\Delta s_z\right]\right]. \tag{5.7}$$

The expression for the total wavefield perturbation $\Delta\mathcal{U}$ from equation (5.5) becomes

$$\Delta\mathcal{U}_{z+\Delta z} = \mathbf{E}_z\left[\Delta\mathcal{U}_z\right] + \mathbf{E}_z\left[\mathbf{S}_z\left(\widetilde{\mathcal{U}}_z\right)\left[\Delta s_z\right]\right], \tag{5.8}$$

which is also a recursive relation that can be written in matrix form as

$$\begin{pmatrix} \mathbf{1} & 0 & 0 & \cdots & 0 & 0 \\ -\mathbf{E}_0 & \mathbf{1} & 0 & \cdots & 0 & 0 \\ 0 & -\mathbf{E}_1 & \mathbf{1} & \cdots & 0 & 0 \\ \vdots & \vdots & \vdots & \vdots & \vdots & \vdots \\ 0 & 0 & 0 & \cdots & -\mathbf{E}_{n-1} & \mathbf{1} \end{pmatrix} \begin{pmatrix} \Delta\mathcal{U}_0 \\ \Delta\mathcal{U}_1 \\ \Delta\mathcal{U}_2 \\ \vdots \\ \Delta\mathcal{U}_n \end{pmatrix} = \begin{pmatrix} \mathbf{0} & 0 & 0 & \cdots & 0 & 0 \\ \mathbf{E}_0 & \mathbf{0} & 0 & \cdots & 0 & 0 \\ 0 & \mathbf{E}_1 & \mathbf{0} & \cdots & 0 & 0 \\ \vdots & \vdots & \vdots & \vdots & \vdots & \vdots \\ 0 & 0 & 0 & \cdots & \mathbf{E}_{n-1} & \mathbf{0} \end{pmatrix} \begin{pmatrix} \mathbf{S}_0 & 0 & 0 & \cdots & 0 \\ 0 & \mathbf{S}_1 & 0 & \cdots & 0 \\ 0 & 0 & \mathbf{S}_2 & \cdots & 0 \\ \vdots & \vdots & \vdots & \vdots & \vdots \\ 0 & 0 & 0 & \cdots & \mathbf{S}_n \end{pmatrix} \begin{pmatrix} \Delta s_0 \\ \Delta s_1 \\ \Delta s_2 \\ \vdots \\ \Delta s_n \end{pmatrix},$$

or in a more compact notation as:

$$(\mathbf{1}-\mathbf{E})\,\Delta\mathcal{U} = \mathbf{E}\mathbf{S}\Delta s. \tag{5.9}$$

The vector Δs stands for the slowness perturbation at all depths.

Finally, if we introduce the notation

$$\mathbf{G} = (\mathbf{1} - \mathbf{E})^{-1}\mathbf{ES}, \tag{5.10}$$

we can write a simple relation between a slowness perturbation Δs and the corresponding wavefield perturbation $\Delta\mathcal{U}$:

$$\Delta\mathcal{U} = \mathbf{G}\Delta s. \tag{5.11}$$

This expression describes wavefield scattering caused by the interaction of the background wavefield with a perturbation of the medium.

5.4 WEMVA objective function

Migration velocity analysis is based on estimating the velocity that optimizes certain properties of the migrated images. In general, measuring such properties involves making a transformation after wavefield extrapolation to the migrated image using a generic differentiation function f characterizing image imperfections

$$\mathcal{P}_z = f\mathbf{R}_z\left[\mathcal{U}_z\right], \tag{5.12}$$

where $\mathbf{R}$ is the imaging operator applied to the extrapolated wavefield $\mathcal{U}$. In compact matrix form, we can write this relation as:

$$\mathcal{P} = f\left(\mathbf{R}\mathcal{U}\right). \tag{5.13}$$

The image $\mathcal{P}$ is subject to optimization from which we derive the velocity updates.

Two examples of transformation functions are:

- $f(u) = u - \bar{u}$ where u denotes an extrapolated wavefield and $\bar{u}$ is a known target wavefield. A WEMVA method based on this criterion optimizes

$$\mathcal{P}_z = \mathbf{R}_z\left[\mathcal{U}_z\right] - \mathbf{R}_z\left[\mathcal{T}_z\right], \tag{5.14}$$

where $\mathcal{T}_z$ stands for the target wavefield. For this method, we can use the acronym TIF standing for *target image fitting* (Biondi and Sava, 1999; Sava and Fomel, 2002; Sava and Biondi, 2004a,b).

- $f(u) = \mathbf{D}[u]$ where $\mathbf{D}$ is a known operator. A WEMVA method based on this criterion optimizes

$$\mathcal{P}_z = \mathbf{D}_z\left[\mathbf{R}_z\left[\mathcal{U}_z\right]\right]. \tag{5.15}$$

  If $\mathbf{D}$ is a differential semblance operator, we can use the acronym DSO standing for *differential semblance optimization* (Symes and Carazzone, 1991; Shen et al., 2003).

In general, such transformations belong to a family of affine functions that can be written as

$$\mathcal{P}_z = \mathbf{A}_z\left[\mathbf{R}_z\left[\mathcal{U}_z\right]\right] - \mathbf{B}_z\left[\mathbf{R}_z\left[\mathcal{T}_z\right]\right], \tag{5.16}$$

or in compact matrix form as

$$\mathcal{P} = \mathbf{AR}\mathcal{U} - \mathbf{BR}\mathcal{T}, \tag{5.17}$$

where the operators $\mathbf{A}$ and $\mathbf{B}$ are known and take special forms depending on the optimization criterion we use. For example, $\mathbf{A} = \mathbf{1}$ and $\mathbf{B} = \mathbf{1}$ for TIF, and $\mathbf{A} = \mathbf{D}$ and $\mathbf{B} = \mathbf{0}$ for DSO. $\mathbf{1}$ stands for the identity operator, and $\mathbf{0}$ stands for the null operator. With the definition in equation (5.16), we can write the objective function J as:

$$J(s) = \frac{1}{2}\sum_{z,\mathbf{m},\mathbf{h}} \|\mathcal{P}_z\|^2 \tag{5.18}$$

$$= \frac{1}{2}\sum_{z,\mathbf{m},\mathbf{h}} \|\mathbf{A}_z\left[\mathbf{R}_z\left[\mathcal{U}_z\right]\right] - \mathbf{B}_z\left[\mathbf{R}_z\left[\mathcal{T}_z\right]\right]\|^2, \tag{5.19}$$

where s is the slowness function, and $z, \mathbf{m}, \mathbf{h}$ stand respectively for depth, and the midpoint and offset vectors. In compact matrix form, we can write the objective function as:

$$J(s) = \frac{1}{2}\|\mathbf{AR}\mathcal{U} - \mathbf{BR}\mathcal{T}\|^2. \tag{5.20}$$

In the Born approximation, the total wavefield $\mathcal{U}$ is related to the background wavefield

$\widetilde{\mathcal{U}}$ by the linear relation

$$\mathcal{U} \approx \widetilde{\mathcal{U}} + \mathbf{G}\Delta s \; . \tag{5.21}$$

If we can replace the total wavefield in the objective function equation (5.20), we obtain

$$J(s) = \frac{1}{2}\|\mathbf{AR}\widetilde{\mathcal{U}} - \mathbf{BR}\mathcal{T} + \mathbf{ARG}\Delta s\|^2 \; . \tag{5.22}$$

Equation (5.22) describes a linear optimization problem, where we obtain Δs by minimizing the objective function

$$J(\Delta s) = \|\Delta\mathcal{R} - \mathbf{L}\Delta s\|^2 \; , \tag{5.23}$$

where $\Delta\mathcal{R} = -\left(\mathbf{AR}\widetilde{\mathcal{U}} - \mathbf{BR}\mathcal{T}\right)$, and $\mathbf{L} = \mathbf{ARG}$. The operator $\mathbf{L}$ is constructed based on the Born approximation (Lo and Inderweisen, 1994), and involves the pre-computed background wavefield through the background medium. A discussion on the implementation details for operator $\mathbf{L}$ is presented in Appendix C. The convex optimization problem defined by the linearization in equation (5.22) can be solved using standard conjugate-gradient techniques.

Since, in most practical cases, the inversion problem is not well conditioned, we need to add constraints on the slowness model via a regularization operator. In these situations, we use the modified objective function

$$J(\Delta s) = \|\mathbf{W}(\Delta\mathcal{R} - \mathbf{L}\Delta s)\|^2 + \epsilon^2\|\mathbf{H}\Delta s\|^2 \; . \tag{5.24}$$

Here, $\mathbf{H}$ is a regularization operator, $\mathbf{W}$ is a weighting operator on the data residual, and ϵ is a scalar parameter which balances the relative importance of the data residual ($\mathbf{W}(\Delta\mathcal{R} - \mathbf{L}\Delta s)$) and of the model residual ($\mathbf{H}\Delta s$).

5.5 WEMVA operator

The computation of the velocity updates from the results of migrating the data with the current (background) velocity model comprises three main components that are summarized by the flow-chart in figure 5.1. The three components are labeled as A, B and C on the chart. Box A corresponds to the computation of the background wavefield, based on the surface data

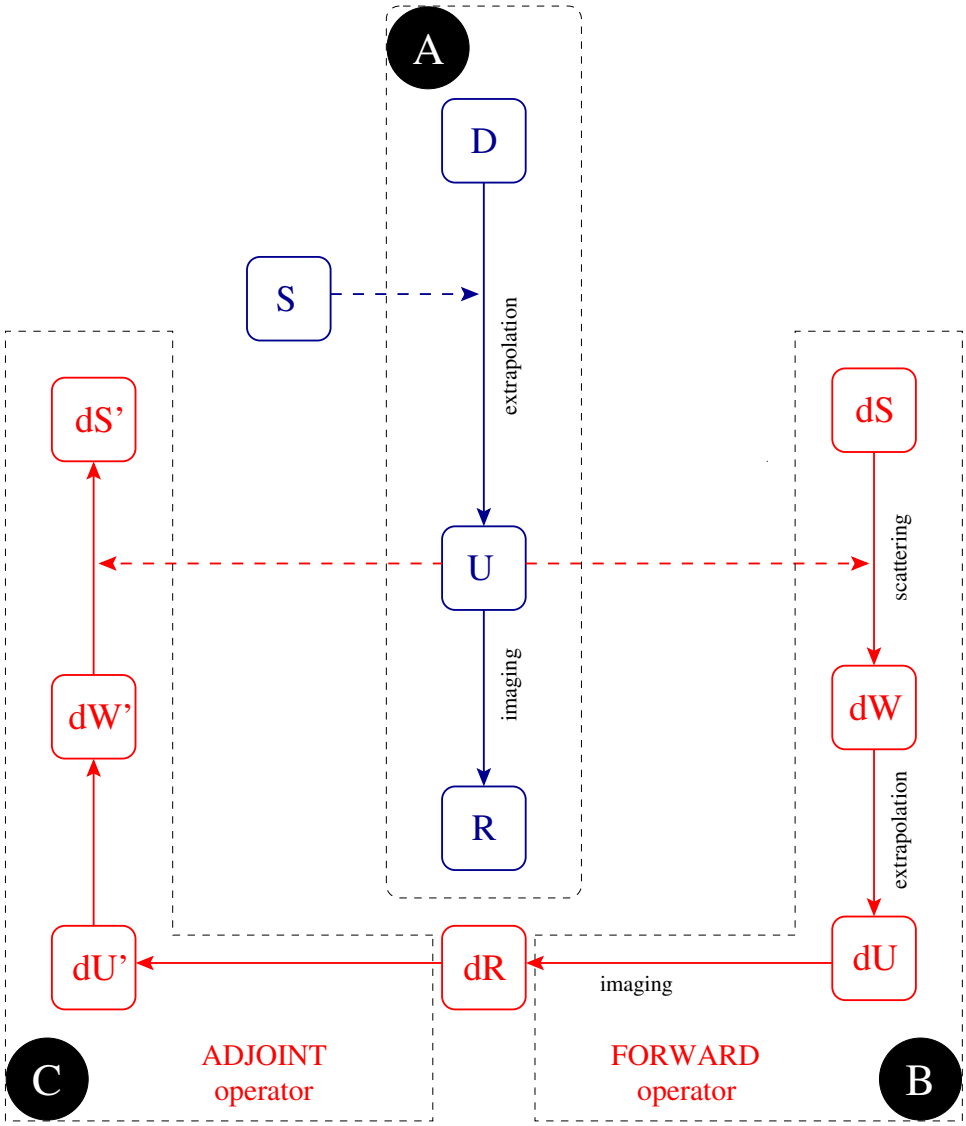


Figure 5.1: WEMVA flowchart. Box A: background wavefield. Box B: forward WEMVA operator. Box C: adjoint WEMVA operator. wemva-wemva_chart [NR]

and background slowness. Boxes B and C correspond respectively to the forward and adjoint WEMVA operator.

The data recorded at the surface (D) are downward continued using wavefield extrapolation to all depth levels using the background slowness (S), to generate a background wavefield (U). The known background slowness (S) can incorporate lateral variations. Extrapolation can be done with kernels corresponding to such methods as Fourier finite-difference (Ristow and Ruhl, 1994), or generalized screen propagator (Rousseau et al., 2003). From the extrapolated wavefield, we can construct the background image (R) by applying a standard imaging condition, for example a simple summation over frequencies.

The background wavefield (U) is an important component of the WEMVA operator. This wavefield plays a role analogous to the one played in traveltime tomography by the rayfield obtained by ray tracing in the background model. The wavefield is the carrier of information and defines the multivalued wavepaths along which we spread the velocity errors measured from the migrated images obtained using the background slowness function. The wavefield is band limited, unlike a rayfield which describes propagation of waves with an infinite frequency band. Therefore, the background wavefield provides a more accurate description of wave propagation through complicated media than a corresponding rayfield. Typical examples are salt bodies characterized by large velocity contrasts where ray tracing is both unstable and inaccurate.

When evaluating the forward operator (Box B), the background wavefield (U) interacts with a slowness perturbation (dS) and generates a scattered wavefield (dW) at every depth level. In this method, scattering is based on the first-order Born approximation, which assumes perturbations to be small both in size and magnitude. This approximation is appropriate, because scattering occurs independently at every depth level. The contribution to the scattered wavefield, is added at each depth level, and the total scattered wavefield (dU) is extrapolated to depth, using the same numerical propagator as the one used to extrapolate the background wavefield from the surface data. Therefore, the wavefield perturbation at any depth level contains the accumulated effects of scattering and extrapolation from all the levels above it. Finally, I apply an imaging condition to the wavefield perturbation (dU) and obtain an image perturbation (dR) corresponding to the slowness perturbation (dS) and the background

wavefield (U).

In migration velocity analysis, we are interested in the inverse process, where we take an image perturbation (dR) and construct a slowness perturbation (dS). We obtain image perturbations via image enhancement operators (residual moveout, residual migration etc.) applied to the background image (R). Since the scattering operator is based on the Born approximation, we need to take special precautions to avoid cycle-skipping of phase function. I overcome the Born approximation limitations by using linearized image perturbations discussed in a following section.

To invert the linearized image perturbation into slowness updates by an iterative algorithm, such as conjugate directions, we need to evaluate the adjoint WEMVA operator (Box C) as well as the forward operator. From the image perturbation (dR), we can construct an adjoint wavefield perturbation (dU) by applying the adjoint imaging operator. This wavefield is then upward continued to all levels and an adjoint scattered wavefield (dW') is accumulated. Finally, using the background wavefield (U), we can generate the adjoint slowness perturbation (dS').

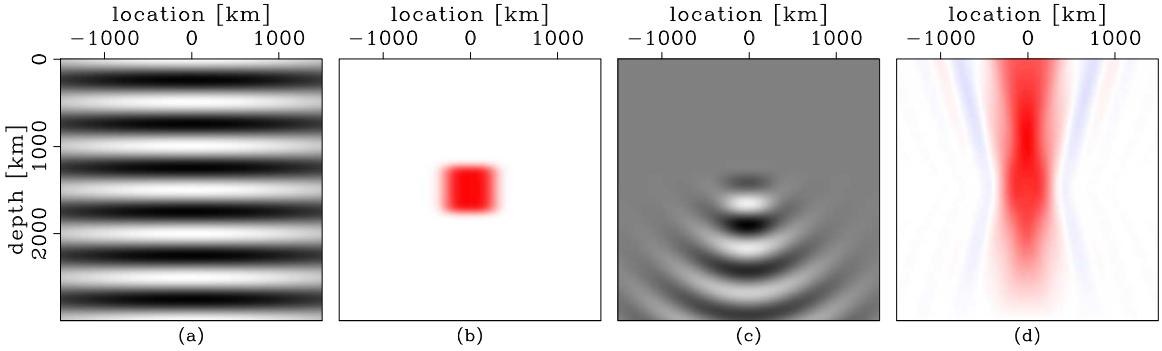


Figure 5.2: Monochromatic WEMVA example: background wavefield (a), slowness perturbation (b), wavefield perturbation (c), slowness backprojection (d). wemva-SCATbas1.scat [CR]

Figures 5.2 and 5.3 illustrate the flow-chart shown in Figure 5.1 by showing its application to two simple examples. In the first example (Figure 5.2), I use a monochromatic wavefield, whereas in the second one (Figure 5.3), I use a wideband wavefield. For both examples the data are recorded above a planar horizontal reflector.

Figure 5.2a shows a snapshot (taken at time zero) of the monochromatic background wavefield obtained by downward continuation of an incident plane wave in a constant medium. Figure 5.2b shows a slowness perturbation, that under the influence of the incident wavefield (a), generates a wavefield perturbation (c). The snapshots at zero time shown in panels (a) and (c) can also be regarded as images. Finally, I backpropagate the image perturbation (c) and obtain the adjoint slowness perturbation (d).

Figure 5.3 shows the analogous panels shown Figure 5.2, but for wide-band data. Figure 5.3a shows the image obtained by wavefield extrapolation of a wide-band plane wave in the background medium. From the same slowness perturbation (b) as in the preceding example, I obtain an image perturbation (c), from which I generate an adjoint slowness perturbation (d) using the background wavefield used to compute the background image.

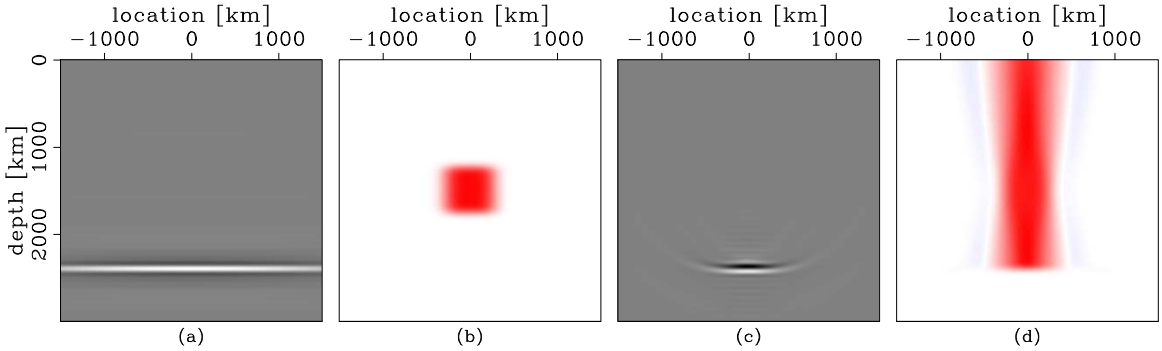


Figure 5.3: Wide-band WEMVA example: background image (a), slowness perturbation (b), image perturbation (c), slowness backprojection (d). wemva-SCATbasN.scat [CR]

5.6 Cycle skipping in image perturbations

I illustrate the WEMVA method with a simple model depicted in Figure 5.4. The velocity is constant and the data are represented by an impulse in space and time. I consider two slowness models: one regarded as the correct slowness s, and the other as the background slowness $\tilde{s}$. The two slownesses are related by a scale factor $\frac{s}{\tilde{s}} = \rho$. For this example, I consider $\rho = 1.001$ to ensure that I do not violate the requirements imposed by the Born approximation.

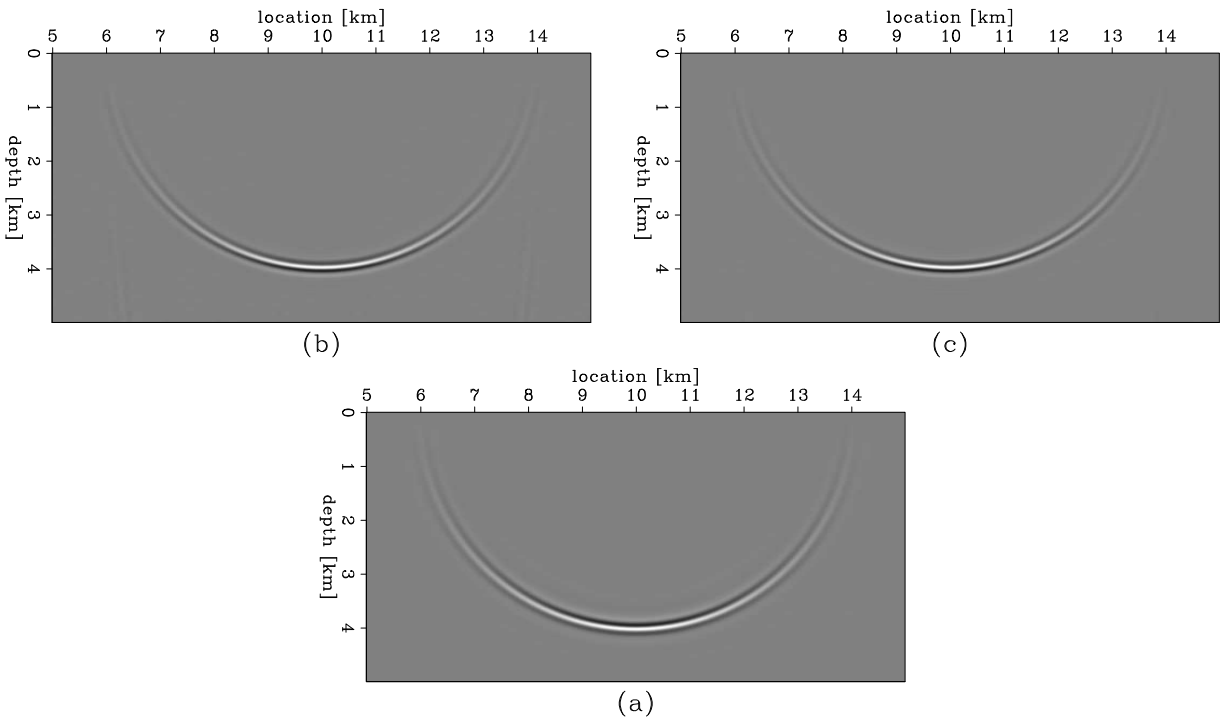


Figure 5.4: Comparison of image perturbations obtained as a difference between two migrated images (b) and as the result of the forward WEMVA operator applied to the known slowness perturbation (c). Panel (a) depicts the background image corresponding to the background slowness. Since the slowness perturbation is small (0.1%), the image perturbations in panels (b) and (c) are practically identical. wemva-WEP1.imag [CR]

Next, I migrate the data with the background slowness $\tilde{s}$ and store the extrapolated wavefield at all depth levels. Figure 5.4a shows the image corresponding to the background slowness $\widetilde{\mathcal{R}}$. I also migrate the data with the correct slowness and obtain a second image $\mathcal{R}$. A simple subtraction of the two images gives the image perturbation in Figure 5.4b.

Finally, I compute an image perturbation by a simple application of the forward WEMVA operator defined in equation (5.23) to the slowness perturbation $\Delta s = s - \tilde{s}$ (Figure 5.4c). Since the slowness perturbation is very small, the requirements imposed by the Born approximation are fulfilled, and the two images in Figures 5.4b and 5.4c are identical. The image perturbations are phase-shifted by 90° relative to the background image.

A simple illustration of the adjoint operator $\mathbf{L}$ defined in equation (5.23) is depicted in Figure 5.5. Panel (a) shows the background image, panels (b) and (c) show image perturbations, and panels (d) and (e) show slowness perturbations. I extract a small subset of each image perturbation to create the impulsive image perturbations in Figures 5.5b and 5.5c. The left panels (b and d) correspond to the image perturbation computed as an image difference, while the panels on the right (c and e) correspond to the image perturbation computed with the forward WEMVA operator. In this way, the data corresponds to a single point on the surface, and the image perturbation corresponds to a single point in the subsurface. By backprojecting the image perturbations in Figures 5.5b and 5.5c with the adjoint WEMVA operator, I obtain identical wavepaths or "fat rays" shown in Figures 5.5d and 5.5e, respectively.

Prestack Stolt Residual Migration (Chapter 4) can be used to create image perturbations. Given an image migrated with the background velocity, I can construct another image by using an operator $\mathbf{K}$ function of a parameter ρ which represents the ratio of the original and modified velocities. The improved velocity map is unknown explicitly, although it is described indirectly by the ratio map of the two velocities:

$$\mathcal{R} = \mathbf{K}(\rho)\left[\widetilde{\mathcal{R}}\right] . \tag{5.25}$$

The simplest form of an image perturbation can be constructed as a difference between an

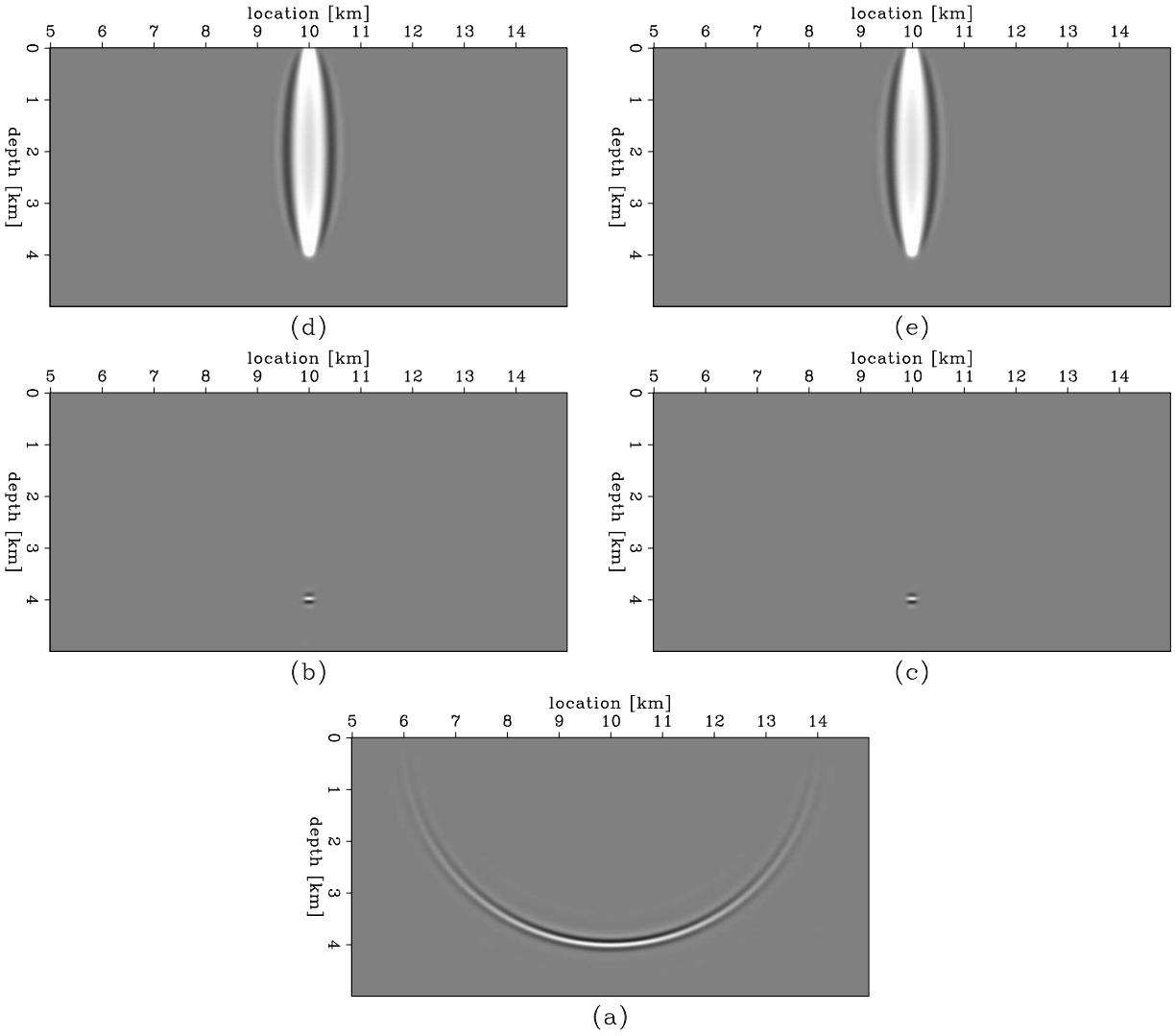


Figure 5.5: Comparison of slowness backprojections using the WEMVA operator applied to image perturbations computed as a difference between two migrated images (b,d) and as the result of the forward WEMVA operator applied to a known slowness perturbation (c,e). Panel (a) depicts the background image corresponding to the background slowness. Since the slowness perturbation is small (0.1%), the image perturbations in panels (b) and (c), and the fat rays in panels (d) and (e) are practically identical. wemva-WEP1.rays [CR]

improved image ($\mathcal{R}$) and the *background* image ($\widetilde{\mathcal{R}}$):

$$\Delta\mathcal{R} = \mathcal{R} - \widetilde{\mathcal{R}} \,. \tag{5.26}$$

The main challenge with this method of constructing image perturbations for WEMVA is that the two images can be phase-shifted too much with respect to one-another. Thus, we can violate the requirements of the Born approximation and risk subtracting images that are out of phase. This problem is common for all wavefield-based velocity analysis or tomographic methods using the Born approximation (Woodward, 1992; Pratt, 1999; Dahlen et al., 2000).

A simple illustration of this problem is depicted in Figures 5.6 and 5.7. This example is similar with the one in Figures 5.4 and 5.5, except that the velocity ratio linking the two slownesses is much larger: $\rho = 1.20$. In this case, the background and correct images are not at all in phase, and when I subtract them I obtain two distinct events, as shown in Figure 5.6b. In contrast, the image perturbation obtained by the forward WEMVA operator, Figure 5.6c, shows only one event as in the previous example. The only difference between the image perturbations in Figures 5.4c and 5.6c is a scale factor related to the magnitude of the slowness anomaly.

Figure 5.7 depicts fat rays for each kind of image perturbation: on the left, the image perturbations obtained by subtraction of the two images, and on the right, the image perturbation obtained with the forward WEMVA operator. The fat rays corresponding to the ideal image perturbation (panels c and e) do not change from the previous example, except for a scale factor. However, in case we use image differences (panels b and d), we can violate the requirements of the Born approximation. In this case, we see slowness backprojections of opposite sign relative to the true anomaly, and also the two characteristic migration ellipsoidal side-events indicating cycle-skipping (Woodward, 1992).

5.7 Linearized image perturbations

I address the problem of cycle skipping by employing linearized image perturbations. If we define $\Delta\rho = \rho - 1$, we can write a discrete version of the image perturbation using a Taylor

series expansion of equation (5.25) as

$$\Delta\mathcal{R} \approx \mathbf{K}'\Big|_{\rho=1}\left[\widetilde{\mathcal{R}}\right]\Delta\rho\ , \tag{5.27}$$

where the $'$ sign denotes differentiation relative to the velocity ratio parameter ρ. For the image perturbations computed with equation (5.27), I use the name *linearized image perturbations*. Figure 5.8 graphically illustrates this procedure.

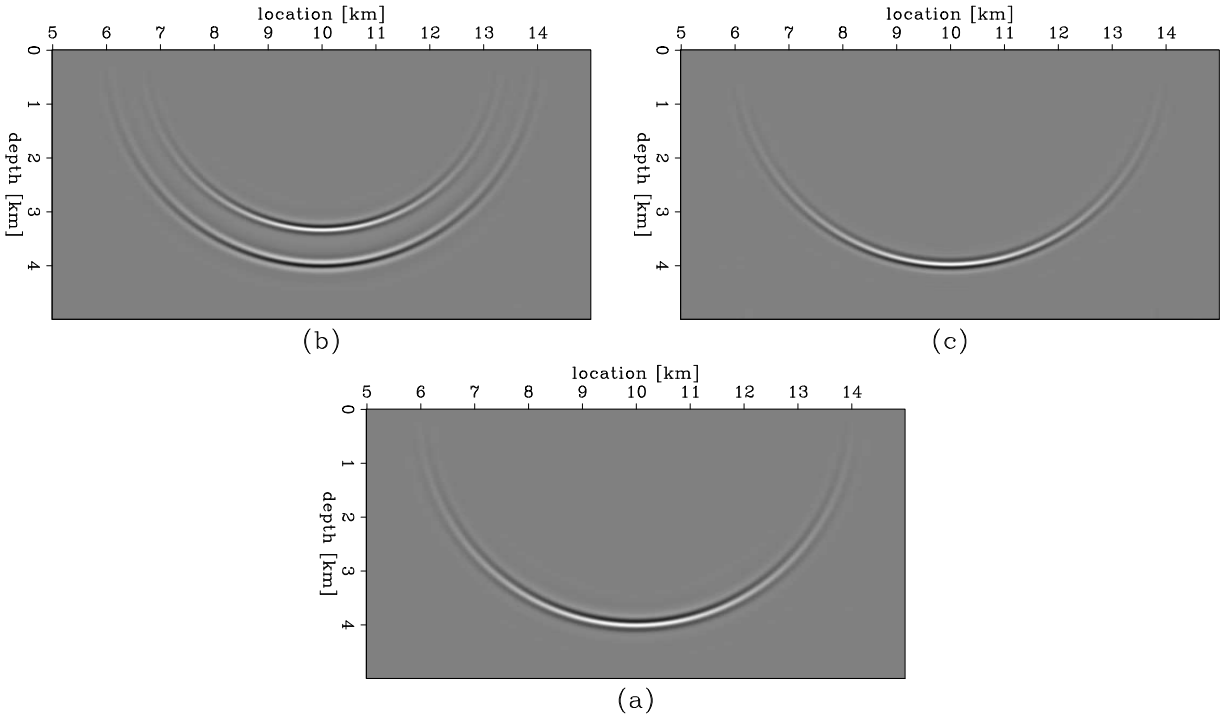


Figure 5.6: Comparison of image perturbations obtained as a difference between two migrated images (b) and as the result of the forward WEMVA operator applied to the known slowness perturbation (c). Panel (a) depicts the background image corresponding to the background slowness. Since the slowness perturbation is large (20%), the image perturbations in panels (b) and (c) are different from each-other. wemva-WEP2.imag [CR]

The linearized prestack Stolt residual migration operator $\mathbf{K}'\Big|_{\rho=1}$ can be computed analytically, as described in Appendix C. With this operator, I can compute linearized image perturbations in two steps. First, I run residual migration for a large range of velocity ratios and pick at every image point the ratio which maximizes flatness of the gathers. Then, I apply

the operator in equation (5.27) to the background image $\widetilde{\mathcal{R}}$ and scale the result with the picked $\Delta\rho$.

The linearized image perturbations approximate the non-linear image perturbations caused by arbitrary velocity model changes. They are based on the gradient of the image change relative to a velocity model change, and are less restrictive than the Born approximation limits.

Figure 5.9 shows how the linearized image perturbation methodology applies to the synthetic example used earlier in this section. All panels are similar to the ones in Figures 5.5 and 5.7, except that the left panels (b and d) correspond to linearized image perturbations, instead of simple image perturbations. Again, I compare image and slowness perturbations with the ideal perturbations obtained by the forward WEMVA operator (c and e). Both the image and slowness perturbations are identical in shape and magnitude.

5.8 WEMVA sensitivity kernels

Depth imaging of complex structures depends on the quality of the velocity model. However, conventional Migration Velocity Analysis (MVA) procedures often fail when the wavefield is severely distorted by lateral velocity variations and thus complex multipathing occurs. In the preceding sections, I introduce a method of migration velocity analysis using wave-equation techniques (WEMVA), which aims to improve the quality of migrated images, mainly by correcting moveout inaccuracies of specular energy. WEMVA finds a slowness perturbation which corresponds to an image perturbation. It is thus similar to ray-based migration tomography (Bishop et al., 1985; Al-Yahya, 1989; Stork, 1992; Etgen, 1993; Kosloff et al., 1996), where the slowness perturbation is derived from depth errors, and to wave-equation inversion (Tarantola, 1986) or tomography (Woodward, 1992; Pratt, 1999; Dahlen et al., 2000) where the slowness perturbation is derived from measured wavefield perturbations.

WEMVA has the potential of improving velocity estimation when complex wave propagation makes conventional ray-based MVA methods less reliable. Imaging under rugged salt bodies is an important case where WEMVA has the potential of making a difference in the imaging results. Here, I analyze the characteristics of the tomographic operator inverted in

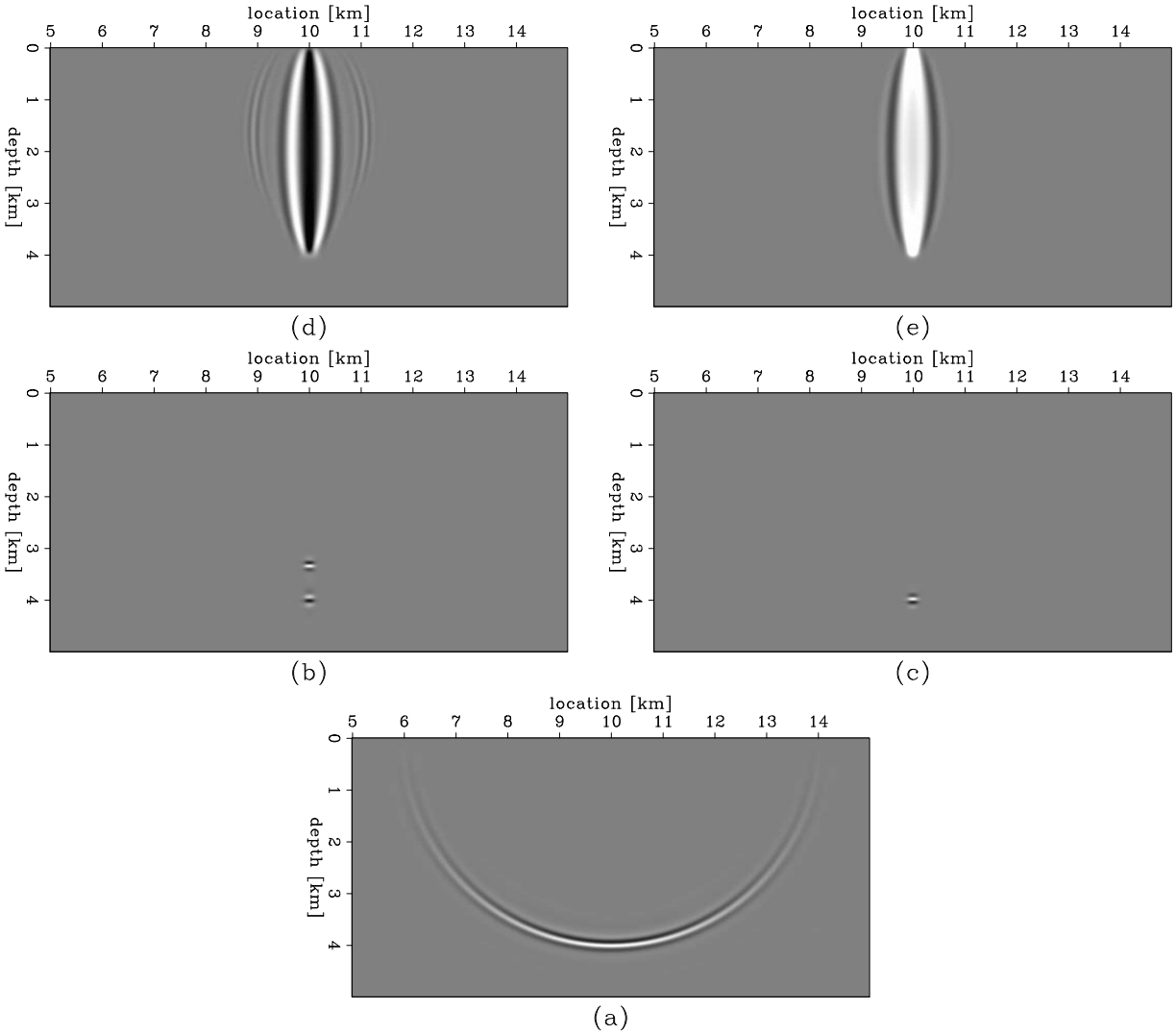


Figure 5.7: Comparison of slowness backprojections using the WEMVA operator applied to image perturbations computed as a difference between two migrated images (b,d) and as the result of the forward WEMVA operator applied to a known slowness perturbation (c,e). Panel (a) depicts the background image corresponding to the background slowness. Since the slowness perturbation is large (20%), the image perturbations in panels (b) and (c) and the fat rays in panels (d) and (e) are different from each-other. Panel (d) shows the typical behavior associated with the breakdown of the Born approximation. wemva-WEP2.rays [CR]

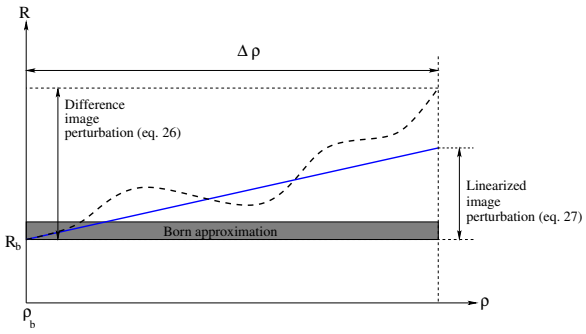


Figure 5.8: A schematic description of the method used for computing linearized image perturbations. The dashed line corresponds to image changes described by residual migration with various values of the velocity ratio parameter (ρ). The straight solid line corresponds to the linearized image perturbation computed with an image gradient operator applied to the reference image scaled at every point by the difference of the velocity ratio parameter $\Delta\rho$. wemva-dip [NR]

WEMVA to update the velocity model, and contrast these characteristics with the well-known characteristics of ray-based tomographic operators.

One way of characterizing integral operators, e.g. tomography operators, is through sensitivity kernels, which describe the sensitivity of a component of a member of the data space to a change of a component of a member of the model space. In this section, I formally introduce the sensitivity kernels for wave-equation migration velocity analysis and show 2D and 3D examples.

The analysis of WEMVA sensitivity kernels provides an intuition on WEMVA's potential for overcoming limitations of ray-based MVA. Some of these limitations are intrinsic, other are practical. An important practical difficulty encountered when using rays to estimate velocity below salt bodies with rough boundaries is the instability of ray tracing. Rough salt topographies create poorly illuminated areas, or even shadow zones, in the subsalt region. The spatial distribution of these poorly illuminated areas is very sensitive to the velocity function. Therefore, it is often extremely difficult to trace the rays that connect a given point in the poorly illuminated areas with a given point at the surface (two-point ray-tracing). Wavefield-extrapolation methods are robust with respect to shadow zones and they always provide wavepaths (i.e. sensitivity kernels) usable for velocity inversion.

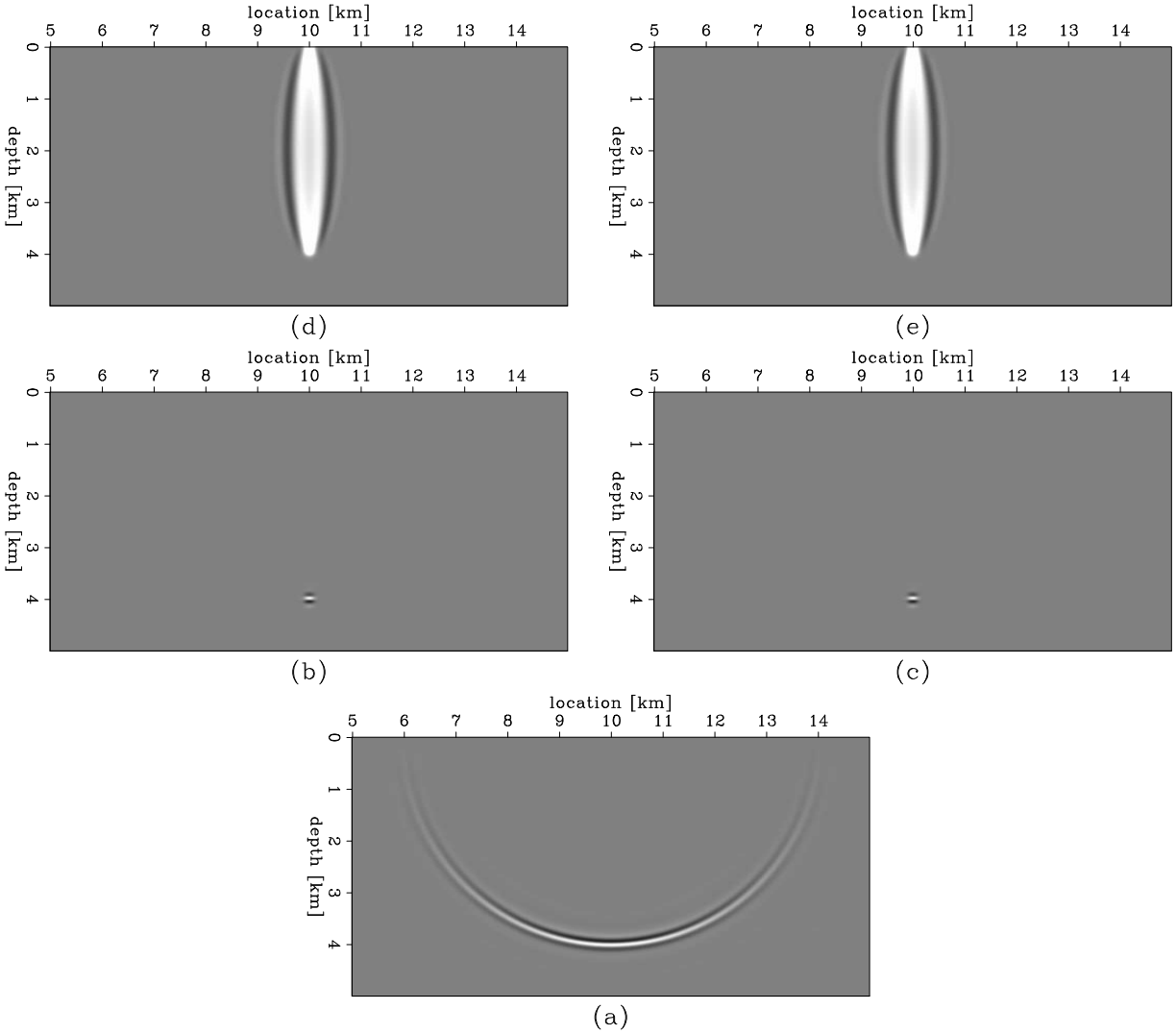


Figure 5.9: Comparison of slowness backprojections using the WEMVA operator applied to image perturbations computed with the differential image perturbation operator (b,d) and as the result of the forward WEMVA operator applied to a known slowness perturbation (c,e). Panel (a) depicts the background image corresponding to the background slowness. Despite the fact that the slowness perturbation is large (20%), the image perturbations in panels (b) and (c) and the fat rays in panels (d) and (e) are practically identical, both in shape and in magnitude. wemva-WEP2.raan [CR]

Ray-tracing has intrinsic limitations when modeling wave-propagation through salt bodies with complex geometry, because of the asymptotic assumption on which it is based. This intrinsic limitation prevent ray-tracing from modeling the frequency-dependency of full-bandwidth wave propagation. The comparison of sensitivity kernels computed assuming different frequency bandwidths illustrates clearly the drawbacks of the asymptotic assumptions. Top-salt rugosity causes the WEMVA sensitivity kernels to be strongly dependent on the bandwidth. Furthermore, in these conditions, sensitivity kernels are drastically different from simple "fat rays". Therefore, they cannot be approximated by kernels computed by a bandwidth-dependent fattening of geometric rays (Lomax, 1994).

I compute the sensitivity kernels for perturbations in the phase as well as perturbations in the amplitude. It is interesting to notice that the 3D kernels for phase perturbations are hollow in the middle, exactly where the geometric rays would be. This result is consistent with the observations first made by Woodward (1990); then extensively discussed in the global seismology community (Marquering et al., 1999; Dahlen et al., 2000), and further analyzed by Rickett (2000).

5.8.1 Fréchet derivative integral kernels

Consider a (nonlinear) function $\mathbf{f}$ mapping one element of the functional model space $\mathbf{m}$ to one element of the functional data space $\mathbf{d}$:

$$\mathbf{d} = \mathbf{f}(\mathbf{m}) \ . \tag{5.28}$$

The tangent linear application to $\mathbf{f}$ at point $\mathbf{m} = \mathbf{m}_0$ is a linear operator $\mathbf{F}_0$ defined by the expansion

$$\mathbf{f}(\mathbf{m_0} + \delta\mathbf{m}) = \mathbf{f}(\mathbf{m_0}) + \mathbf{F_0}\delta\mathbf{m} + \dots \ , \tag{5.29}$$

where $\delta\mathbf{m}$ is a small perturbation in the model space. The tangent linear application $\mathbf{F}_0$ is also known under the name of *Fréchet derivative* of $\mathbf{f}$ at point $\mathbf{m}_0$ (Tarantola, 1987).

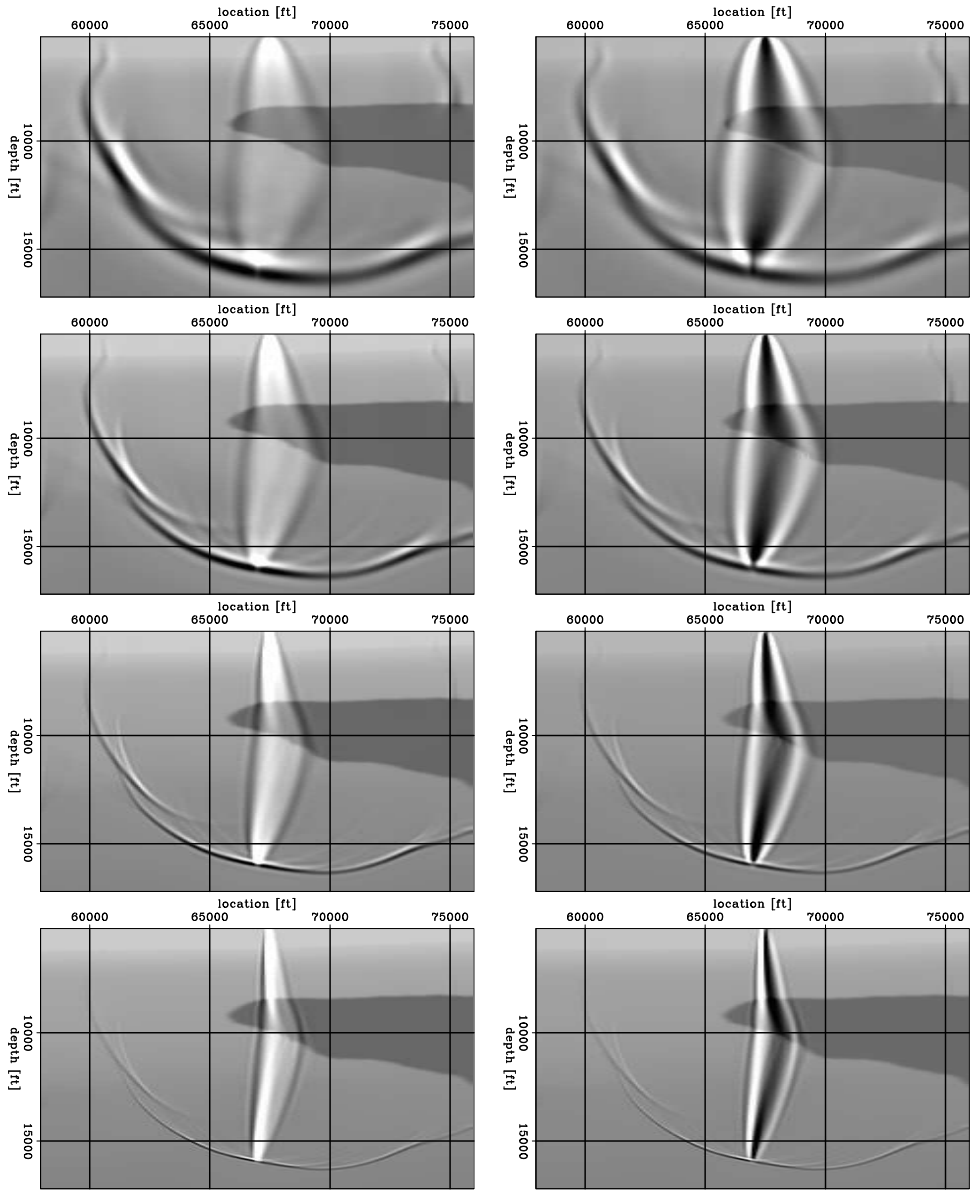


Figure 5.10: The dependence of sensitivity kernels to frequency and image perturbation. From top to bottom, the frequency range is $1-4$ Hz, $1-8$ Hz, $1-16$ Hz and $1-32$ Hz. The left column corresponds to kinematic image perturbations, and the right column corresponds to dynamic image perturbations. The wavefield is produced from a point source. wemva-fat2d.Tray2a [CR,M]

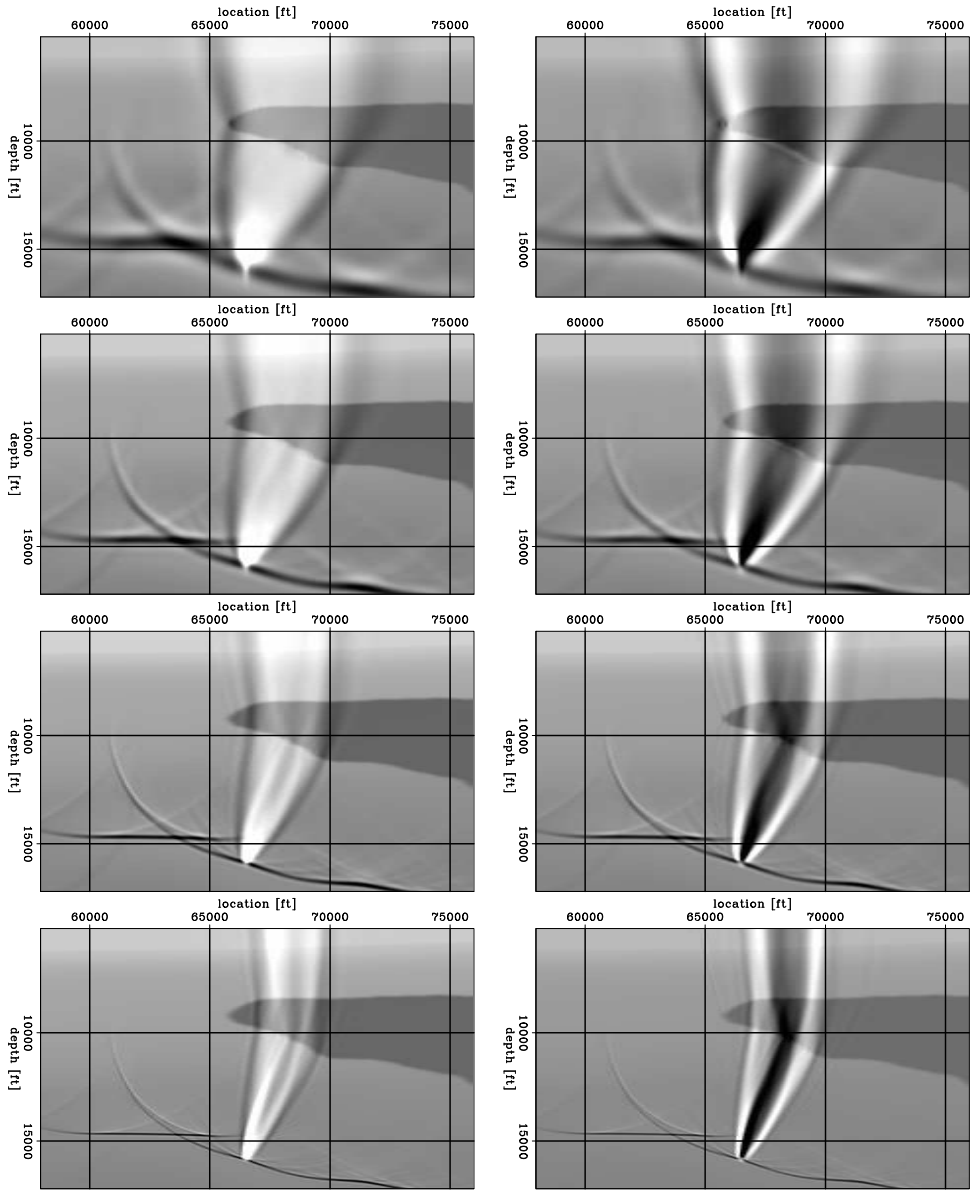


Figure 5.11: The dependence of sensitivity kernels to frequency and image perturbation. From top to bottom, the frequency range is $1-4$ Hz, $1-8$ Hz, $1-16$ Hz and $1-32$ Hz. The left column corresponds to kinematic image perturbations, and the right column corresponds to dynamic image perturbations. The wavefield is produced by a horizontal incident plane-wave. wemva-fat2d.Tray2b [CR,M]

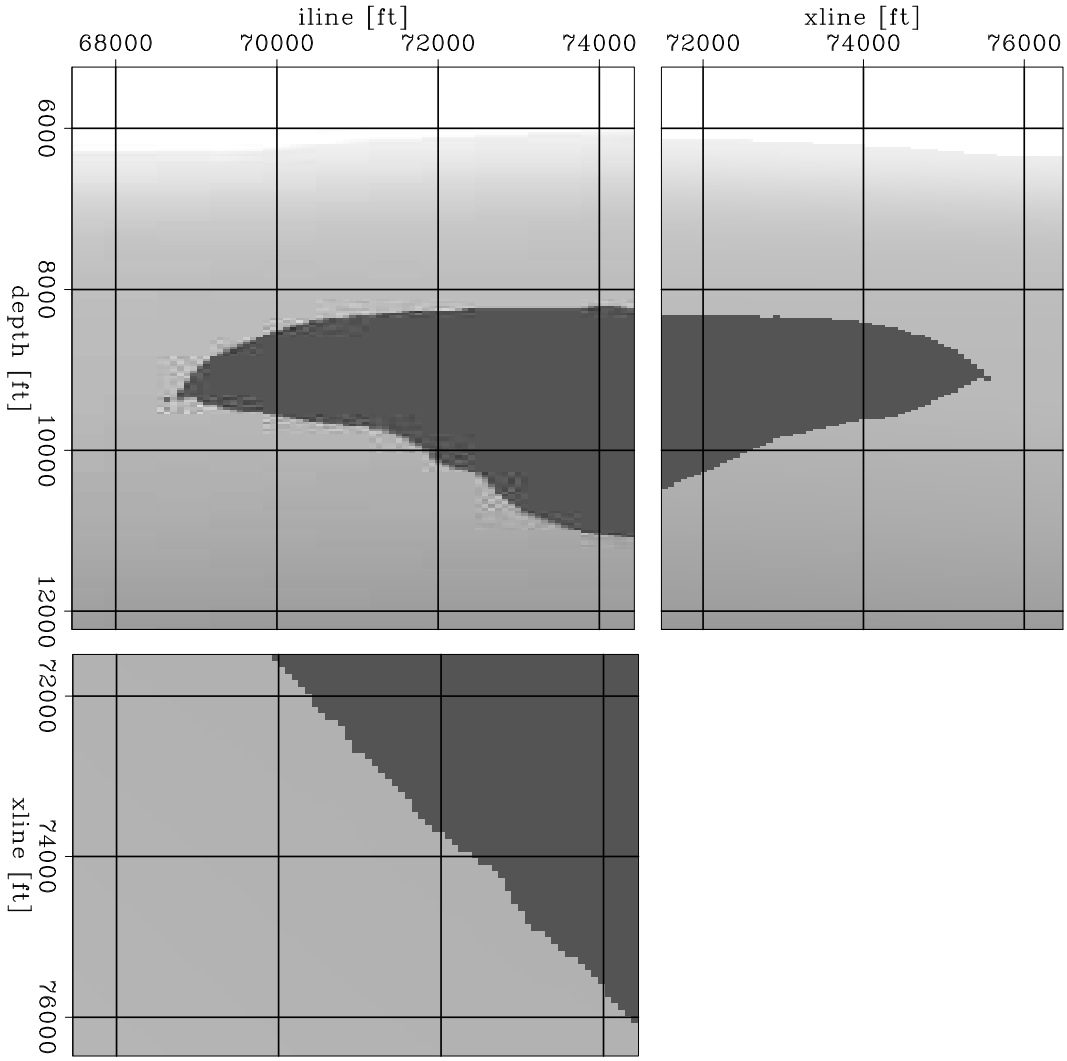


Figure 5.12: 3D slowness model. wemva-fat3.sC [CR]

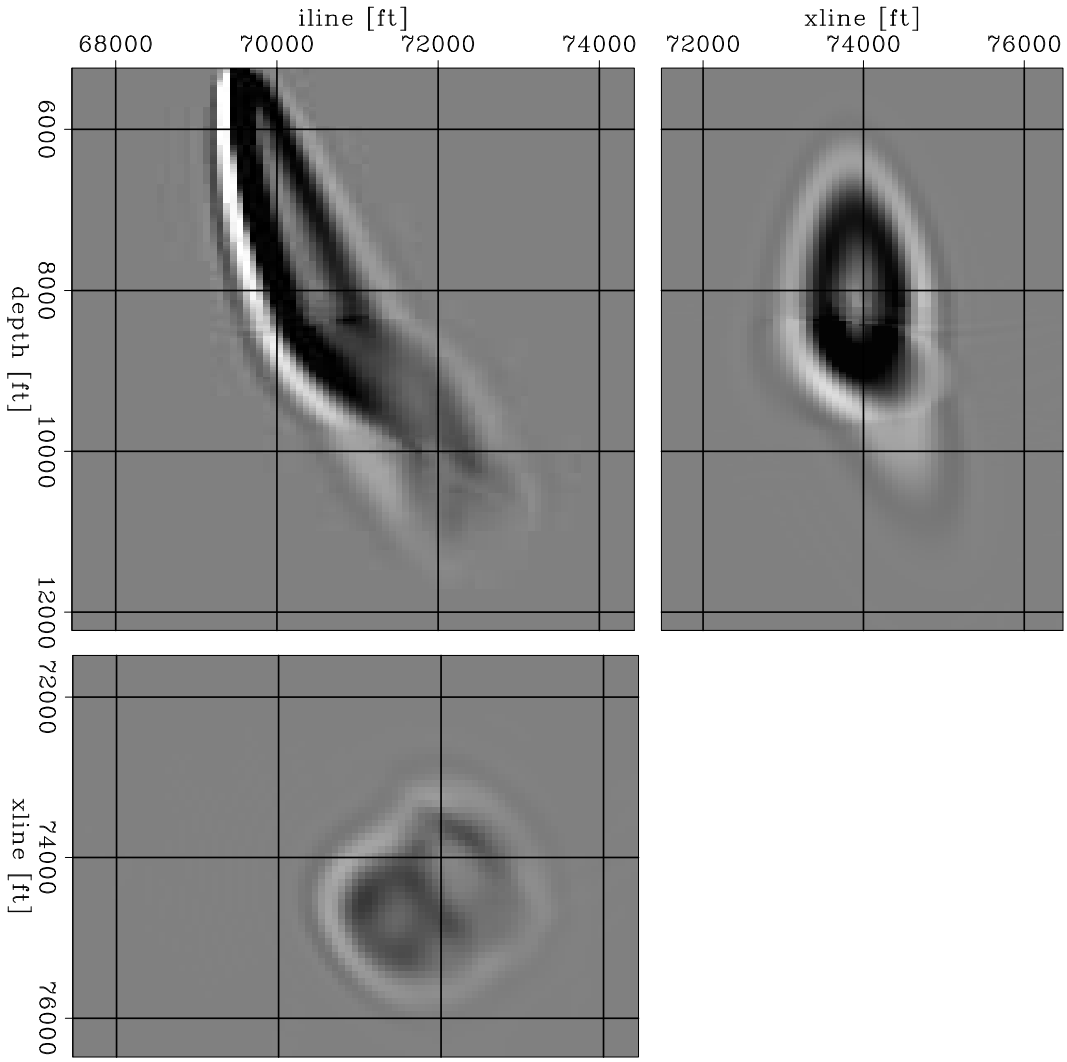


Figure 5.13: 3D sensitivity kernels for wave-equation MVA. The frequency range is $1-16$ Hz. The kernels are complicated by the multipathing occurring as waves propagate through the rough salt body. The image perturbation corresponds to a kinematic shift. wemva-fat3.fp3 [CR]

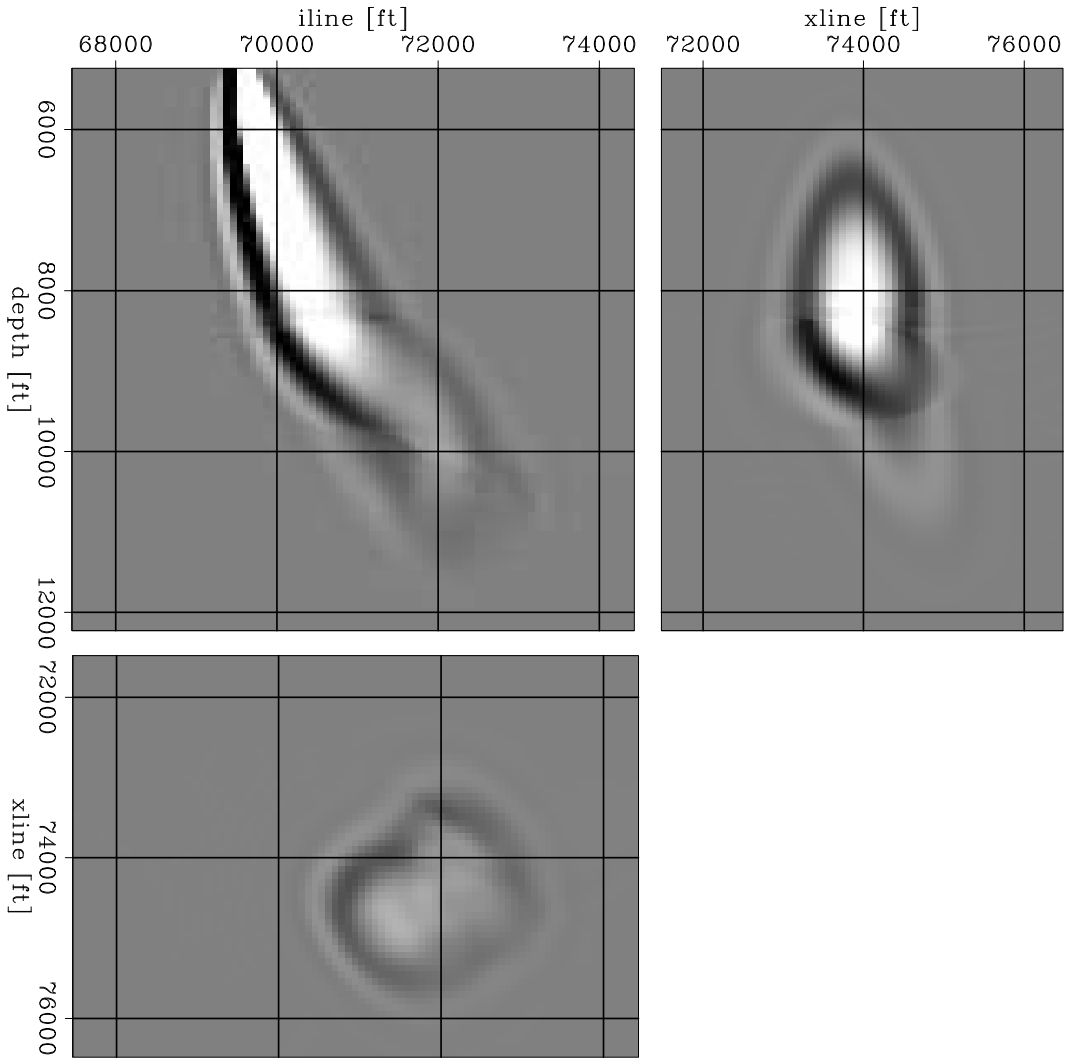


Figure 5.14: 3D sensitivity kernels for wave-equation MVA. The frequency range is $1-16$ Hz. The kernels are complicated by the multipathing occurring as waves propagate through the rough salt body. The image perturbation corresponds to an amplitude scaling. wemva-fat3.fq3 [CR]

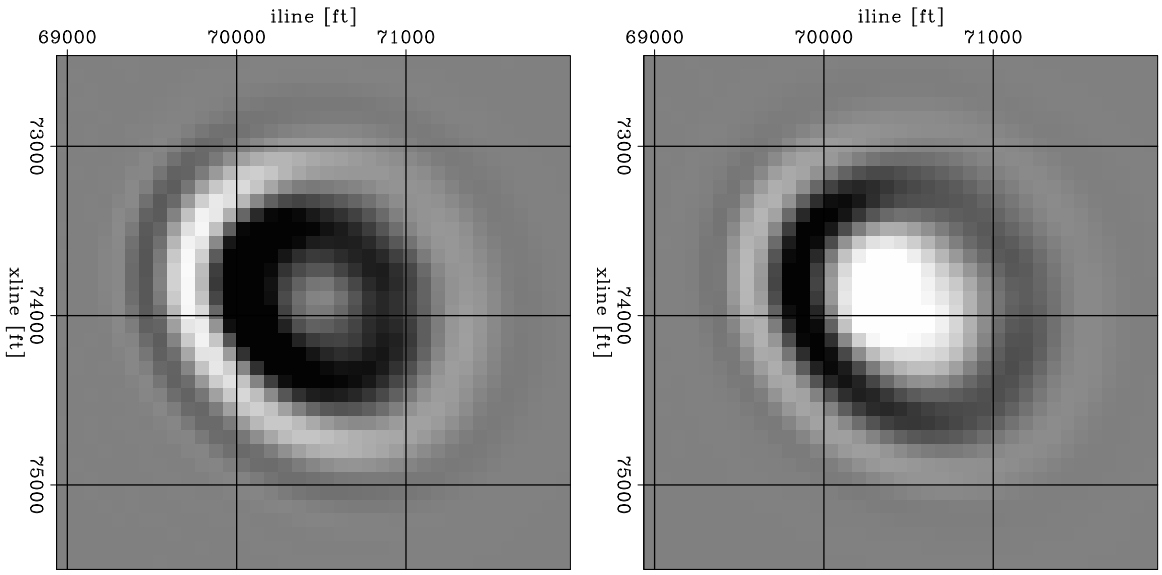


Figure 5.15: Cross-section of 3D sensitivity kernels for wave-equation MVA. The left panel corresponds to an image perturbation produced a kinematic shift, while the right panel corresponds to an image perturbation produced by amplitude scaling. The lowest sensitivity occurs in the center of the kinematic kernel (left). In contrast, the maximum sensitivity occurs in the center of the kernel (right). wemva-fat3.svty [CR]

Equation (5.29) can be written formally as

$$\delta\mathbf{d} = \mathbf{F}_0 \delta\mathbf{m} \,, \tag{5.30}$$

where $\delta\mathbf{m}$ is a perturbation in the model space, and $\delta\mathbf{d}$ is a perturbation in the image space. If we denote by δd^i the i^{th} component of $\delta\mathbf{d}$, and by $\delta\mathbf{m}(x)$ an infinitesimal element of $\delta\mathbf{m}$ at location x, we can write

$$\delta d^i = \int_V F_0^i(x)\ \delta\mathbf{m}(x)\ dv(x) \ . \tag{5.31}$$

F_0^i is, by definition, the integral kernel of the Fréchet derivative $\mathbf{F}_0$, V is the volume under investigation, dv is a volume element of V and x is the integration variable over V. The sensitivity kernel, a.k.a. *Fréchet derivative kernel*, F_0^i expresses the sensitivity of δd^i to a perturbation of $\delta\mathbf{m}(x)$ for an arbitrary location x in the volume V.

Sensitivity kernels occur in every inverse problem and have different meanings depending of the physical quantities involved:

- For **wideband traveltime tomography** (Bishop et al., 1985; Al-Yahya, 1989; Stork, 1992; Etgen, 1993; Kosloff et al., 1996), $\delta\mathbf{d}$ is represented by traveltime differences between recorded and computed traveltimes in a reference medium. The sensitivity kernels are infinitely-thin rays computed by ray tracing in the background medium.

- For **finite-frequency traveltime tomography** (Marquering et al., 1999; Dahlen et al., 2000; Hung et al., 2000; Rickett, 2000), $\delta\mathbf{d}$ is represented by time shifts measured by crosscorelation between the recorded wavefield and a wavefield computed in a reference medium. The sensitivity kernels are represented by hollow fat rays (a.k.a. "banana-doughnuts") which depend on the background medium.

- For **wave-equation tomography** (Woodward, 1992; Pratt, 1999; Pratt and Shipp, 1999), $\delta\mathbf{d}$ is represented by perturbations between the recorded wavefield and the computed wavefield in a reference medium. The sensitivity kernels are represented by fat rays with similar forms for either the Born or Rytov approximation.

- For **wave-equation migration velocity analysis** (Biondi and Sava, 1999; Sava and

Fomel, 2002; Sava and Biondi, 2004a,b), $\delta\mathbf{d}$ is represented by image perturbations. The sensitivity kernels are discussed in the following sections.

Wave-equation migration velocity analysis (WEMVA) establishes a linear relation between perturbations of the slowness model Δs and perturbations of migrated images $\Delta\mathcal{R}$. Δs and $\Delta\mathcal{R}$ correspond, respectively, to $\delta\mathbf{m}$ and $\delta\mathbf{d}$ in equation (5.30).

Formally, we can write

$$\Delta\mathcal{R} = \mathbf{L}\Delta s \ , \tag{5.32}$$

where $\mathbf{L}$ is the linear first-order Born wave-equation MVA operator. The operator $\mathbf{L}$ incorporates all first-order scattering and extrapolation effects for media of arbitrary complexity. The major difference between WEMVA and wave-equation tomography is that $\delta\mathbf{d}$ is formulated in the image space for the former as opposed to the data space for the later. Thus, with WEMVA we are able to exploit the power of residual migration in perturbing migrated images – a goal which is much harder to achieve in the space of the recorded data.

By construction, the linear operator $\mathbf{L}$ depends on the wavefield computed by extrapolation of the surface data using the background slowness, which corresponds to $\mathbf{m}_0$ in equation (5.29). Thus, the operator $\mathbf{L}$ depends directly on the type of recorded data and its frequency content, and it also depends on the background slowness model. Thus, the main elements that control the shape of the sensitivity kernels are

- the frequency content of the background wavefield,
- the type of source from which we generate the background wavefield (e.g. point source, plane wave), and
- the type of perturbation introduced in the image space, which for this problem corresponds to the data space.

In the next examples, I define two types of image perturbations: a purely kinematic type $\Delta\mathcal{R}_k$, implemented simply as a derivative of the image with respect to depth, which can be

implemented as a multiplication in the depth domain as follows:

$$\Delta\mathcal{R}_k = -iz\widetilde{\mathcal{R}}\,, \tag{5.33}$$

and a purely dynamic type $\Delta\mathcal{R}_a$, implemented by scaling the reference image $\widetilde{\mathcal{R}}$ with an arbitrary number:

$$\Delta\mathcal{R}_a = \epsilon\widetilde{\mathcal{R}}\,. \tag{5.34}$$

In both cases, the perturbations are limited to a small portion of the image. The main difference between $\Delta\mathcal{R}_k$ and $\Delta\mathcal{R}_a$ is given by the 90° phase-shift between the two image perturbations.

5.8.2 Sensitivity kernels examples

In the first example (Figures 5.10 and 5.11), I compare the shapes of sensitivity kernels when changing the type of source for the background wavefield, its frequency content and the method used to generate an image perturbation in the subsurface. I show the results as a superposition of the velocity model, the background wavefield and the sensitivity kernels from a fixed point in the subsurface.

Figure 5.10 shows the sensitivity kernels for a point source on the surface, and Figure 5.11 shows the sensitivity kernels for a plane-wave propagating vertically at the surface. In both pictures, the left column corresponds to kinematic image perturbations of equation (5.33), and the right column corresponds to amplitude image perturbations of equation (5.34) obtained by scaling of the background image by an arbitrary number. From top to bottom, we show sensitivity kernels of increasing frequency range: $1-4$ Hz, $1-8$ Hz, $1-16$ Hz and $1-32$ Hz. Once again, we can see the large frequency dependence of the sensitivity kernels. The area of sensitivity reduces with increased frequency which is a clear indication that a frequency dependent migration velocity analysis method like WEMVA can better handle subsalt environments with patchy illumination and that illumination itself is a frequency dependent phenomenon which needs to be addressed in this way.

Finally, I show wave-equation MVA sensitivity kernels for a 3D velocity model figure 5.12 corresponding to a salt environment. I consider the case of a point source on the surface

and data with a frequency range of $1-16$ Hz. figure 5.13 shows the sensitivity kernelfor a kinematic image perturbation, while figure 5.14 for a amplitude image perturbation. In both cases, the shapes of the kernels are complicated, which is an expression of the multipathing occurring as waves propagate through rough salt bodies. The horizontal slice indicates multiple paths linking the source point on the surface with the image perturbation in the subsurface.

One noticeable characteristic is that the sensitivity kernels constructed from amplitude image perturbations show the largest sensitivity in the center of the kernel, as opposed the kinematic kernels which show the largest sensitivity away from the central path. This phenomenon was discussed by Dahlen et al. (2000) in the context of finite-frequency traveltime tomography. I illustrate it for WEMVA in Figure 5.15 with two horizontal slices in the sensitivity kernels shown in Figures 5.13 and 5.14.

5.9 WEMVA cost

In the most general case, the data storage required by wave-equation migration velocity analysis is roughly proportional to the size of the wavefield space, i.e. the size of the data times the number of depth steps used in downward continuation. The computational cost is roughly proportional to two migrations by wavefield extrapolation for every linear iteration. Thus, for most exploration 3D datasets, the storage and computational cost involved are tremendous such that the method may reach the limits of even the largest computers available today. However, as computational power increases, WEMVA becomes more and more feasible. The real question is not whether we can use this method today, but rather if it provides additional information which is not available from conventional traveltime-based methods.

WEMVA can exploit the efficiency of distributed cluster computers, with independent processing and storage units. Parallelization is done over frequencies distributed to separate cluster nodes, in a distribution pattern similar to that of wave-equation migration. For example, one frequency of a full 3-D prestack dataset with midpoint samples $n_{mx} = 1000$ and $n_{my} = 500$, offset samples $n_{hx} = 64$ and $n_{hy} = 64$ and depth samples $n_z = 1000$, requires storage of approximately 1.9 Tb on every cluster node, assuming processing of one frequency/node. This volume is large, even for today's largest computers, although it is not completely infeasible.

Wide application of WEMVA, however, requires techniques that reduce substantially the computational and storage cost. Several options, which can be used alone or in combinations, are the following:

1. Restrict data to a common-azimuth.

   This is a common procedure used to reduce data volumes for wave-equation migration. In many instances, reducing data to a common-azimuth is an appropriate approximation, for example for marine data acquired with a narrow azimuth. This approximation was demonstrated to be accurate in imaging complex structures. It is, furthermore, appropriate for velocity analysis, since the background velocity is likely to be inaccurate, degrading the accuracy wave-equation migration more than the common-azimuth approximation does.

2. Datum the recorded data above the region with inaccurate velocity

   This procedure effectively sinks the survey from the surface to an arbitrary depth in the subsurface, thus reducing the number of depth steps needed for velocity analysis. The assumption is that the velocity in the upper portion of the model can be effectively constrained using traveltime tomography methods.

3. Reduce the frequency band.

   Each frequency of the downward continued wavefield interacts with the velocity to create a different scattered wavefield. In principle, each frequency can be used independently to estimate velocity. Naturally, the low frequencies produce smoother velocities than the high frequencies. For a given size and smoothness of the estimated anomalies, we can limit the maximum frequency to less than what is needed to define the velocity anomalies. A narrow frequency band also acts as a regularizer or smoother applied to the inverted velocity. Furthermore, if we estimate velocities by regularized inversion, the sharper anomalies constrained by the high frequencies are smoothed-out, which is another reason to reduce the frequency band to an effective range.

4. Limit the wavefield to a volume of interest.

We could synthesize a dataset and wavefield by windowing the image in a region of interest and then de-migrating by upward continuation. Then, we can use the data generated this way to create the wavefield used in WEMVA. This method is related conceptually to data datuming from the surface which also limits the volume of investigation. However, if we generate data by de-migration we are also able to limit other characteristics of it, for example the frequency content or the maximum reflection angle, further reducing cost.

The theoretical justification for this process is that the background wavefield is the band-limited equivalent of a rayfield. In traveltime tomography, we use rays obtained by ray tracing which represents an approximate data modeling process. Here, we can model the equivalent of a rayfield, but by using wavefield extrapolation methods.

5. Limit the wavefield to normal incidence.

   A drastic reduction of the WEMVA cost can be achieved by limiting the reflection angles represented in the wavefield to normal incidence. This method is similar to the normal incidence velocity analysis involving traveltimes. However, normal-incidence WEMVA is superior to normal-incidence traveltime tomography since the rays used by the wave-equation method are wider than asymptotic rays, and thus more stable and better samplers of the velocity space.

All methods described above reduce the cost of WEMVA. However, each one of these approximations reduces the accuracy of the method. A judgment needs to be made *a priori* as of which method to use and how. Various velocity analysis scenarios require more or less accuracy and resolution. In the examples presented in Chapter 6, I use one or more of the techniques described above, either alone or in combination.

5.10 Conclusions

I present a migration velocity analysis method using wavefield-extrapolation techniques that can address the challenges posed by velocity estimation in complicated media with sharp contrasts and fine-scale features. This method is formulated in the migrated image space, with an

objective function aimed at improving the image quality. The method is based on a linearization of the downward continuation operator that relates perturbations of slowness models to perturbations of migrated images. Since the method is based on finite-difference extrapolation of band-limited waves, it naturally takes into account the multipathing that characterizes wave propagation in complex environments with large and sharp velocity contrasts. It also takes into account the full wavefield information, and not only selectively picked traveltimes, as it is currently done in state-of-the-art traveltime tomography.

I use prestack Stolt residual migration (Chapter 4) to define image perturbations by maximizing focusing and flatness of angle-domain common image gathers (Chapter 3). In general, the image perturbations computed with this method can be too different from the background image, and we are in danger of subtracting images that are not in phase, violating the first-order Born approximation assumption. I avoid divergence of the inversion procedure when the velocity perturbations are too large, by not inverting directly the image perturbations obtained by residual migration, but by inverting linearized versions of them. Thus, I achieve a method which is robust with respect to large model perturbations, a crucial step for a practical MVA method.

5.11 Acknowledgment

I would like to acknowledge Biondo Biondi with whom I collaborated on developing the wave-equation migration velocity analysis method (Sava and Biondi, 2004a,b).

Chapter 6

Examples

6.1 Simple WEMVA example

The first example concerns linearized image perturbations computed for prestack images. I use a simple model with flat reflectors and constant velocity. The image perturbation methodology is identical to the one outlined in Chapter 5. The main point of this example is to illustrate the WEMVA methodology in a situation when the requirements of the first-order Born approximation are clearly violated. In this case, the slowness perturbation is 50% of the background slowness.

Figure 6.1 shows representative common image gathers in the angle-domain (Chapter 3) for the background image (a), the correct image (b), the image perturbation obtained as a difference of the two images (c), the image perturbation obtained using the forward WEMVA operator (d), and the linearized image perturbation (e). Panels (d) and (e) are identical within numeric precision, indicating that the WEMVA methodology can successfully be employed to create correct image perturbations well beyond the limits of the first-order Born approximation.

Next, I apply the wave-equation migration velocity analysis algorithm (Chapter 5) to the example in Figure 6.1. First, I compute the background wavefield represented by the background image (Figures 6.1a and 6.2a). Next, I compute the linearized image perturbation,

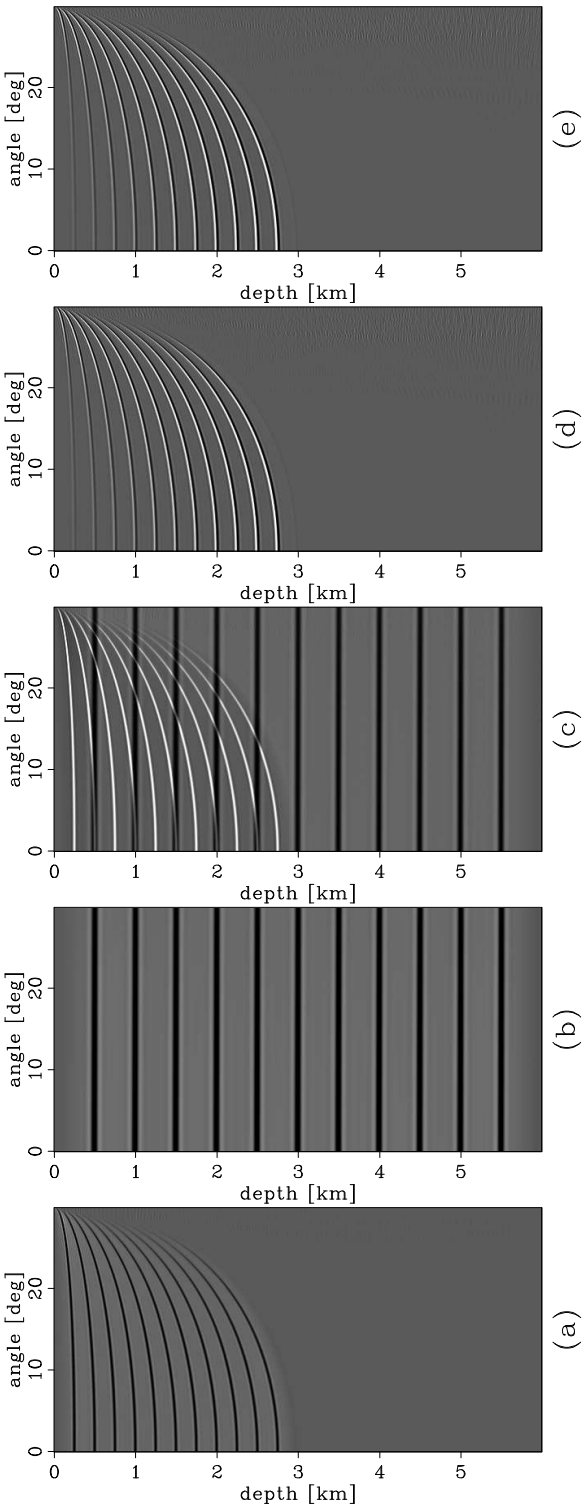


Figure 6.1: Comparison of common image gathers for image perturbations obtained as a difference between two migrated images (c), as the result of the forward WEMVA operator applied to the known slowness perturbation (d), and as the result of the differential image perturbation operator applied to the background image (e). Panel (a) depicts the background image corresponding to the background slowness, and panel (b) depicts an improved image obtained from the background image using residual migration. example-WEPf.imag [CR]

shown in Figure 6.3a (stack) and in Figure 6.1e (angle gather from the middle of the image).

From this image perturbation, I invert for the slowness perturbation (Figure 6.3b). I stop the inversion after 19 linear iterations when the data residual has stopped decreasing (Figure 6.3c). The slowness updates occur in the upper half of the model. Since no reflectors exist in the bottom part of the model, no slowness update is computed for this region.

Finally, I remigrate the data using the updated slowness and obtain the image in Figure 6.2b. For comparison, Figure 6.2c depicts the image obtained after migration with the correct slowness. The two images are identical in the upper half where we have updated the slowness model. Further updates to the model would require more non-linear iterations.

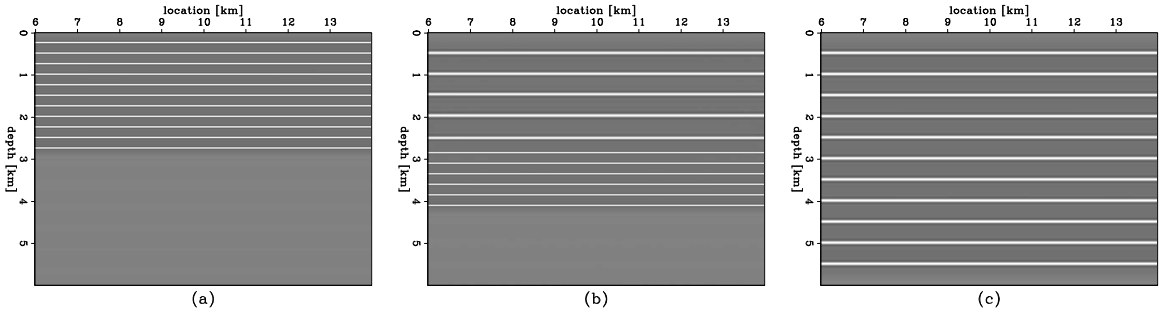


Figure 6.2: WEMVA applied to a simple model with flat reflectors. The background image (a), the image updated after one non-linear iteration (b), and the image computed with the correct slowness (c). example-zflat.back [CR]

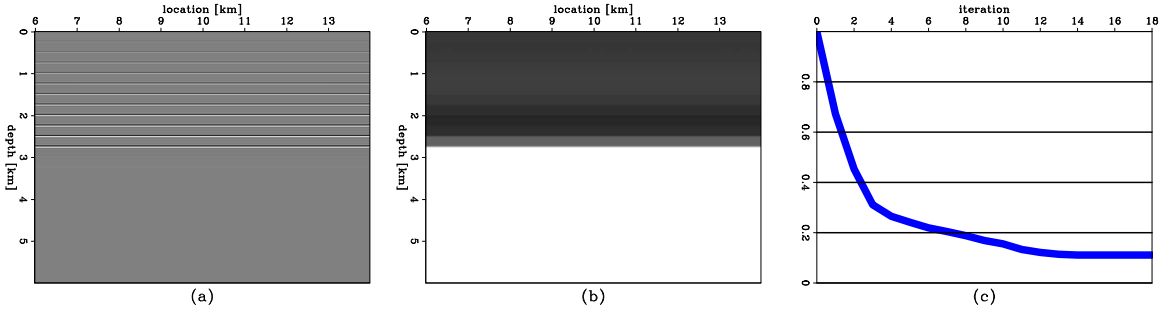


Figure 6.3: WEMVA applied to a simple model with flat reflectors. The zero-offset of the image perturbation (a), the slowness update after the first non-linear iteration (b), and the convergence curve of the first linear iterations (c). example-zflat.pert [CR]

The main point of this simple example is to illustrate that linearized image perturbations are capable of handling large velocity perturbations. In this example, the velocity change is so large that corresponding reflectors are not even close to one another, let alone within a fraction of the wavelet. Straight image differences are not able to handle correctly even this simple example. However, linearized image perturbations handle such large perturbations correctly and the velocity updates correct the starting image. Next sections illustrate the WEMVA methodology with more complex examples.

6.2 Subsalt WEMVA examples

Depth imaging of complex structures depends on the quality of the velocity model. However, conventional Migration Velocity Analysis (MVA) procedures often fail when the wavefield exhibits complex multi-pathing caused by strong lateral velocity variations. Imaging under rugged salt bodies is an important case when ray-based MVA methods are not reliable. In Chapter 5, I introduce the theory and methodology of an MVA procedure based on wavefield extrapolation with the potential of overcoming the limitations of ray-based MVA methods. In this section, I present the application of the proposed procedure to Sigsbee 2A, a realistic and challenging 2D synthetic data set created by the SMAART JV (Paffenholz et al., 2002), and to a 2D line of a 3D real dataset from the Gulf of Mexico.

Many factors determine the failure of ray-based MVA in a sub-salt environment. Some of them are successfully addressed by the wave-equation MVA (WEMVA) method, whereas others, for example the problems that are caused by essential limitations of the recorded reflection data, are only partially solved by WEMVA.

An important practical difficulty encountered when using rays to estimate velocity below rugose salt bodies is the instability of ray tracing. Rough salt topology creates poorly illuminated areas, or even shadow zones, in the subsalt region. The spatial distribution of these poorly illuminated areas is very sensitive to the velocity function. Therefore, it is often extremely difficult to trace rays connecting a given point in the poorly illuminated areas with a given point at the surface (two-point ray-tracing). Wavefield extrapolation methods are robust with respect to shadow zones and they always provide wavepaths usable for velocity inversion.

A related and more fundamental problem with ray-based MVA, is that rays poorly approximate actual wavepaths when a band-limited seismic wave propagates through a rugose top of the salt. Figure 6.4 illustrates this issue by showing three band-limited ($1-26$ Hz) wavepaths, also known in in the literature as fat rays or sensitivity kernels (Woodward, 1992; Pratt, 1999; Dahlen et al., 2000). Each of these three wavepaths is associated with the same point source located at the surface but corresponds to a different sub-salt "event". The top panel in Figure 6.4 shows a wavepath that could be reasonably approximated using the method introduced by Lomax (1994) to trace fat rays using asymptotic methods. In contrast, the wavepaths shown in both the middle and bottom panels in Figure 6.4 cannot be well approximated using Lomax' method. The amplitude and shapes of these wavepaths are significantly more complex than a simple fattening of a geometrical ray could ever describe. The bottom panel illustrates the worst-case-scenario situation for ray-based tomography because the variability of the top salt topology is at the same scale as the spatial wavelength of the seismic wave. The fundamental reason why true wavepaths cannot be approximated using fattened geometrical ray is that they are frequency dependent. Figure 6.5 illustrates this dependency by depicting the wavepath shown in the bottom panel of Figure 6.4 as a function of the temporal bandwidth: $1-5$ Hz (top), $1-16$ Hz (middle), and $1-64$ Hz (bottom). The width of the wavepath decreases as the frequency bandwidth increases, and the focusing/defocussing of energy varies with the frequency bandwidth.

The limited and uneven "illumination" of both the reflectivity model and the velocity model in the subsalt region is a challenging problem for both WEMVA and conventional ray-based MVA (see Figure 6.7 for an example of this problem). For the reflectors under salt, the angular bandwidth is drastically reduced in the angle-domain common image gathers (Chapter 3). This phenomenon is caused by a lack of oblique wavepaths in the subsalt, which deteriorates the "sampling" of the velocity variations in the subsalt. Consequently, the velocity inversion is more poorly constrained in the subsalt sediments than in the sediments on the side of the salt body.

Uneven illumination of subsalt reflectors is even more of a challenge than reduced angular coverage. It makes the velocity information present in the ADCIGs less reliable by causing discontinuities in the reflection events and creating artifacts. MVA methods assume that when

the migration velocity is correct, events are flat in ADCIGs along the aperture-angle axis. Velocity updates are estimated by minimizing curvature of events in ADCIGs. MVA methods may provide biased estimates where uneven illumination creates events that are bending along the aperture-angle axis, even where the image is created with correct velocity. I address this issue by weighting the image perturbations before inverting them into velocity perturbations, as described in Chapter 5. The weights are function of the "reliability" of the moveout measurements in the ADCIGs. I demonstrate the WEMVA method using synthetic and real datasets corresponding to subsalt environments.

6.2.1 Sigsbee 2A synthetic model

First, I illustrate the WEMVA method with a realistic and challenging synthetic data set created by the SMAART JV (Paffenholz et al., 2002). I use the same model for the sensitivity kernel analysis in Chapter 5 (Figures 6.4 and 6.5). In this section, I concentrate on the lower part of the model, under the salt body. The top panel in Figure 6.6 shows the background slowness model, and the bottom panel shows the slowness perturbation of the background model relative to the correct slowness. Thus, I simulate a common subsalt velocity analysis situation where the shape of the salt is known, but the smoothly varying slowness subsalt is not fully known. Throughout this example, I denote horizontal location by x and depth by z.

The original data set was computed with a typical marine off-end recording geometry. Preliminary studies of the data demonstrated that in some areas the complex overburden causes events to be reflected with negative reflection angle (i.e. the source and receiver wavepaths cross before reaching the reflector). To avoid losing these events I applied the reciprocity principle and created a split-spread data set from the original off-end data set. This modification of the data set enabled us to compute symmetric ADCIGs that are easier to visually analyze than the typical one-sided ADCIGs obtained from marine data. Therefore, I display the symmetric ADCIGs in Figure 6.9 and Figures 6.13- 6.15. Doubling the dataset also doubles the computational cost of the WEMVA process.

Figure 6.7 shows the migrated image using the correct slowness model. The top panel shows the zero offset of the prestack migrated image, and the bottom panel depicts ADCIGs

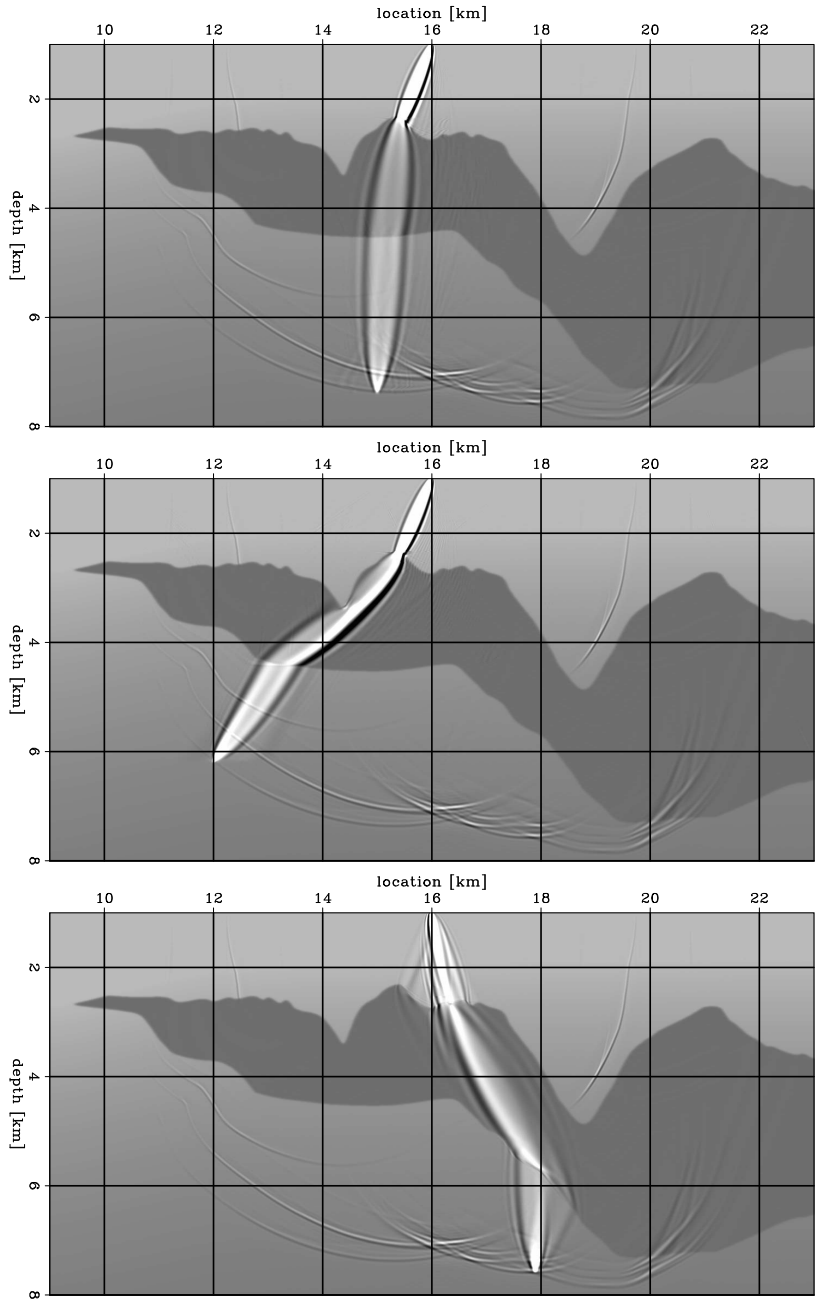


Figure 6.4: Wavepaths for frequencies between 1 and 26 Hz for various locations in the image and a point on the surface. Each panel is an overlay of three elements: the slowness model, the wavefield corresponding to a point source on the surface at $x = 16$ km, and wavepaths from a point in the subsurface to the source. example-zifat [CR]

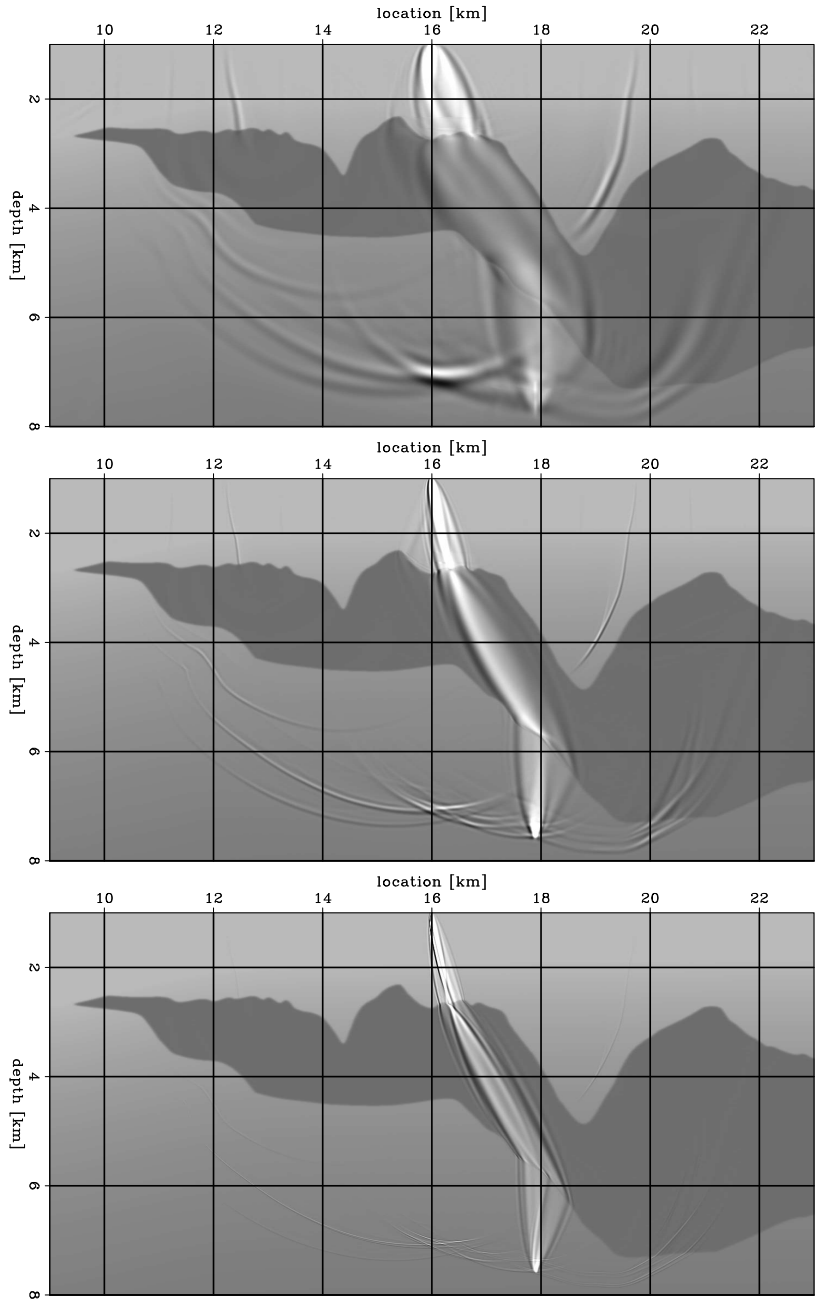


Figure 6.5: Frequency dependence of wavepaths between a location in the image and a point on the surface. The different wavepaths correspond to frequency bands of $1-5$ Hz (top), $1-16$ Hz (middle) and $1-64$ Hz (bottom). The larger the frequency band, the narrower the wavepath. example-zifrq2 [CR]

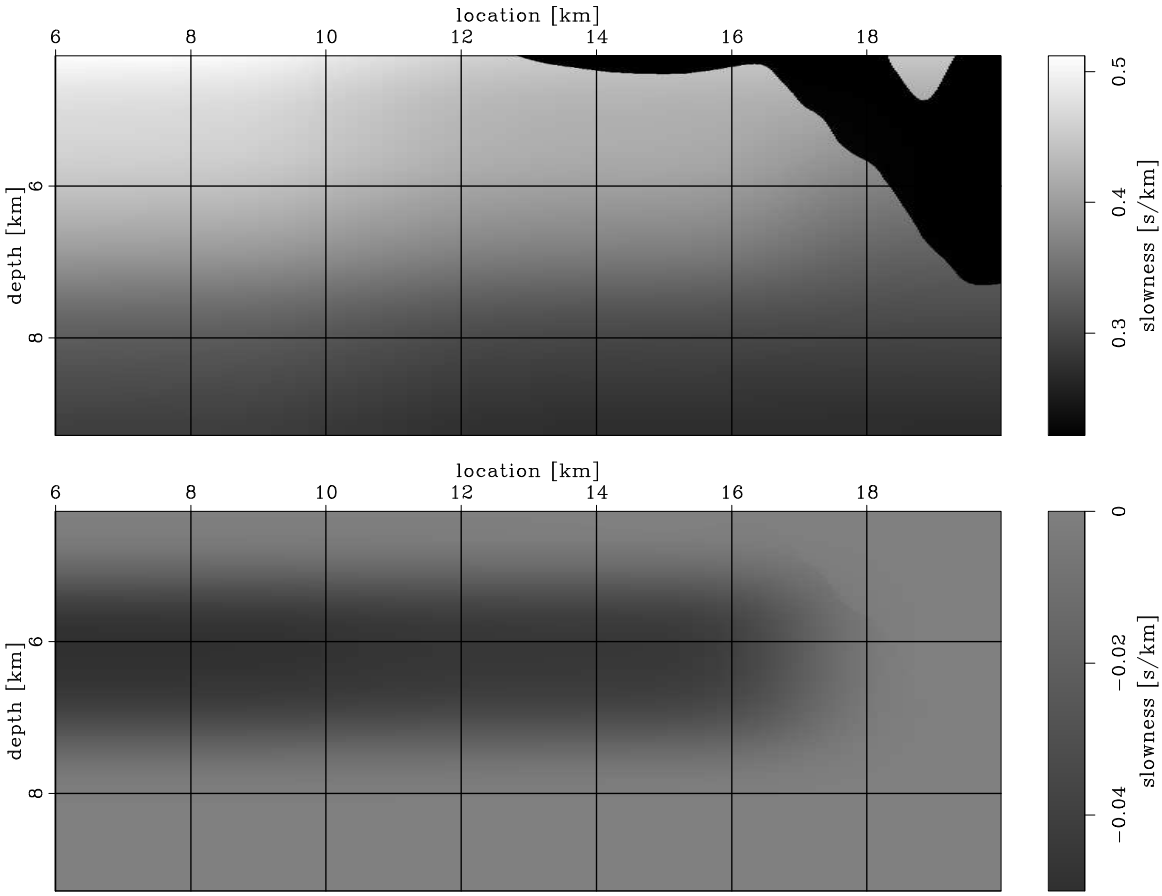


Figure 6.6: Sigsbee 2A synthetic model. The background slowness model (top) and the correct slowness perturbation (bottom). example-SIG.slo [CR]

at equally spaced locations in the image. Each ADCIG corresponds roughly to the location right above it.

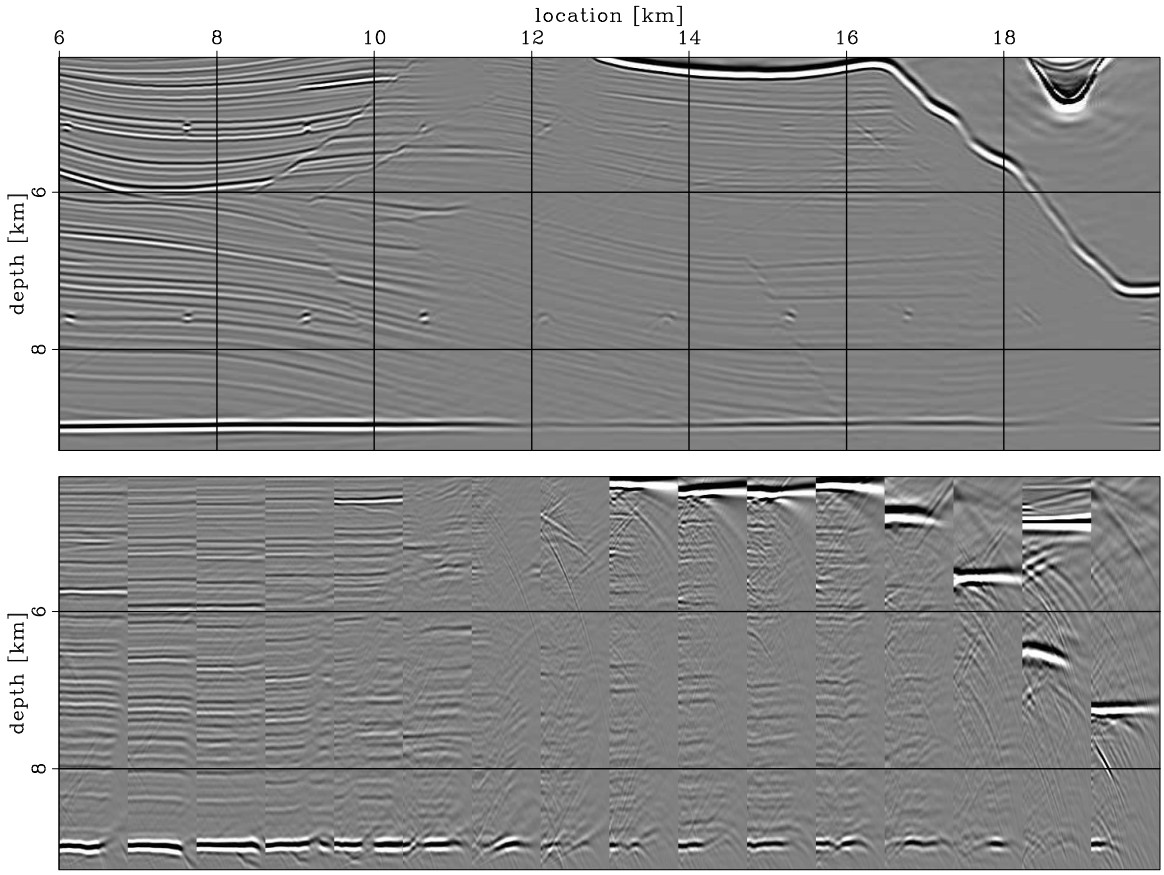


Figure 6.7: Migration with the correct slowness. Sigsbee 2A synthetic model. The zero offset of the prestack migrated image (top) and angle-domain common image gathers at equally spaced locations in the image (bottom). Each ADCIG corresponds roughly to the location right above it. example-SIG.imgC [CR]

This image highlights several characteristics of this model that make it a challenge for migration velocity analysis. Most of them are related to the complicated wavepaths in the subsurface under rough salt bodies. First, the angular coverage under salt ($x > 11$ km) is much smaller than in the sedimentary section uncovered by salt ($x < 11$ km). Second, the subsalt region is marked by many illumination gaps or shadow zones, the most striking being located at $x = 12$ and $x = 19$ km. The main consequence is that velocity analysis in the poorly

illuminated areas are much less constrained than in the well illuminated zones, as will become apparent later on in this example.

I begin by migrating the data with the background slowness (Figure 6.8). As before, the top panel shows the zero offset of the prestack migrated image, and the bottom panel depicts angle-domain common image gathers at equally spaced locations in the image. Since the migration velocity is incorrect, the image is defocused and the angle gathers show significant moveout. Furthermore, the diffractors at depths $z = 7.5$ km, and the fault at $x = 15$ km are defocused.

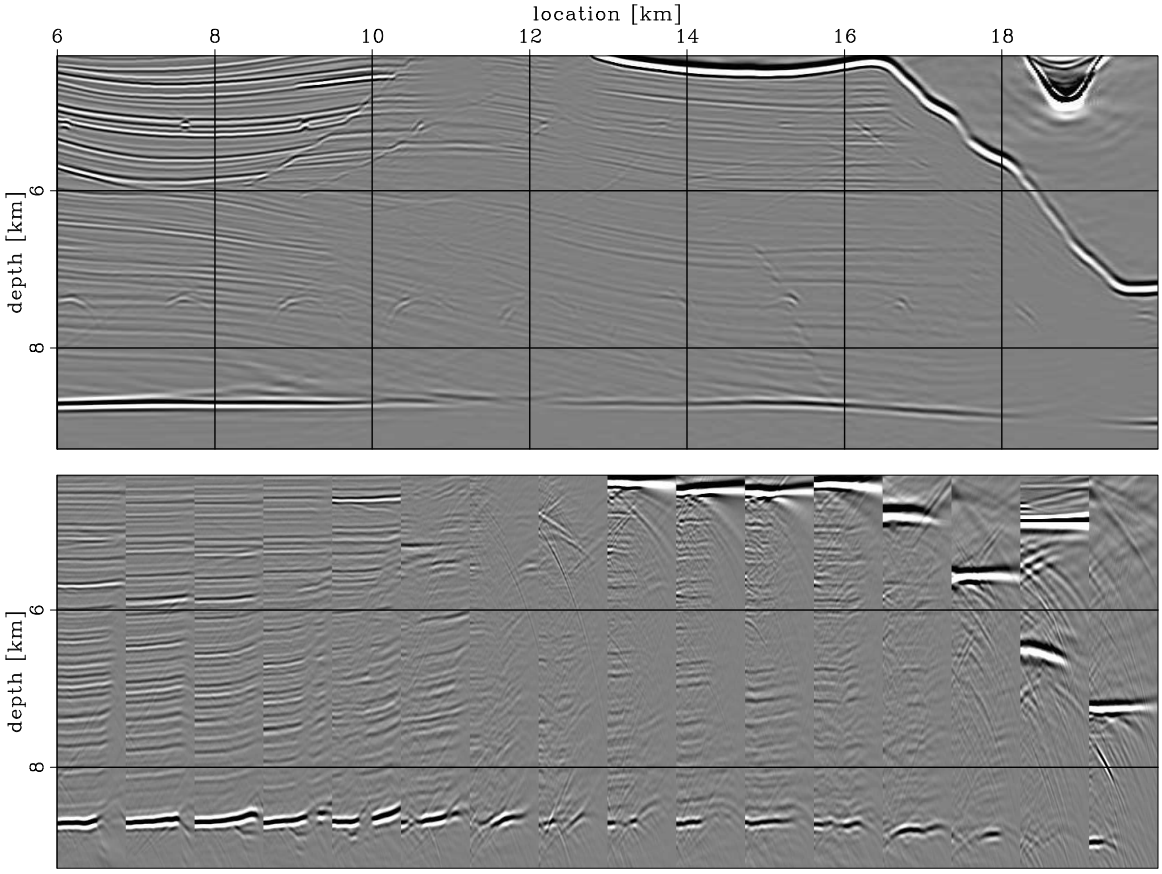


Figure 6.8: Migration with the background slowness. Sigsbee 2A synthetic model. The zero offset of the prestack migrated image (top) and angle-domain common image gathers at equally spaced locations in the image (bottom). Each ADCIG corresponds roughly to the location right above it. example-SIG.img1 [CR]

I run prestack Stolt residual migration Chapter 4 for various values of a velocity ratio parameter ρ between 0.9 and 1.6, which ensures that a fairly wide range of the velocity space is spanned. Although residual migration operates on the entire image globally, for display purposes I extract one gather at $x = 10$ km. Figure 6.9 shows at the top the ADCIGs for all velocity ratios and at the bottom the semblance panels computed from the ADCIGs. I pick the maximum semblance at all locations and all depths (Figure 6.10), together with an estimate of the reliability of every picked value which I use as a weighting function on the data residuals during inversion.

Based on the picked velocity ratio, I compute the linearized differential image perturbation, as described in the preceding sections. Next, I invert for the slowness perturbation depicted in the bottom panel of Figure 6.11. For comparison, the top panel of Figure 6.11 shows the correct slowness perturbation relative to the correct slowness. I can clearly see the effects of different angular coverage in the subsurface: at $x < 11$ km, the inverted slowness perturbation is better constrained vertically than it is at $x > 11$ km.

Finally, I update the slowness model and remigrate the data (Figure 6.12). As before, the top panel shows the zero offset of the prestack migrated image, and the bottom panel depicts angle-domain common image gathers at equally spaced locations in the image. With this updated velocity, the reflectors have been repositioned to their correct location, the diffractors at $z = 7.5$ km are focused and the ADCIGs are flatter than in the background image, indicating that the slowness update has improved the quality of the migrated image.

Figures 6.13- 6.15 show a more detailed analysis of the results of the inversion displayed as ADCIGs at various locations in the image. In each figure, the panels correspond to migration with the correct slowness (left), the background slowness (center), and the updated slowness (right). Figure 6.13 corresponds to an ADCIG at $x = 8$ km, in the region which is well illuminated. The angle gathers are clean, with clearly identifiable moveouts that are corrected after inversion. Figure 6.14 corresponds to an ADCIG at $x = 10$ km, in the region with illumination gaps, clearly visible on the strong reflector at $z = 9$ km at a scattering angle of about 20°. The gaps are preserved in the ADCIG from the image migrated with the background slowness, but the moveouts are still easy to identify and correct. Finally, Figure 6.15 corresponds to an ADCIG at $x = 12$ km, in a region which is poorly illuminated. In this

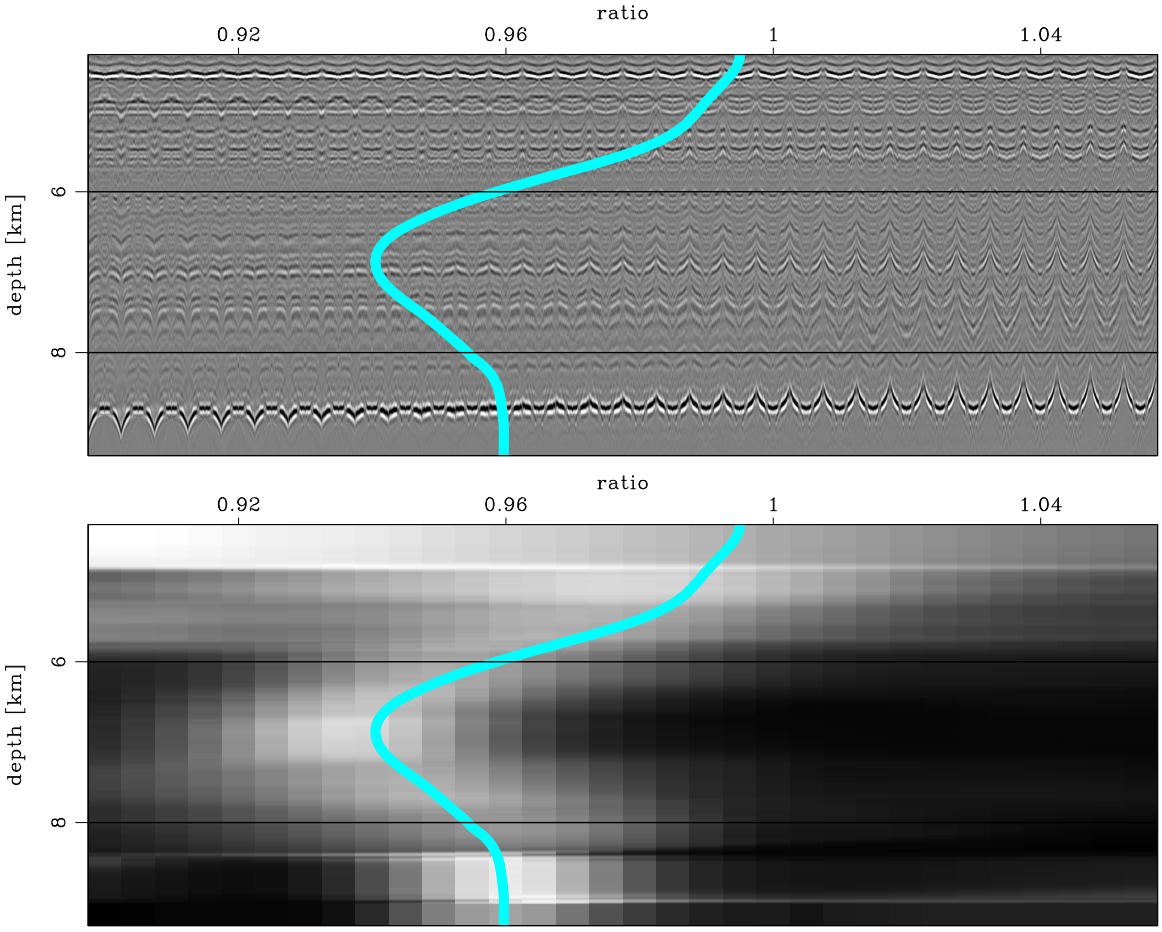


Figure 6.9: Residual migration for a CIG at $x = 10$ km. Sigsbee 2A synthetic model. The top panel depicts angle-domain common image gathers for all values of the velocity ratio, and the bottom panel depicts semblance panels used for picking. All gathers are stretched to eliminate the vertical movement corresponding to different migration velocities. The overlain line indicates the picked values at all depths. example-SIG.srm [CR]

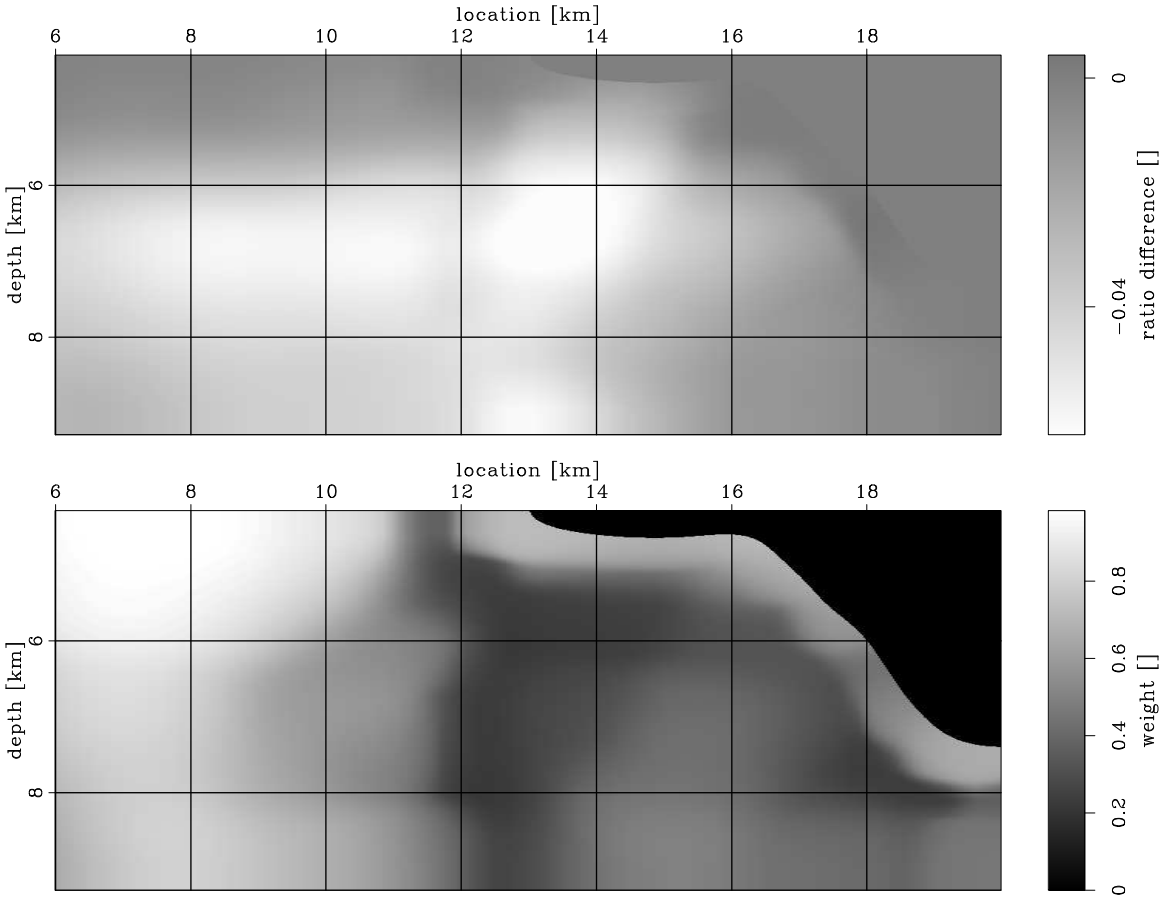


Figure 6.10: Sigsbee 2A synthetic model. The top panel depicts the velocity ratio difference $\Delta\rho = 1 - \rho$ at all locations, and the bottom panel depicts a weight indicating the reliability of the picked values at every location. The picks in the shadow zone around $x = 12$ km are less reliable than the picks in the sedimentary region around $x = 8$ km. All picks inside the salt are disregarded. example-SIG.pck [CR]

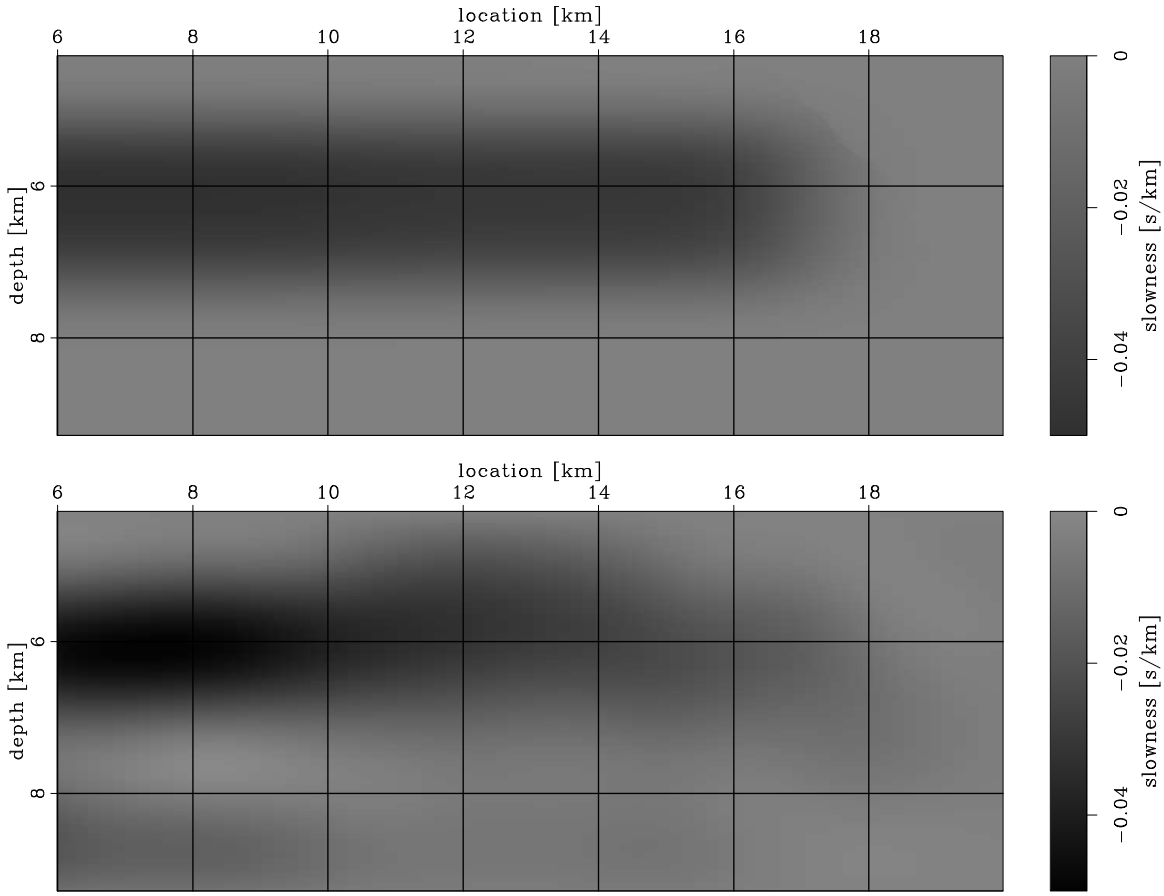


Figure 6.11: Sigsbee 2A synthetic model. The correct slowness perturbation (top) and the inverted slowness perturbation (bottom). example-SIG.dsl [CR]

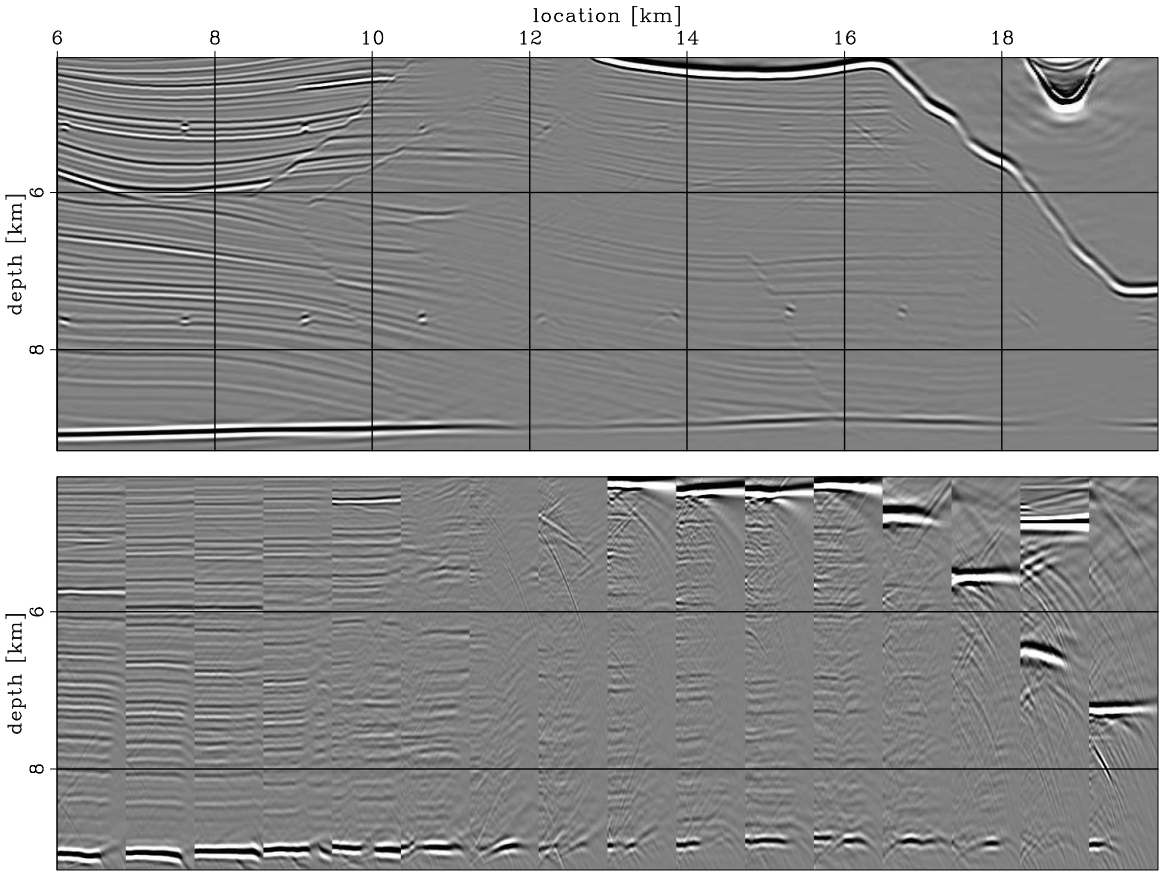


Figure 6.12: Migration with the updated slowness. Sigsbee 2A synthetic model. The zero offset of the prestack migrated image (top) and angle-domain common image gathers at equally spaced locations in the image (bottom). Each ADCIG corresponds roughly to the location right above it. example-SIG.img2 [CR]

case, the ADCIG is much noisier and the moveouts are harder to identify and measure. This region also corresponds to the lowest reliability, as indicated by the low weight of the picks (Figure 6.10). The gathers in this region contribute less to the inversion and the resulting slowness perturbation is mainly controlled by regularization. Despite the noisier gathers, after slowness update and re-migration I recover an image reasonably similar to the one obtained by migration with the correct slowness.

A simple visual comparison of the middle panels with the right and left panels in Figures 6.13- 6.15 unequivocally demonstrates that the WEMVA method overcomes the limitations related to the linearization of the wave equation by using the first-order Born approximation. The images obtained using the initial velocity model (middle panels) are vertically shifted by several wavelengths with respect to the images obtained using the true velocity (left panels) and the estimated velocity (right panels). If the Born approximation were a limiting factor for the magnitude and spatial extent of the velocity errors that could be estimated with the WEMVA method, I would have been unable to estimate a velocity perturbation sufficient to improve the ADCIGs from the middle panels to the right panels.

6.2.2 2D field data example

The next example concerns a 2D line extracted from a 3D subsalt dataset from the Gulf of Mexico. I follow the same methodology as the one used for the preceding synthetic example. In this case, however, I run several non-linear iterations of WEMVA, each involving wavefield linearization, residual migration and inversion.

Figure 6.16 (top) shows the image migrated with the background velocity superimposed on the background slowness. This image serves as a reference against which I check the results of the velocity analysis. Two regions of interest are labeled A and B in the figure. The right edge of the model corresponds to a salt body. The top edge of the image is not at the surface, because I have datumed the surface data to a depth below the well-imaged overhanging salt body.

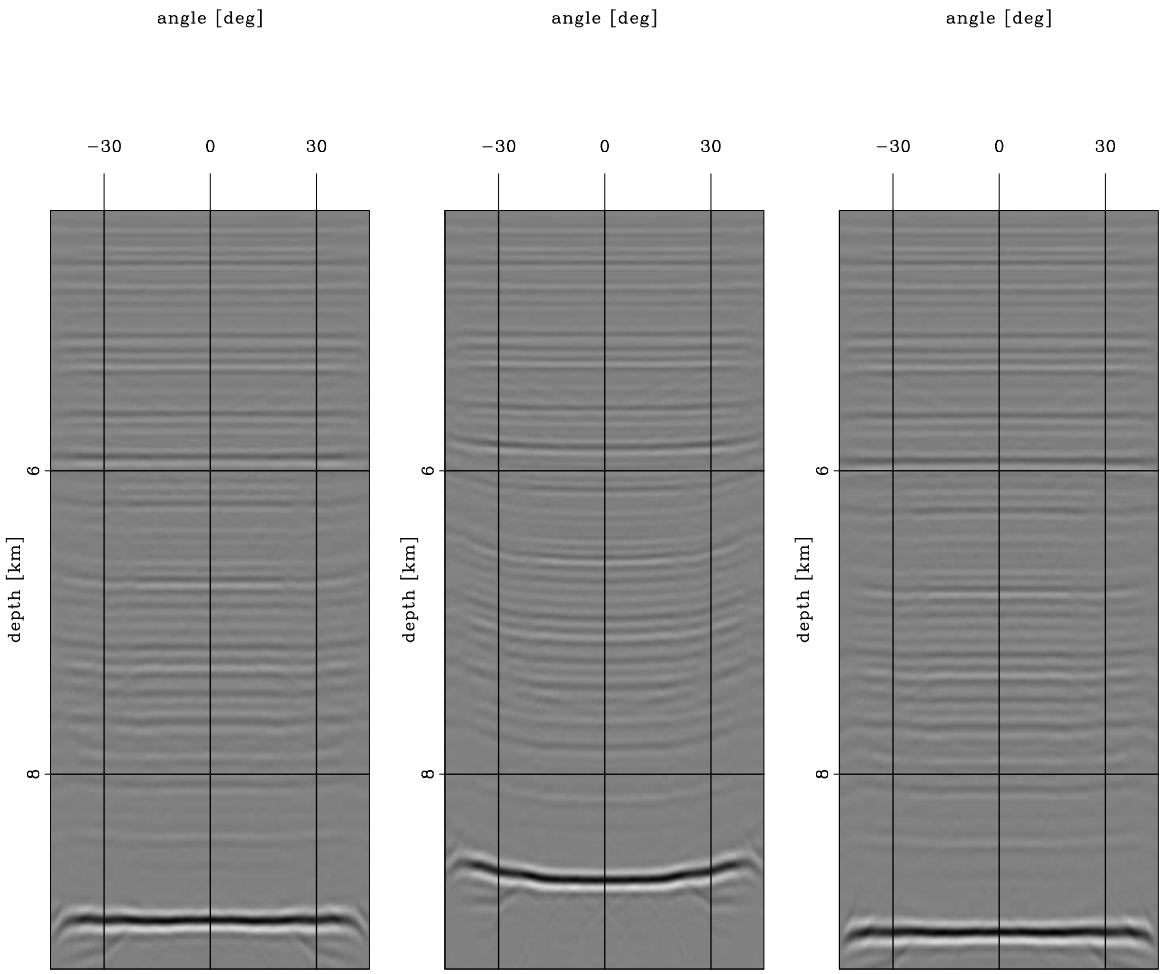


Figure 6.13: Angle-domain common image gathers at $x = 8$ km. Sigsbee 2A synthetic model. Each panel corresponds to a different migration velocity: migration with the correct velocity (left), migration with the background velocity (center) and migration with the updated velocity (right). example-SIG.ang08 [CR]

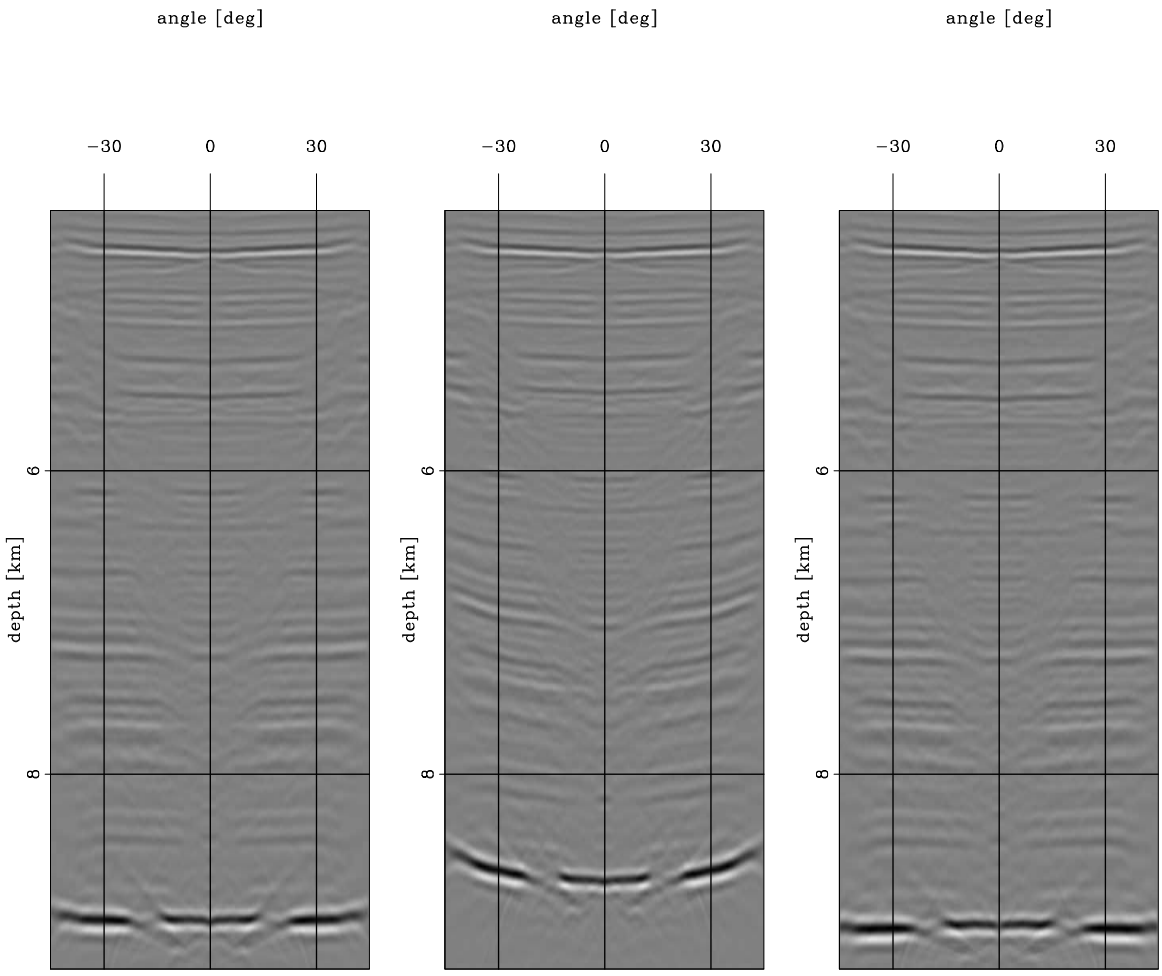


Figure 6.14: Angle-domain common image gathers at $x = 10$ km. Sigsbee 2A synthetic model. Each panel corresponds to a different migration velocity: migration with the correct velocity (left), migration with the background velocity (center) and migration with the updated velocity (right). example-SIG.ang10 [CR]

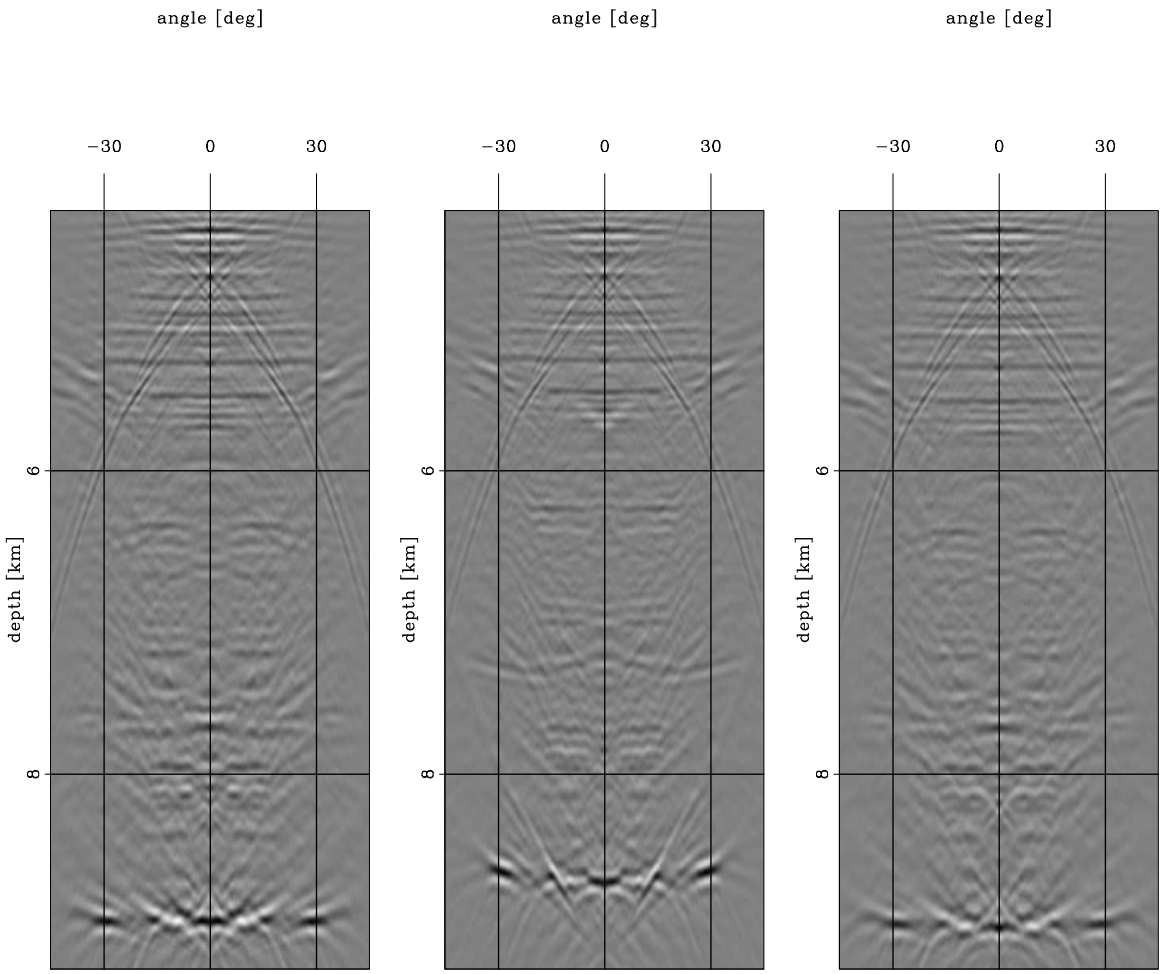


Figure 6.15: Angle-domain common image gathers at $x = 12$ km. Sigsbee 2A synthetic model. Each panel corresponds to a different migration velocity: migration with the correct velocity (left), migration with the background velocity (center) and migration with the updated velocity (right). example-SIG.ang12 [CR]

As for the preceding example, I run residual migration and analyze the moveouts of ADCIGs. Figure 6.17 shows this analysis at one location in the left part of the model. The left panel shows this ADCIG changing according to the velocity ratio parameter, while the right panel shows the semblance scan corresponding to each of these ratios. The overlain line is a pick of maximum semblance, indicating the flattest ADCIG at every depth level. This analysis is repeated at every location from which I obtain two maps: a map of the residual migration parameter at every location in the image (figure 6.16, middle), and a map of the weight indicating the reliability of the picks (figure 6.16, bottom). The residual migration parameter is plotted relative to 1 (indicated in white), therefore the whiter the map, the flatter the ADCIGs. Overlain is the stack of the background images for visual identification of image features. Next, I generate an image perturbation based on the residual migration picks in figure 6.16 (middle) and invert for slowness perturbation using the weights in figure 6.16 (bottom) as an approximation for the inverse data covariance matrix.

The results obtained after two non-linear iterations of WEMVA are shown in Figures 6.18 and 6.19. As for figure 6.16, the three panels show the migrated image superimposed on slowness (top), residual migration picks (middle), and pick weights (bottom). Two regions in which changes occur are labeled A and B.

For both iterations 1 and 2, the residual migration picks converge toward 1, indicating flatter ADCIGs, therefore better focused images. Reflectors in both regions shift vertically, according to the slowness changes. A notable feature is the improved continuity of the strongest reflectors in the region labeled B.

Both image improve after migration with the updated slownesses from WEMVA. However, there are regions where the image changes are small, if at all present. For example, the region to the left of “B”, which corresponds to a shadow zone caused by the salt structure in the upper part of the model, does not change. Better velocity could be estimated in this region with 3D data, since the shadow zones have three-dimensional expressions.

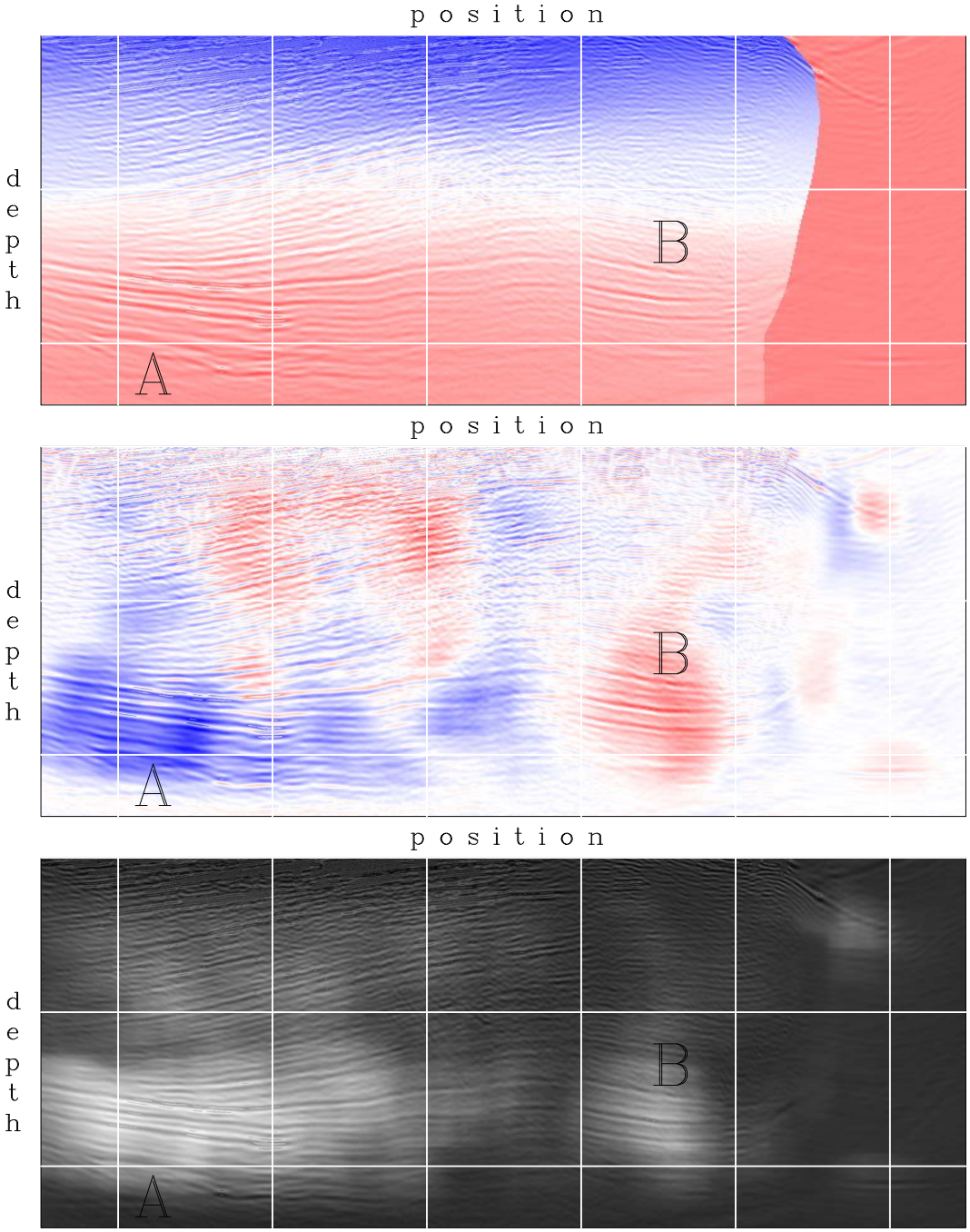


Figure 6.16: Gulf of Mexico data. Migrated image superimposed on slowness (top), residual migration picks (middle), and picking weight (bottom). The migration corresponds to the background slowness. example-BPGOM.it0 [CR]

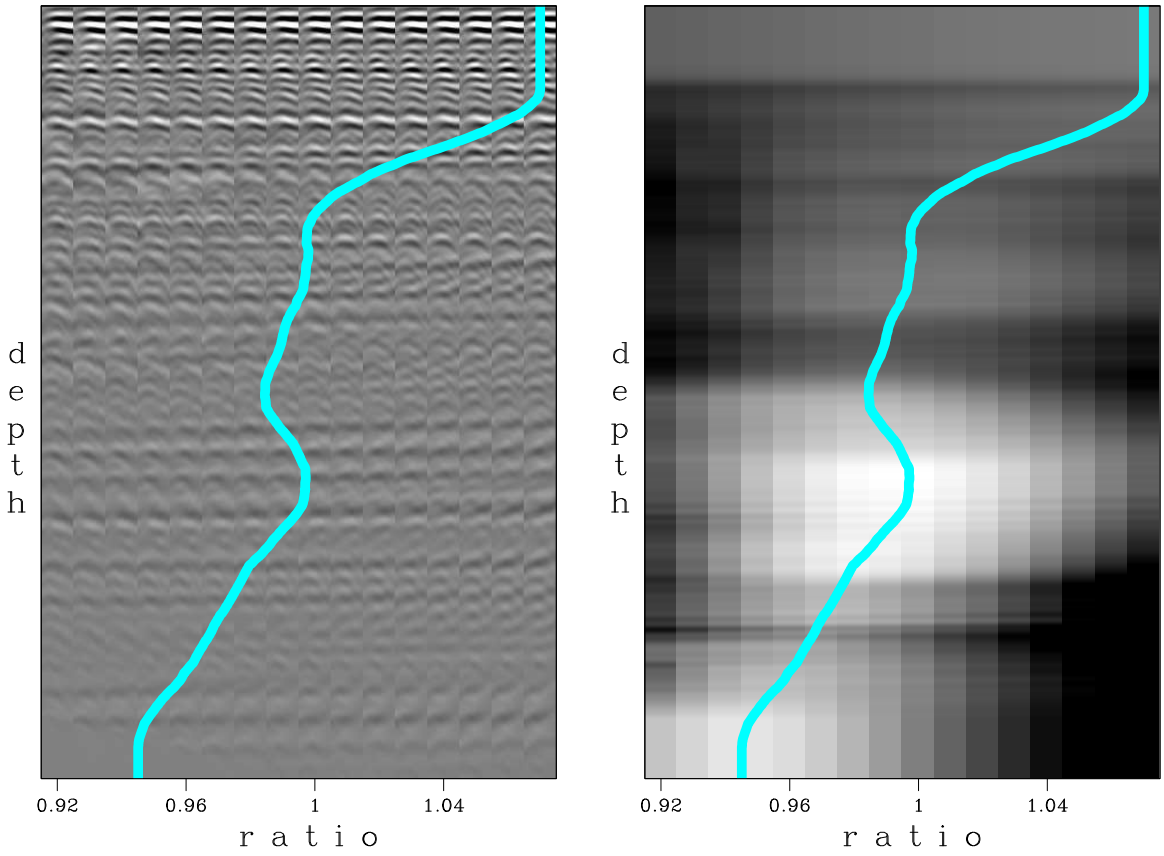


Figure 6.17: Gulf of Mexico data. Residual migration for a common image gather about one third from the left edge of the image in figure 6.16. Angle-domain CIGs (left) and semblance (right) with the picked velocity ratio. example-BPGOM.srm [CR]

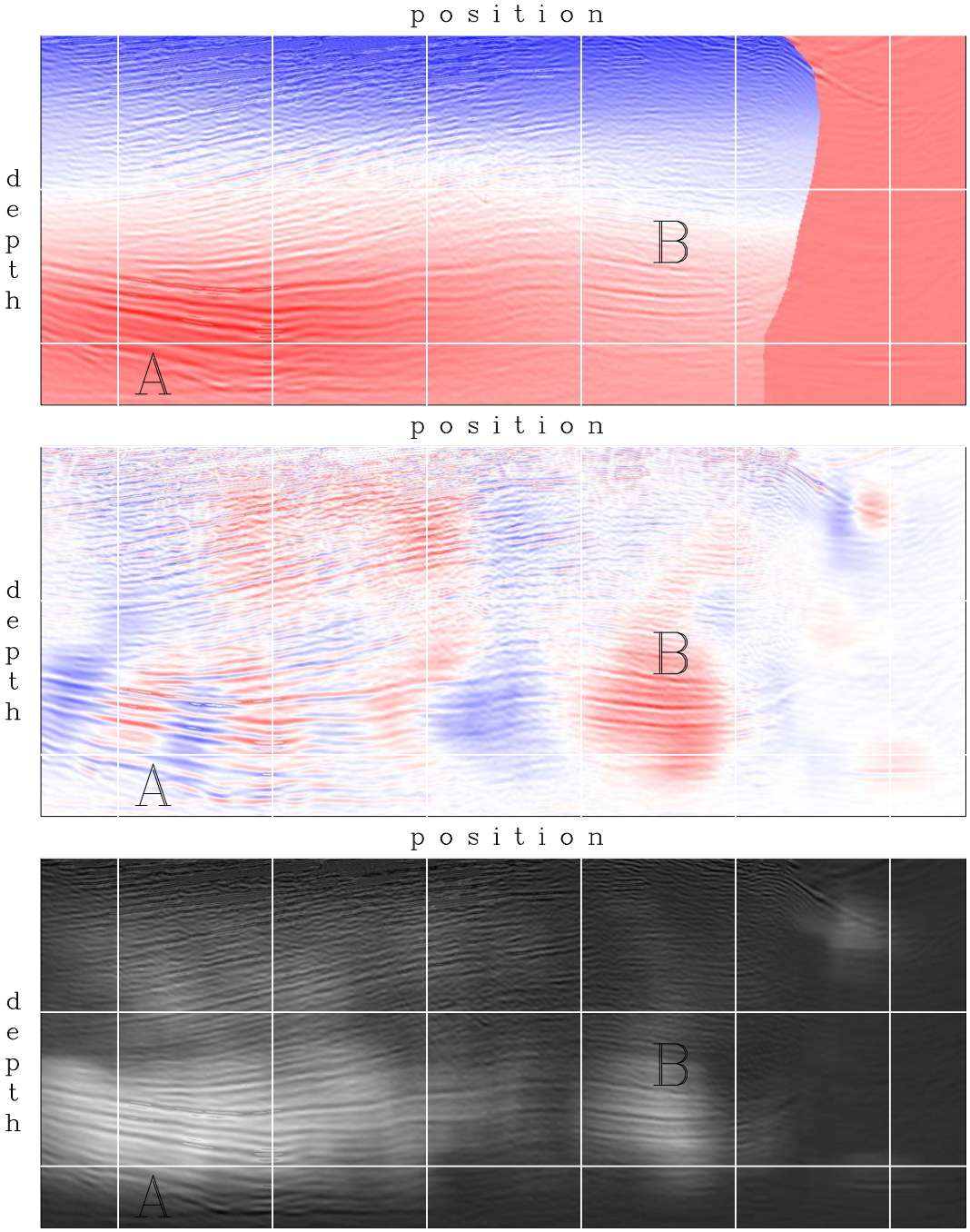


Figure 6.18: Gulf of Mexico data. Migrated image superimposed on slowness (top), residual migration picks (middle), and picking weight (bottom). The migration corresponds to the updated slowness after iteration 1. Compare with figure 6.16. example-BPGOM.it1 [CR]

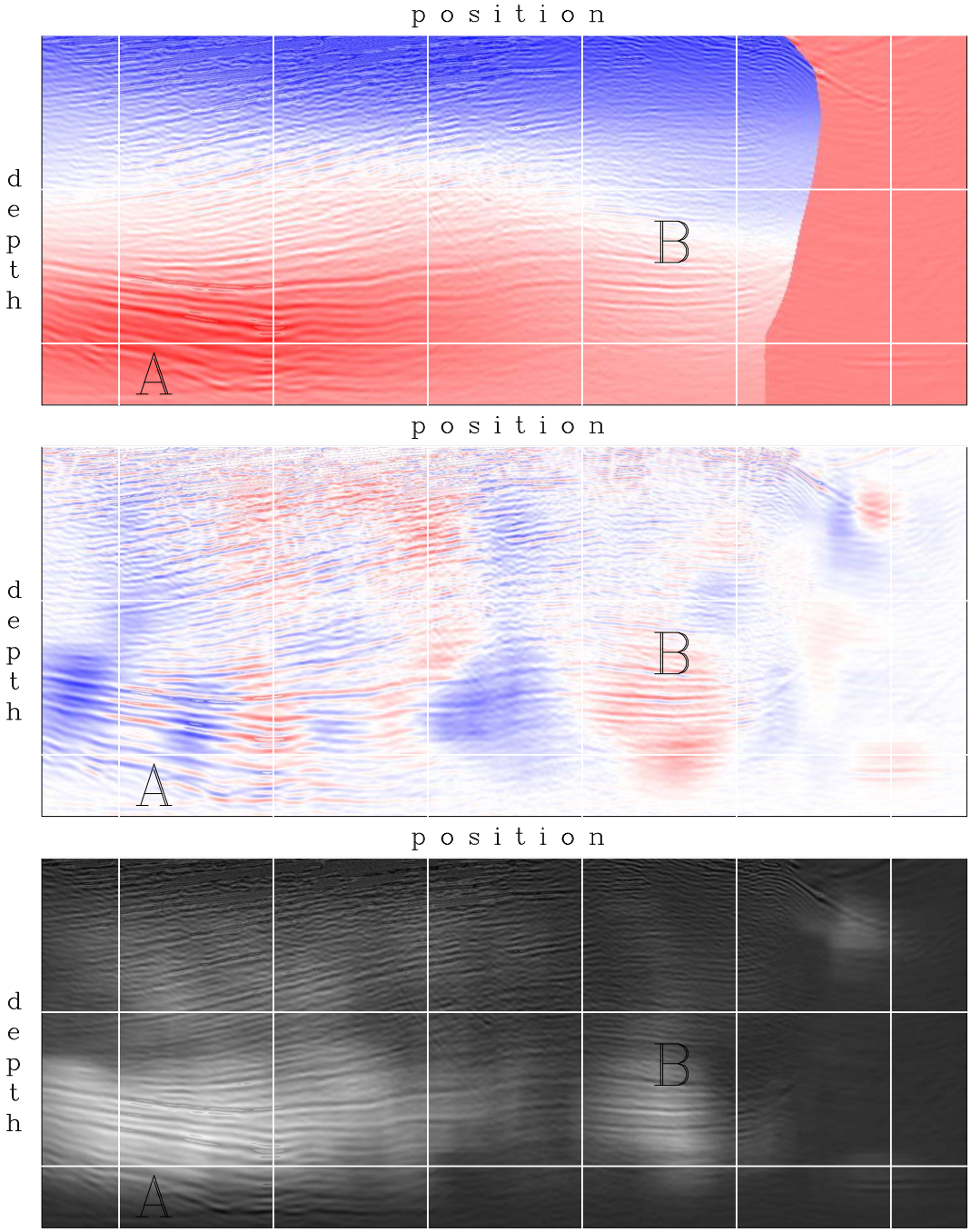


Figure 6.19: Gulf of Mexico data. Migrated image superimposed on slowness (top), residual migration picks (middle), and picking weight (bottom). The migration corresponds to the updated slowness after iteration 2. Compare with figure 6.16. example-BPGOM.it2 [CR]

Normal incidence WEMVA

Figure 6.20 shows a comparison of normal incidence with prestack wave-equation MVA. The top panel corresponds to normal incidence WEMVA, and the bottom panel corresponds to prestack WEMVA. The general shape of the velocity anomaly is similar, although the vertical resolution of prestack WEMVA is significantly higher. This is a direct result of the increased angular coverage with wavepaths away from the vertical.

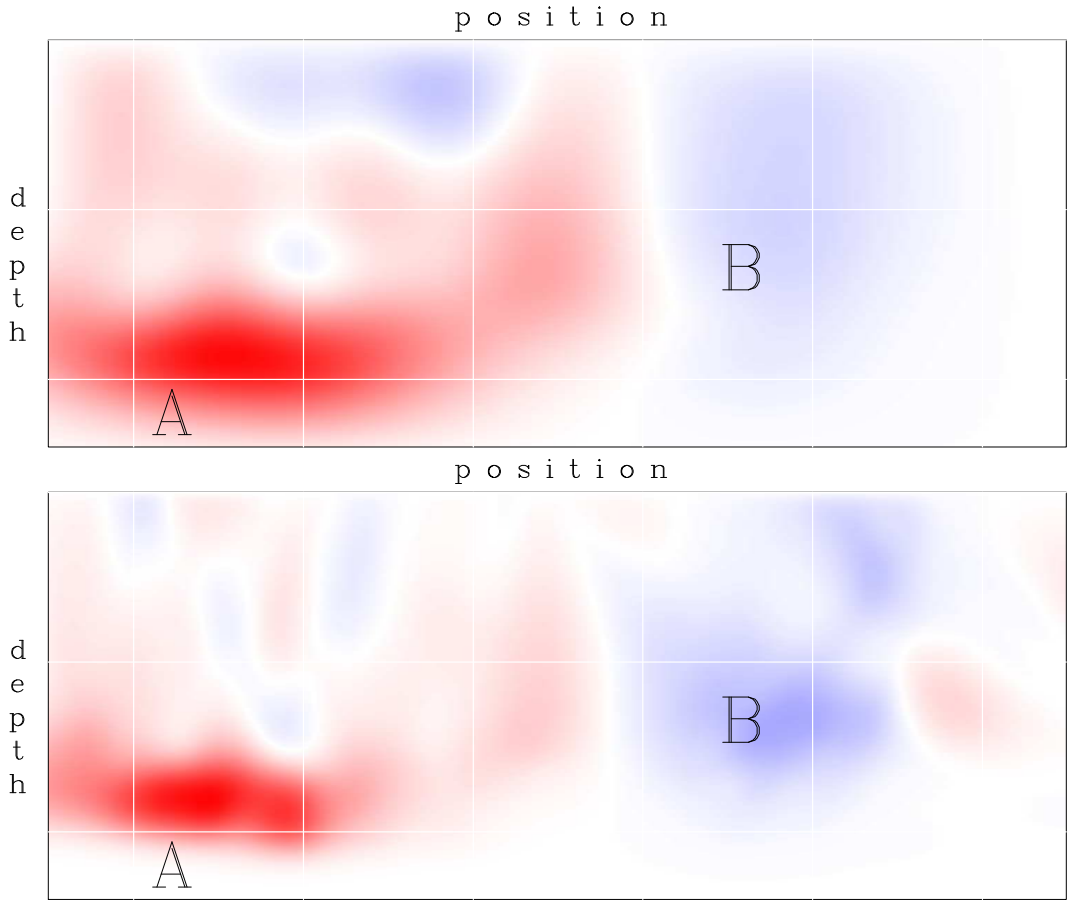


Figure 6.20: A comparison of normal incidence WEMVA (top panel) with prestack WEMVA (bottom panel). Prestack inversion produces anomalies with higher vertical resolution, due to the increased angular coverage. example-BPGOM.zpc.dsl [CR]

Figure 6.21 shows a comparison of three images superimposed on their corresponding

velocity model. From top to bottom, the background velocity, the velocity updated by normal incidence WEMVA, and the velocity updated by prestack WEMVA. The updated images have similar characteristics, since the velocity updates are also similar, except for the higher resolution of the prestack inversion. The lesson we can draw from this example is that normal incidence WEMVA is a cheap and convenient alternative to prestack WEMVA, at least for the cases of smooth velocity anomalies. However, if we seek higher vertical resolution, we need to use prestack WEMVA.

6.2.3 3D field data example

This section presents an example of wave-equation migration velocity analysis applied to a 3D dataset from the Gulf of Mexico (Figures 6.22 – 6.37).

Figure 6.22 shows the initial velocity model, obtained after multiple iterations of traveltime tomography. As for the preceding 2D example, the model consists of a large overhanging salt body which creates both complicated wave propagation and un-illuminated regions subsalt. Both phenomena reduce the ability of traveltime tomography to properly describe wavepaths subsalt, which leads to less accurate velocities in the complicated areas with multipathing and shadows. An example is illustrated along the inline direction in Figure 6.22, approximately at the location of the vertical line. Figure 6.23 shows the image corresponding to the model in Figure 6.22.

For cost reasons, in this example I do not use the entire image. I concentrate my attention on the small anomalies located right under the salt nose as pictured in Figure 6.22. Figure 6.24 indicates the portion of the image/velocity used for this analysis. I use this part of the starting (background) image to generate the wavefield corresponding to the initial (background) velocity. Then, I run normal-incidence WEMVA as discussed in Chapter 5.

The first step in WEMVA is to generate an image perturbation. For this, I run prestack residual migration starting from the background image pictured in Figure 6.23. The velocity ratios I use are between 0.92 and 1.07. Figure 6.25 shows the picked velocity ratio that optimizes angle gather flatness at every location in the 3D image. Figure 6.26 is the associated

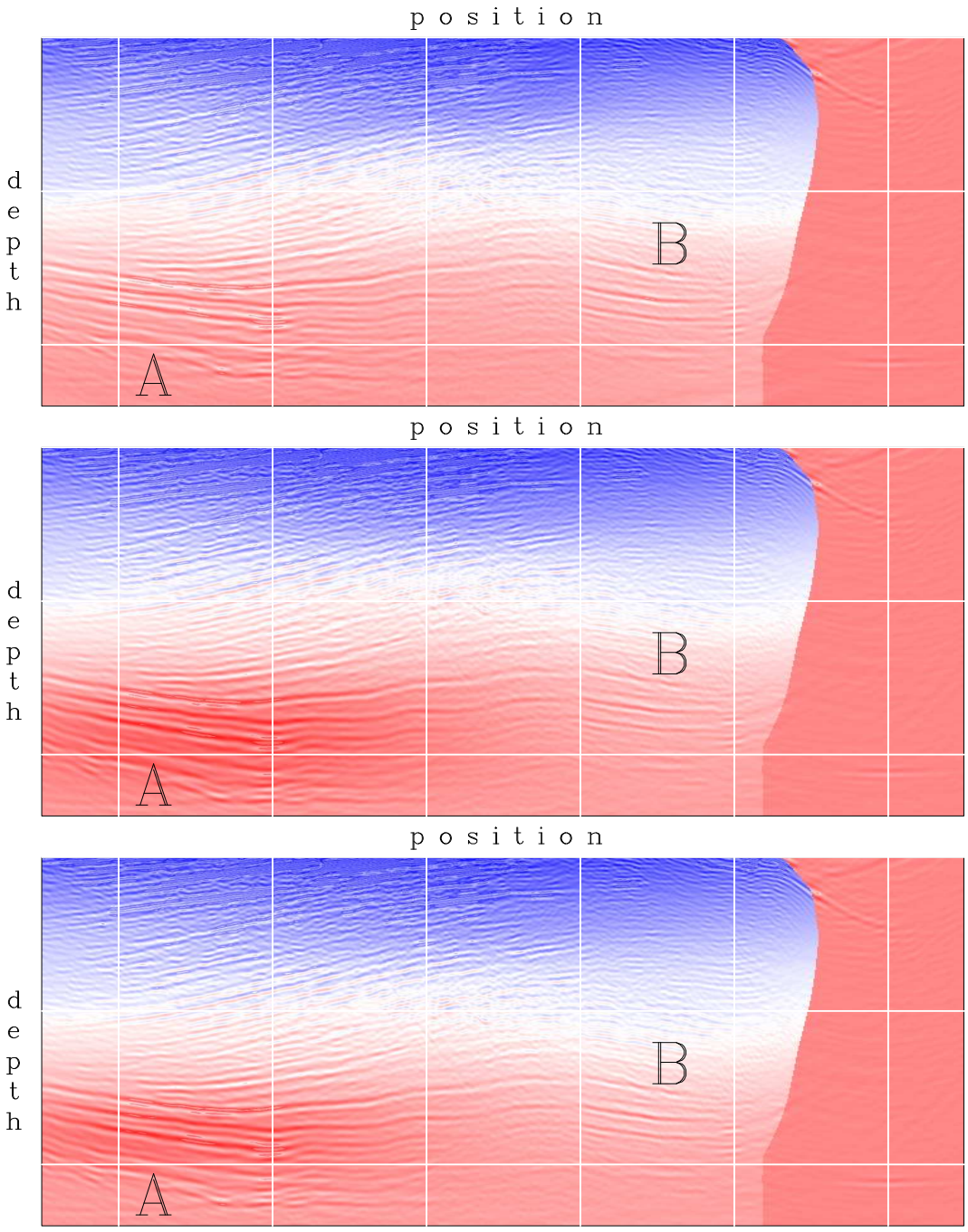


Figure 6.21: Image and velocity comparison for various types of velocity updates in WEMVA. From top to bottom, the image created with the background velocity (top), the image created with the velocity updated with normal incidence WEMVA (middle), and the image created with the velocity updated with prestack WEMVA (bottom). example-BPGOM.zpc [CR]

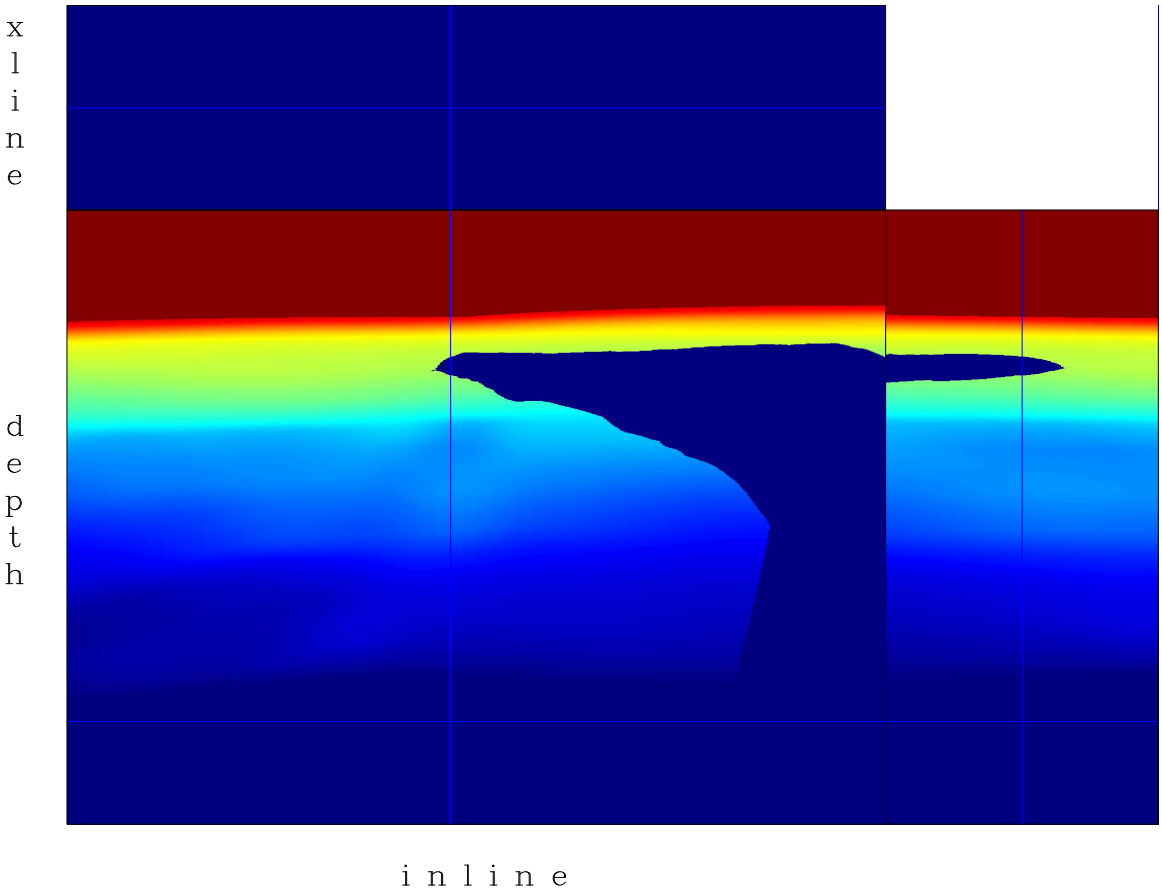


Figure 6.22: 3D Gulf of Mexico example. Initial slowness model. Compare with Figure 6.32. example-BP3d.sini [CR]

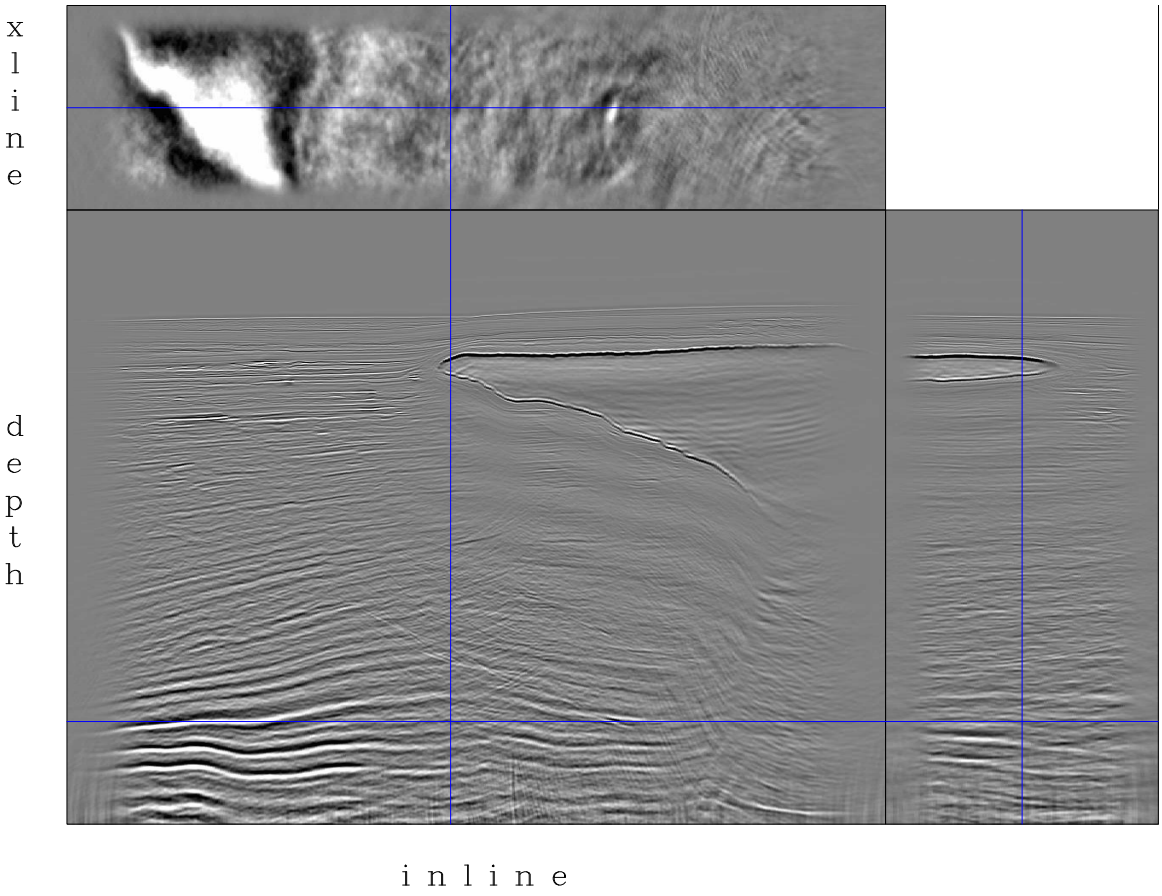


Figure 6.23: 3D Gulf of Mexico example. Initial image. Compare with Figure 6.33. example-BP3d.pini [CR]

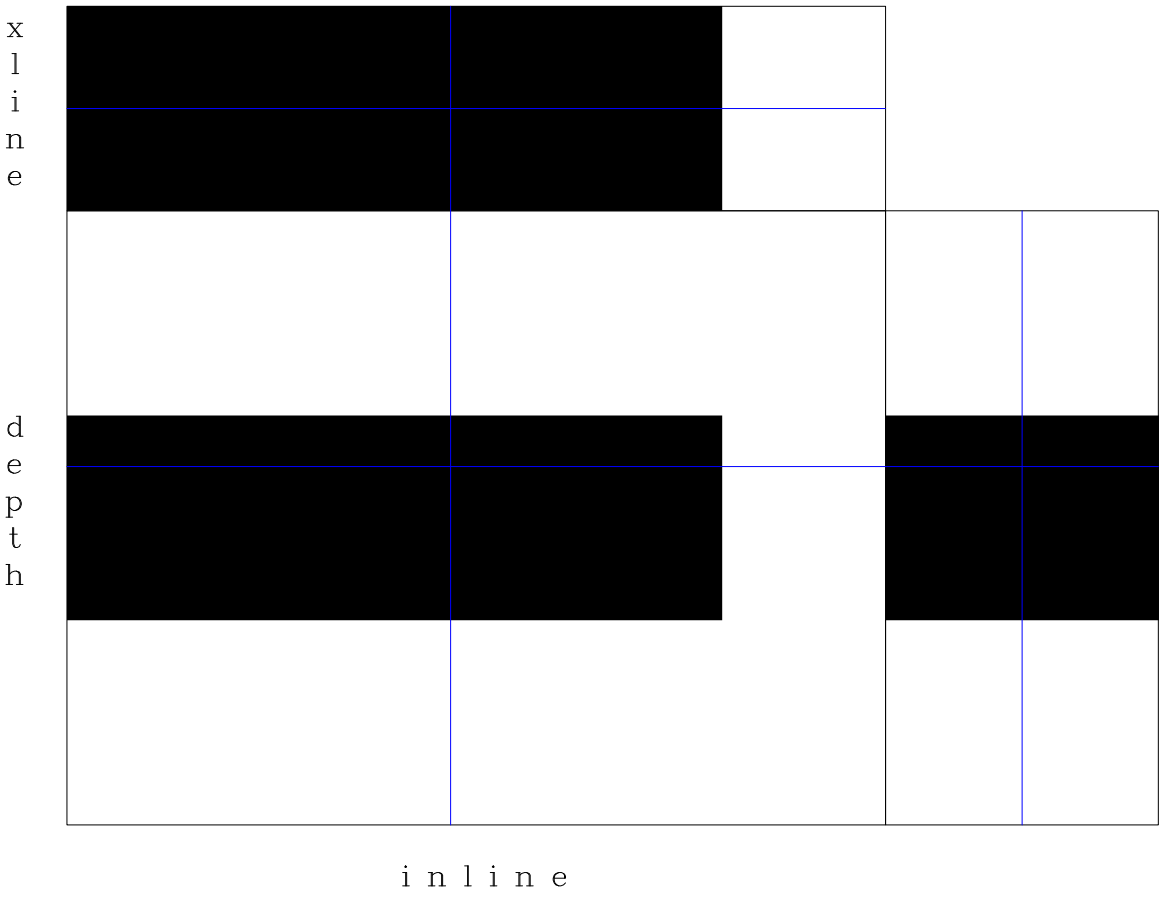


Figure 6.24: 3D Gulf of Mexico example. Box selected for WEMVA. example-BP3d.mask [CR]

weight quantifying the reliability of the picks in Figure 6.25. The brighter colors indicate higher reliability than the darker ones. The subsalt picks are less reliable than those in the sedimentary region away from the salt.

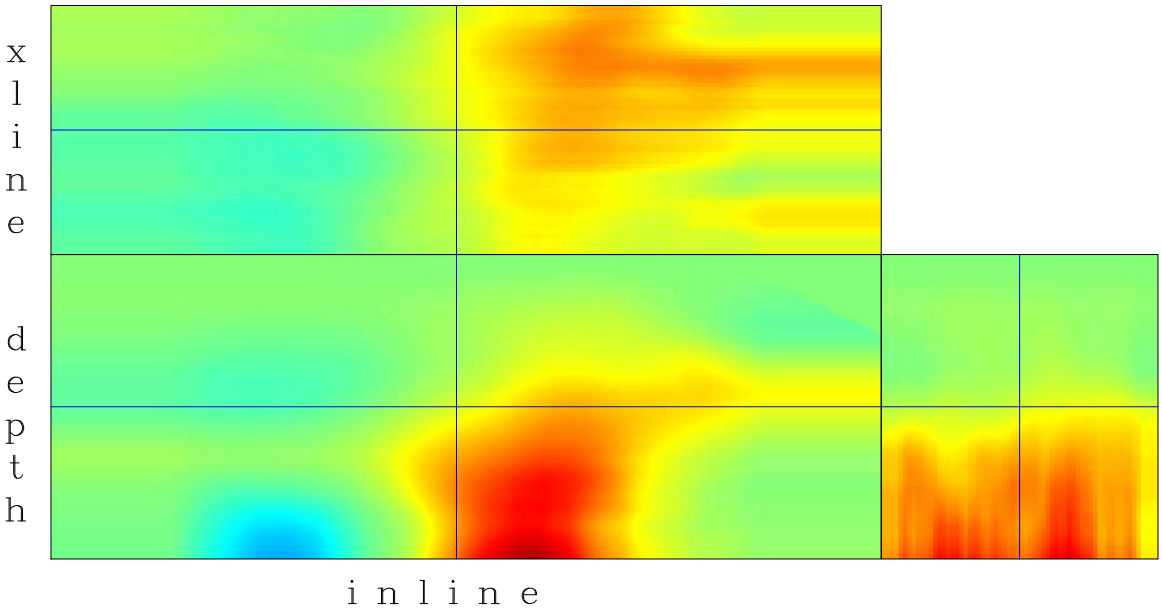


Figure 6.25: 3D Gulf of Mexico example. Velocity ratio perturbation picked after residual migration. example-BP3d.dro [CR]

Based on the background image in Figure 6.23 and the picks in Figure 6.25, I construct the image perturbation in Figure 6.27. As indicated earlier, this image perturbation corresponds to normal incidence, although it incorporates moveout/focusing information extracted from prestack residual migration. After 25 linear iterations of WEMVA, I obtain the slowness perturbation in Figure 6.28. I use preconditioned regularized inversion (Claerbout, 1999), where for regularization I use an isotropic Laplacian operator.

Figure 6.29 shows the data residual at a fixed crossline, function of iterations. The number associated with each panel indicates the iteration number. We can observe that the data residual is decreasing in absolute magnitude and that it becomes less structured function of iterations. The plot in the lower-right panel shows the absolute magnitude of the data residual monotonically decaying function of iterations, indicating that the conjugate gradient procedure is converging.

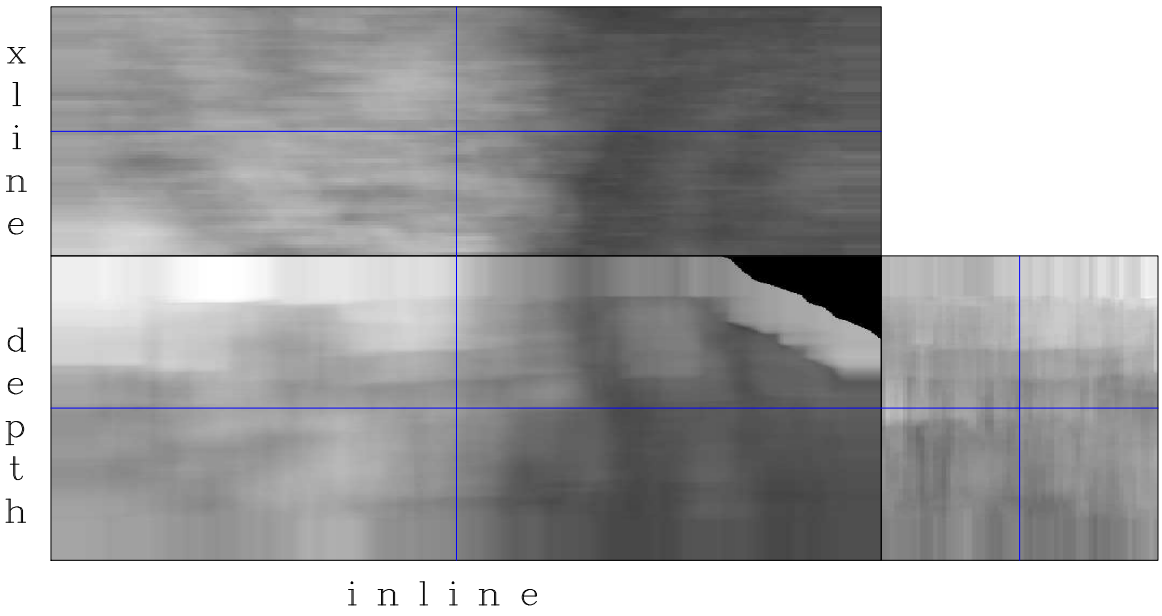


Figure 6.26: 3D Gulf of Mexico example. Data residual weight. example-BP3d.www [CR]

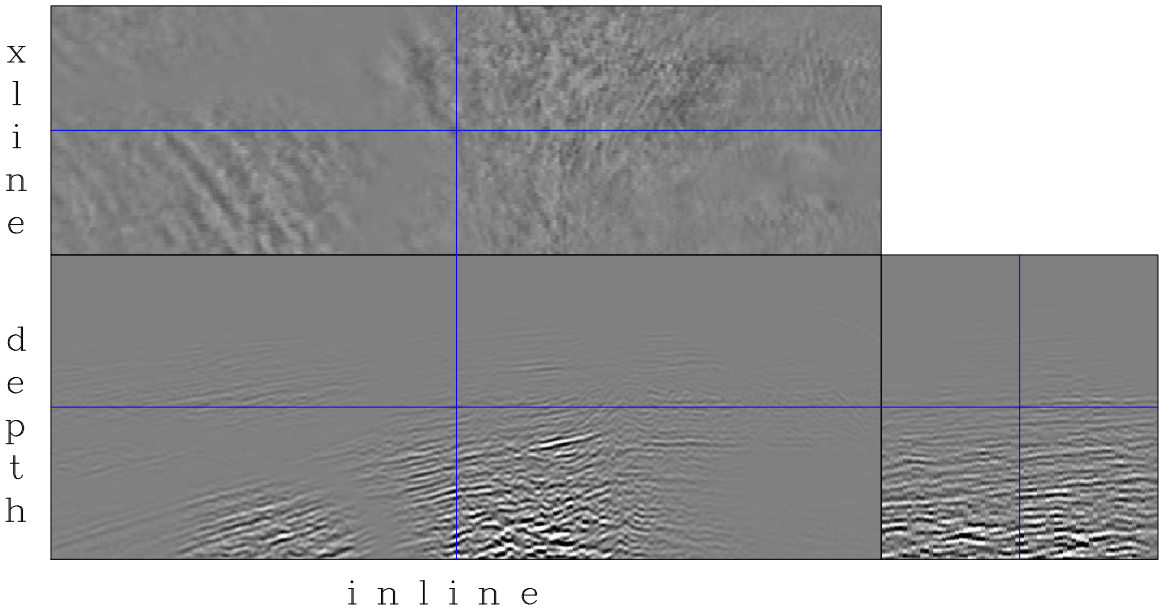


Figure 6.27: 3D Gulf of Mexico example. Image perturbation. example-BP3d.dia [CR]

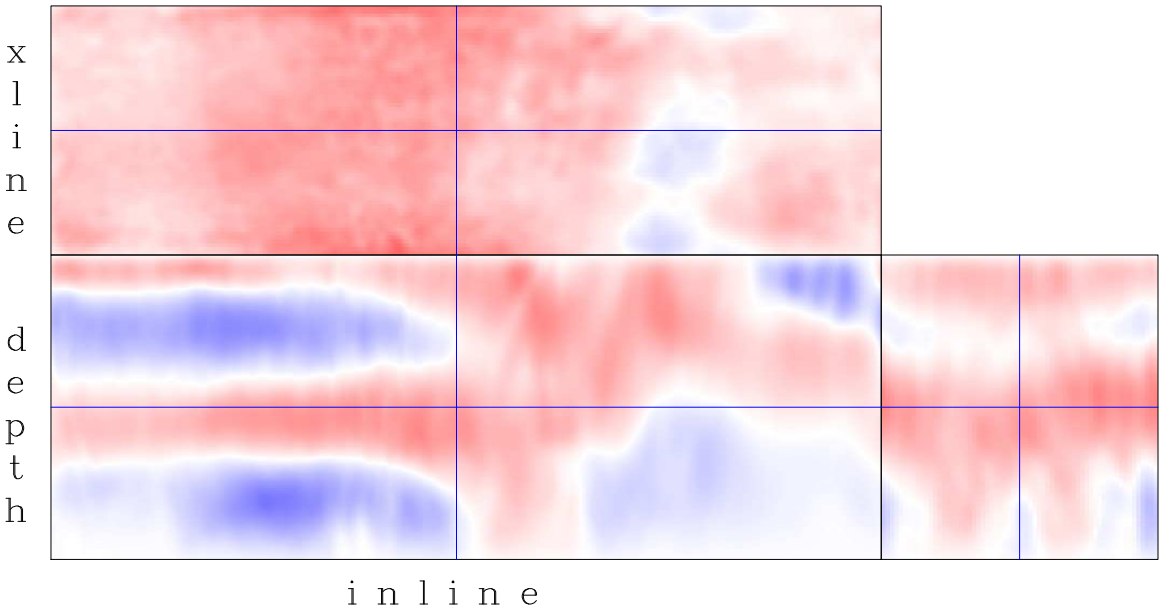


Figure 6.28: 3D Gulf of Mexico example. Slowness perturbation. example-BP3d.isx [CR]

Next, I update the background slowness model by adding a smooth version of the computed perturbation to the background velocity. Figure 6.30 shows the initial slowness inside the box used for WEMVA. For comparison, Figure 6.31 shows the updates slowness model in the same region. The most obvious observation we can make is that the anomalies associated with the shadow zones corresponding to the salt body are reduced, although the general trends of the slowness model remain the same. This is not a surprise, since the starting model is already a good model which does not need much updating.

Figure 6.32 shows the slowness obtained by embedding the slowness from the inversion box in the initial slowness. This process is not ideal, since it may create velocity discontinuities that need to be smoothed-out. The model in Figure 6.32 needed such smoothing under salt, close to the vertical salt pillar. Figure 6.33 shows the updated image obtained by migration with the slowness in Figure 6.32.

Finally, Figures 6.34 to 6.37 show two inlines and two crosslines taken from the prestack image obtained by migration of the 3D prestack data with the initial and updated slowness model. From top to bottom, the panels correspond to the migrated image, a few angle gathers

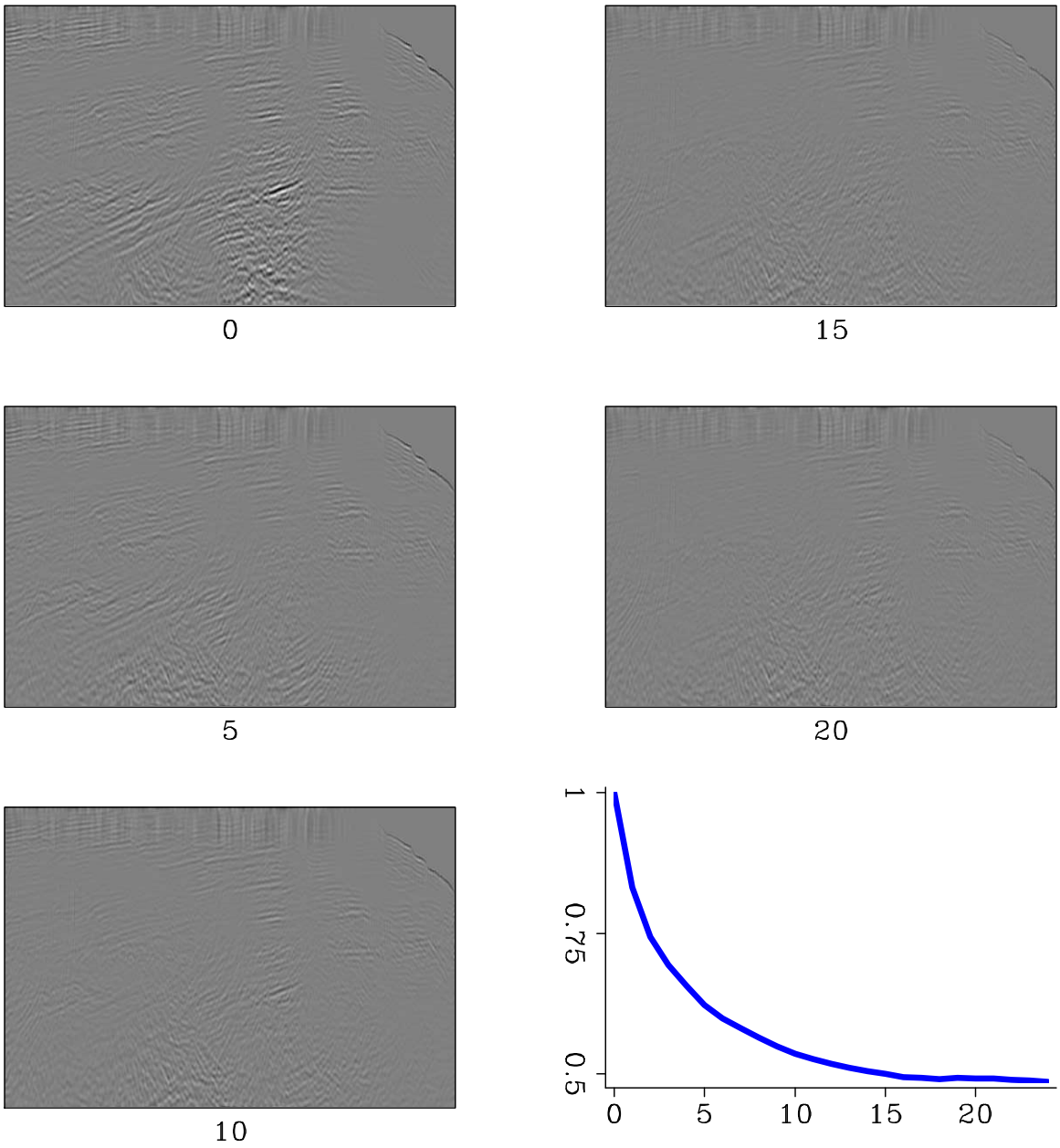


Figure 6.29: 3D Gulf of Mexico example. Data residual function of iterations. example-BP3d.datres [CR]

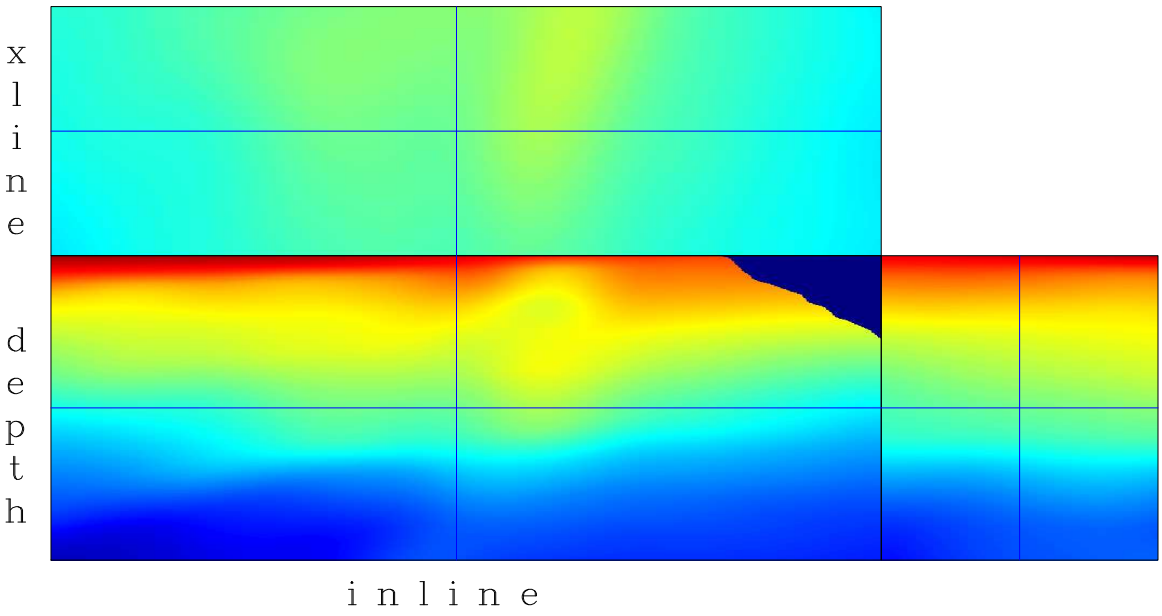


Figure 6.30: 3D Gulf of Mexico example. Initial slowness model in the inversion box. Compare with Figure 6.31. example-BP3d.wso [CR]

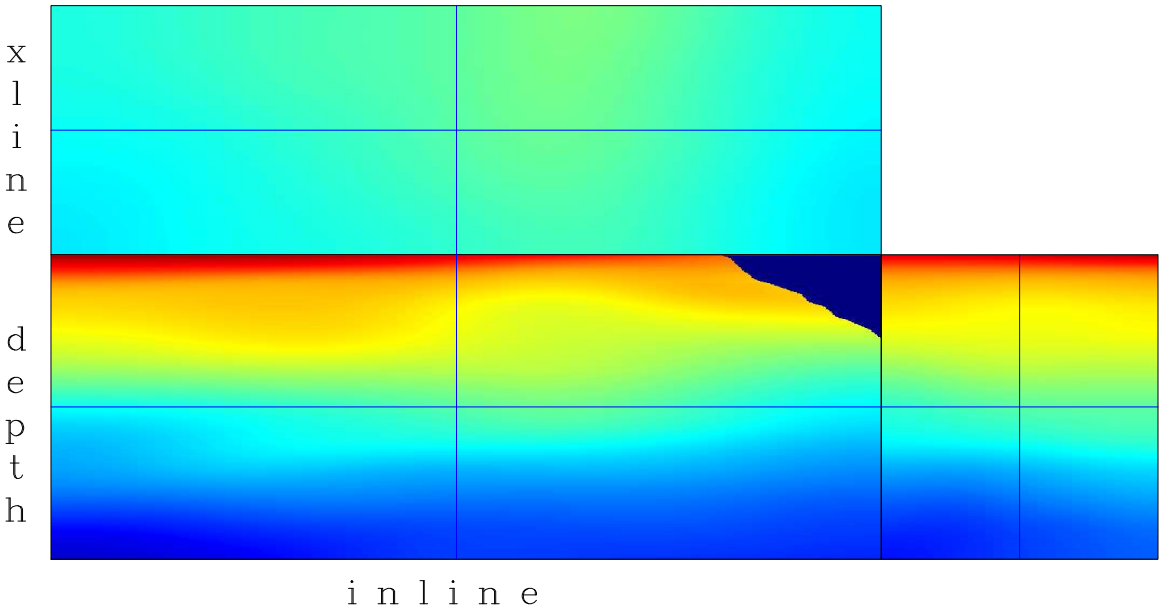


Figure 6.31: 3D Gulf of Mexico example. Updated slowness model in the inversion box. Compare with Figure 6.30. example-BP3d.wsz [CR]

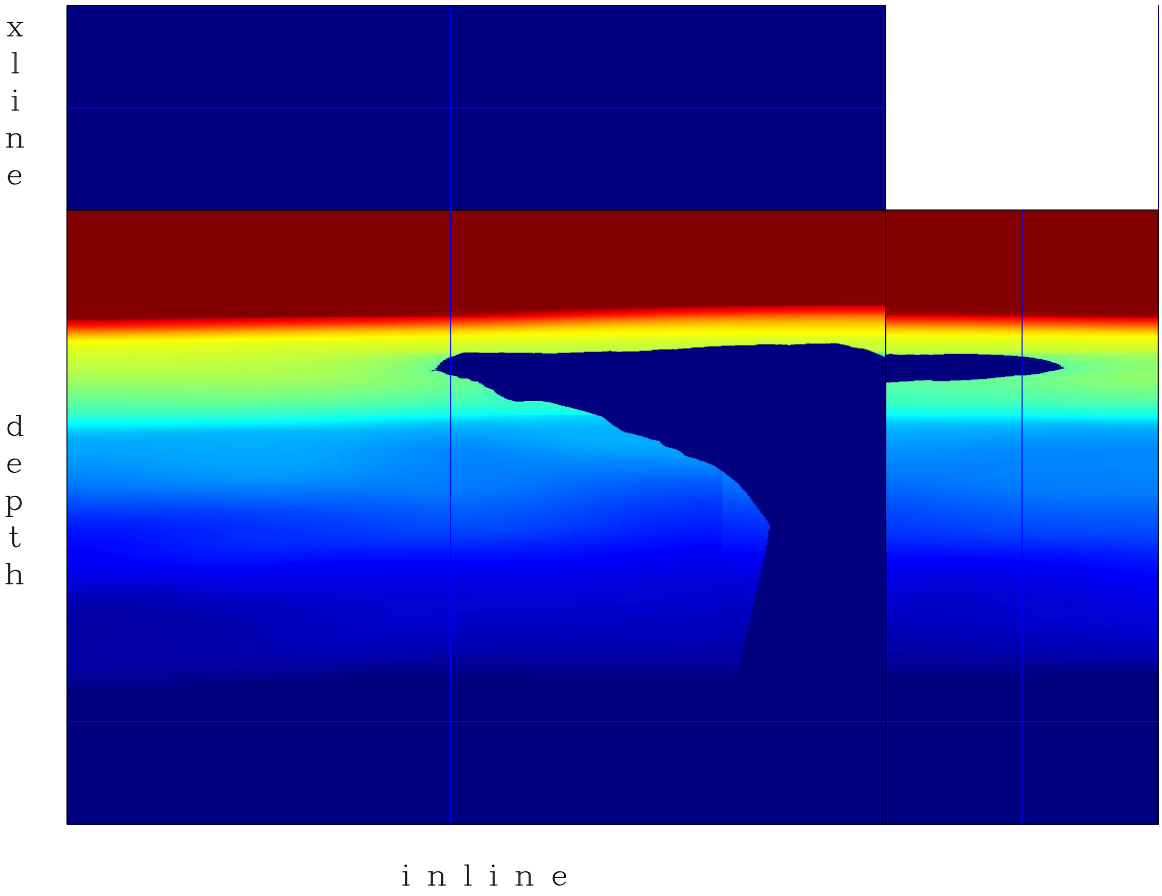


Figure 6.32: 3D Gulf of Mexico example. Updated slowness model. Compare with Figure 6.22. example-BP3d.smix2 [CR]

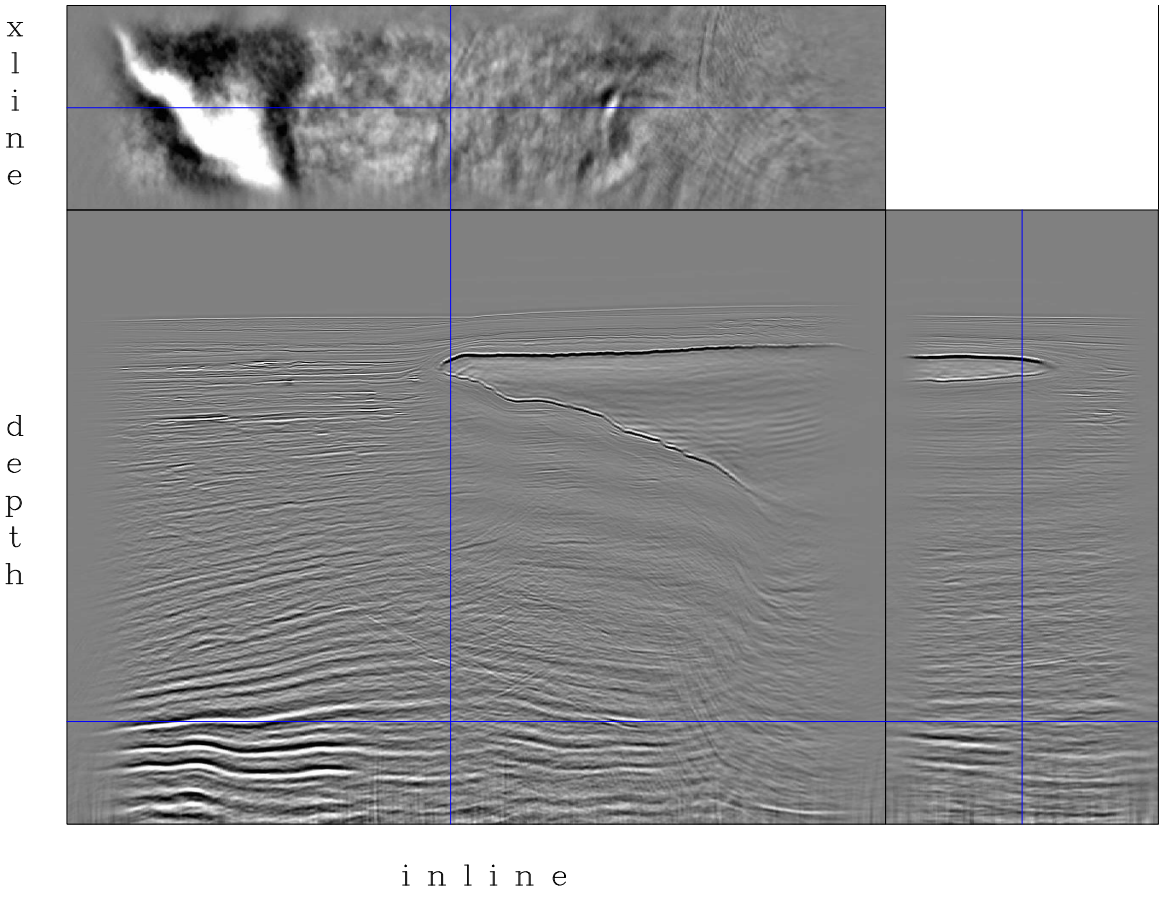


Figure 6.33: 3D Gulf of Mexico example. Updated image. Compare with Figure 6.23. example-BP3d.pmix2 [CR]

taken at equally spaced locations, and the semblance map computed on the angle gathers around the horizontal direction.

Since the initial and the updated velocity models are close to one-another, there are no large changes in the image. Most of the changes are marginal, and cannot be properly displayed without "before-after" movies. Slight increases in semblance are visible, mostly under the salt indicating better velocity and flatter gathers. Of course, since the starting model is very close to the correct one, not everything in the image improves. There are portions where the semblance actually decreases. However, the overall image quality measured by semblance increases slightly.

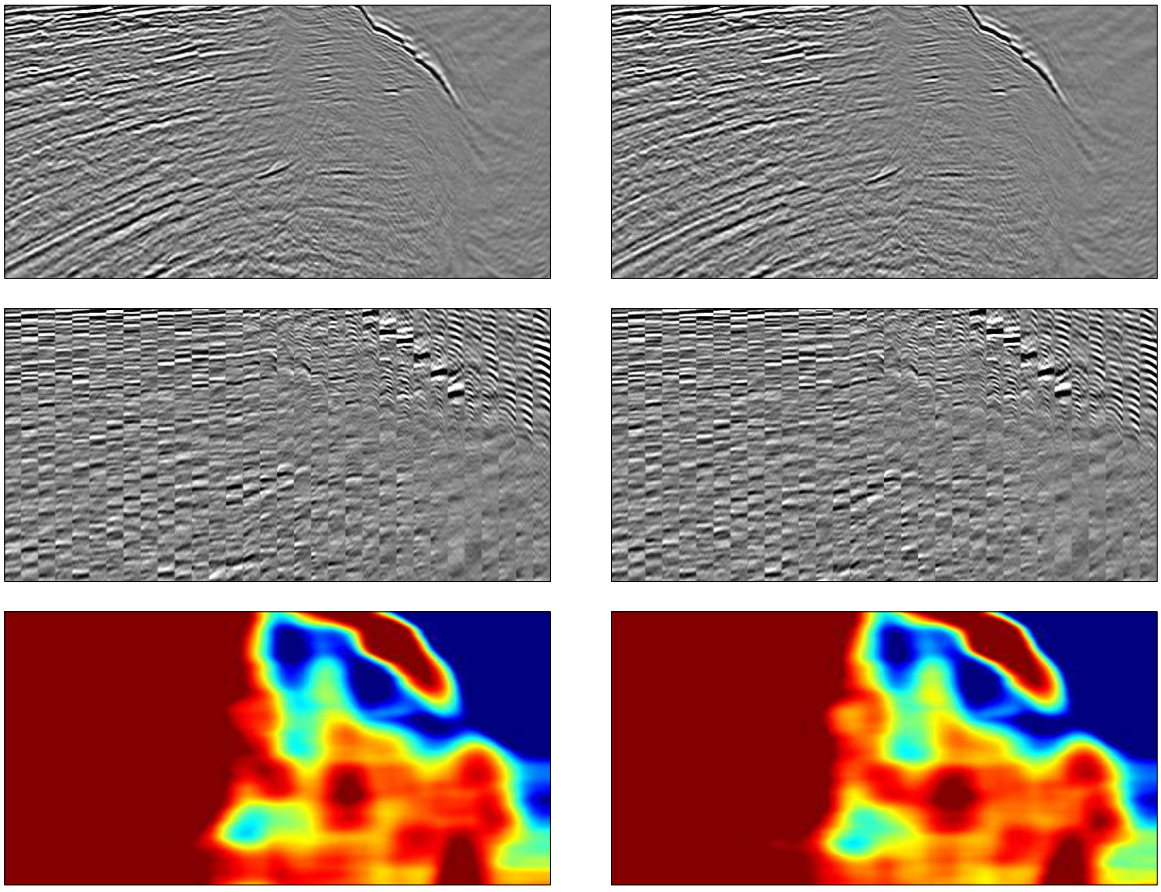


Figure 6.34: 3D Gulf of Mexico example. Inline comparison of initial (left) and final (right) models. Image stack (top), angle gathers (middle) and image semblance (bottom). example-BP3Di.70700 [CR,M]

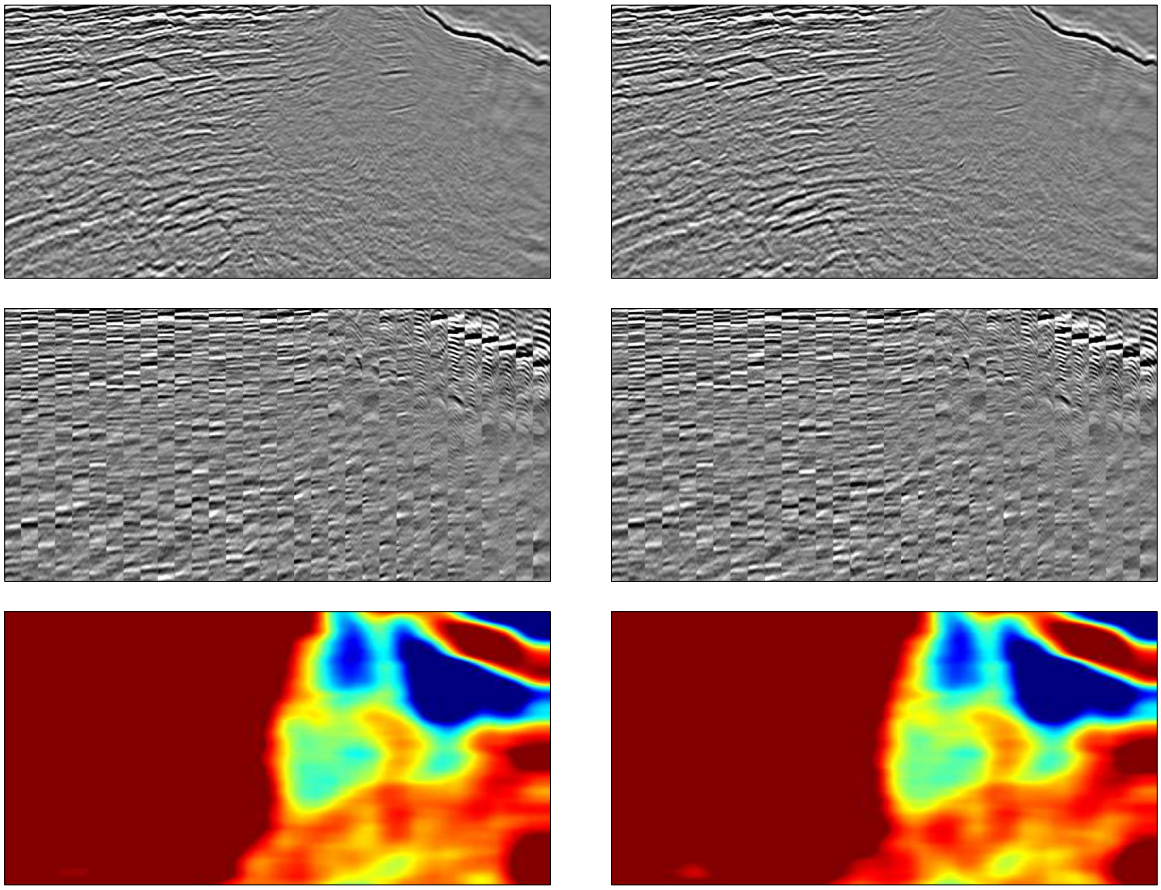


Figure 6.35: 3D Gulf of Mexico example. Inline comparison of initial (left) and final (right) models. Image stack (top), angle gathers (middle) and image semblance (bottom). example-BP3Di.77426 [CR,M]

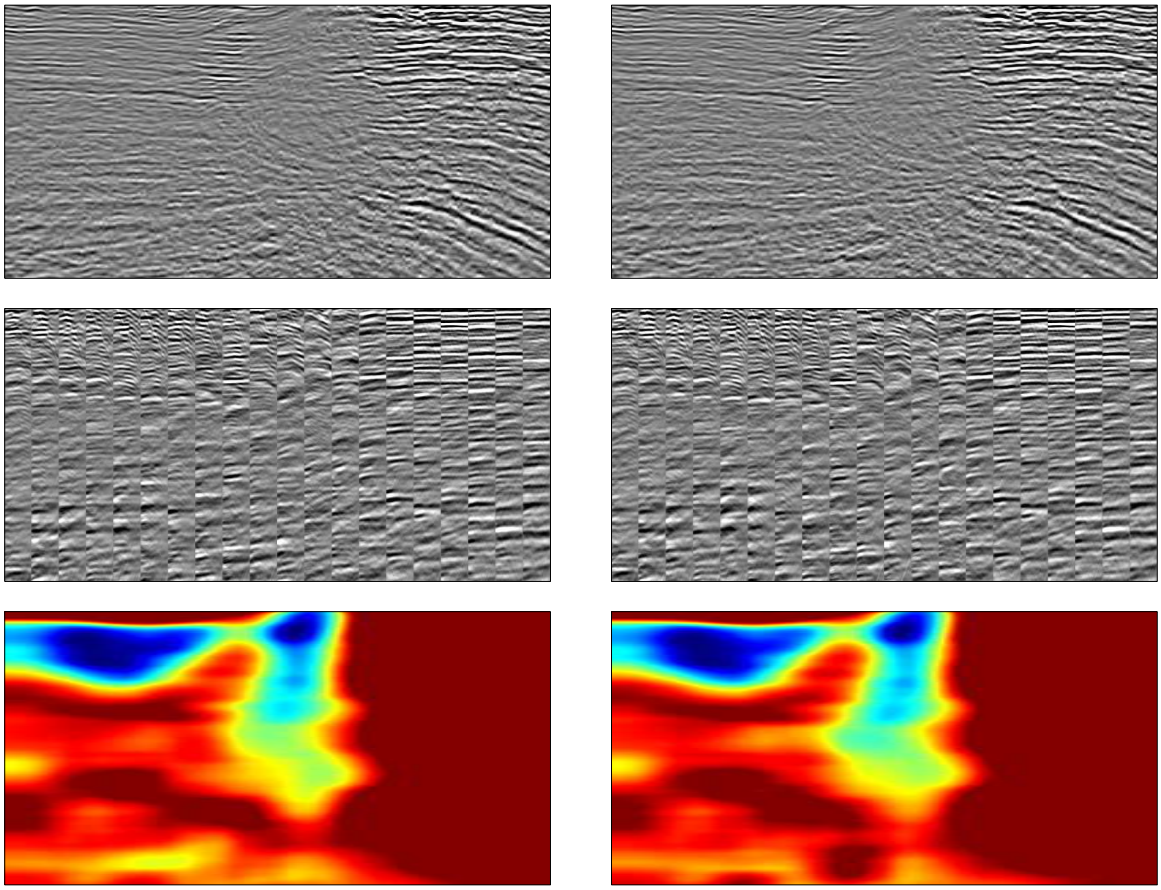


Figure 6.36: 3D Gulf of Mexico example. Crossline comparison of initial (left) and final (right) models. Image stack (top), angle gathers (middle) and image semblance (bottom). example-BP3Dx.74000 [CR,M]

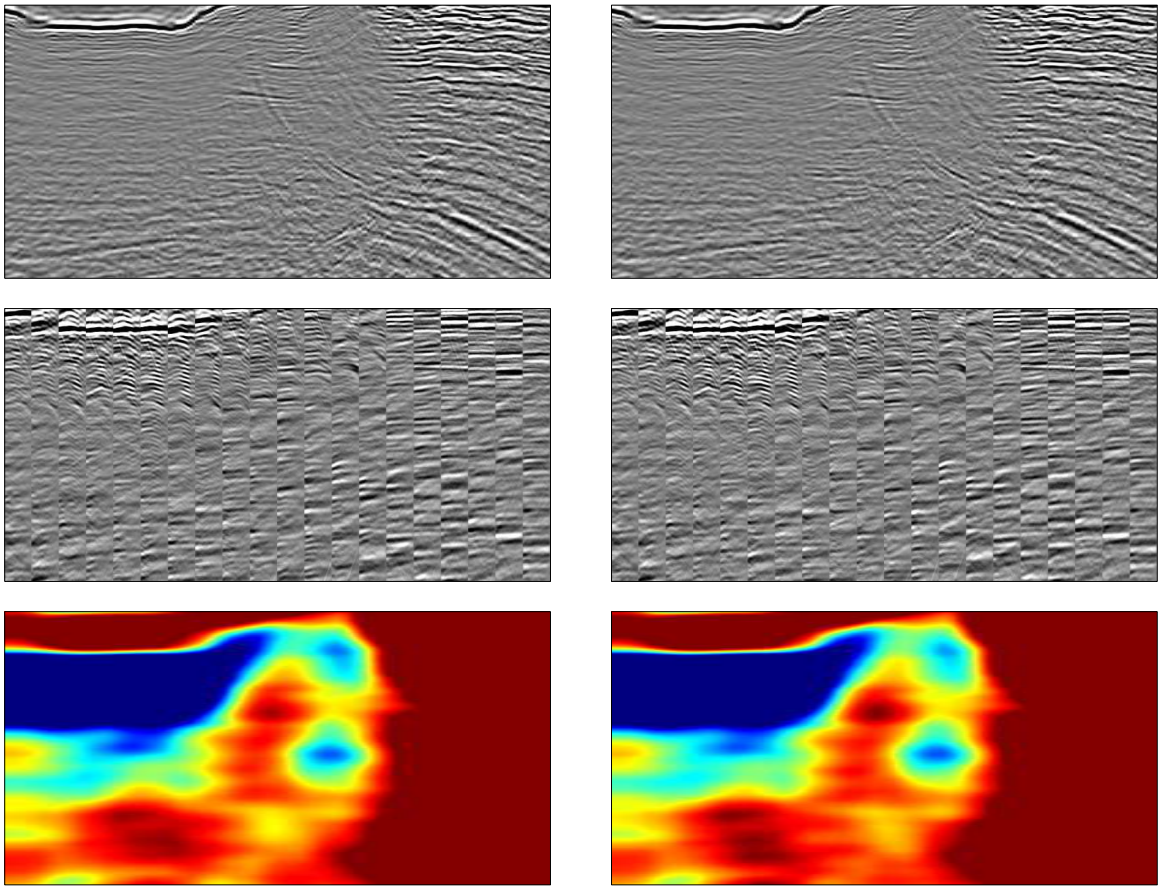


Figure 6.37: 3D Gulf of Mexico example. Crossline comparison of initial (left) and final (right) models. Image stack (top), angle gathers (middle) and image semblance (bottom). example-BP3Dx.77000 [CR,M]

6.3 Diffraction-focusing WEMVA example

Migration velocity analysis (MVA) using diffracted events is not a new concept. Harlan (1986) addresses this problem and proposes methods to isolate diffraction events around faults, quantifies focusing using statistical tools, and introduces MVA techniques applicable to simple geology, e.g. constant velocity or $v(z)$. Similarly, de Vries and Berkhout (1984) use the concept of minimum entropy to evaluate diffraction focusing and apply this methodology to MVA, again for the case of simple geology. Soellner and Yang (2002) use focusing of diffractions simulated using data-derived parameters to estimate interval velocities.

In Chapter 5, I introduce a method of migration velocity analysis using wave-equation techniques (WEMVA), which aims to improve the quality of migrated images, mainly by correcting moveout inaccuracies of specular energy. WEMVA finds a slowness perturbation which corresponds to an image perturbation, that is similar to ray-based migration tomography (Al-Yahya, 1989; Stork, 1992; Etgen, 1993), where the slowness perturbation is derived from depth errors, and to wave-equation inversion (Tarantola, 1986) or tomography (Woodward, 1992; Pratt, 1999; Dahlen et al., 2000) where the slowness perturbation is derived from measured wavefield perturbations.

The moveout information given by the specular energy is not the only information contained by an image migrated with the incorrect slowness. Non-specular diffracted energy is present in the image and clearly indicates slowness inaccuracies. Traveltime-based MVA methods cannot easily deal with the diffraction energy, and are mostly concerned with moveout analysis. In contrast, a difference between an inaccurate image and a perfectly focused target image contains both specular and non-specular energy; therefore WEMVA is naturally able to derive velocity updates based on both these types of information.

In this section, I use WEMVA to estimate slowness updates based on focusing of diffracted energy using residual migration. One possible application of this technique in seismic imaging concerns areas with abundant, clearly identifiable diffractions. Examples include highly fractured reservoirs, carbonate reservoirs, rough salt bodies and reservoirs with complicated stratigraphic features. Another application is related to imaging of zero-offset Ground-Penetrating Radar (GPR) data, where moveout analysis is simply not an option.

Of particular interest is the case of salt bodies. Diffractions can help estimate more accurate velocities at the top of the salt, particularly in the cases of rough salt bodies. Moreover, diffraction energy may be the most sensitive velocity information we have from under the salt, since most of the reflected energy we record at the surface has only a narrow range of angles of incidence at the reflector, rendering the analysis of moveout ambiguous. The first example concerns a synthetic dataset obtained by acoustic finite-difference modeling over a salt body. Although in this example I use the WEMVA technique to constrain the top of the salt, I emphasize that we can use the same technique in any situation where diffractions are available. For example, in sub-salt regions where angular coverage is small, uncollapsed diffractions carry substantial information which is disregarded in typical MVA methodologies.

The second example is a real dataset of single-channel, Ground-Penetrating Radar (GPR) data. Many GPR datasets are single-channel and no method has thus far been developed to estimate a reasonable interval velocity models in the presence of lateral velocity variations. Typically, the velocity estimated by Dix inversion at sparse locations along the survey line is smoothly extrapolated, although this is not optimal from an imaging point of view.

6.3.1 Delineation of rough salt bodies

Figure 6.38 shows the zero-offset data we use for velocity analysis to delineate the top of the rough salt body. The section contains a large number of diffractors, whose focusing allows us to constrain the overburden velocity model.

Figure 6.39(a) depicts the starting velocity model, and Figure 6.39(b) depicts the initial image obtained by zero-offset migration. The starting velocity is a typical Gulf of Mexico $v(z)$ function hanging from the water bottom. Uncollapsed diffractions are visible at the top of the salt, indicating that the velocity in the overburden is not accurate. Such defocusing also hampers our ability to pick accurately the top of the salt and, therefore, degrades imaging at depth.

As for the preceding synthetic example, I run residual migration on the background image (Figure 6.39). Figure 6.40 shows this image after residual migration with various velocity

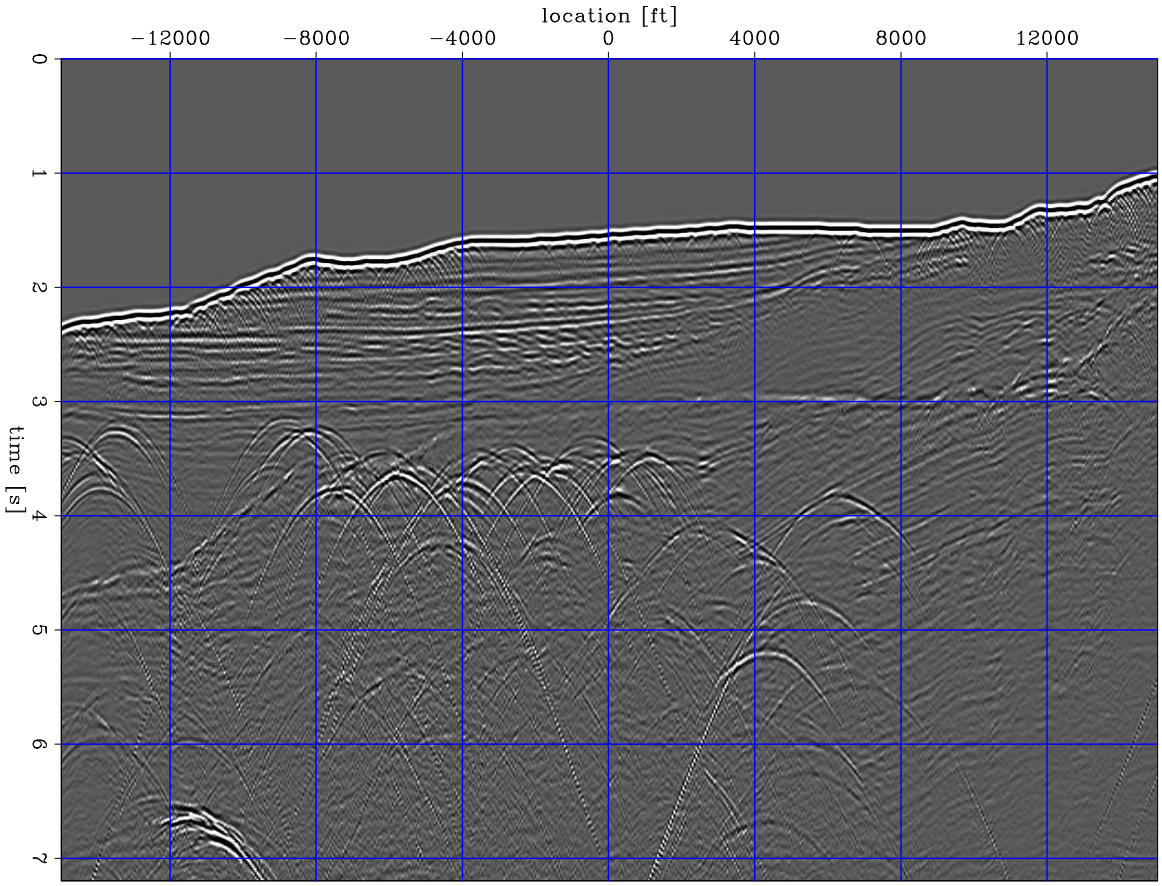


Figure 6.38: Zero-offset synthetic data used for focusing migration velocity analysis. example-BPAITdat [CR]

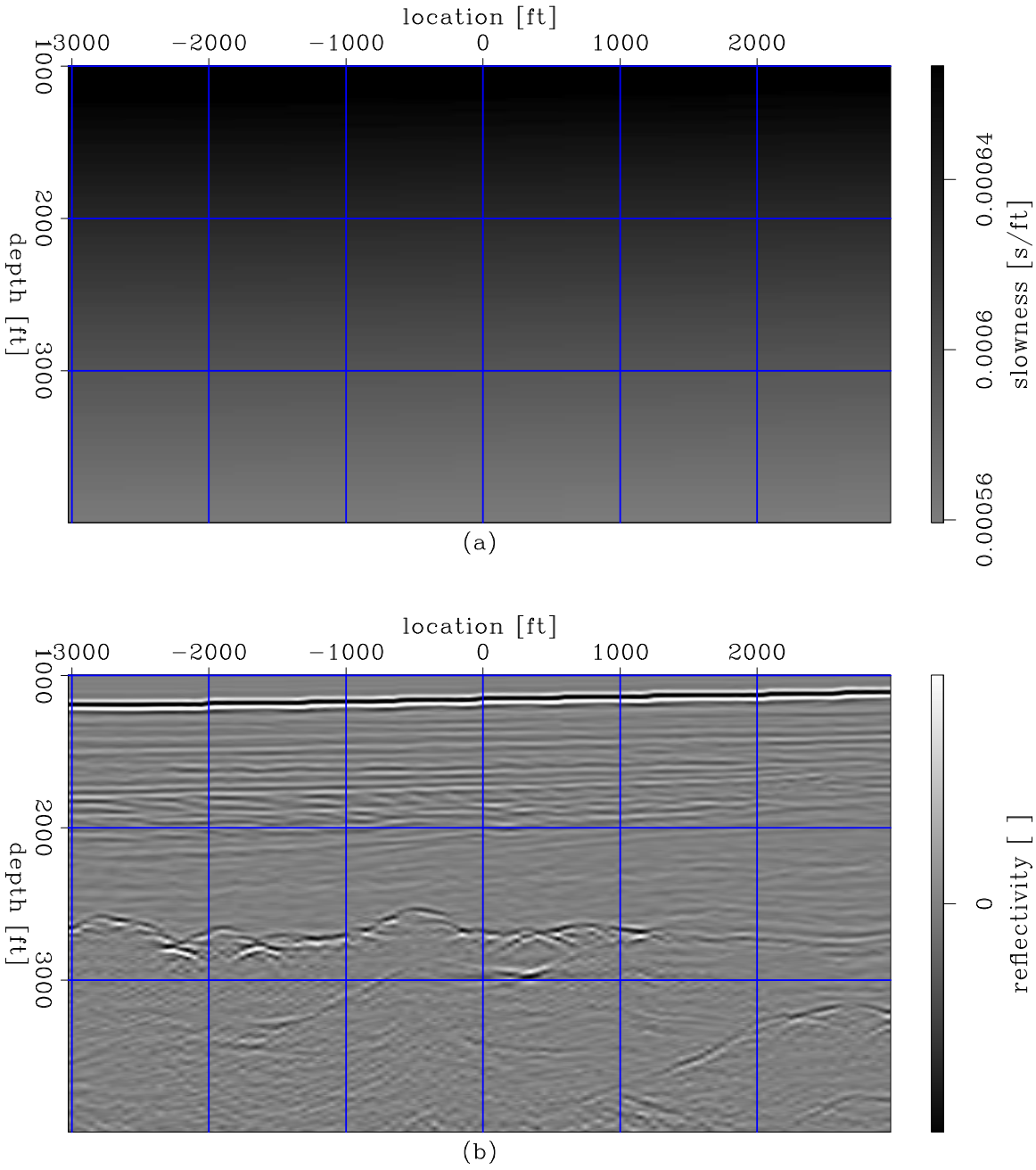


Figure 6.39: Zero-offset migrated image for the synthetic data in figure 6.38: velocity model (a), and migrated image (b). Migration using the initial $v(z)$ velocity model. example-BPAITimg1 [CR,M]

ratios (Chapter 4). From top to bottom, the ratios are: $1.04, 1.00, 0.96, 0.92, 0.88$. At $\rho = 1.00$ we recover the initial image. Different parts of the image come into focus at different values of the velocity ratio.

Figure 6.41(a) shows the picked velocity ratios at various locations in the image. The white background corresponds to picked $\Delta\rho = 0$, and the gray shades correspond to $\Delta\rho$ between 0 and 0.08. Figure 6.41(b) shows a map of the weights ($\mathbf{W}$) associated to each picked value. The white background corresponds to $\mathbf{W} = 0$, indicating low confidence in the picked values, and the dark regions correspond to $\mathbf{W} = 1$, indicating high confidence in the picked values. In this example, we disregard regions where we did not pick any diffractions. All other regions receive an arbitrary ratio value ($\rho = 1.0$), but also a low weight such that they do not contribute to the inversion. Exceptions include the water bottom, for which we assign a high weight of the picked ratio $\rho = 1.0$, and a few other reflectors for which we did not have any diffraction focusing information.

Figure 6.42(a) shows the slowness perturbation obtained after 20 iterations of zero-offset inversion from the image perturbation in Figure 6.42(b). The image perturbation is non-zero only in the regions where we had diffractions we could pick, as indicated by Figure 6.41. The smooth slowness perturbation is further constrained by the regularization operator we use, which is a simple Laplacian penalizing the rough portions of the model.

Figure 6.43(a) shows the updated slowness model and Figure 6.43(b) shows the zero-offset migrated image corresponding to the updated model. Most of the diffractions at the top of the salt have been collapsed, and the rough top of the salt can be easily picked. The diffractions corresponding to the salt bodies at $x = 2000 - 4000$ ft, $z = 3500$ ft are not fully collapsed, indicating that another nonlinear iteration involving residual migration and picking might be necessary.

Finally, Figure 6.44 shows prestack migrated images using the initial velocity model (a) and the one updated using zero-offset focusing (b). The top panels depict stacks, and the bottom panels depict angle-domain common image gathers (Chapter 3). The ADCIGs show substantial bending after migration with the initial velocity, but they are mostly flat after migration with the updated velocity, although none of the moveout information has been used for

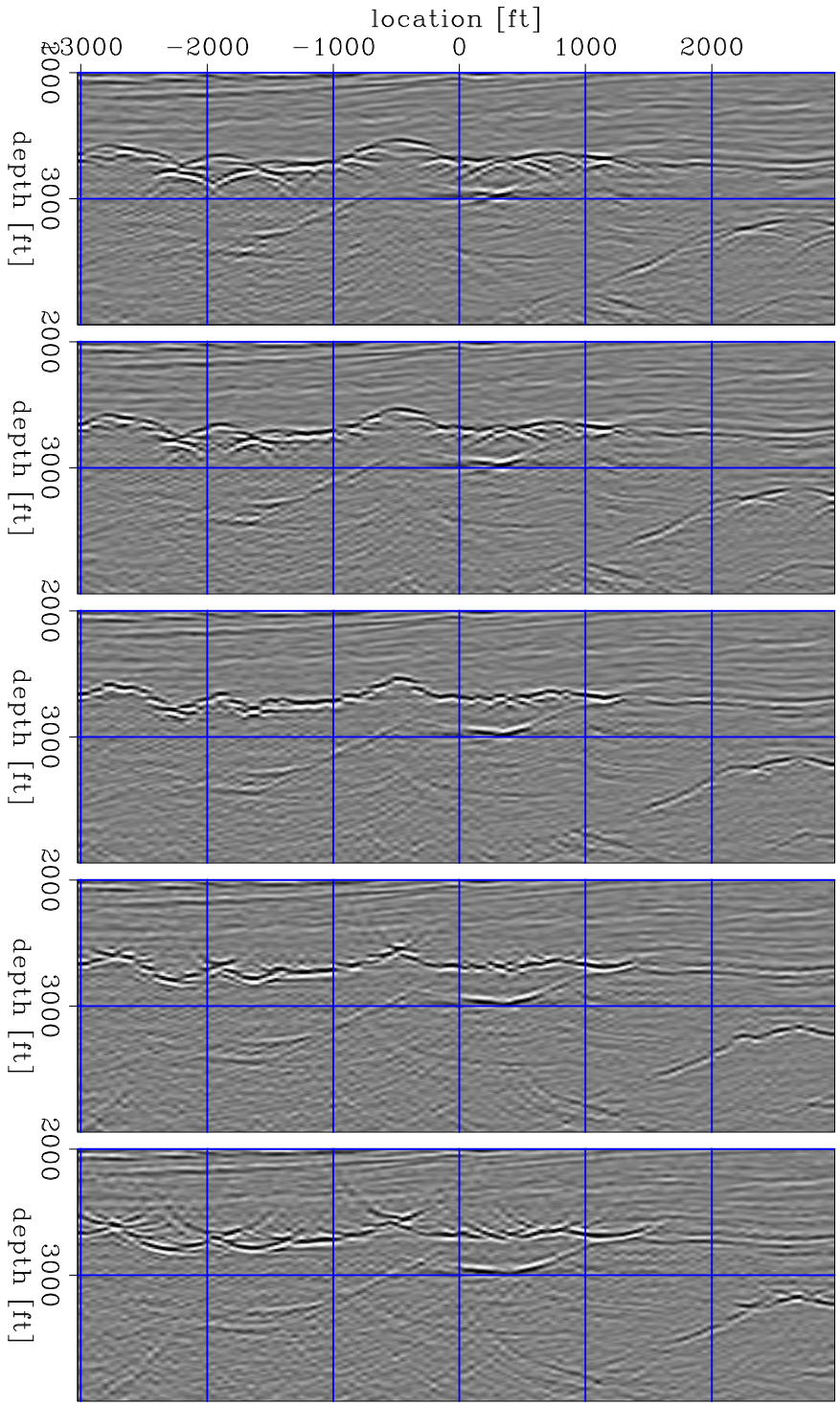


Figure 6.40: Residual migration applied to the image migrated with the initial velocity model, figure 6.39. From top to bottom, the images correspond to the ratios $\rho = 1.04, 1.00, 0.96, 0.92, 0.88$. example-BPAITsrm [CR,M]

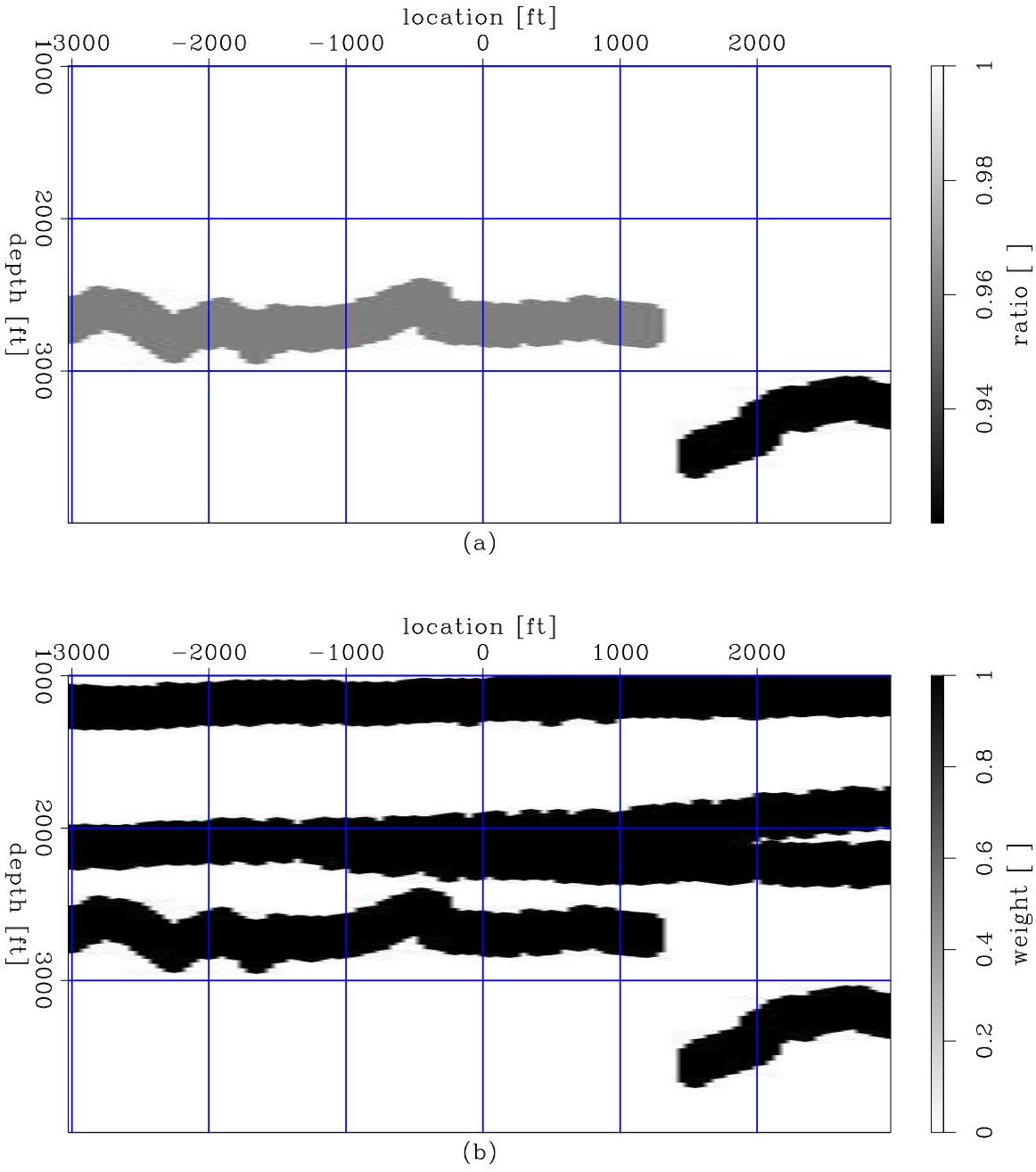


Figure 6.41: Residual migration picks (a) and the associated confidence weights (b). example-BPAITpck [CR,M]

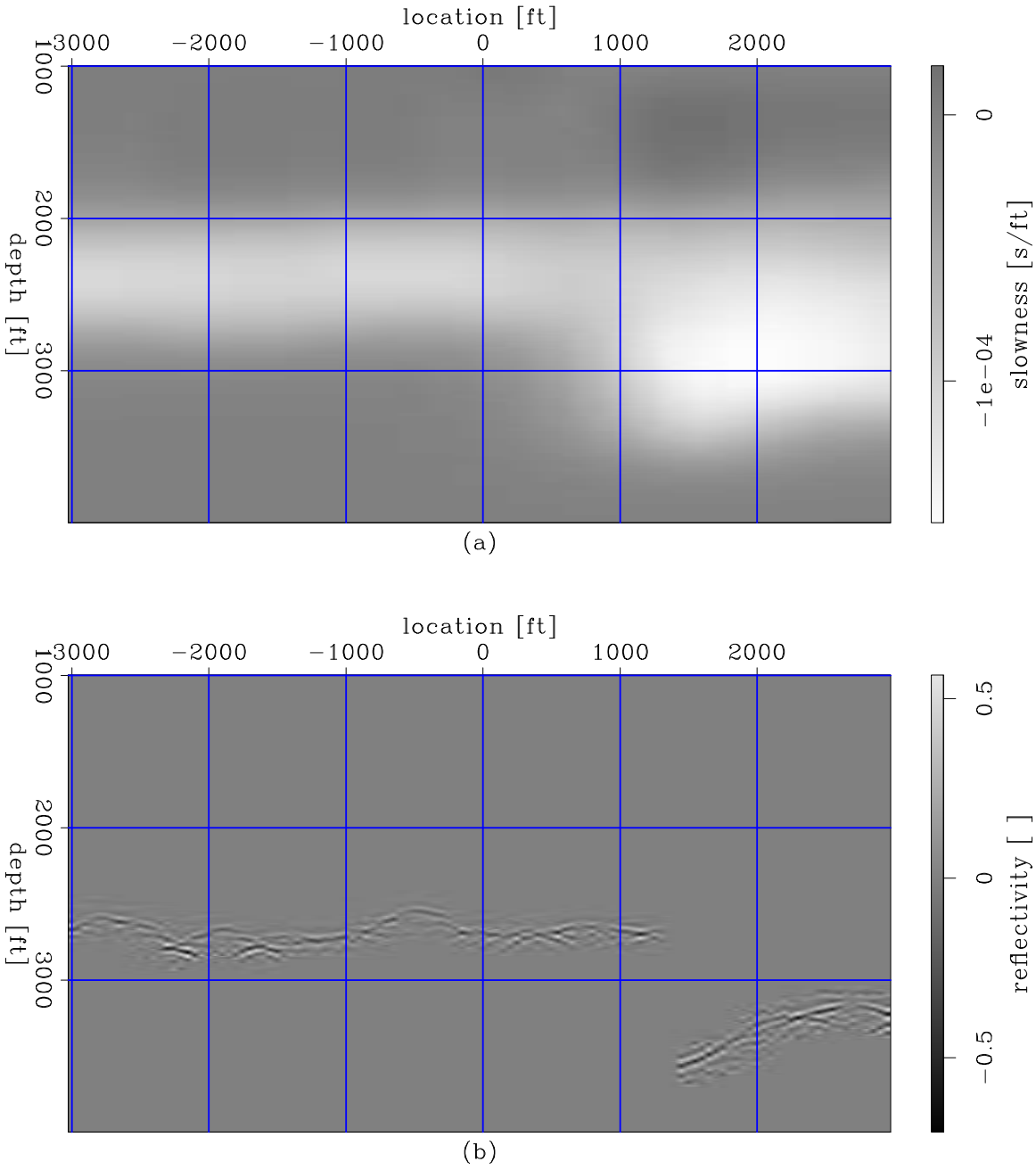


Figure 6.42: Slowness perturbation (a), derived from an image perturbation (b) derived from the background image in figure 6.39 and the velocity ratio picks in figure 6.41. example-BPAITmva [CR,M]

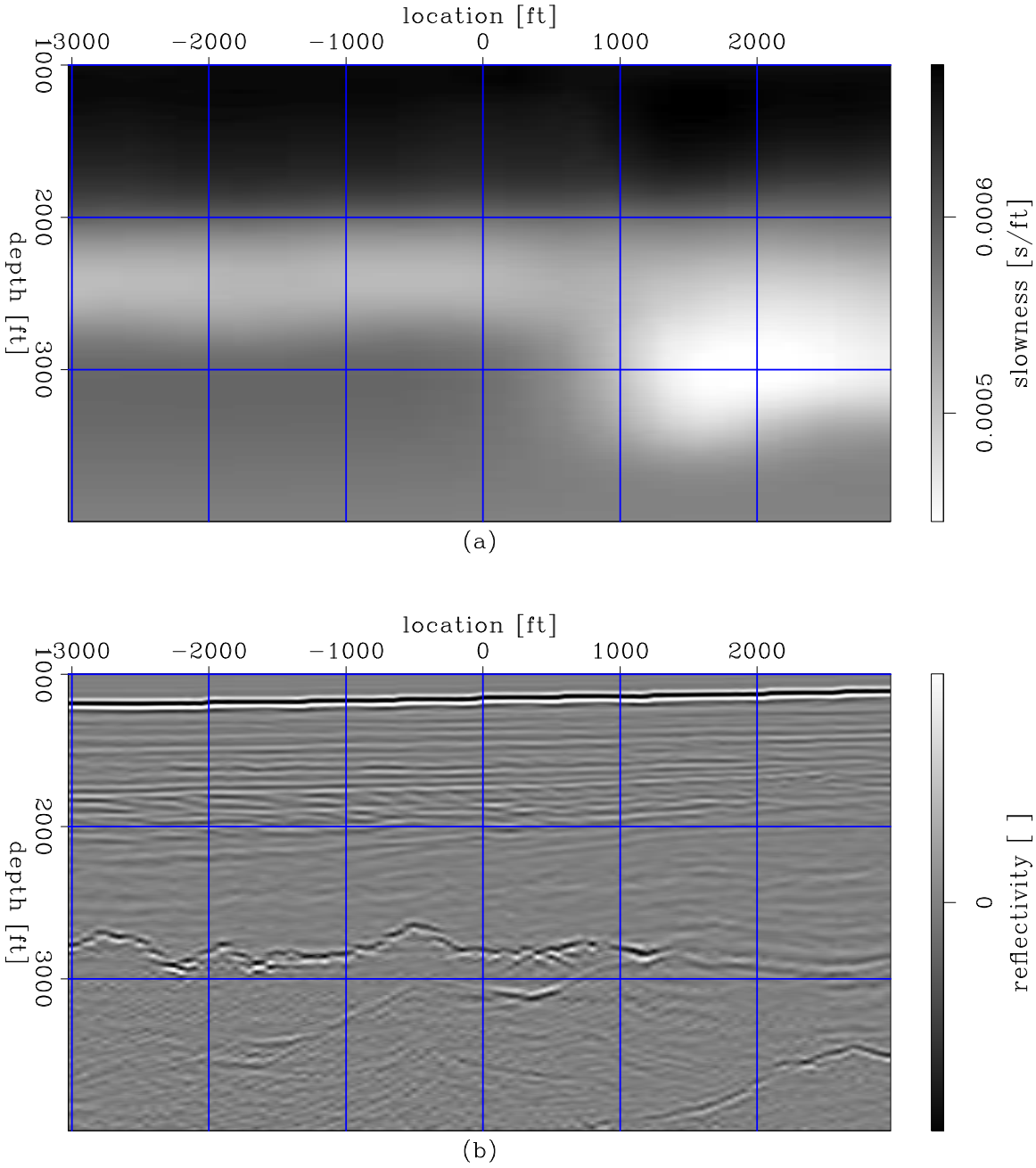


Figure 6.43: Zero-offset migrated image for the synthetic data in figure 6.38: velocity model (a), and migrated image (b). Migration using the updated velocity. example-BPAITimg2 [CR,M]

velocity update. Figure 6.45 shows two ADCIGs at $x = -2350$ ft from the images obtained with the initial velocity model (a) and the updated velocity model (b). The ADCIG in panel (a) corresponds to a notch in the top of the salt and is complicated to use for velocity analysis. However, after migration with the updated velocity model, panel (b), the ADCIG is much simpler, and the small residual moveouts can be picked for velocity updates.

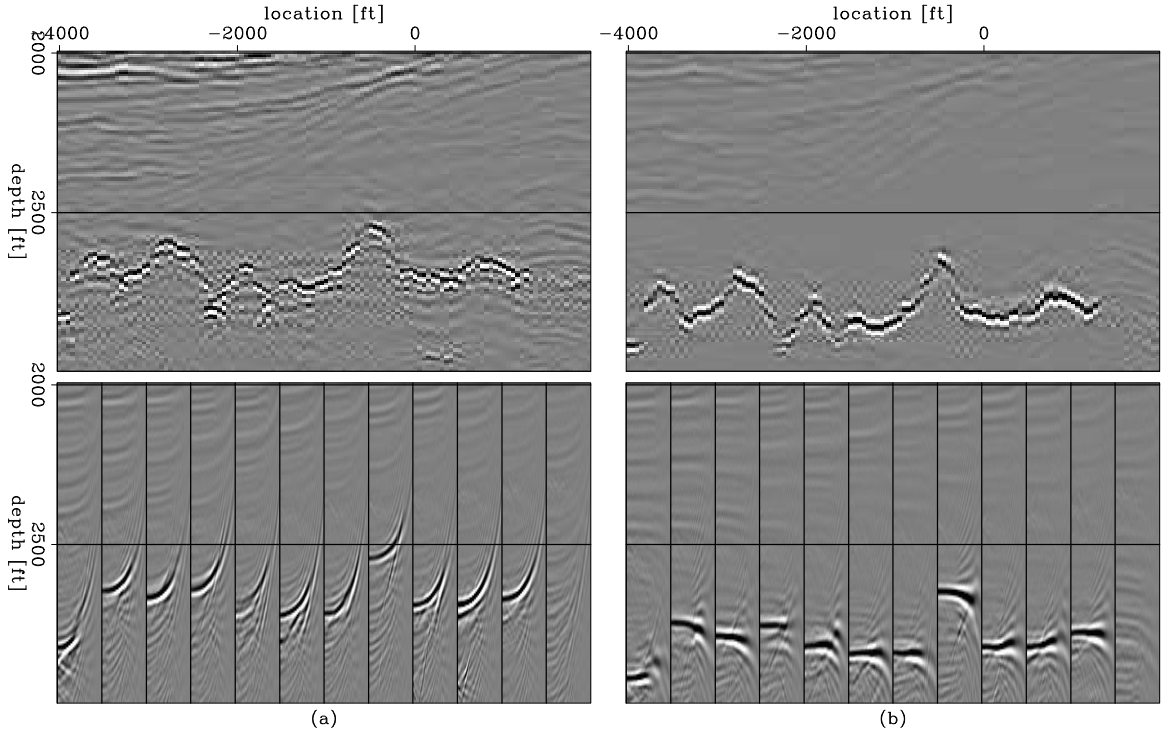


Figure 6.44: Prestack migrated images using the initial velocity model (a) and the updated velocity model (b). The top panels depict image stacks and the bottom panels depict angle-domain common image gathers. example-BPAITpre [CR]

A comparison of Figures 6.43(b) and 6.44(b) shows a potential limitation of this technique in the presence of prismatic waves (Biondi, 2004). Both images are obtained with the same velocity, the first one with zero-offset data and the second one with prestack data. The imaging artifacts visible at the bottom of the deep canyons at the top of the salt in Figure 6.43(b) are created by prismatic waves that are not properly imaged from zero-offset data. Prismatic waves are better (though not perfectly) handled by full prestack migration, and thus the artifacts are not visible in the prestack-migrated image shown in Figure 6.44(b). Since these artifacts

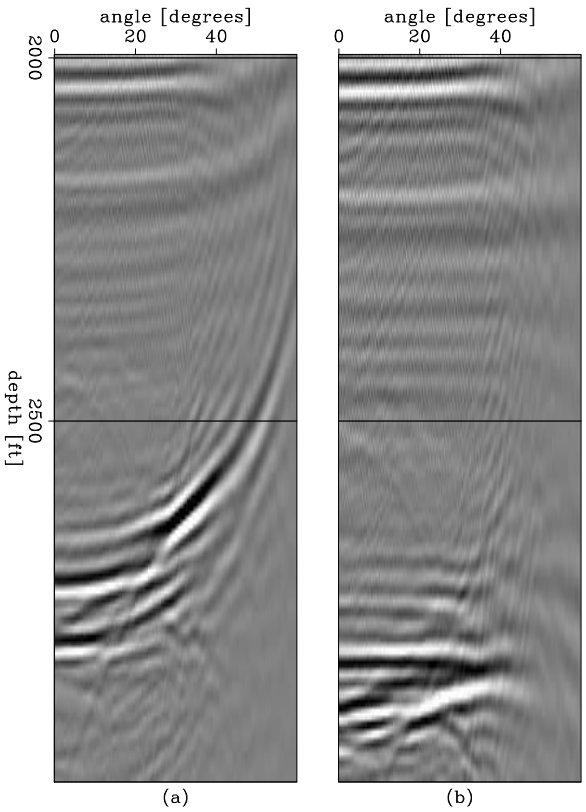


Figure 6.45: Angle-domain common image gather obtained after migration with the initial velocity model (a) and the updated velocity model (b). example-BPAITcig [CR]

resemble uncollapsed diffractions, they may mislead the analysis of the residual migrated images and be interpreted as symptoms of velocity inaccuracies.

6.3.2 Imaging of GPR data

The next example concerns a zero-offset GPR dataset over a lava flow region. In this situation, diffraction focusing is the only option available for migration velocity analysis. The data depicted in Figure 6.46 show many diffractions spread over the entire dataset. A few obvious ones are at $x = 22$ ft, $t = 27$ ns, at $x = 28$ ft, $t = 22$ ns, and at $x = 35$ ft, $t = 23$ ns.

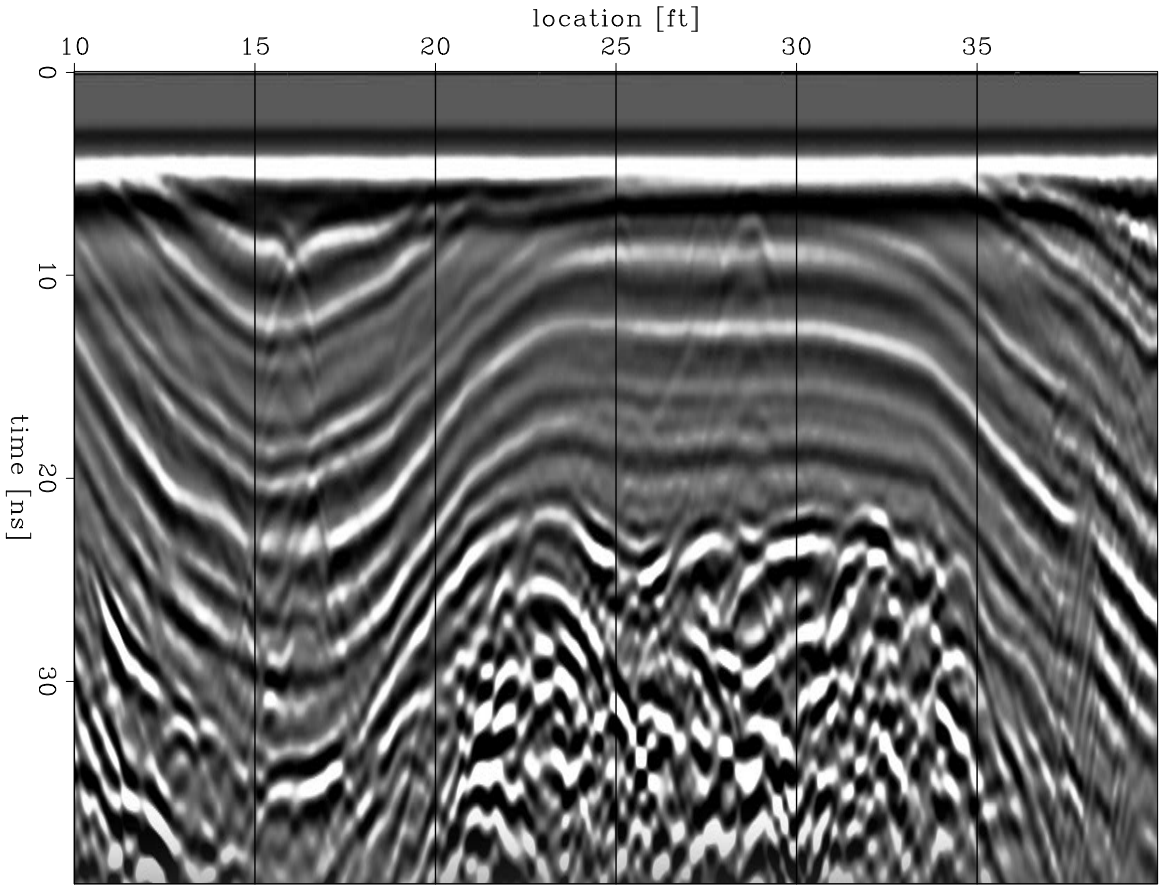


Figure 6.46: Zero-offset GPR data used for focusing migration velocity analysis. example-LAVAdata [CR]

I follow the same procedure for migration velocity analysis as the one described for the preceding example. Figure 6.47(a) shows the initial image obtained by migration with a constant velocity of 0.2 ft/ns, and Figure 6.47(b) shows the final image obtained after velocity update. We can notice that the image has been vertically compressed, since the velocity update indicated a faster velocity, and most of the diffractions have been collapsed.

Figures 6.48 and 6.49 are detailed views of the initial and final images and slownesses at various locations of interest. Figure 6.48 shows collapsed diffractions in the left part of the image. We can also observe features with better continuity in the updated image than in the original image, for example at $x = 20 - 24$ ft and $z = 2$ ft in Figure 6.48(a,c). Likewise, Figure 6.49 shows a better focused image than in the original, for example at $x = 34$ ft and $z = 1.8$ ft in Figure 6.49(a,c).

6.3.3 Discussion

Diffracted events contain useful velocity information that is overlooked by conventional MVA methods, which use flatness of common image gathers as the only criterion for the accuracy of migration velocity. In this section, I demonstrate that accurate interval-velocity updates can be estimated by inverting the results of a residual-focusing analysis of migrated diffracted events. To convert residual-focusing measurements into interval-velocity updates, I employ the WEMVA methodology (Chapter 5) which is ideally suited for this task because it is capable of inverting image perturbations directly, without requiring an estimate of the reflector geometry. In contrast, ray-based MVA methods require the reflector geometry to be provided by interpreting the migrated image. However, since the interpretation of partially-focused diffracted events is an extremely difficult task, ray-based methods are never employed for diffraction-focusing velocity analysis.

The seismic-data example demonstrates how the WEMVA method can exploit the velocity information contained in the event generated by a rugose salt-sediment interface. This kind of events is present in many salt-related data sets, and the ability of using the diffracted energy to further constrain the velocity model might significantly improve the final imaging results.

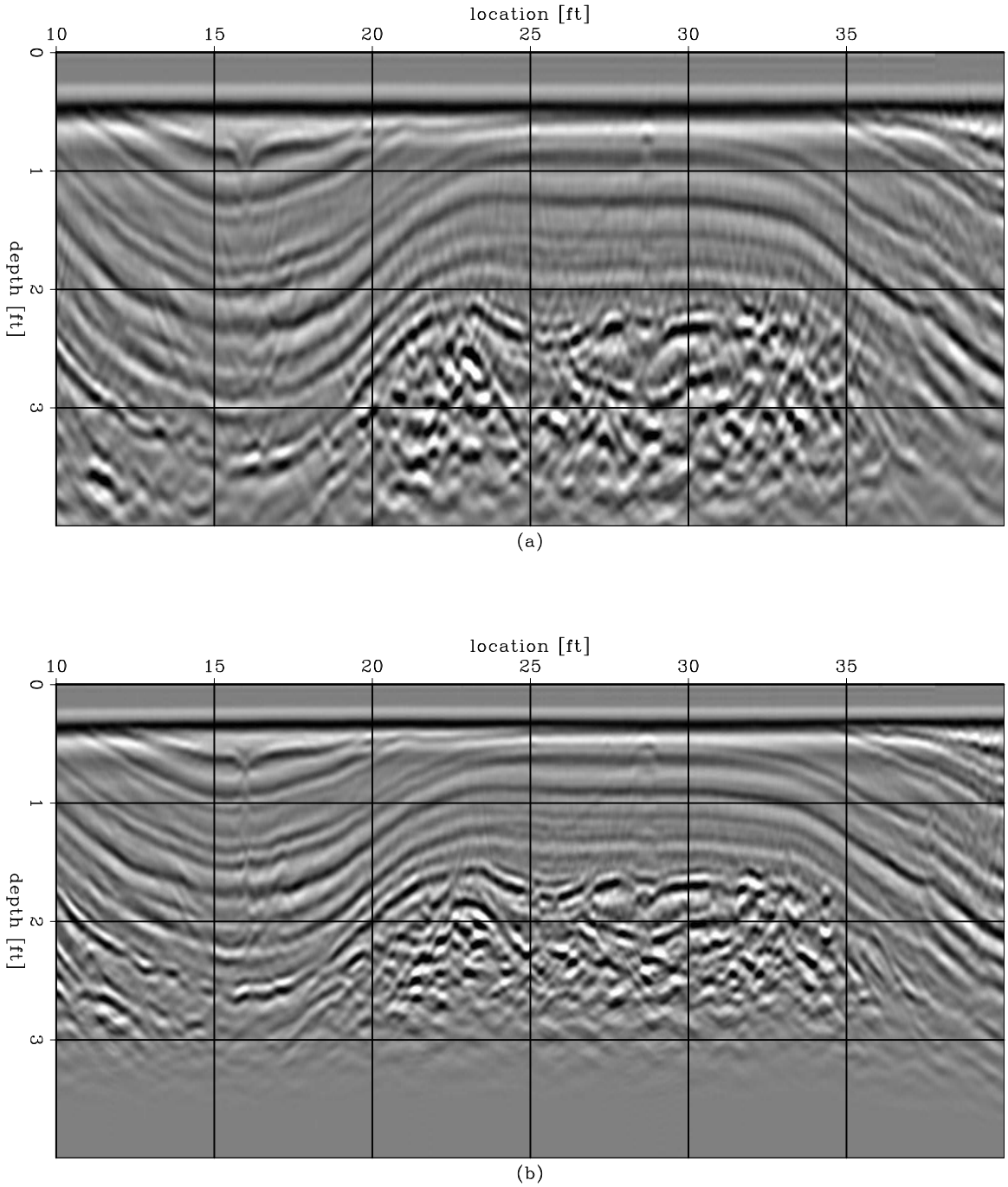


Figure 6.47: Zero-offset migrated images for the data in figure 6.46 using the initial velocity (a) and the updated velocity (b). example-LAVAimag [CR,M]

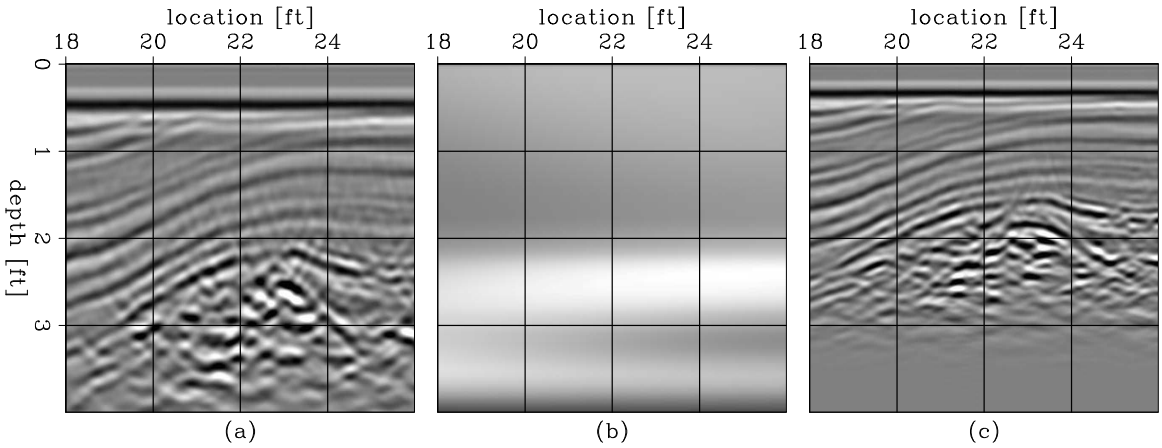


Figure 6.48: Detail of the images depicted in figure 6.47. Migration with the initial velocity (a), updated slowness model (b) and migration with the updated slowness (c). The window corresponds to $x = 20 - 24$ ft and $z = 2$ ft. example-LAVAyoom [CR,M]

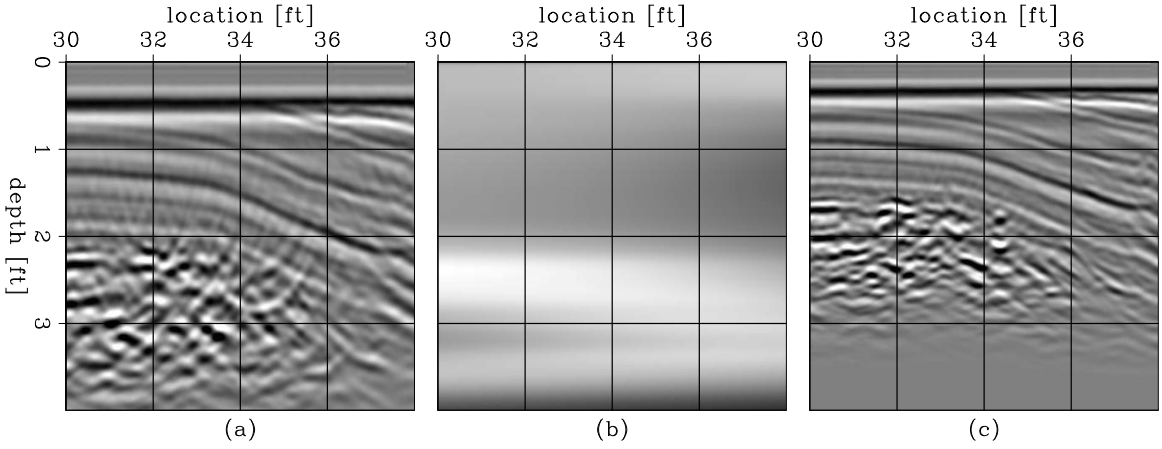


Figure 6.49: Detail of the images depicted in figure 6.47. Migration with the initial velocity (a), updated slowness model (b) and migration with the updated slowness (c). The window corresponds to $x = 34$ ft and $z = 1.8$ ft example-LAVAzoom [CR,M]

The GPR-data example demonstrates the significant potential of the WEMVA method for improving the imaging of GPR data. I demonstrate that the interval-velocity model obtained by extracting velocity information from the diffracted events improves the reflector continuity in the migrated image and facilitates geological interpretation of the images. Since a large number of GPR data sets are limited to zero-offset data, the possibility of using diffractions to define the lateral variations in interval velocity can substantially widen the range of applications of GPR methods.

6.4 Conclusions

Subsalt imaging is one of the most challenging problems of modern seismic imaging because the sharp and irregular salt-sediments interface causes multipathing and uneven illumination. Wavefield-continuation migration methods produce high-quality images under salt, but the estimation of the migration velocity function in the subsalt is an unresolved problem. Conventional MVA methods based on traveltimes computed by ray tracing often fail to provide reliable velocity estimates because ray tracing is unstable and sensitive to the fine details of the salt-sediment interface.

In this chapter, I demonstrate that the wave-equation migration velocity analysis (WEMVA) method presented in Chapter 5 overcomes many of the problems encountered by ray-based MVA methods when estimating velocity under salt. I use a complex and realistic subsalt datasets to test this methodology. I also illustrate with numerical examples that wavepaths computed by wavefield extrapolation are robust with respect to shadow zones, and that they model the finite-frequency wave propagation that occurs in such environments better than rays do. I demonstrate that velocity errors can be effectively measured by residual migration scans. These scans provide useful velocity information almost in all the subsalt areas, although the reliability of these measurements decreases where poor illumination drastically deteriorates the quality of the angle-domain common image gathers.

I demonstrate that WEMVA is capable of overcoming the limitations of the first-order Born approximation, by testing the convergence of WEMVA in presence of large velocity anomalies. The magnitude and spatial extents of the anomalies are such that reflectors in the

migrated images shift by several wavelengths. Notwithstanding these large shifts, WEMVA converges to an accurate approximation of the true velocity function.

I also demonstrate that WEMVA is applicable to velocity analysis using focusing of uncollapsed diffractions. This application makes use of information that is commonly overlooked in traditional migration velocity analysis. This application shows potential for imaging subsalt, but also for imaging datasets where moveout information is not readily available, e.g. typical Ground-Penetrating Radar data.

6.5 Acknowledgment

I would like to acknowledge Frederic Billette and John Etgen of BP for access to and processing of the 3D data used in this chapter. The 3D seismic data was donated by BP and ExxonMobil. Kevin Williams of the Smithsonian Institution in Washington, D.C. provided the GPR dataset.

Chapter 7

Conclusions

The main goal of this thesis is to develop new seismic imaging methods for complex geological structures based on the unifying concept of one-way wavefield extrapolation. Depth imaging requires two main elements: velocity estimation and depth migration. I address both the problem of migration, with *Riemannian wavefield extrapolation*, and the problem of velocity estimation, with *wave-equation migration velocity analysis*.

The main contributions of this thesis are the following:

- Migration using Riemannian wavefield extrapolation (Chapter 2) addresses the intrinsic limitations of migration by downward continuation in presence of waves propagating away from the vertical axis of extrapolation. I demonstrate that one-way Riemannian wavefield extrapolation allows waves to propagate beyond the limit of 90° relative to the vertical axis, while preserving the main characteristics of wavefield imaging methods: multipathing and robustness in presence of large velocity contrasts.

- Angle-domain common image gathers (Chapter 3) enable velocity (MVA) and amplitude (AVA) analysis, as well as multiple attenuation for images created using wavefield extrapolation. I demonstrate that this method can be used to create angle gathers from depth migrated images, after migration by wavefield extrapolation. Many artifacts of angle transformation by slant-stacking are addressed by regularization in the Fourier

domain.

- Prestack residual migration in the Fourier domain (Chapter 4) enables definition of image perturbations for wave-equation migration velocity analysis. I demonstrate that this residual migration method can be used to investigate how prestack images change relative to changes in velocity. Such changes concern both moveout and spatial focusing, and can be used for robust migration velocity analysis.

- Velocity analysis using wavefield extrapolation (Chapter 5) overcomes many of the difficulties of ray-based methods in complex structures. I demonstrate that band-limited velocity analysis methods are robust in presence of large velocity contrasts and that such methods handle in a natural way frequency-dependent and multiple wavepaths. This method can be used for velocity analysis subsalt or for velocity analysis using diffracted energy (Chapter 6).

Appendix A

Riemannian wavefield extrapolation

A.1 2D point-source ray coordinates

For the case of 2D point-source ray coordinates the acoustic wave equation (2.7) takes the form

$$\frac{1}{\alpha J}\left[\frac{\partial}{\partial \tau}\left(\frac{J}{\alpha}\frac{\partial \mathcal{U}}{\partial \tau}\right)+\frac{\partial}{\partial \gamma}\left(\frac{\alpha}{J}\frac{\partial \mathcal{U}}{\partial \gamma}\right)\right]=-\frac{\omega^2}{v^2(\tau,\gamma)}\mathcal{U}\,, \tag{A.1}$$

where, by definition,

$$\begin{aligned}\alpha &= \sqrt{\left(\frac{\partial z}{\partial \tau}\right)^2+\left(\frac{\partial x}{\partial \tau}\right)^2}=v\,,\\ J &= \sqrt{\left(\frac{\partial z}{\partial \gamma}\right)^2+\left(\frac{\partial x}{\partial \gamma}\right)^2}\,.\end{aligned} \tag{A.2}$$

The extrapolation axis is τ (one-way traveltime from the source) and γ is the shooting angle at the source.

We can expand the parentheses in equation (A.1)

$$\frac{1}{v^2}\frac{\partial^2 \mathcal{U}}{\partial \tau^2}+\frac{1}{vJ}\frac{\partial (J/v)}{\partial \tau}\frac{\partial \mathcal{U}}{\partial \tau}+\frac{1}{vJ}\frac{\partial (v/J)}{\partial \gamma}\frac{\partial \mathcal{U}}{\partial \gamma}+\frac{1}{J^2}\frac{\partial^2 \mathcal{U}}{\partial \gamma^2}=-\frac{\omega^2}{v^2(\tau,\gamma)}\mathcal{U} \tag{A.3}$$

and make the notations

$$\begin{aligned} a &= \frac{1}{\alpha^2}\,, \\ b &= \frac{1}{\alpha\, J}\frac{\partial}{\partial \tau}\left(\frac{J}{\alpha}\right)\,, \\ c &= \frac{1}{\alpha\, J}\frac{\partial}{\partial \gamma}\left(\frac{\alpha}{J}\right)\,, \\ d &= \frac{1}{J^2}\,, \end{aligned} \tag{A.4}$$

from which the acoustic wave equation for 2D point-source ray coordinates becomes:

$$a\frac{\partial^2 \mathcal{U}}{\partial \tau^2} + b\frac{\partial \mathcal{U}}{\partial \tau} + c\frac{\partial \mathcal{U}}{\partial \gamma} + d\frac{\partial^2 \mathcal{U}}{\partial \gamma^2} = -\frac{\omega^2}{v^2}\mathcal{U}\,. \tag{A.5}$$

The 2D dispersion relation is

$$-ak_\tau^2 + ibk_\tau + ick_\gamma - dk_\gamma^2 = -\omega^2 s^2\,, \tag{A.6}$$

from which we can obtain the one-way wave equation for 2D point-source ray coordinates:

$$k_\tau = i\frac{b}{2a} \pm \sqrt{\frac{(\omega s)^2}{a} - \left(\frac{b}{2a}\right)^2 + i\frac{c}{a}k_\gamma - \frac{d}{a}k_\gamma^2}\,. \tag{A.7}$$

A.2 2D finite-difference solution to the 15° equation

The 15° one-way wave equation (2.25) takes in two dimensions the simpler form:

$$k_\tau \approx i\frac{b}{2a} + k_o + \frac{ic}{2a\,k_o}k_\gamma + \frac{1}{2\,k_o}\left[\left(\frac{c}{2a\,k_o}\right)^2 - \frac{d}{a}\right]k_\gamma^2\,, \tag{A.8}$$

where

$$k_o^2 = \frac{(\omega s)^2}{a} - \left(\frac{b}{2a}\right)^2\,. \tag{A.9}$$

If we substitute the Fourier-domain wavenumbers by their equivalent space-domain partial derivatives, we obtain

$$\frac{\partial \mathcal{U}}{\partial \tau} \approx -\frac{b}{2a} + i\, k_o + \frac{ic}{2a\, k_o}\frac{\partial \mathcal{U}}{\partial \gamma} - \frac{i}{2\, k_o}\left[\left(\frac{c}{2a\, k_o}\right)^2 - \frac{d}{a}\right]\frac{\partial^2 \mathcal{U}}{\partial \gamma^2}\,. \tag{A.10}$$

A finite-difference implementation of equation (A.10) involving the Crank-Nicolson method is

$$\begin{aligned}\frac{\mathcal{U}_{\tau+1}^{\gamma} - \mathcal{U}_{\tau}^{\gamma}}{\Delta\tau} &\approx \frac{ic}{2a\, k_o}\frac{\left(\mathcal{U}_{\tau}^{\gamma+1} - \mathcal{U}_{\tau}^{\gamma-1}\right) + \left(\mathcal{U}_{\tau+1}^{\gamma+1} - \mathcal{U}_{\tau+1}^{\gamma-1}\right)}{4\Delta\gamma} \\ -\frac{i}{2\, k_o}\left[\left(\frac{c}{2a\, k_o}\right)^2 - \frac{d}{a}\right]&\frac{\left(\mathcal{U}_{\tau}^{\gamma-1} - 2\mathcal{U}_{\tau}^{\gamma} + \mathcal{U}_{\tau}^{\gamma+1}\right) + \left(\mathcal{U}_{\tau+1}^{\gamma-1} - 2\mathcal{U}_{\tau+1}^{\gamma} + \mathcal{U}_{\tau+1}^{\gamma+1}\right)}{2\Delta\gamma^2}\,.\end{aligned} \tag{A.11}$$

If we make the notations

$$\begin{aligned}\mu &= \frac{ic}{2a\, k_o}\frac{\Delta\tau}{4\Delta\gamma} \\ \nu &= -\frac{i}{2\, k_o}\left[\left(\frac{c}{2a\, k_o}\right)^2 - \frac{d}{a}\right]\frac{\Delta\tau}{2\Delta\gamma^2}\,,\end{aligned} \tag{A.12}$$

we can write equation (A.11) as

$$\begin{aligned}\mathcal{U}_{\tau+1}^{\gamma} - \mathcal{U}_{\tau}^{\gamma} &\approx \mu\left(\mathcal{U}_{\tau}^{\gamma+1} - \mathcal{U}_{\tau}^{\gamma-1} + \mathcal{U}_{\tau+1}^{\gamma+1} - \mathcal{U}_{\tau+1}^{\gamma-1}\right) \\ &+ \nu\left(\mathcal{U}_{\tau}^{\gamma-1} - 2\mathcal{U}_{\tau}^{\gamma} + \mathcal{U}_{\tau}^{\gamma+1} + \mathcal{U}_{\tau+1}^{\gamma-1} - 2\mathcal{U}_{\tau+1}^{\gamma} + \mathcal{U}_{\tau+1}^{\gamma+1}\right)\,,\end{aligned} \tag{A.13}$$

or, if we isolate the terms corresponding to the two extrapolation levels as:

$$\begin{aligned}\mathcal{U}_{\tau+1}^{\gamma} &- \mu\left(\mathcal{U}_{\tau+1}^{\gamma+1} - \mathcal{U}_{\tau+1}^{\gamma-1}\right) - \nu\left(\mathcal{U}_{\tau+1}^{\gamma-1} - 2\mathcal{U}_{\tau+1}^{\gamma} + \mathcal{U}_{\tau+1}^{\gamma+1}\right) = \\ \mathcal{U}_{\tau}^{\gamma} &+ \mu\left(\mathcal{U}_{\tau}^{\gamma+1} - \mathcal{U}_{\tau}^{\gamma-1}\right) + \nu\left(\mathcal{U}_{\tau}^{\gamma-1} - 2\mathcal{U}_{\tau}^{\gamma} + \mathcal{U}_{\tau}^{\gamma+1}\right)\,.\end{aligned} \tag{A.14}$$

After grouping the terms, we obtain

$$-(\nu-\mu)\,\mathcal{U}_{\tau+1}^{\gamma-1}+(1+2\nu)\,\mathcal{U}_{\tau+1}^{\gamma}-(\nu+\mu)\,\mathcal{U}_{\tau+1}^{\gamma+1}=(\nu-\mu)\,\mathcal{U}_{\tau}^{\gamma-1}+(1-2\nu)\,\mathcal{U}_{\tau}^{\gamma}+(\nu+\mu)\,\mathcal{U}_{\tau}^{\gamma+1}\,, \tag{A.15}$$

which is a finite-difference representation of the 15° solvable using fast tridiagonal solvers.

Appendix B

Angle-domain common image gathers

B.1 Reflection angle formula

This appendix shows the derivation of equation (3.3), which serves as the basis of the frequency-domain angle gather construction (Chapter 3).

In the process of downward continuation, the wavefield appears as a function of four variables: time t, depth z, source lateral position s, and receiver lateral position r. Both the source and receiver assume positions at depth z, where the wavefield is continued (Claerbout, 1985). It is often convenient to replace the variables s and r with the midpoint position $x = (s+r)/2$ and the half-offset $h = (r-s)/2$.

Assuming that the reflection event in the continued wavefield is described by the function $t = t(z,s,r)$, we find from the Snell's law the following derivatives:

$$\frac{\partial t}{\partial s} = \frac{\sin(\alpha-\gamma)}{v}\,, \tag{B.1}$$

$$\frac{\partial t}{\partial r} = \frac{\sin(\alpha+\gamma)}{v}\,, \tag{B.2}$$

where v is the wave velocity, α is the dip angle, and γ is the reflection angle (Figure 3.2). The traveltime derivative with respect to the depth of the observation surface z has contributions

from the two branches of the reflected ray, as follows:

$$\frac{\partial t}{\partial z} = \frac{\cos(\alpha-\gamma)}{v} + \frac{\cos(\alpha+\gamma)}{v}\,. \tag{B.3}$$

Equation (B.3) corresponds to the well-known double-square-root equation (Claerbout, 1985). This equation simply reflects the fact that the traveltime increases with increasing depth of the reflector.

Transforming equations (B.1)- (B.3) to the midpoint and half-offset coordinates, we obtain

$$\frac{\partial t}{\partial x} = \frac{\partial t}{\partial s} + \frac{\partial t}{\partial r} = \frac{2\sin\alpha\cos\gamma}{v}\,, \tag{B.4}$$

$$\frac{\partial t}{\partial h} = \frac{\partial t}{\partial r} - \frac{\partial t}{\partial s} = \frac{2\cos\alpha\sin\gamma}{v}\,, \tag{B.5}$$

$$\frac{\partial t}{\partial z} = \frac{2\cos\alpha\cos\gamma}{v}\,. \tag{B.6}$$

At a fixed image location x, we can transform the derivatives of $t(z,x,h)$ to the derivatives of $z(t,x,h)$ by applying the implicit function theorem. Using equations (B.5)- (B.6), we obtain

$$\frac{\partial z}{\partial h} = -\frac{\partial t}{\partial h}\Big/\frac{\partial t}{\partial z} = -\tan\gamma\,. \tag{B.7}$$

Equation (B.7) corresponds to equation (3.3) in the Chapter 3. It is important to note that this equation is only suitable for angle gathers constructed on images obtained by wavefield continuation methods (Figure 3.2), when h does not represent the surface offset, but half the distance between the downward continued sources and receivers.

In deriving equation (B.7), I assumed that the velocity v does not change laterally between the source and receiver positions. While this may not be true in general, equation (B.7) is always satisfied in the vicinity of zero half-offset after migration ($h = 0$). Therefore, this formula is applicable near the focusing points of the downward-continued wavefield.

Appendix C

Wave-equation migration velocity analysis

C.1 First-order Born scattering operators

Imaging by wavefield extrapolation (WE) is based on recursive continuation of wavefields $\mathcal{U}$ from a given depth level to the next by means of an extrapolation operator $\mathbf{E}$. At every extrapolation step, we can write that

$$\mathcal{U}_{z+\Delta z} = \mathbf{E}_z\big[\mathcal{U}_z\big], \tag{C.1}$$

where $\mathcal{U}_z$ is the wavefield at the top of the slab, and $\mathcal{U}_{z+\Delta z}$ is the wavefield at the bottom of the slab. The operator $\mathbf{E}$ involves a spatially-dependent phase shift described by:

$$\mathbf{E}_z\,[\,] = e^{ik_z\Delta z}, \tag{C.2}$$

where k_z represents the depth wavenumber, and Δz the wavefield extrapolation depth step. The relation (C.1) corresponds to the analytical solution of the differential equation

$$\mathcal{U}'(z) = ik_z\mathcal{U}(z) \tag{C.3}$$

which describes depth extrapolation of monochromatic plane waves (Claerbout, 1985). The $'$ sign represents a derivative with respect to the depth z. The depth wavenumber k_z is given by the one-way wave equation, also known as the single square root (SSR) equation

$$k_z = \sqrt{\omega^2 s^2 - |\mathbf{k}|^2}, \tag{C.4}$$

where ω is the temporal frequency, s is the laterally variable slowness of the medium, and $\mathbf{k}$ is the horizontal wavenumber. I use the laterally variable s and the horizontal wavenumber $\mathbf{k}$ in equation (C.4) just for conciseness, although such a notation not mathematically correct in laterally varying media.

Since downward continuation by Fourier-domain phase shift can be applied for slowness models that only vary with depth, we need to split the operator $\mathbf{E}$ into two parts: a constant slowness *continuation operator* applied in the $\omega - \mathbf{k}$ domain, which accounts for the propagation in depth, and a *screen operator* applied in the $\omega - \mathbf{x}$ domain, which accounts for the wavefield perturbations due to the lateral slowness variations. In essence, we approximate the vertical wavenumber k_z with its constant slowness counterpart k_{z0}, corrected by a term describing the spatial variability of the slowness function (Ristow and Ruhl, 1994).

Furthermore, we can separate the depth wavenumber k_z into two components, one which corresponds to the background medium $\widetilde{k_z}$ and one which corresponds to a perturbation of the medium:

$$k_z = \widetilde{k_z} + \Delta k_z \ . \tag{C.5}$$

In a first-order approximation, we can relate those two depth wavenumbers by a Taylor series expansion:

$$k_z \approx \widetilde{k_z} + \left.\frac{dk_z}{ds}\right|_{s=\tilde{s}} (s - \tilde{s}) \tag{C.6}$$

$$\approx \widetilde{k_z} + \omega \frac{\omega \tilde{s}}{\sqrt{\omega^2 \tilde{s}^2 - |\mathbf{k}|^2}} (s - \tilde{s}) \ , \tag{C.7}$$

where $s(z,x)$ is the slowness corresponding to the perturbed medium, and $\tilde{s}(z,x)$ is the background slowness.

Within any depth slab, we can extrapolate the wavefield from the top either in the perturbed or in the background medium. The wavefields at the bottom of the slab, $\widetilde{\mathcal{U}}_{z+\Delta z} = \mathcal{U}_z e^{i\widetilde{k}_z \Delta z}$ and $\mathcal{U}_{z+\Delta z} = \mathcal{U}_z e^{ik_z \Delta z}$ are related by the relation

$$\mathcal{U}_{z+\Delta z} \approx \widetilde{\mathcal{U}}_{z+\Delta z} e^{i\Delta k_z \Delta z} \,. \tag{C.8}$$

Equation (C.8) is a direct statement of the Rytov approximation (Lo and Inderweisen, 1994), since the wavefields at the bottom of the slab correspond to different phase shifts related by a linear equation.

The wavefield perturbation $\Delta\mathcal{V}$ at the bottom of the slab is obtained by subtracting the background wavefield $\widetilde{\mathcal{U}}$ from the perturbed wavefield $\mathcal{U}$:

$$\begin{aligned}
\Delta\mathcal{V}_{z+\Delta z} &\approx \mathcal{U}_{z+\Delta z} - \widetilde{\mathcal{U}}_{z+\Delta z} && \text{(C.9)}\\
&\approx \left(e^{i\Delta k_z \Delta z} - 1\right) \widetilde{\mathcal{U}}_{z+\Delta z} && \text{(C.10)}\\
&\approx e^{i\widetilde{k}_z \Delta z} \left(e^{i \frac{dk_z}{ds}\Big|_{s=\tilde{s}} \Delta s_z \Delta z} - 1 \right) \widetilde{\mathcal{U}}_z, && \text{(C.11)}
\end{aligned}$$

where $\Delta s = s - \tilde{s}$ is the perturbation between the correct and the background slownesses at depth z.

In operator form we can write

$$\Delta\mathcal{V}_{z+\Delta z} = \mathbf{E}_z \left[\mathbf{N}_z \left(\widetilde{\mathcal{U}}_z \right) \left[\Delta s_z \right] \right], \tag{C.12}$$

where $\mathbf{E}_z$ represents the downward continuation operator at depth z, and $\mathbf{N}_z$ represents the *Rytov* scattering operator which is dependent on the background wavefield $\widetilde{\mathcal{U}}_z$ and the slowness perturbation Δs_z at that depth level:

$$\mathbf{N}_z \left(\widetilde{\mathcal{U}}_z \right) \left[\Delta s_z \right] = \left(e^{i \frac{dk_z}{ds}\Big|_{s=\tilde{s}} \Delta s_z \Delta z} - 1 \right) \widetilde{\mathcal{U}}_z \,. \tag{C.13}$$

In this approximation, we assume that the scattered wavefield is generated only by the background wavefield and we ignore all multi-scattering effects. For the Born approximation

(Lo and Inderweisen, 1994), we further assume that the wavefield differences are small, such we can linearize the exponential according to the relation $e^{i\Delta\phi} \approx 1 + i\Delta\phi$. With this new approximation, the expression for the downward-continued scattered wavefield becomes:

$$\Delta\mathcal{V}_{z+\Delta z} \approx e^{i\widetilde{k}_z \Delta z}\left(i\left.\frac{dk_z}{ds}\right|_{s=\tilde{s}} \Delta s_z \Delta z\right)\widetilde{\mathcal{U}}_z. \tag{C.14}$$

In operator form, we can write the scattered wavefield at z as

$$\Delta\mathcal{V}_{z+\Delta z} = \mathbf{E}_z\left[\mathbf{S}_z\left(\widetilde{\mathcal{U}}_z\right)\left[\Delta s_z\right]\right] \tag{C.15}$$

where $\mathbf{E}_z$ represents the downward continuation operator at depth z, and $\mathbf{S}_z$ represents the *Born* scattering operator which is dependent on the background wavefield and operates on the slowness perturbation at that depth level.

The linear scattering operator $\mathbf{S}$ is a mixed-domain operator similar to the extrapolation operator $\mathbf{E}$. This operator depends on the background wavefield and background slowness by the expression:

$$\mathbf{S}_z\left(\widetilde{\mathcal{U}}_z\right)\left[\Delta s_z\right] \approx i\left.\frac{dk_z}{ds}\right|_{s=\tilde{s}} \Delta z \Delta s_z \widetilde{\mathcal{U}}_z\,. \tag{C.16}$$

In practice, we can implement the scattering operator described by equation (C.16) in different ways.

- One option is to implement the Born operator (C.16) in the space domain using an expansion (Huang et al., 1999) like

$$\left.\frac{dk_z}{ds}\right|_{s=\tilde{s}} \approx \omega\left(1 + \frac{1}{2}\left[\frac{|\mathbf{k}|}{\omega\tilde{s}}\right]^2 + \frac{3}{8}\left[\frac{|\mathbf{k}|}{\omega\tilde{s}}\right]^4 + \frac{5}{16}\left[\frac{|\mathbf{k}|}{\omega\tilde{s}}\right]^6 + \frac{35}{128}\left[\frac{|\mathbf{k}|}{\omega\tilde{s}}\right]^8 + \ldots\right). \tag{C.17}$$

  In practice, the summation of the terms in equation (C.17) involves forward and inverse Fast Fourier Transforms (`FFT` and `IFT`) and multiplication in the space domain with the

spatially variable $\tilde{s}$:

$$\Delta \mathcal{V}_z = i\omega \Delta z \Delta s_z \left[1 + \sum_{j=1,\ldots} c_j \frac{1}{(\omega \tilde{s})^{2j}} \texttt{IFT}\left[|\mathbf{k}|^{\mathbf{2j}} \texttt{FFT}\left[\widetilde{\mathcal{U}}_{\mathbf{z}} \right] \right] \right] , \tag{C.18}$$

where $c_j = \frac{1}{2}, \frac{3}{8}, \ldots$

- Another option is to implement the Born operator (C.16) in the Fourier domain relative to the constant reference slowness in any individual slab. In this case, we can write

$$\left. \frac{dk_z}{ds} \right|_{s=s_o} \approx \omega \frac{\omega s_o}{\sqrt{\omega^2 {s_o}^2 - (1 - i\eta)^2 |\mathbf{k}|^{\mathbf{2}}}} , \tag{C.19}$$

where η as a damping parameter which avoids division by zero (de Hoop et al., 1996). In practice, the implementation of equation (C.19) involves forward and inverse Fast Fourier Transforms (FFT and IFT):

$$\Delta \mathcal{V}_z = i \Delta z \, \texttt{IFT} \left[\left. \frac{dk_z}{ds} \right|_{s=s_o} \texttt{FFT}\left[\widetilde{\mathcal{U}}_z \Delta s_z \right] \right] . \tag{C.20}$$

C.2 Linearized image perturbations

A linearized image perturbation is computed using a prestack residual migration operator ($\mathbf{K}$) using a relation like

$$\Delta \mathcal{R} \approx \left. \mathbf{K}^{'} \right|_{\rho=1} \left[\widetilde{\mathcal{R}} \right] \Delta \rho \, . \tag{C.21}$$

The operator $\mathbf{K}$ depends on the scalar parameter ρ which is a ratio of the velocity to which we residually migrate and the background velocity (Chapter 4). The background image corresponds to $\rho = 1$.

Using the chain rule of differentiation, we can write

$$\Delta \mathcal{R} \approx \left. \frac{d\mathbf{K}}{dk_z} \frac{dk_z}{d\rho} \right|_{\rho=1} \left[\widetilde{\mathcal{R}} \right] \Delta \rho \, , \tag{C.22}$$

where k_z is the depth wavenumber defined for prestack Stolt residual migration.

Equation (C.22) offers the possibility to build the image perturbation directly, by computing three elements: the derivative of the image with respect to the depth wavenumber, and two weighting functions, one for the derivative of the depth wavenumber with respect to the velocity ratio parameter (ρ), and the other one for the magnitude of the $\Delta\rho$ perturbation from the reference to the improved image.

Firstly, the image derivative in the Fourier domain, $\frac{d\mathbf{K}}{dk_z}$, is straightforward to compute in the space domain as

$$\left.\frac{d\mathbf{K}}{dk_z}\right|_{\rho=1}\left[\widetilde{\mathcal{R}}\right] = -iz\widetilde{\mathcal{R}}\,. \tag{C.23}$$

The derivative image is represented by the imaginary part of the migrated image, scaled by depth.

Secondly, we can obtain the weighting representing the derivative of the depth wavenumber with respect to the velocity ratio parameter, $\left.\frac{dk_z}{d\rho}\right|_{\rho=1}$, starting from the double square root (DSR) equation written for prestack Stolt residual migration (Sava, 2003):

$$\begin{aligned} k_z &= k_{z_s} + k_{z_r} \\ &= \frac{1}{2}\sqrt{\rho^2\mu^2 - |\mathbf{k}_s|^2} + \frac{1}{2}\sqrt{\rho^2\mu^2 - |\mathbf{k}_r|^2}\,, \end{aligned}$$

where μ is given by the expression:

$$\mu^2 = \frac{\left[4\left(k_{z0}\right)^2 + (\mathbf{k}_r - \mathbf{k}_s)^2\right]\left[4\left(k_{z0}\right)^2 + (\mathbf{k}_r + \mathbf{k}_s)^2\right]}{16{k_{z0}}^2}\,. \tag{C.24}$$

The derivative of k_z with respect to ρ is

$$\frac{dk_z}{d\rho} = \rho\left(\frac{\mu^2}{4k_{z_s}} + \frac{\mu^2}{4k_{z_r}}\right)\,, \tag{C.25}$$

therefore, at $\rho = 1$, we can write:

$$\left.\frac{dk_z}{d\rho}\right|_{\rho=1} = \frac{\mu^2}{2\sqrt{\mu^2 - |\mathbf{k}_s|^2}} + \frac{\mu^2}{2\sqrt{\mu^2 - |\mathbf{k}_r|^2}} \,. \tag{C.26}$$

For common-azimuth data, the double square root (DSR) equation written for prestack Stolt residual migration (Sava, 2003) is:

$$\begin{cases} k_{z_x} = k_{z_{x_s}} + k_{z_{x_r}} \\ k_z = \sqrt{k_{z_x}^2 - k_{m_y}^2} \,, \end{cases} \tag{C.27}$$

where $k_{z_{x_s}}$ and $k_{z_{x_r}}$ are given by the expressions

$$k_{z_{x_s}} = \frac{1}{2}\sqrt{\rho^2\mu_c^2 - (k_{m_x} - k_{h_x})^2} \tag{C.28}$$

$$k_{z_{x_r}} = \frac{1}{2}\sqrt{\rho^2\mu_c^2 - (k_{m_x} + k_{h_x})^2} \,, \tag{C.29}$$

and μ_c is given by the expression:

$$\mu_c^2 = \frac{\left[{k_{z_0}}^2 + k_{m_y}^2 + k_{h_x}^2\right]\left[{k_{z_0}}^2 + k_{m_y}^2 + k_{m_x}^2\right]}{{k_{z_0}}^2 + k_{m_y}^2} \,. \tag{C.30}$$

The derivative of k_z with respect to ρ is

$$\frac{dk_z}{d\rho} = \frac{dk_z}{dk_{z_x}}\frac{dk_{z_x}}{d\rho} \tag{C.31}$$

$$= \rho\frac{k_{z_x}}{k_z}\left(\frac{\mu_c^2}{4k_{z_{x_s}}} + \frac{\mu_c^2}{4k_{z_{x_r}}}\right) \,. \tag{C.32}$$

At $\rho = 1$, we can write:

$$\left.\frac{dk_z}{d\rho}\right|_{\rho=1} = \left.\frac{k_{z_x}}{k_z}\right|_{\rho=1}\left[\frac{\mu_c^2}{2\sqrt{\mu_c^2 - (k_{m_x} - k_{h_x})^2}} + \frac{\mu_c^2}{2\sqrt{\mu_c^2 - (k_{m_x} + k_{h_x})^2}}\right] \,. \tag{C.33}$$

Bibliography

Al-Yahya, K., 1987, Velocity analysis by iterative profile migration: Ph.D. thesis, Stanford University. URL `http://sepwww.stanford.edu/oldreports/sep53/index.html`.

Al-Yahya, K. M., 1989, Velocity analysis by iterative profile migration: Geophysics, **54**, 718–729.

Albertin, U., Yingst, D., and Jaramillo, H., 2001, Comparing common-offset Maslov, Gaussian beam, and coherent state migrations *in* 71st Ann. Internat. Mtg. Soc. of Expl. Geophys., 913–916.

Albertin, U., Yingst, D., Jaramillo, H., Wiggins, W., Chapman, C., and Nichols, D., 2002, Towards a hybrid raytrace-based beam/wavefield-extrapolated beam migration algorithm *in* 72nd Ann. Internat. Mtg. Soc. of Expl. Geophys., 1344–1347.

Biondi, B., 1997, Azimuth moveout + common-azimuth migration: Cost-effective prestack depth imaging of marine data *in* 67th Ann. Internat. Mtg. Soc. of Expl. Geophys., 1375–1378.

—, 2002, Stable wide-angle Fourier finite-difference downward extrapolation of 3-D wavefields: Geophysics, **67**, 872–882.

—, 2004, 3-D Seismic Imaging: Stanford Exploration Project.

Biondi, B., and Palacharla, G., 1996, 3-D prestack migration of common-azimuth data: Geophysics, **61**, 1822–1832.

Biondi, B., and Sava, P., 1999, Wave-equation migration velocity analysis *in* 69th Ann. Internat. Mtg. Soc. of Expl. Geophys., 1723–1726.

Biondi, B., and Shan, G., 2002, Prestack imaging of overturned reflections by reverse time migration *in* 72nd Ann. Internat. Mtg. Soc. of Expl. Geophys., 1284–1287.

Biondi, B., and Symes, W., 2004, Angle-domain common-image gathers for migration velocity analysis by wavefield-continuation imaging: Geophysics, in press.

Biondi, B., and Tisserant, T., 2004, 3-D angle-domain common-image gathers for migration velocity analysis: Geophysical Prospecting: accepted for publication.

Bishop, T. N., Bube, K. P., Cutler, R. T., Langan, R. T., Love, P. L., Resnick, J. R., Shuey, R. T., Spindler, D. A., and Wyld, H. W., 1985, Tomographic determination of velocity and depth in laterally varying media: Geophysics, **50**, 903–923.

Brandsberg-Dahl, S., and Etgen, J., 2003, Beam-wave migration: 65th Mtg., Eur. Assoc. Geosc. Eng., Abstracts.

Brandsberg-Dahl, S., de Hoop, M. V., and Ursin, B., 1999, The sensitivity transform in the common scattering-angle/azimuth domain *in* 61st Mtg. Eur. Assn. Geosci. Eng., Session:4053.

de Bruin, C. G. M., Wapenaar, C. P. A., and Berkhout, A. J., 1990, Angle-dependent reflectivity by means of prestack migration: Geophysics, **55**, 1223–1234.

Bunks, C., Saleck, F. M., Zaleski, S., and Chavent, G., 1995, Multiscale seismic waveform inversion: Geophysics, **60**, 1457–1473.

Cervený, V., 2001, Seismic ray theory: Cambridge Univ. Press.

Chavent, G., and Jacewitz, C. A., 1995, Determination of background velocities by multiple migration fitting: Geophysics, **60**, 476–490.

Chen, L., Chen, Y., and Wu, R., 2002, Target-oriented prestack beamlet migration using Gabor-Daubechies frames *in* 72nd Ann. Internat. Mtg. Soc. of Expl. Geophys., 1356–1359.

Claerbout, J., 1999, Geophysical estimation by example: Environmental soundings image enhancement: Stanford Exploration Project, `http://sepwww.stanford.edu/sep/prof/`.

Claerbout, J. F., 1976, Fundamentals of Geophysical Data Processing: Blackwell.

—, 1985, Imaging the Earth's Interior: Blackwell Scientific Publications.

Clayton, R. W., and Stolt, R. H., 1981, A born-WKBJ inversion method for acoustic reflection data: Geophysics, **46**, 1559–1567.

Cohen, J. K., and Bleistein, N., 1979, Velocity inversion procedure for acoustic waves: Geophysics, **44**, 1077–1087.

Courant, R., and Hilbert, D., 1989, Methods of mathematical physics: John Wiley & Sons.

Dahlen, F. A., Hung, S. H., and Nolet, G., 2000, Frechet kernels for finite frequency traveltimes—I. Theory: Geophys. J. Int., **141**, 157–174.

Devaney, A. J., 1981, Inverse-scattering theory within the rytov approximation: Optics Lett., **6**, 374–376.

—, 1982, A filtered backprojection algorithm for diffraction tomography: Ultrasonic Imaging, **4**, 336–350.

Devaney, A. J., and Oristaglio, M. L., 1984, Geophysical diffraction tomography *in* 54th Ann. Internat. Mtg. Soc. of Expl. Geophys., Session:RS.3.

Etgen, J., 1990, Residual prestack migration and interval velocity estimation: Ph.D. thesis, Stanford University.

—, 1993, Interval velocity estimation using residual prestack migration *in* 63rd Ann. Internat. Mtg. Soc. of Expl. Geophys., 669–672.

—, 2002, Waves, beams and dimensions: an illuminating if incoherent view of the future of migration: 72nd Ann. Internat. Mtg, Soc. of Expl. Geophys.

Etgen, J. T., 1988, Velocity analysis using prestack depth migration: Linear theory *in* 58th Ann. Internat. Mtg. Soc. of Expl. Geophys., Session:S9.7.

Fomel, S., 2004, Theory of 3-D angle gathers in wave-equation imaging *in* 74th Ann. Internat. Mtg. Soc. of Expl. Geophys.

Forgues, E., Scala, E., and Pratt, R. G., 1998, High resolution velocity model estimation from refraction and reflection data *in* 68th Ann. Internat. Mtg. Soc. of Expl. Geophys., 1211–1214.

Gazdag, J., and Sguazzero, P., 1984, Migration of seismic data by phase-shift plus interpolation: Geophysics, **49**, 124–131.

Gray, S., Notfors, C., and Bleistein, N., 2002, Imaging using multi-arrivals: Gaussian beams or multi-arrival Kirchhoff? *in* 72nd Ann. Internat. Mtg. Soc. of Expl. Geophys., 1117–1120.

Gray, S. H., Etgen, J., Dellinger, J., and Whitmore, D., 2001, Seismic migration problems and solutions: Geophysics, **66**, 1622–1640.

Hale, D., 1991, Stable explicit depth extrapolation of seismic wavefields: Geophysics, **56**, 1770–1777.

Hale, D., Hill, N. R., and Stefani, J., 1992, Imaging salt with turning seismic waves: Geophysics, **57**, 1453–1462.

Harlan, W. S., 1986, Signal-noise separation and seismic inversion: Ph.D. thesis, Stanford University. URL `http://sepwww.stanford.edu/oldreports/sep47/index.html`.

Harris, J. M., 1987, Diffraction tomography with arrays of discrete sources and receivers: IEEE trans. Geosci. and Remote Sensing, **25**, 448–455.

Harris, J. M., and Wang, G. Y., 1996, Diffraction tomography for inhomogeneities in layered background medium: Geophysics, **61**, 570–583.

Hill, N. R., 1990, Gaussian beam migration: Geophysics, **55**, 1416–1428.

—, 2001, Prestack Gaussian-beam depth migration: Geophysics, **66**, 1240–1250.

de Hoop, M., le Rousseau, J. H., and Wu, R. S., 1996, Generalization of the phase-screen approximation for the scattering of acoustic waves: Wave Motion, **31**, 43–70.

de Hoop, M. V., 1996, Generalization of the Bremmer coupling series *in* J. Math. Phys. 3246–3282.

Huang, L. Y., Fehler, M. C., and Wu, R. S., 1999, Extended local Born Fourier migration method: Geophysics, **64**, 1524–1534.

Huang, L. Y., and Wu, R. S., 1996, Prestack depth migration with acoustic screen propagators *in* 66th Ann. Internat. Mtg. Soc. of Expl. Geophys., 415–418.

Hung, S. H., Dahlen, F. A., and Nolet, G., 2000, Frechet kernels for finite frequency traveltimes—II. Examples: Geophys. J. Int., **141**, 175–203.

Karcher, C. L., 1973, The reflection seismograph, its invention and use in the discovery of oil and gas fields: American Institute of Physics, College Park, MD.

Kjartansson, E., 1979, Attenuation of seismic waves in rocks and applications in energy exploration: Ph.D. thesis, Stanford University. URL `http://sepwww.stanford.edu/oldreports/sep23/index.html`.

Kosloff, D., Sherwood, J., Koren, Z., MacHet, E., and Falkovitz, Y., 1996, Velocity and interface depth determination by tomography of depth migrated gathers: Geophysics, **61**, 1511–1523.

Lo, T. W., and Inderweisen, P. L., 1994, Fundamentals of Seismic Tomography: Soc. of Expl. Geophys.

Lomax, A., 1994, The wavelength-smoothing method for approximating broad-band wave propagation through complicated velocity structures: Geoph. J. Int., **117**, 313–334.

Marquering, H., Dahlen, F. A., and Nolet, G., 1999, Three-dimensional sensitivity kernels for finite-frequency traveltimes: the banana-doghnut paradox: Geophys. J. Int., **137**, 805–815.

Mora, P., 1989, Inversion = migration + tomography: Geophysics, **54**, 1575–1586.

Mora, P. R., 1987, Nonlinear two-dimensional elastic inversion of multioffset seismic data: Geophysics, **52**, 1211–1228.

Mosher, C., and Foster, D., 2000, Common angle imaging conditions for prestack depth migration *in* 70th Ann. Internat. Mtg. Soc. of Expl. Geophys., 830–833.

Mosher, C. C., Foster, D. J., and Hassanzadeh, S., 1997, Common angle imaging with offset plane waves *in* 67th Ann. Internat. Mtg. Soc. of Expl. Geophys., 1379–1382.

Mueller, R. K., 1980, Diffraction tomography i: the wave equation: Ultrasonic Imaging, **2**, 213–222.

Nichols, D. E., 1994, Imaging complex structures using band-limited Green's functions: Ph.D. thesis, Stanford University. URL `http://sepwww.stanford.edu/public/docs/sep81/index.html`.

—, 1996, Maximum energy traveltimes calculated in the seismic frequency band: Geophysics, **61**, 253–263.

Noble, M., Lindgren, J., and Tarantola, A., 1991, Large-sized, nonlinear inversion of a marine data set: Retrieving the source, the background velocity and the impedance contrasts *in* 61st Ann. Internat. Mtg. Soc. of Expl. Geophys., 893–896.

Nolan, C. J., and Symes, W. W., 1996, Imaging and coherency in complex structures *in* 66th Ann. Internat. Mtg. Soc. of Expl. Geophys., 359–362.

O'Brien, M. J., and Etgen, J. T., 1998, Wavefield imaging of complex structures with sparse, point-receiver data *in* 68th Ann. Internat. Mtg. Soc. of Expl. Geophys., 1365–1368.

Ottolini, R., 1982, Migration of reflection seismic data in angle-midpoint coordinates: Ph.D. thesis, Stanford University. URL `http://sepwww.stanford.edu/oldreports/sep33/index.html`.

Paffenholz, J., McLain, B., Zaske, J., and Keliher, P., 2002, Subsalt multiple attenuation and imaging: Observations from the Sigsbee2B synthetic dataset *in* 72nd Ann. Internat. Mtg. Soc. of Expl. Geophys., 2122–2125.

Popovici, A. M., 1996, Prestack migration by split-step DSR: Geophysics, **61**, 1412–1416.

Pratt, R. G., 1999, Seismic waveform inversion in the frequency domain, Part 1: Theory and verification in a physical scale model: Geophysics, **64**, 888–901.

Pratt, R. G., and Shipp, R. M., 1999, Seismic waveform inversion in the frequency domain, Part 2: Fault delineation in sediments using crosshole data: Geophysics, **64**, 902–914.

Pratt, R. G., and Worthington, M. H., 1988, The application of diffraction tomography to cross-hole seismic data: Geophysics, **53**, 1284–1294.

Prucha, M., Biondi, B., and Symes, W., 1999, Angle-domain common image gathers by wave-equation migration *in* 69th Ann. Internat. Mtg. Soc. of Expl. Geophys., 824–827.

Rickett, J., 2000, Traveltime sensitivity kernels: Banana-doughnuts or just plain bananas?: SEP– **103**, 61–69.

Rickett, J., Claerbout, J., and Fomel, S. B., 1998, Implicit 3-D depth migration by wavefield extrapolation with helical boundary conditions *in* 68th Ann. Internat. Mtg. Soc. of Expl. Geophys., 1124–1127.

Rickett, J. E., and Sava, P. C., 2002, Offset and angle-domain common image-point gathers for shot-profile migration: Geophysics, **67**, 883–889.

Riemann, B., 1953, Grundlagen für eine allgemeine Theorie der Funktionen einer veränderlichen komplexen Grösse (1851), in Collected Works: Dover Publications Inc, New York.

Rietveld, W. E. A., and Berkhout, A. J., 1994, Prestack depth migration by means of controlled illumination: Geophysics, **59**, 801–809.

Ristow, D., and Ruhl, T., 1994, Fourier finite-difference migration: Geophysics, **59**, 1882–1893.

—, 1997, 3-D implicit finite-difference migration by multiway splitting: Geophysics, **62**, 554–567.

Rosales, D., and Rickett, J., 2001, PS-wave polarity reversal in angle domain common-image gathers *in* 71st Ann. Internat. Mtg. Soc. of Expl. Geophys., 1843–1846.

Rothman, D. H., Levin, S. A., and Rocca, F., 1985, Residual migration - Applications and limitations: Geophysics, **50**, 110–126.

Rousseau, J. H. L., Calandra, H., and de Hoop, M. V., 2003, Three-dimensional dept imaging with generalized screens: A salt body case study: Geophysics, **68**, 1132–1139.

Rousseau, J. H. L., and de Hoop, M. V., 1998, Modeling and imaging with the generalized screen algortihm *in* 68th Ann. Internat. Mtg. Soc. of Expl. Geophys., 1937–1940.

Sava, P., 2003, Prestack residual migration in the frequency domain: Geophysics, **67**, 634–640.

Sava, P., and Biondi, B., 2004a, Wave-equation migration velocity analysis - I: Theory: Geophysical Prospecting, in press.

—, 2004b, Wave-equation migration velocity analysis - II: Subsalt imaging examples: Geophysical Prospecting, in press.

Sava, P., Biondi, B., and Etgen, J., 2004, Diffraction-focusing migration velocity analysis with application to seismic and GPR data: submitted for publication in Geophysics.

Sava, P., Biondi, B., and Fomel, S., 2001a, Amplitude-preserved common image gathers by wave-equation migration: 71st Ann. Internat. Mtg., Soc. of Expl. Geophys., Expanded Abstracts, 296–299.

—, 2001b, Amplitude-preserved common image gathers by wave-equation migration *in* 71st Ann. Internat. Mtg. Soc. of Expl. Geophys., 296–299.

Sava, P., and Fomel, S., 2001, 3-D traveltime computation using Huygens wavefront tracing: Geophysics, **66**, 883–889.

—, 2002, Wave-equation migration velocity analysis beyond the Born approximation *in* 72nd Ann. Internat. Mtg. Soc. of Expl. Geophys., 2285–2288.

—, 2003, Angle-domain common image gathers by wavefield continuation methods: Geophysics, **68**, 1065–1074.

—, 2004, Seismic imaging using Riemannian wavefield extrapolation: submitted for publication in Geophysics.

Sava, P., and Guitton, A., 2004, Multiple attenuation in the image space: Geophysics, in press.

Shen, P., Symes, W. W., and Stolk, C. C., 2003, Differential semblance velocity analysis by wave-equation migration *in* 73rd Ann. Internat. Mtg. Soc. of Expl. Geophys., 2132–2135.

Shragge, J., and Sava, P., 2004, Adaptive phase-rays wavefield extrapolation: 74th Ann. Internat. Mtg., Soc. of Expl. Geophys., Expanded Abstracts.

Soellner, W., and Yang, W., 2002, Diffraction response simulation: A 3D velocity inversion tool *in* 72nd Ann. Internat. Mtg. Soc. of Expl. Geophys., 2293–2296.

Stoffa, P. L., Fokkema, J. T., de Luna Freire, R. M., and Kessinger, W. P., 1990, Split-step Fourier migration: Geophysics, **55**, 410–421.

Stolk, C., and Symes, W., 2002, Artifacts in Kirchhoff common image gathers *in* 72nd Ann. Internat. Mtg. Soc. of Expl. Geophys., 1129–1132.

Stolt, R. H., 1996, Short note - A prestack residual time migration operator: Geophysics, **61**, 605–607.

Stolt, R. H., and Weglein, A. B., 1985, Migration and inversion of seismic data: Geophysics, **50**, 2458–2472.

Stork, C., 1992, Reflection tomography in the postmigrated domain: Geophysics, **57**, 680–692.

Symes, W. W., and Carazzone, J. J., 1991, Velocity inversion by differential semblance optimization: Geophysics, **56**, 654–663.

Synge, J. L., and Schild, A., 1978, Tensor Calculus: Dover.

Tarantola, A., 1984, Inversion of seismic reflection data in the acoustic approximation: Geophysics, **49**, 1259–1266.

—, 1986, A strategy for nonlinear elastic inversion of seismic reflection data: Geophysics, **51**, 1893–1903.

—, 1987, Inverse Problem Theory: Elsevier.

Thomson, T., 1999, The gap between seismic ray theory and full wavefield extrapolation: Geophys. J. Int, **137**, 364–380.

Vaillant, L., Sava, P., Biondi, B., and Calandra, H., 2000, 3-D wave-equation migration of a common-azimuth North Sea dataset: 62nd Mtg., Eur. Assoc. Geosc. Eng., Abstracts, 231–235.

de Vries, D., and Berkhout, A. J., 1984, Velocity analysis based on minimum entropy: Geophysics, **49**, 2132–2142.

Woodward, M., 1990, Wave equation tomography: Ph.D. thesis, Stanford University.

Woodward, M. J., 1992, Wave-equation tomography: Geophysics, **57**, 15–26.

Woodward, M. J., and Rocca, F., 1988, Wave equation tomography *in* 58th Ann. Internat. Mtg. Soc. of Expl. Geophys., Session:S21.3. Slide set available from the SEG Publications Department.

Wu, R. S., and Toksoz, M. N., 1987, Diffraction tomography and multisource holography applied to seismic imaging: Geophysics, **52**, 11–25.

Wu, R. S., Wang, Y., and Gao, J., 2000, Beamlet migration based on local perturbation theory *in* 70th Ann. Internat. Mtg. Soc. of Expl. Geophys., 1008–1011.

Xu, S., Chauris, H., Lambare, G., and Noble, M. S., 1998, Common angle image gather: A new strategy for imaging complex media *in* 68th Ann. Internat. Mtg. Soc. of Expl. Geophys., 1538–1541.

Yilmaz, O., 1979, Prestack partial migration: Ph.D. thesis, Stanford University. URL `http://sepwww.stanford.edu/oldreports/sep18/index.html`.